"NOVEL MINIATURIZED ANTENNAS AND ARRAYS FOR IMPLANTABLE, INGESTIBLE AND BODY-WORN APPLICATIONS"

A thesis submitted
in fulfilment of the requirements for the degree of
Doctor of Philosophy (PhD)

by

Farhad Gozasht

University of Technology Sydney

June 2018

Certificate of Original Authorship

I certify that the work in this thesis has not previously been submitted for a degree nor has it been submitted as part of requirements for a degree except as fully acknowledged within the text.

I also certify that the thesis has been written by me. Any help that I have received in my research work and the preparation of the thesis itself has been acknowledged. In addition, I certify that all information sources and literature used are indicated in the thesis.

This research is supported by an Australian Government Research Training Program.

Signature of Student: Production Note:
Signature removed prior to publication.

Date: 12.June.2018

ACKNOWLEDGEMENTS

There are many people, whom I am indebted to, without whose assistance, this thesis would not have been possible. I would like to take this opportunity to express my outmost gratitude to them.

I consider it my privilege to work with A/Prof. Ananda M. Sanagavarapu. His motivation, supervision and commitment to his beliefs in strengthening my fundamentals have been instrumental in my growth.

I would like to explicitly thank Mr. Russell Nicholson for his efforts in providing me with the measurement facility and safe experimental environment without which, this thesis would not be in its present state. I wish to express my heartfelt gratitude to Mr. Raymond Clout for his support and providing the SAR measurement tools, that added value to my research work.

Furthermore, the CHT group needs a special mention here, for standing by me and making my life here eventful.

Last, but never the least, I am very grateful to my family, who have always worked hard to help me reach my goals without much discomfort.

Above all, I thank the Almighty for showering me with His Grace & Blessings.

Farhad Gozasht

Contents

CHAPTER – 02

A REVIEW OF EXISTING LITERATURE

CHAPTER – 03

DUAL SLOT PIFAs FOR BODY IMPLANTABLE DEVICES

CHAPTER – 04

TRANSMITTER AND RECEIVER ANTENNA FOR INGESTIBLE WIRELESS CAPSULE ENDOSCOPY SYSTEMES

LIST OF FIGURES

LIST OF TABLES

LIST OF ARONYMS USED

Acronym	Expansion
ACMA	Australian Communications and Media Authority
ANSI	American National Standards Institute
A.R	Axial Ratio
AWGN	Additional White Gaussian Noise
BP	Blood Phantom
BS	Base Station
BSN	Body Sensor Node
CAD	Computer Aided Design
CP	Circular Polarization
CP-PIFA	Circular Polarization Planar Inverted-F Antenna
CSRR	Complementary Split Ring Resonator
CPW	Coplanar Waveguide
CSF	Cerebrospinal fluid
DGF	Dyadic Green's Function
DS-PIFA	Dual Slot Planar Inverted-F Antenna
EIRP	Equivalent Isotropically Radiated Power
EM	Electromagnetic
ERP	Effective radiated power
FCC	Federal Communications Commission
FDTD	Finite-difference Time Domain
FHBP	Full Human-Body Phantom
FPCB	Flexible Printed Circuit Board
GI	Gastrointestinal

HWD	Half-Wavelength Dipole
ICP	Intracranial Pressure Monitoring
IEEE	Institute of Electrical and Electronics Engineers
IMD	Implantable Medical Devices
LNA	Low Noise Amplifier
IOP	Intraocular pressure
ISM	Industrial, Scientific and Medical
LS	Least Squares
MBAN	Medical Body Area Network
MBSS-PIFA	Multi Band Single Slot Planar Inverted-F Antenna
MedRadio	Medical Device Radio communications Service
MICS	Medical Implant Communications Service
MLE	Maximum Likelihood Estimation
MRI	Magnetic Resonance Imaging
NI-LMH	Non-Invasive Local Microwave Hyperthermia
NFF	Near-field Focused
PL	Path Loss
PIFA	Planar Inverted-F Antenna
PDF	Probability Density Function
PDMS	Polydimethylsiloxane
PEC	Perfect Electric Conductors
RF	Radio Frequency
RFID	Radio Frequency Identification
RMSE	Root Mean Square Error
RSSI	Received Signal Strength Indicator
Rx	Receiver

SAR	Specific Absorption Rate
SLL	Side lobe level
SS-PIFA	Single Slot Planar Inverted-F Antenna
SRR	Split Ring Resonator
TAP	Transmitter Antenna Position
TBI	Traumatic Brain Injury
Tx	Transmitter
UWB	Ultra Wide Band
VHF	Very High Frequency
VNA	Vector Network Analyzer
WBAN	Wireless Body Area Networks
WCE	Wireless Capsule Endoscopy
WC-PLA	Wideband co-planar loop antenna
WFC-PLA	Wideband folded co-planar loop antenna
WFOLA	Wideband folded oval loop antenna
WMTS	Wireless Medical Telemetry Service
WOLA	Wideband oval loop antenna
WPC-PLA	Wideband printed co-planar loop antenna
WPOLA	Wideband printed oval loop antenna
WPT	Wireless Power Transfer

LIST OF SYMBOLS USED

Symbol	Quantity	Symbol	Quantity
α	Attenuation constant	n	Path loss exponent
β'	Phase constant	Pl	Path Loss
λ	Wavelength	ρ	Density
λ'	Wavelength in lossy mediums	$P_r(d)$	received power
ε	Dielectric constant	P_t	transmitted power
μ	Permeability	σ	Conductivity
G_t	Transmitter antenna gain	G_r	Receiver antenna gain
ϵ_r	Relative permittivity	G_c	Coding gain
S	Scattering parameter	G_d	Fixing deterioration
d	Tx-Rx separating distance	E_b	Energy per bit
$\tan\delta$	Loss tangent	R	Bit rate
l_m	Distance where the mutual coupling reduces significantly between the Tx and Rx antennas	X	Zero mean log-normally distributed random variable
L	Miscellaneous system losses	φ	Phase shift
N_0	Noise power spectral density	VF	Velocity factor
c_b	Blood specific heat	c	Specific heat
T_b	Blood Temperature	T	Temperature
η	Power transmission efficiency	F	Blood flow rate
L_{feed}	Antenna feeding loss	K	Thermal conductivity
C	Distributed capacitance	L	Distributed inductance
Z_0	Characteristic impedance	t	Time
λ_{eff}	Effective Wavelength	$E_{mn}(p)$	Array radiated field
I_0	Feeding current amplitude	F_0	Array focal point

ABTRACT

Implantable medical devices (IMDs) introduced to monitor and transfer physiological information from inside the human body have superb potentials to provide major contributions to disease diagnosis, prevention and therapy. Moreover, minimally invasive biomedical devices helps to reduce the period of long-term hospitalization, so that enhancing the patients' quality of life. Understanding and developing biotelemetry devices, recording/transmitting data from inside the body to the external base station, requires a multi-disciplinary approach. Such a challenging task merges applied solutions, concepts and models from various fields, including biology, electronics, electromagnetism and package/system engineering. Among the device components, the transmitter antenna plays a key role.

Antenna design for biotelemetry applications is extremely challenging due to the effect of the surroundings on the radiator, the essential requirement to miniaturize the antenna structure size, reduced antenna efficiency and the robust effect of multipath losses. More specifically, in this thesis, I design and fabricate several antennas to be integrated in ingestible and implantable devices useful for remote monitoring as well as data biotelemetry. This work also focuses on arrays of body-worn antennas for both wireless endoscope base stations and cancer treatment nearfield microwave systems. Here, my aim is to reduce the physical size of the implantable antennas at specified operating standards frequency bands, while maintaining the antenna electromagnetic performance satisfactory. To achieve this, I introduce and use valuable miniaturization techniques for implantable patch antennas for biotelemetry applications.

Additionally, I design and fabricate compact microwave systems for cancer treatment using electromagnetic (EM) energy. Non-Invasive Local Microwave Hyperthermia (NI-LMH), which is my interest in this thesis, is a heat treatment serves to enhance the effectiveness of chemotherapy or radiation therapy and leads to gain remarkable results. The system may directly apply heat to a fairly small specific area such as tumors to destroy the local cancer cells. To achieve this, the heat effect is developed in the target by the transmission of EM energy, using array of antennas, which is adjusted in frequency, time and strength in order to work together to form a focus in the target. This places high demands on the precision of the system.

In this thesis, I present different planar antenna array for non-invasive microwave hyperthermia applications. The new Near Field Focused (NFF) arrays operates at ISM 2.45 GHz band and consists of 5 to 25 miniaturized dual slot PIFAs, depends on the array geometry arrangement. The arrays immersed inside a coupling bolus occupies a very small volume of space results in an easy fitting to contoured patient anatomy. These arrays, which are low profile and lightweight, have both superficial and deep focusing properties. The novel NFF body worn arrays are capable to focus on a single target with a high level of accuracy to concentrate the EM energy only on the target. I employ optimized dual slot PIFAs as array elements to reduce the size of the focusing area so that destroying very small tumors and avoid heating up the surrounding healthy cells.

I have also introduced size reduced NFF array to simplify the feeding network of the applicator and reduce the system cost, this array configuration satisfies system requirements and can focus on small targets precisely while keep the penetration depth high enough to heat up the deep seated targets.

In addition, the performance of both fabricated narrowband and wideband single antennas and array of antennas verified using experimental tissue mimicking phantoms. To validate the dielectric properties of experimental phantoms, over different frequency bands, dielectric probe kit employed, furthermore, optical fibre thermometers employed to confirm specific absorption rate (SAR) values for implanted radiators.

Index Terms – Antennas in lossy matter, Electrically small antennas, PIFA miniaturization method, SAR, Biocompatible insulation, Implantable and ingestible antennas, Rx and Tx antenna for wireless capsule endoscopy, Body centric wireless communications, compact antenna for head implants, Body Sensor Node (BSN), standards biotelemetry bands, array antenna for non-invasive local hyperthermia, Medical Device Radio communications Service (MedRadio), Medical Implanted Communication System (MICS).

CHAPTER – 01

1. INTRODUCTION

Electromagnetism has been continuously growing and facilitate medical care since the first X-ray medical experiment conducted at the end of the 19th century. With increasing sophistication of wireless communication, implantable and wearable medical devices integrated with wireless small sensors, ever-expanding ranges of diagnostic and therapeutic applications are being followed by the commercial and research organisations. These innovative compact wireless devices include but not limited to, context aware implanted pacemakers and cardiac defibrillators, fully wireless active platform for monitoring parameters in the vascular system (cardiac pressure), integrated drug delivering therapeutic devices i.e. quick delivery of insulin in diabetics, implantable wireless neural recording system to measure local neural activity and transmit action potential occurrences to an external interface, Intracranial Pressure Monitoring (ICP), implantable wireless pressure sensing paradigm for long range and continuous intraocular pressure (IOP) monitoring of glaucoma patients, acute and chronic bladder pressure monitoring system using low power wireless micromanometer and wirelessly controlled valves in the urinary tract operating when patient needs restoring bladder control [1-3].

Additionally, wireless wearable and implantable devices provide economic benefits to the healthcare system. For instance, remote monitoring healthcare devices may facilitate the diseases prevention and favour the hospital at living place. The

model of such a system is depicted in Figure 1-1. Both economical aspects reduce the cost of healthcare significantly by decreasing the hospitalization period and treating the patient at home.

For overall system design, the design of miniaturized antennas and analysis of the wireless channel for communicating with the device, are the most important research challenges due to the complex dielectric characteristics of human body and significant power consumption. This work deals with analysis, realization, design and characterization of body-worn arrays and integrated antennas for EM energy deposition and data telemetry. This is a multidisciplinary research area that merges several electromagnetism aspects (i.e. field propagation in lossy matters, small antenna design and theory, and interactions with biological tissues, etc.) with privacy and security matters [4], telecomm and biocompatible packaging [5, 6], and biological and material science [7].

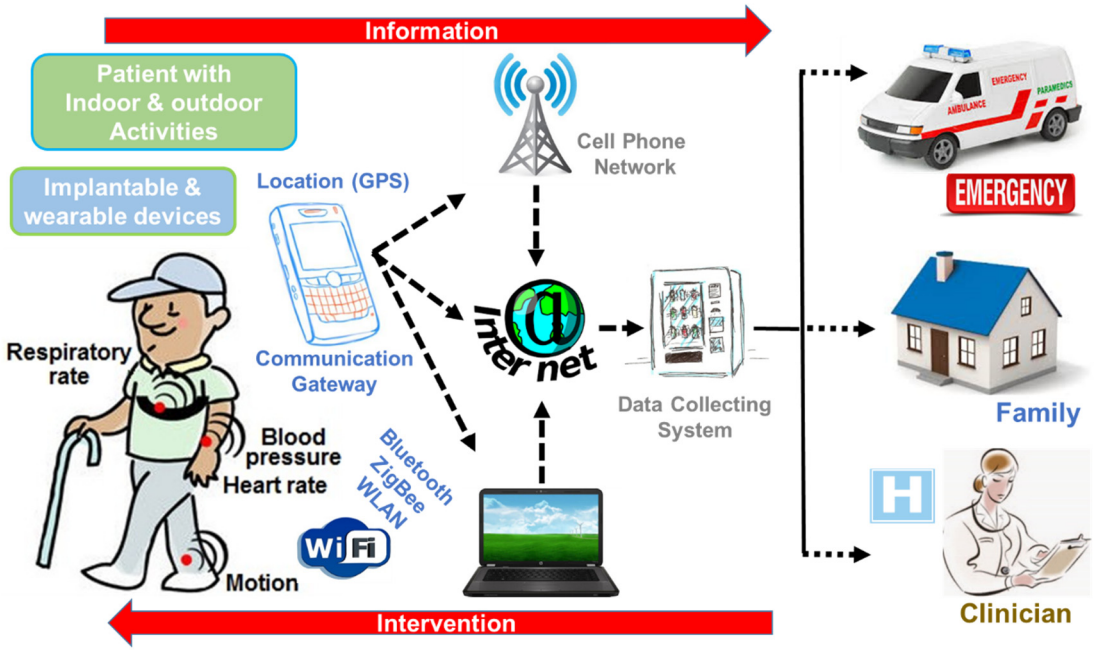

Figure 1-1. Example of monitoring home healthcare system using wireless implantable devices.

1.1 Principal Characteristic of Wireless Body-worn and Implantable Systems for EM Energy Deposition and Data Biotelemetry

The main goal of exposing the electromagnetic energy inside an unhealthy human tissue, using array of antenna for a microwave cancer treatment, is to kill the cancerous cells. On the other hand, the primary aim of employing wireless implantable devices for healthcare monitoring systems is providing reliable data from inside the human body to the base station (BS) outside the body. These systems designed for biomedical applications involves several important aspects. Such aspects, for both cancer treatment and healthcare monitoring, identified from the antenna engineer point of view, are illustrated in Figure 1-2 and Figure 1-3 respectively.

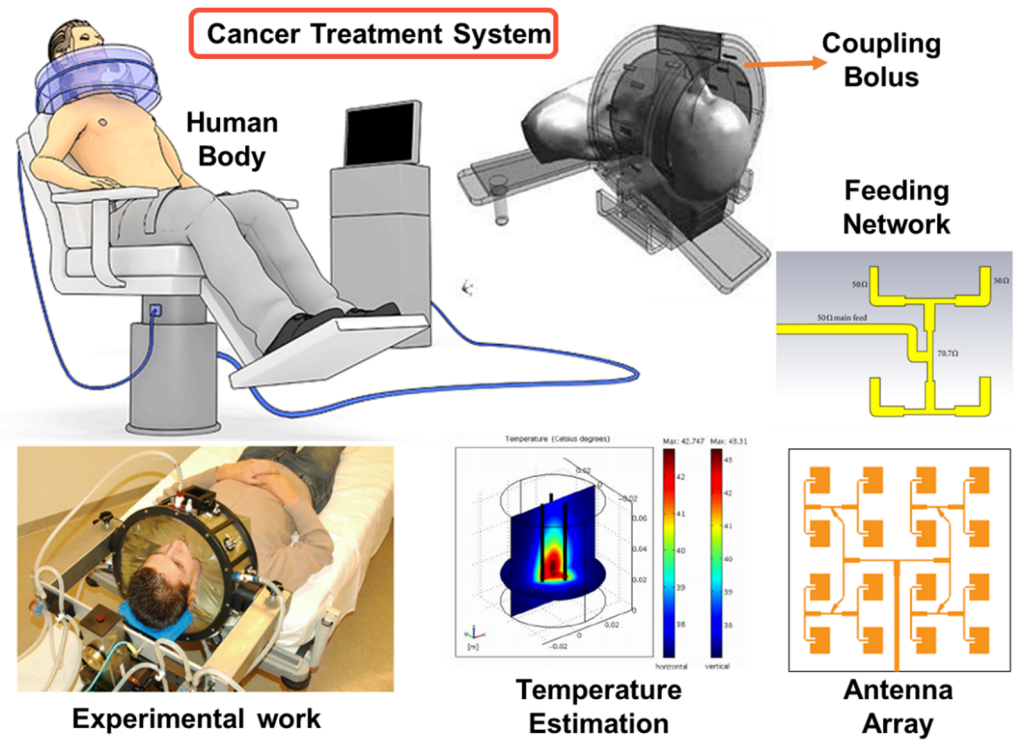

Figure 1-2. Different aspects from antenna engineer point of view for microwave cancer treatment system.

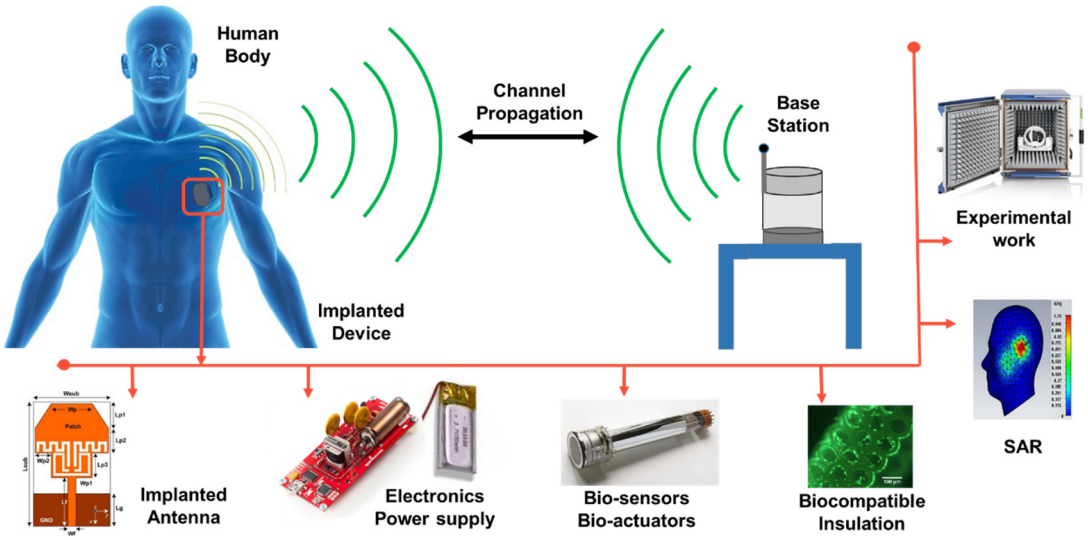

Figure 1-3. Different aspects from antenna engineer point of view for wireless implantable system for data biotelemetry.

1.1.1 Frequency Bands and Spectrum Allocation

This section reports standard bands of frequency and relevant Australian Communications and Media Authority (ACMA) regulations for the current and emerging wireless biomedical devices, also outlines similarities and differences with those of Federal Communications Commission (FCC). Wireless medical devices and networks operate in several frequency bands, under various national and international rules, based on the application, operational range, data rate and required power transfer. In this work, I focus on standard biotelemetry bands such as Industrial, Scientific and Medical (ISM) band, 2400 MHz, and Implant Communications Service (MICS) band, 400 MHz [8]. limitations of Equivalent Isotropic Radiated Power (EIRP) for ISM and MICS bands are -20 dBm and -16 dBm respectively. However, the demand on radio spectrum is increasing for use in wireless biomedical applications. This demand is motivated by a rapid growth in the usage rate of current medical devices, emerging field of biomedical applications, development in wireless technology, and quality/reliability and provision of wireless healthcare. Therefore, in

this research, miniaturized antennas operating over different wireless medical telemetry service such as (WMTS), 1430 MHz, and ZigBee, 868 MHz standard bands are also proposed. Since different regulatory frameworks may be defined in different countries, it is necessary to refer to the national licensing authority.

Medical systems commonly use 5.8 GHz, 2.4 GHz, 900 MHz and 433 MHz bands where the FCC emissions regulations and power level requirements are secured. The FCC has set very strict rules for well-established MICS band 402 - 405 MHz, allocated only for implantable medical device applications, to ensure interoperability. Moreover, the FCC specifically allocated the ultra wide band (UWB) band, 3.1 - 10.6 GHz for broad band applications, and 608 - 614 MHz, 1395 - 1400 MHz and 1429 - 1432 MHz frequency bands for WMTS applications.

According to ACMA, “Australian Radiofrequency Spectrum, Plan 2017”, the band of 918 - 926 MHz is also allocated for medical applications [9]. Moreover, ACMA nominated the following radio frequency Spectrum for bio medical applications as tabulated in Table 1-1. Where the use of these bands of frequency for biomedical application is subject to special authorisation from administrations whose radio communication services might be affected. Australia has utilised the benefits of imported VHF wireless biomedical telemetry products under Biomedical Sharing Broadcast Television Bands arrangements. For many years biomedical telemetry systems have shared radio frequency spectrum successfully with TV broadcasting services because of outstanding technical features of both services [10]. Most recent biomedical telemetry facilities and equipment operate over higher frequency bands. However, some biomedical devices employed in Australia beforehand may use the 520 - 820 MHz band; low power biomedical devices allowed to utilise unused television channels for many years.

Table 1-1
FREQUENCY SPECTRUM ALLOCATION FOR BIOMEDICAL APPLICATIONS [9].

Band	Start Frq.	Stop Frq.	Center Frq.	Bandwidth
VHF	40.66 MHz	40.70 MHz	40.68 MHz	40KHz
MICS	433.05 MHz	434.79 MHz	433.92 MHz	1.74 Mhz
UHF	902 MHz	928 MHz	915 MHz	20 MHz
ISM	2400 MHz	2485 MHz	2450 MHz	85 MHz
WMT	5725 MHz	5875 MHz	5800 MHz	150 MHz

1.1.2 Human Body

The human body is complex, dispersive and highly lossy environment for wireless signals. Accurate analysis and modelling of exposed EM fields and propagation in human body is one of the main requirements for designing the implantable and body-worn antennas for wireless sensing.

1.1.3 Array of Antennas

To focus the EM energy on a small desired spot inside the body, the radiated beam has to be narrow, this can be achieved by employing a properly designed array of antennas. Hence, the configuration of active array play a key role for the microwave cancer treatment system. Furthermore, the transmitted signal from the implanted device inside the body can be received by the body-worn antenna array from different directions. The performance of the antennas such as directivity, efficiency, polarization and the sensitivity of the receiver are the main importance for the receiving unit of a monitoring healthcare system.

1.1.4 Feeding Network and Coupling Bolus

The feeding network for array of active antennas has to be carefully designed to match with array requirements and system specifications. This module may directly effect and control the amplitude and phase of each single element in the array to form the radiation beam. The feeding network also has to provide quality impedance matching to maintain the antenna radiation efficiency remarkable.

The coupling bolus is also necessary, especially for high power radiation, to prevent body skin burns. It also helps to match the antenna impedance when placed fairly close to the human body skin.

1.1.5 SAR and Temperature Rise

For wireless active healthcare systems, power limits are also determined to avoid hazardous heating of the biological tissue. Electromagnetic field deposit energy into the human body when passing through, this will raise the tissue temperature depend on the exposed power and operating frequency. The temperature increment of human body by microwave can be defined from specific absorption rate (SAR) and the bio-heat transfer equation. The bio-heat transfer equation defines pace of the temperature elevation with SAR, blood perfusion, and thermal conductivity, simply, it represents the relationship between the rate of electromagnetic energy absorbed into the human body and the temperature incensement.

The transmitted maximum power from any active implanted device should comply with the maximum spatial average SAR limitations, 2W/kg per 10 gram averaging [11] and 1.6 W/kg per 1 gram averaging [12].

1.1.6 Base Station

Typical base stations for healthcare systems consists of different sub-systems such as receiver module including receiving antennas, control sub-systems to drive the entire unit, data collecting and storage sub system and internet gateway. The performance and sensitivity of the receiver, beside lightweight and portability are essential requirements for realization of systems which target real life applications.

1.1.7 Implantable Antennas

Wireless implantable devices are restricted to electrically small radiators which need to be fully characterised and effectively coupled to the transceiver. The design of a particular antenna is the key aspect of a system operating in healthcare monitoring system. The specifications such as resonating frequency, bandwidth and radiation efficiency beside coupling with highly conductive biological tissues are crucial for the data biotelemetry. Moreover, the overall size of the implant depends on the size of the attached antenna considerably; as the operating frequency decreases, the antenna size increases, hence, antenna physical size miniaturization is necessary.

1.1.8 Channel Propagation

Another key aspect of the home healthcare monitoring system is the analysis of electromagnetic wave propagation from the implanted device to the base station. The study and analysis of the multipath propagation and scattering of the electromagnetic waves, due to the nearby objects, is essential since the implanted devices mainly employed for indoor application. The channel analysis beside proper design of the base station antennas improve the entire system performances significantly.

1.1.9 Insulations

To avoid any harmful and adverse reaction of the human body living tissues, it is necessary to use biocompatible insulation for any implantable device. This will also protect the antenna surface from the tissue fluid. However, the dielectric properties of such an insulation is different from the free space, so that the antenna radiation characteristics may change significantly.

1.1.10 Bio Actuators and Bio Sensors

Based on the application and placement of the device in the human body, the bio actuators and biosensors may be integrated with the implantable device. Active implants such as drug delivery apparatus or monitoring devices such as capsule endoscopy and instance glucose meter already employed such actuators and sensor.

1.1.11 Electronics and Power Supply

The functionality of the implantable device, base station and microwave cancer treatment system depend on the electronic components generating signals or providing signal processing and data communication. The power supply capacity and power consumption of the apparatus, determine the lifetime of the device. To extend the battery life, different solutions i.e. wireless power transfer and energy harvesting are investigated.

1.1.12 Experiments and Characterization

The last but not least is to validate the calculations results using the equivalent human body mimicking phantoms, at this stage, it is required to test the performance of the antenna alone and confirm the functionality of all the components constituting the wireless systems. For safety and regulatory requirements, it is also necessary to carry out in vitro and in vivo measurements to verify the appropriate functioning of the entire system and prior implanting in humans.

1.2 Thesis Outlook

While having a complete system of non-invasive microwave hyperthermia and wireless implantable and wearable devices in mind, the key focuses of this dissertation are on the following main aspects of wireless healthcare systems:

- Implantable Antennas for human body
- Embedded antennas in head
- Body-worn arrays
- Arrays for thermotherapy
- Human Body
- Characterization and Experiments.

This thesis investigates the realization of Body-worn antennas, NNF, arrays and embedded antennas for healthcare systems and biomedical devices. The context and the organisation of this dissertation are presented in next subsection.

1.2.1 Thesis Outline and Original Contributions

This subsection summarizes the contents, findings and the original contributions of each chapter of this dissertation. An introduction about the wireless healthcare system is given in Chapter 2 while each chapter includes a selective literature review. the four main chapters of this work focus on the realization, design and characterization of body-worn arrays and implantable antennas. These reviews are presented in chapter 3, chapter 4, chapter 5 and chapter 6 of this thesis.

Chapter 3, Dual Slot PIFAs for Body Implantable Devices: In this chapter, a general design methodology for miniaturized DS-PIFAs is presented. This generalized method is employed to design different compact implantable antennas operating in different standard biotelemetry bands. These antennas could be used for different types of implants and applications. Since the antenna radiation performance, including radiation efficiency, bandwidth, etc., is dependent on the employed human tissue model, the available possibilities is presented and discussed for mimicking the human tissue in terms of numerical studies and physical realizations. This chapter is a key chapter since it establishes the basic background for the concepts and investigations in the following chapters.

Original scientific contribution: New miniaturized implantable antennas, covering different biotelemetry bands, are proposed which radiate highly efficient. In addition, realistic human body employed to validate the performance robustness of the proposed implantable antennas over a variation of thickness and dielectric properties of surrounding tissue. This investigation leads to the formulation of a strategy to design versatile compact embedded antennas.

Chapter 4, Transmitter and Receiver Antennas for Ingestible Wireless Capsule Endoscopy Systems: This chapter has three main sections, the first one deals with the utilization of advance loop antenna structure for highly efficient wireless capsule endoscopy antenna. The second part of this chapter investigates the suitable receiving antenna that its radiation performance is perfectly match with the proposed folded loop antenna integrated with the wireless capsule endoscopy microsystem. This potentially improves the overall system performance specifically the transmission from the embedded antenna inside the human body to the external receiver. The proposed body worn antenna later employed to design an array of body worn antenna to enhance the communication quality. The third part quantifies and estimates the loss of a communication path between the wireless capsule device and base station antenna used for receiving high quality images. The path losses must be precisely estimated to establish efficient communication. Therefore, I estimate and verify the path loss between the proposed printed loop antenna and body worn array for a power transfer communication. I also evaluates the effect of variation of capsule location and orientation on the path loss for in-on body communications.

Original scientific contribution: The proposed folded coplanar loop antenna shows a very wide band impedance bandwidth, small size and reduced absorbed power by GI tract. In the other hand, the proposed CP body worn array is perfectly match with the wireless capsule endoscopy system requirements and improves the communication link quality. The results of pathloss estimation provides a good source of data for engineers and doctors in the field. It also represents the link margins for different locations and orientations of the wireless capsule inside the body.

Chapter 5, Miniaturized Antennas for Head Implantable Devices: Design, realization and in vitro characterization of head implantable antennas are presented in this chapter. The proposed radiators are designed according to the strategy formulated in the previous chapter. Design process is based on multiple aspects such as antenna size, radiation efficiency, bandwidth, possible interference as well as SAR values. The resulting miniaturized radiators could cover different biotelemetry bands suitable for head implantable devices, furthermore, the proposed SS-PIFA has triple band capability appropriate for body implementation. The analysis in this chapter delivers useful guidelines for a precise evaluation of the radiation performance. This chapter also elaborates effective parameters that must be considered during the design and surgery processes. The related measurements including SAR in the experimental mimicking phantom are presented.

Original scientific contribution: The state of the art head implanted radiators are proposed in such a way that clearly identify the challenges for the realization of such antennas. I present three new categories of implantable antennas all featuring superior physical and electromagnetics characteristics. The original strategy for the design and validation of head embedded radiators is presented based on the comprehensive knowledge acquired.

Chapter 6, Near Field Focused Body-Worn Array for None-invasive Microwave Hyperthermia: In this chapter, a derivative investigation of this study for near field focusing array design is presented for none-invasive microwave hyperthermia application. It covers the NFF array design as well as the calculation and measurement results of the proposed system. Various compact antenna array topologies are discussed and process variations are considered during the array design to achieve robust applicator. The comprehensive knowledge necessary for the design

of NFF array immersed inside a dielectric bolus and placed close to the lossy biological tissues is presented and their consequences on the characteristics of the proposed array are discussed. Consequently, the necessary electronics interface including array feeding network is designed and optimized in great detail to achieve the most reliable focusing properties. This chapter deals with the measurement of compact NFF antenna array at the component level. Effects of mutual coupling between array elements when characterizing the radiators impedance matching properties, in presence of human body phantom, are discussed.

Original scientific contribution: The proposed NFF arrays answers to minimum number of hot spots requirements, small focusing area demands and tight packaging constraints. The novel compact applicator optimally integrates with all the components of none-invasive microwave hyperthermia systems. Realistic human tissue phantom are employed to provide extensive information on focusing and temperature distribution performance of the proposed array.

Finally, this dissertation concluded, in Chapter 7, by signifying the major findings in this study as well as recommendations as a continuation of this research work.

CHAPTER – 02

2. A REVIEW OF EXISTING LITERATURE

2.1 Background

The challenging demand to achieve miniaturized implantable device and robust communication links reflects on complexity of the embedded antenna design. In fact, the radiator, among all the components required for implantable biotelemetry device, is a key component for improved wireless performances and miniaturization of the entire device.

Implantable systems are widely studied for several fields of applications such as tracking for both animals and humans (i.e. tracking lost pets or dependent people) [13]. Furthermore, embedded small microstrip patches have been employed for numerous sensing applications such as sensing the existence of dielectric materials [14, 15], measurement of moisture [16] and dielectric properties [17, 18], and geophysical applications such as well logging [19, 20]. In addition, wire antennas, coaxial antennas and arrays implanted in a number of lossy environments have been previously investigated for such applications [13]. Furthermore, miniaturized antennas have also been employed therapeutically for different applications such as cancer treatment i.e. microwave local hyperthermia [21], monitoring vital signs or transmitting data such

as intracranial pressure and gastrointestinal (GI) tract images, cardiac ablation [22] and balloon angioplasty [23].

For instance, to enhance the quality of life for patients transferring diagnostic information using wireless technology from an implanted electronic device to an external RF receiver, such as a pacemaker for human safety and care, has been investigated in [24]. Patients with the biomedical device implanted in their body frequently coming back to the clinic for examinations and checkups to verify their and the implant status. The recorded data by the embedded device would be wirelessly transmitted to the base station by employing the RF wireless technology. This might be happening while the patient is waiting in the sitting room and waiting in the queue. More over some patients may need more regular checks even every day or every six hours. In this case a home healthcare monitoring system can be used where patient lives and then the unit communicates with the medical embedded device and may also connected to the internet or digital landline to send and receive data frequently to the base station located in the hospital [25].

In this chapter, a review of literature for wearable and implantable antennas featuring narrow and wide band useful for biomedical applications will be reported. Depends on the application, the location of the implant, so that the antenna, will be determined, this could be anywhere close to the human body for body-worn antennas or most commonly positions inside the human body such as head, arm, chest, eye and tooth for implantable antennas and devices.

2.2 Implantable and Wearable Antennas

Several types of antennas have been proposed for a range of implantable wireless communication applications. Traditionally wire coils are employed for both data transmitting and power coupling. However, the performance of these systems is restricted by their poor efficiency and limited operating distance. Moreover, coils of wire around a ferrite or dielectric core, called Inductive antennas, have been successfully employed for biotelemetry [26, 27], although, size and weight cause serious issues beside the low data rates. Also dipoles and microstrip antennas implanted in the arms and the shoulders were investigated for cardiac telemetry using the Finite Difference Time Domain (FDTD) method [28, 29].

Implantable and body-worn antenna design faces major challenges including size miniaturization, impedance bandwidth enhancement, improved radiation performance, and patient safety [30-32]. In this context, electrically small implantable antennas form an essential and integral part of any biomedical wireless communication system, the implanted antenna acts as a transmitting radiator in the proposed one-way communication link. To establish efficient and effective wireless links with the implanted device, a corresponding wearable receiver wideband antenna/ array has to be designed with unidirectional radiation characteristics, circular polarization, high gain, small size and low profile. Furthermore, to deposit EM energy for microwave hyperthermia cancer treatment, it is necessary to design an array of antennas as an applicator featuring small size, low profile, high gain and low side lobe level (SLL).

2.2.1 Implantable Antennas: Applications and Miniaturization

For wireless healthcare system, not only the antenna technical specification is dictated by the system requirements but also the antenna physical characteristics such as size and shape is determined by the space available in the system. This is more challenging when dealing with implantable radiators for biotelemetry applications. Implantable devices such as cardiac pacemaker and continuous glucose monitoring devices should to be implanted in the chest. Design of a dual band implantable antenna for continuous glucose monitoring which could be implanted either in chest or arm is presented in [31] by Topsakal et al. This work demonstrate design of a dual band small size implantable antenna proposed for continuous glucose monitoring applications using ISM band 2.4 GHz and MICS band 400 MHz.

Moreover implantation in head is also studied in [33, 34] for application such as increased intracranial pressure (ICP) monitoring, tracking of persons with Alzheimer's disease, brain wave sensors for paralyzed patients and etc. Characterization of implantable planar inverted-F antennas (PIFAs), designed for ICP monitoring at 2.4 GHz, is presented in [35]. Since the human body is a diverse multi-layer media with varying dielectric properties, the surrounding tissue of the implanted device has significant effects on the antenna performance; however, high performance antennas still can be used for different locations and biomedical applications inside the human body [36].

Choosing a higher resonance frequency band such as ISM band 2.4 GHz is another alternative way to reduce the antenna physical size. Additionally, a larger bandwidth is covered by ISM band allows for higher bitrates. Implantable H-shaped slot antennas are proposed for 2400 MHz ISM band [37, 38]. To validate simulation

results, measurements are carried out but no biocompatible material used to surround the antenna and the feeding cable. Dual band biomedical implantable radiators are presented in [31, 39] operating at MICS and ISM bands. Measurements are conducted employing human skin mimicking gel and in rat skin phantom respectively, however, none of the antennas are not surrounded in biocompatible cover. In [40] the presented cardiovascular stent, resonating at 2400 MHz, implanted in a live porcine subject. However, the stents have no insulation material and have a direct contact with the tissue. Furthermore, the communication range is short due to the extreme attenuation of EM field in human body at 2.4 GHz. Here, for implantable biomedical applications, designing electrically small antennas are extremely challenging because of the effect of the environment on the antenna, the robust effect of multipath losses and the essential requirements to reduce the antenna size so that reduced antenna efficiency [41]. To increase the communication rang and reduce the power absorption of electromagnetic signals in the human body, standard frequency bands below 1 GHz are preferred; this can result in larger antenna size. One way for miniaturization is to use higher frequencies to obtain smaller antenna sizes but this can come at the cost of larger attenuation of the signal in the human body. Consequently, miniaturization becomes one of the main challenges in implantable antenna structure design.

The small size implantable antenna can help to reduce the invasive surgical procedures during the implantation. Human body tissue, in which implantable devices are supposed to operate, reduce wave propagation velocity due to fairly high permittivity characteristic; this can be useful to reduce the physical size of the antenna. However, the level of miniaturization achieved may reduce when low permittivity biocompatible materials are used as superstrate layer to cover the antenna for safety reasons; this decreases the value of the effective permittivity [41]. Employing a thicker

superstrates could increase the resonant frequency of the radiator, therefore, to re-tune the resonance frequency, the antenna physical dimensions needs to be adjusted [42]. On the other hand, superstrate consists of thin layers of dielectric materials with higher permittivity are preferred for small embedded antenna for biotelemetry. Therefore, introducing advance miniaturization techniques are necessary to fulfil the wireless healthcare system requirements.

Microstrip patch antennas are also employed for implantable devices as their physical size could be reduced more effectively using different miniaturization techniques [43]. These methods may be used individually or in combination to reduce the antenna physical size at specified operating frequency while maintain the antenna radiation performance as required. These techniques, introduced in the literature, can be categorise as follow:

1- Increasing the current flow path on the radiator surface: By providing a longer effective path for the surface current flow, the resonance frequency of the radiating patch decreases so that it is possible to achieve a more compact size for the implantable antenna. Spiral and meandered [44], waffle type [45], and hook slotted [46] shaped radiators are miniaturized using this method.

2- Patch stacking: Vertically stacking two or more radiating patches properly reduces the antenna size by increasing the current flow path length [36, 47]. A miniaturized stacked structure antenna, built on Rogers 3210 substrate, using meandered patches is proposed in [47], the radiator operates in the MICS band and has a small volume of 214.9 mm^3. However, these types of antennas, stacked patches, have quite low radiation efficiency.

3- Employing high permittivity dielectric materials for substrate and superstrate: high permittivity dielectrics materials increase the effective wavelength and result in lower resonance frequencies, so that helping antenna size reduction[36].

4- The shorting pins: the effective size of the radiator may increase by employing shorting pins between the patch and the ground plane, in return, the antenna physical size can be reduced at a particular resonating frequency. When only a single pin is employed, the shorted antenna structure is similar to PIFA structure [48].

5- Combination of above techniques: small antennas reported in the literature combine all or a few of the above mentioned miniaturization methods in order to reduce the size of the antenna.

In next subsections, I will review the current literature for the wearable and implanted antennas immersed inside the human body chest, arm, GI tract, and head, and placed close by the body skin for body-worn applications.

2.2.1.1 Chest Implantable Antennas

The most common locations to implant a biomedical device are chest, head and arm [30-32, 49-51]. Implantable devices such as cardiac pacemaker and continuous glucose monitoring devices need to be implanted in chest. For existing continuous glucose monitoring devices, the subcutaneous biosensors are used and connected to a microwave transmitter outside the human body. There are several issues associated with these systems, such as frequent replacement for the battery, long response time of 3 – 5 minutes for the sensor, replacement of the glucose sensor every 2 – 3 days and the RF unit is not small enough so that adding discomfort for the patient already

wearing an insulin pump. As an alternative to the current continuous glucose monitoring devices, Topsakal et al. [31] introduced a compact long-term implantable continuous monitoring device. The fully implantable system includes an interface circuit with transmitter antenna and a biosensor. The biosensor collect the data and the interface circuit processes this information and transmits the relevant results through the radiator to either a nearby base station (personal computer) or an external wearable device. The presented dual band implantable radiator resonates at 2.4 GHz, ISM band and 400 MHz, MICS band [31]. The radiator has been optimized for dual band operation using the combination of the particle swarm optimization algorithm and a finite element boundary integral electromagnetic simulation code. The gels mimicking the dielectric properties of the human body skin are developed to validate the antenna performance in vitro.

Flexible folded slot dipole antenna implantable resonating at 2.4 GHz ISM band has been presented in [49] for biomedical applications. The proposed small antenna is sealed off using biocompatible Polydimethylsiloxane (PDMS) to protect the antenna and the tissue. The antenna impedance characteristics calculated and then measured using the MSL2450 liquid, provided by Speag, imitating the dielectric properties of the human muscle at 2400 MHz. SAR measurement also indicates that the radiator meets the required safety regulations. The sensitivity of the radiator performance as a function of the surroundings dielectric parameters has been investigated for different human tissues. The dielectric nominal values were varied from 20% smaller to 20% larger to confirm that the radiator operates properly for different type of the human body environment. The disadvantage of this antenna is its low radiation efficiency and impedance bandwidth of the proposed antenna. Generally, to improve the antenna gain, fractional bandwidth and efficiency adding a superstrate layer of high relative

permittivity could help [31]. The loading of the superstrate slightly improves the impedance bandwidth, decreases the operating frequency and the resonant resistance. Another way to achieve a compact antenna is to integrate the antenna with the RF circuits on the same chip, but this can also enhance losses due to the resistivity of the substrates [35].

In recent years, several research work performed on small sized antennas for implanting inside the human body [30, 31], [49-51]. Among these, the design of embedded patch radiators resonating at lower frequency bands such as MICS band has drawn much interest. Kim and Rahmat Samii [50] reported the resonance and impedance characteristics of PIFA and spiral microstrip antennas operating over MICS band, 400 MHz. In this work, Finite Difference Time Domain (FDTD) code and the spherical dyadic Green's function (DGF) expansions are applied to analyze the electromagnetic characteristics of low-profile patch radiators and dipole antennas immersed inside the human head and body. Shoulder effects is also considered on the dipole antenna performance immersed inside the head employing FDTD method. Furthermore, two types of low-profile antennas, a PIFA and a spiral microstrip antenna, with superstrate dielectric layers are initially designed for biomedical devices to be implanted in the human body chest. However, all of the proposed antennas have large structure, occupy high volume of space and not suitable to tune for higher standard frequency bands such as ISM band 2400 MHz.

In a recent study, a small size embedded dual band antenna, with dimensions of $23 \times 23 \times 2.5$ mm^3, has been proposed [51], the antenna resonates at 400 MHz, MICS band, and 2400 MHz, ISM band. The effects of the live human tissue on the performance of the antenna, including measurements in vivo, has been investigated. Three identical antennas have been designed and fabricated that were surgically

implanted into rats; X-ray imaging was also used to make sure that the antennas are properly placed within the rats. Moreover, investigations also performed for the possible materials to coat the antenna for the biocompatibility. The fabricated antenna, printed on Rogers RO3210 (ε_r = 10.2, tan δ = 0.003), was in vitro tested using both real skin samples and rat skin mimicking materials. Measurements results on reflection coefficient revealed that calculation set up needs to be redesigned to simulate the realistic environment properly for the antenna implantation. The performance comparisons for the embedded antennas, proposed in the literature [47, 50, 52-56] for biotelemetry applications, are tabulated in **Error! Reference source not found.**. This indicate that the PIFA configuration is the common structure type used for implantable radiator design.

Table 2-1
PERFORMANCE COMPARISIONS FOR THE STATE OF ART ISM-BAND IMPLANTABLE ANTENNAS

Ref.	Antenna Type	Volume/Size mm^3	Bandwidth $S_{11} \leq -10$ dB	Peak Gain dBi	1g-avg SAR W/Kg	Miniaturization Method	Input Power mW
[52]	PIFA	12.5×12.5×1.27	7.26%	-29	190	Meandered PIFA	7.8
[53]	Patch	10×16×1.27	22.8%	-30.5	609.2	Meandered Slot	2.63
[54]	Diploe	16.5×15.7×1.27	37.8	-33.5	748	Loop loading	1.88
[55]	Monopole	18×16×1	33.5%	---	---	Ceramic substrate	---
[50]	PIFA	6144	5.95%	---	209	???	7.656
[47]	PIFA	203.6	6.72%	-37	324.7	Stacked	4.928
[56]	PIFA	121.6	30.3%	-38	900	Meandered	1.78

2.2.1.2 Arm Implantable Antennas

Arms and shoulders of human body are another parts of the human body that can be used for implanting biomedical devices. Compare to the chest and head, these

parts of the human body are relatively small, so that more miniaturization would be desirable for the implants. In the literature, small implantable antennas have been proposed using stacked PIFA structure to miniaturize the size of antennas as well as improving the impedance bandwidth. This include spiral PIFAs [50], [48] the rectangle stacked PIFA [57], the meandered PIFA [58], and the circular stacked PIFA [59]. Although the antenna proposed in [59] is as small as $\pi \times (7.5)^2 \times 1.9$ mm^3, and the one presented in [57] has the remarkable compact size of $10 \times 10 \times 1.9$ mm^3, both of the antennas provide a narrow fractional bandwidth.

Koichi Ito, et al. [30] demonstrated use of implantable devices as a future tool for in-body wireless communication and explained the implantable devices potential to upgrade the cable connectivity for the biological telemetry monitoring. The proposed small size folded antenna has dimension of $0.8 \times 0.8 \times 20.3$ mm^3 operating over the UHF band, 951 - 956 MHz. The presented antenna could be used in small implantable devices such as capsule. The measurements are carried out using equivalent human body arm phantom. The antenna has a maximum gain of -23.5 dBi, also, the wireless communication is possible since the margin exceeds 20 dB, based on the link budget calculations. Additionally, different numerical mimicking phantoms for human arm such as rectangular, cylindrical, and layered phantoms are employed and investigated based on the strength of the electric field and the far field radiation performance. The advantage of the proposed antenna is its low radiation efficiency and narrow impedance bandwidth at resonance frequency.

The stacked PIFA structure is the most used antenna structure to have the impedance bandwidth wider and reduce the antenna size. In the literature, different shape of stacked PIFAs including the circular stacked PIFAs, the meandered PIFAs and the spiral PIFAs has been presented. However, these antennas have a very low

radiation efficiency and generally narrow impedance bandwidth for practical applications. A miniaturized implantable broadband stacked antenna for biomedical applications presented in [57]. The three layer rectangular patch antenna, resonating at 400 MHz MICS band, has the size of 10 × 10 × 1.9 mm^3 that has an fractional bandwidth of 10%. The presented antenna has a small electrical size, however, the radiation efficiency is quite low, 0.65%.

A small stacked PIFA radiator, for implantable biomedical applications, operating in MICS band is presented in [60]. The radiator structure consist a three layer round PIFA structure which its round structure is easy to be implanted in human body. The antenna is printed on Rogers 3210 substrate and has dimensions of $\pi \times (7.5)^2 \times 1.9$ mm^3, with a bandwidth of 50 MHz at return loss of -10 dB measured at operating frequency of 402 MHz. The 1-g averaged calculated SAR, for the proposed small antenna, meets the requirements of American National Standards Institute (ANSI/IEEE) for short range biotelemetry. The performance comparisons for the embedded antennas, proposed in the literature for biotelemetry applications, are tabulated in Table 2-2.

Table 2-2
PERFORMANCE COMPARISIONS FOR THE STATE OF ART ISM-BAND IMPLANTABLE ANTENNAS

Patch Shape	Type	Radiation efficiency	Vol. mm^3
[49]	Slot dipole	0.34%	500
[62]	Annular slot	1.1 %	450
[69]	Spiral antenna	0.5%	600
[70]	Cavity loaded	0.88%	120
[72]	PIFA	1.5%	315

Liu et. al. [56] introduced a stacked PIFA with embed hook shaped slots at the edges of the radiating patches suitable for implantable biotelemetry devices. The

antenna consist of three layer stacked PIFA with compact size and good radiation characteristics. The presented 400 MHz radiator has a total size of 8 × 8 × 1.9 mm^3 and provides a monopole like radiation pattern. The embedment technique of shaped slots into the radiating patches was employed to increase the length of the effective current path so that achieving more compact size and wider bandwidth than those reported in [57, 59]. Although the antenna covers a wide fractional bandwidth of 18% which simply satisfy MICS band requirement, however, the radiation efficiency is only 0.55% which is quite low.

2.2.1.3 Ingestible Capsule Type Microsystems

Ingestible capsule devices capable to transmit images from inside the human body have revolutionized wireless biotelemetry systems in the healthcare area [61]. These microsystems may also employ for measuring the physiological parameters such as pH value, temperature and pressure inside the human body at different parts of the GI tract. The capsule travels in GI tract because of the peristalsis activity, results in random orientation for the capsule, so that establishing a continuous robust communication link is extremely challenging. Therefore, the radiator needs to be electromagnetically characterized in details [50].

2.2.1.3.1 Radiators for Wireless Capsules

Antenna inside the capsule has a key role as the quality of detected signal is dependent on the antenna performance inside the human body. Several antenna designs have been proposed and implemented for the ingestible wireless capsule devices including the spiral antenna [62], helical antenna [63], conformal meandered

dipole antenna [64] and patch antenna with complementary split-ring resonator loading [65]. The radiator design solutions face various challenges including limited available room inside the capsule, human body effects, interaction and coupling with other electrical components inside the capsule device, diverse polarization because of the random orientation of the device.

To overcome these issue, a comprehensive radiator performance evaluation between two different ingestible radiators resonating at 1430 MHz, WMTS band has been presented [66]. Moreover, a systematic evaluation of the wireless biotelemetry characterization for the presented inverted conical helical antenna and the reference conformal meandered offset dipole antenna is also implemented. The antennas are small and resonate within a standard frequency band, however, the bandwidth is not wide enough for wireless endoscopy systems, the provided fractional bandwidth must be wide enough to compensate the shifting in center frequency [54, 67] due to the varying dielectric properties of different surrounding tissues.

For the patient comfort and safety, the antenna has to be small while its radiation efficiency has to remain reasonable, the enhanced antenna radiation efficiency may extend the device battery life and allow high data rate transmission. Conformal configuration for the antenna design useful for capsule endoscopy beside printed patches on dielectric materials are also investigated [41, 68, 69]. To reduce the occupied space by the radiator inside the capsule and save the space for the necessary components, the printed radiator on the wall of a capsule has been proposed in [64, 70]. However, these antennas are more sensitive to surrounding environment variation results in frequency shifting. Therefore, the antenna structure ideally has must be less sensitive to the variation of dielectric properties of human body tissue especially GI tract [62, 64, 70, 71].

Flexible substrates are also employed to introduce a patch loaded with a complementary split-ring resonator in [65], covering the ISM band at 2.4 GHz. Radiators operates in ISM band can provide higher bandwidth allows transmit high resolution images and larger amount of data. A multilayer miniaturized circularly polarized helical antenna for capsule endoscope systems is presented in [67] operating in ISM band. However, the ISM band, 2400 MHz, is not suitable for wireless communication deep inside the human body compare to MICS 400 MHz as it leads to higher absorption loss. The performance comparisons for the embedded antennas, proposed in the literature for biotelemetry applications, are tabulated in Table 2 2.

TABLE 2-3
SIZE AND PERFORMANCE COMPARISON OF THE CAPSULE TX ANTENNA

Ref.	Frequency MHz	Antenna Type	Fractional Bandwidth	Vol. mm^3
[65]	400	Outer-Wall Loop Conformal	60%	150
[62]	500	Spiral antenna	21%	390
[66]	2400	Meandered dipole	35%	350
[63]	2400	Helical antenna	22%	300

2.2.1.3.2 Body-worn Antennas

Wireless communication systems that enable data transfer between wearable and electronic devices implanted into the human body are so called Wireless Body Area Networks (WBAN). Such systems attract much interest for various applications including medicine and health care, sport, biomedical imaging, indoor localisation and tracking, cognitive radio, radars and etc [72, 73]. Wideband body-worn antenna solution has also developed for wireless body area communication interface with high data rate in the future telemedicine systems [74, 75]. For wireless healthcare

monitoring systems, active devices implanted in human body facilitate movement among patients and allow faster diagnosis, thus, improve the patient quality of life. For instance, development of wireless capsule endoscopy system enabled the examination of the small intestine in GI tract which cannot be seen clearly by other types of endoscopy. Body-worn antennas form an important part of the remote patient monitoring biotelemetry systems. To communicate with capsule inside the gastrointestinal tract the base station antennas play an dominate role to detect the low power transmitted signal from the capsule inside the body [76].

For a reliable communication link between the capsule and the base station, using small antennas with circular polarization is necessary since the GI tract is not a straight and the capsule orientation may changes frequently results in polarization mismatch. A ground radiation antenna operating in ISM band, 2400 MHz, with circular polarization (CP) properties is presented [77] for biotelemetry applications. The CP radiation property is achieved using an asymmetric antenna structure with respect to its coplanar waveguide (CPW) feed. Reactive components such as two capacitances are included to obtain the impedance matched as well as those requirements to generate the CP waves. The tuning mechanisms for the capacitances are provided and the effects of varying them are also studied. The presented radiator exhibits a wide axial ratio bandwidth and a low profile which is less than 1 mm including two biomedical coating layers. Although the antenna (implantable) has not been designed for wearable applications, yet, it is still possible to use the design concept for body-worn CP antennas. A low profile slot patch antenna for on body wireless biosensor is also presented in [78] useful for the medical body area network. The radiator, resonates at 2400 MHz, consists of a patch with slots for radiating element and a rectangular loop for balanced feeding. The radiator is designed using

flexible printed circuit board (FPCB) and has a size of 70 mm × 25 mm × 1 mm. To improve the antenna gain, bandwidth and efficiency air substrate is employed. However, the size of the antenna is large, to satisfy the patient comfort, the receiving element must be electrically small featuring low profile while its radiation efficiency has to remain reasonable.

PIFA type antennas with different configurations are also proposed for wireless body area network (WBAN) applications [79, 80], however, the occupied volume is large and the polarization is not circular. A general design of the coplanar waveguide excited IIFA, traditionally excited by a microstrip is presented [81]. This coplanar excitation permits the bandwidth improvement up to 50% by exciting a new resonance on the ground plane. These antennas cover only the ISM band at 2.4 GHz. Since the wireless capsule device transmits data, using 400 MHz carrier frequency, the base station receiving antenna has to operate within the same frequency band to detect the transmitted signal. Furthermore, since the GI tract is quite long and large, it is recommended to employ more than one antenna, as receiving on-body antenna, to enhance the received signal quality, this can also be useful to form an array of antennas which can be employed to localize the capsule location while it is traveling through the digestive system.

The physical layer characterization is another important step for design and development of in-to-out body communication for WBANs. In the literature, on-body propagation has been investigated widely [74, 75, 82-87], however, less literature is available for the propagation loss modelling of in-to-out or within the human body communication link [47, 88-90] which are mainly focused on ISM band 2400 MHz. The path loss (PL) of a wireless link (in-to-out body) for the capsule endoscopy system, between the wireless capsule and the receiver outside the body, has been

investigated [76]. The FDTD 3D electromagnetic solver is used to predict the PL numerically and the effects of the different dielectric properties of the human tissue on the path loss is also evaluated. A spiral antenna is tuned, to operate in MICS band 400 MHz, as the transmitter antenna inside the capsule, and for the base station antenna, a half wavelength dipole (reference antenna) is employed. Additionally, the effects of different human tissues at various frequency bands are characterized in [91] for an in-to-out channel, however, the radiator design was not specified. The performance comparisons for the embedded antennas, proposed in the literature for biotelemetry applications, are tabulated in Table 2-4.

TABLE 2-4
SIZE AND PERFORMANCE COMPARISON OF THE CAPSULE RX ANTENNA

Reference	Freq. Band	Type	Bandwidth	Vol. mm^3
[82]	400 MHz	Folded meandered dipole	12%	4000
[83]	400 MHz	Circular patch	5%	880
[84]	400 MHz	Fractal antenna	3%	6200
[85]	2400 MHz	Button antenna	4%	6900

2.2.1.4 Head Implantable Antennas

Antennas suitable for implanting inside the human body head have also been investigated. People suffering from craniocerebral trauma due to the skull injury as well as patients facing neurological disorders such as hydrocephalus need monitoring of increased Intracranial Pressure (ICP) for their medical management [92]. Increased ICP may leads to permanent damage to the patient's brain or cause disability or even death. In recent years, the communication link performance of a small loop antenna resonating at 400 MHz, MICS band, is characterized when placed under the scalp for ICP monitoring [93], while in [94], comparative analysis carried out for short dipole and loop antennas embedded in human head phantom for several frequency bands.

Arye Rosen et al. [33] developed and verified a compact implantable wireless ICP sensor, incorporating a small radiator and packaging preparation. To demonstrate the robustness of the proposed RF pressure monitoring device, experiments implemented in both vivo and vitro. Moreover, the results of employing the DICP device for dynamic ICP monitoring in a swine model of traumatic brain injury (TBI) is also provided. The device structure is a combination of small and thin radiator implementation and packaging material to achieve acceptable radiation efficiency through the scalp. The presented antenna is an annular slot radiator with coaxial feeding from the back side. The fabricated antenna has dimensions of 20 × 22 mm which is not small enough for patient comfort. Based on the thickness of coating The antenna can achieve an efficiency of 0.5% – 1.0% when it is implanted inside, however, the radiation efficiency of the radiator is not the best obtainable.

Monitoring and controlling of the ICP are necessary for the treatment of the people suffering from the head injuries (e.g., traumatic brain injury) and diseases of the brain such as hydrocephalus. Improved RF components and downscaled electronic subsystems are motivating research and development in the area of biomedical wireless implants [95-97], which are expected to improve patients' comfort and reduce healthcare costs. Nikita et al. [36] demonstrated performance of a miniaturized implantable antenna immersed inside the human head for wireless indoor healthcare systems. The presented small biocompatible antenna operates in MICS band 400 MHz and has a radius of 4 mm suitable for integration with wireless biotelemetry devices. Although implantation in head has been investigated for several biomedical applications such as integration in ICP monitors, trackers for patients with Alzheimer's disease, brain wave sensors for paralyzed persons etc., the radiator can also be used for different wireless biotelemetry applications as well. The antenna

consists of a circular ground plane with radios of 4 mm and two vertically stacked circular meandered radiating patches with radios of 3.9 mm. The radiating patches are printed separately on an alumina substrate (ε_r = 9.4, tanσ = 0.06) with 0.25 mm thickness. An alumina superstrate layer with 0.15 mm thickness covers the structure to preserve its robustness and biocompatibility. SAR conformance with IEEE C95.1 2005 and excellence of the communication link with an external receiving antenna are also confirmed. The size of the antenna is quite smaller than previously reported work in the literature resonating at the same frequency, however, the radiation efficiency is only 0.80% which is quite low.

Warty et al. [35] demonstrated use of PIFA at 2.4 GHz ISM band for scalp implantation to monitor ICP. Embedded PIFA with a serpentine radiator was reported in [48] where as a waffle-type antenna built on silicon substrate was investigated in [45] to improve the radiation efficiency. However, these antennas also limited by their large volume. Since the structure size of the antennas are large and not suitable for increasing the effective length of the current flow path, and hence any further miniaturization may not be achievable. A smaller radiator with a stacked and spiral structure was developed in [34] which support triple band operations. The radiator resonates at different frequencies such as 2400 MHz, ISM band, and 400 MHz and 433 MHz, MICS band, employing a π-shaped radiator with a stacked and spiral structure. The experimental prototype of the compact stacked antenna with the compact size of 254 mm^3 is printed on Roger 3210 substrate. The designed antenna was used in a rectifying antenna (rectenna) for 433 MHz RF powering transmission, and can provide 86% conversion efficiency at 433 MHz when 11 dBm RF power was received by the antenna. However, for measurements, it fails to cover 2.4 to 2.5 GHz fully (only a small part of the band can be covered).

Microstrip structures for embedded antennas has attracted much of interest due to the flexibility in design. Several methods has been introduced to reduce the size of the antenna such as spiralling the conductor geometry, using high dielectric substrate materials, etc. Chung et al. [48] employed microstrip antennas configuration for potential use in biomedical wireless implants. The proposed microstrip radiator operates in MICS band, 400MHz, and its design parameters are investigated using the FDTD method and then compared with measurement results. The effects of the length, size, shape, substrate and superstrate thicknesses and materials, location of feeding point and ground plane are investigated. The proposed antenna is not small enough (17 mm × 27 mm) to be implanted in human body. Microstrip patch antennas have also been investigated for implantable applications by Soontornpipit et al. [45], who evaluated serpentine and spiral antennas at 400 MHz. However, these antennas also limited by their large volume, further size miniaturization was reported in the literature [56, 57, 60] using vertically stacked radiating patches and multilayer structures to increase the path length of the current flow. However, even these antennas could not be reduced in size and can cover only one single frequency band (i.e. 400 MHz). Stacked PIFA elements with very compact volume of 32.7 mm^3 were also reported in the literature [36]. Although these antennas have a smaller size, however, the radiation efficiency is still low. Furthermore, several applications in wireless healthcare telemetry need multiple bands of frequency to operate; none of these antennas can be made to cover multiple frequency bands. Hence, there is a need for compact implantable antennas that can cover multiple frequency bands viz., MICS (433 MHz), WMTS (1400 MHz) and ISM (2.4 GHz).

2.2.1.5 Wearable Active Arrays for Cancer Treatment

Surgery, chemotherapy, and radiotherapy are the most commonly used treatments for cancer; however, a new method called microwave hyperthermia is also evolving rapidly [98, 99]. Generally, hyperthermia is a form of cancer treatment exposing cancerous tissues to controlled high temperatures which may results in destruction of cancer cells. Based on the difference in thermal sensitivity between healthy tissues and tumors, the raised temperatures cause minimal damage to surrounding normal tissues. The healthy cells are able to dissipate the artificial heat quick and effectively while most of the tumours do not have this capability [100-102]. Therefore, to ensure the most effective treatment is provided without compromising the peripheral cells, heat levels must be constantly monitored during the treatment.

Methods of hyperthermia treatment, also referred to as Thermal Therapy, may differ based on the cancer growth type. Treatment can be whole-body, regional or local hyperthermia, depending on the extent of the area being treated [103, 104]. Whole body hyperthermia is used for metastatic cancers which have spread throughout the human body. Whole body heating is being studied as a way to make chemotherapy more effective in treating spread cancer. Here, body temperature may be raised by employing thermal chambers, whole-body warm-water immersion or electrical heating blankets. On the other hand, in regional hyperthermia a part of the human body, such as a limb, organ, or body cavity may be heated. Generally, the generated heat in this method is not sufficient to destroy all the cancer cells in the target so that this method is usually combined with chemotherapy or radiation therapy. Unlike the X-ray radiation used in conventional radiotherapy, this method is not radioactive and employs advance technology to target and destroy tumours and not harmful to surrounding normal tissue.

EM wave technology is finding applications in local hyperthermia, exposing microwave energy generates heat inside the human tissue. Here, high temperatures are used to kill the local cancer cells and may destroy nearby blood vessels when radio frequency waves are not controlled properly [105]. Near-field focused (NFF) array antennas are capable to focus the electromagnetic waves in small prescribed regions such as tumors so that useful for microwave thermal therapy [106-109]. Since most of the tumors are located in the near field zone of the antenna array, employing array of antenna performing near field focused radiation is necessary.

Various non-invasive microwave hyperthermia applicators are presented and experimentally analysed in the literature to heat up the cancerous cells and destroy them permanently [110-112]. For instance, to kill tumors located in the superficial regions of the breast, head and neck, arrays of microwave small antennas have been employed [113-116]. Moreover, extensive theoretical and experimental work has been carried out to introduce non-invasive focused hyperthermia systems using complete ellipsoidal beam-formers [117, 118]. Here, to achieve superficial and deep focused NI-LMH, different operating frequencies used beside an arrangement of several dielectric matching layers placed around multi-layered head model. Ishihara et al. [116] employed a homogeneous human tissue phantom and introduced a re-entrant cavity hyperthermia applicator to heat up neck and head tumors and provide the calculated temperature distribution in the tissue model. However, these applicators are not suitable to heat up the deep-seated tumors properly. Despite the fact that NI-LMH has proven to be an useful approach in the treatment of superficial tumors [99], further research is still required for heating up the deep seated tumors effectively. Focus and deposit electromagnetic power into the deeply located targets possess a challenge since muscle and high water content tissues such as blood rapidly attenuate the

propagated wave and absorb the radiated electromagnetic power, thus preventing deep penetration into the target.

To reduce the human body effects on EM wave, lower frequencies are used to increase the penetration depth. On the other hand, to achieve maximum therapeutic effect, the electromagnetic energy must be precisely focused only on the target area, however, a slight heating distinction of tumor location is expected when using lower frequencies. Dipole type antenna designed specifically in [119] to deposit electromagnetic energy inside the human head. However, the distribution of temperature in the brain tumors, positioned at different locations in the numerical head phantom, was not investigated. Moreover, several hot regions observed in the phantom temperature measurement, this identifies that healthy surrounding tissues may also affected by heat. In addition, to match the impedance, as it is generally necessary for dipole type antennas, a balun had to be added to the feeding network which absorbs large amount of electromagnetic power, thus the efficiency of the proposed antenna decreased. Likewise, the actual size of the antenna increased.

Focusing in small region is one of the key advantages of NFF arrays for Non-Invasive Local Microwave Hyperthermia systems. For NFF radiating arrays, featuring small size to fit the patient anatomy is foremost to other required properties such as low profile, light weight and low cost.

CHAPTER – 03

3. DUAL SLOT PIFAs FOR BODY IMPLANTABLE DEVICES

3.1 Introduction

In this chapter, I present a class of implantable miniaturized dual slot planar inverted-F antennas (DS-PIFAs) for biomedical implantable telemetry applications. A simple antenna geometry is proposed for DS-PIFAs so that they can operate over a variety of standard biomedical telemetry bands. The tuning techniques offer DS-PIFA to resonate in Medical Implant Communication Service (MICS) at 400 MHz, Zigbee at 868 MHz, Wireless Medical Telemetry Service (WMTS) band at 1430 MHz and Industrial, Scientific, and Medical (ISM) band at 2.4 GHz as discussed. I have investigated the effect of antenna geometry parameters on radiator performance using empirical parametric studies with an aim to miniaturize the antenna. I report the design of highly compact DS-PIFA printed either on FR4 or on Rogers substrate. I have studied antenna performance when it is implanted inside human body using numerical phantoms. The effects of interstitial fluid and air gap between the human body skin and the antenna when it is implanted are investigated. Furthermore, the effects of the surrounding environment such as skin and fat thickness on the antenna performance are also considered using numerical human tissue phantoms. The impedance characteristics of the proposed antennas are measured using experimental tissue

mimicking meat phantoms. Moreover, I have calculated the SAR inside the human body when the antenna is implanted by using an indirect thermal method inside the human body mimicking meat experimental phantom.

3.2 Background Review and Motivation

Implantable medical devices with wireless telemetry capabilities are useful for diagnostic and therapeutic applications [49, 92]. Based on the various wireless biomedical applications there are different implantable systems which operate over different frequency bands requiring specific types of antennas. This would make the antenna design exclusive to only given set of applications operating over a similar frequency band which increases the need for many design iterations to achieve operation over other telemetry bands. Therefore, employing a class of antennas which is capable to cover different telemetry bands by small changes in its size and geometry would be advantageous to system design.

However, implantable antenna design, regardless of the operating frequency band, faces major challenges including improved radiation performance, miniaturization and bandwidth enhancement [33]. It has been well established that implantable antenna efficiency decreases due to the high dielectric loss caused by the human tissue. Moreover, for an antenna to be implanted into the human body, it has to have a small size. The smaller size and lower efficiencies coupled with lower radiation power can lead to a shorter communication range.

To overcome these issues, many implantable antenna designs, such as folded dipoles and multi-layered spiral antenna were proposed [49, 69]. Folded dipoles [49] have simpler structure but their radiation efficiency is as low as 0.14%. On the other

hand, the multi-layered spiral antenna [69] has a complex structure and yet has lower radiation efficiency about 0.5% at 2400 MHz, which is quite low. Annular slot antenna with size of 22 × 20 mm^2 was also reported in [33], however, the reported radiation efficiency was only 1.2%. An implantable loop antenna with complementary split ring resonators (CSRRs) was also reported recently for biomedical telemetric applications [120]. It was claimed that introduction of CSRR reduced the absorbed power inside the body and improved the antenna impedance matching and radiation efficiency. However, the maximum radiation efficiency achieved was only 0.53% at 2.45 GHz with CSRR and 0.46% without CSRRs. Hence, there is a need for compact-sized implantable antennas with improved radiation efficiency.

Enhanced impedance bandwidth is also an important parameter for designing advanced body implanted antennas. Larger bandwidth can accommodate possible shifts in the resonant frequency due to changes in implantation scenarios within different body locations and tissue types, random variations in dielectric properties of human tissues and other perturbations that may occur during implantation. Xiao et al. [121] reported an implantable cavity loaded patch antenna of size 10 × 10 × 1.27 mm^3 at 2.45 GHz and obtained 7.7% impedance bandwidth. But, there is a need to improve obtainable impedance bandwidths.

Biotelemetry [50] and wireless powering problems associated with the recently invented leadless pacemaker systems are addressed in [122]. Conformal spiral type Implantable antennas covering MICS band, 400 MHz are proposed to incorporate into capsule-type leadless pacemakers for telemetry. To remove the batteries and avoid the bulky energy storage component the midfield wireless power transfer (WPT) technique [123] has also been employed along with design and fabrication of a midfield transmitter antenna at 1.5 GHz for feasibility of wireless powering of the

leadless pacemaker. The 400 MHz implantable antenna allows for wireless monitoring and device control in patients, and the inclusion of wireless power transfer at 1500 MHz allows for continuous monitoring beyond normal battery lifetimes [122]. To cover MICS band at 400 MHz, another implantable antenna introduced in [124]. Two spiral resonators coupled with each other were employed to achieve a wide bandwidth over the operating band. The proposed antenna has dimensions of 16.5 × 16.5 × 2.54 mm^3 and a measured bandwidth of 13%, covers the suitable wide bandwidth at both bands. Generally to reduce the size of implantable antennas common miniaturization methods such as stacking multilayers and embedding slots on the ground plane are used [13, 125]. However, Li et al. [52] employed meandering and shorting strategy to introduce a compact implantable antenna for biotelemetry over the 400 MHz MICS band with the dimension of 12.5 × 12.5 × 1.27 mm^3, equivalent to 0.0168 λ_0 × 0.0168 λ_0 × 0.0017 λ_0 (λ_0 is the free-space wavelength at 402 MHz).

The proposed antenna is fabricated on the single layer substrate with a full ground plane. Therefore, the proposed antenna is characterized by the advantages of low cost and easy manufacture and has a measured bandwidth of 7.26%. To achieve a higher bandwidth, an implantable open-end slot antenna with a volume of 139.7 mm^3 for biomedical applications is proposed in [126]. By etching a meandered slot on the top metal with one end open, the overall size of the antenna reduced to 10 × 11 × 1.27 mm^3 covering MICS band fully with a measured bandwidth of 28%. A microstrip line is utilized as excitation with a shorting connected to the radiator, to match the feeding impedance to 50 Ω two U-shaped stubs are used. Moreover, a small single-fed hybrid patch/slot 400 MHz implantable antenna has been achieved by embedding the meander slot and six open slots in the ground [53]. The proposed antenna has dimensions of 10 × 16 × 1.27 mm and measured bandwidth of 22.8%. By embedding

a meandered slot onto the ground plane, the current path on the ground can be lengthened for the radiator, thus lowering the resonant frequency of the antenna, the open slots also extend the current path to enhance the size reduction. Furthermore, microwave dielectric ceramic substrate with high dielectric constant and high-quality factor are employed to introduce broadband non-superstrate implantable CPW-fed monopole antennas operating over 402-405 MHz frequency (MICS) band [55]. These implantable non-superstrate antennas have the advantages of miniaturization, low profile and wide measured bandwidth. For instance the proposed antenna [55] has a wide measured bandwidth of 33%. However, the radiation efficiency is as small as 0.12%.

Dual band microstrip patch antenna covering MICS (402–405 MHz) and ISM (2.4–2.48 GHz) is also proposed for implantable medical devices [127]. The radiating elements of the antenna are a split ring resonator (SRR) coupled to a Spiral. To reduce the size of the structure both elements are short circuited to the ground plane. The antenna has a multilayer configuration where the feeding line and the radiating elements are located at different levels. The independent line feeds the radiating elements by electromagnetic coupling, so that allowing a larger miniaturisation degree [127]. The electrical size of the antenna is $0.018\,\lambda_0 \times 0.018\,\lambda_0 \times$ at the lowest operation band, and $0.11\lambda_0 \times 0.11\lambda_0$ at the highest operation one.

A circularly polarized antenna is proposed for biomedical applications at ISM 900 MHz (902–928 MHz) band [128]. By positioning the feed and shorts in proper location, either right-hand or left-hand circular polarization property can be realized. To minimize the antenna size, slow wave concept is utilized by loading patches to the

radiated loop antenna. The antenna has a small size of 13 × 13 × 1.27 mm^3 and bandwidth of 18% with axial ratio below 3dB.

It worth to mention that none of these implantable antennas offer such a flexible geometry or structure suits for re-tuning the resonant frequency to cover other standard telemetry bands rather than the original ones. In this chapter, I propose a class of PIFAs with a simple geometry capable to resonate at different frequencies when tuned. I present a miniaturized Dual Slot–PIFA with improved radiation efficiency which is capable to operate over several standard telemetry bands such as MICS band at 400 MHz, Zigbee at 868 MHz, WMTS band at 1430 MHz or ISM band at 2400 MHz. The proposed antenna has a simple geometrical structure and obtains 'reduced near field radiation' when implanted inside the human body. The proposed DS-PIFA when immersed inside a multilayered, lossy human tissue mimicking phantom, achieved a radiation efficiency of 2.5% at 2.400 MHz which is higher than the most of the previously reported works in the literature [33, 49, 69, 121]. Moreover, the antenna achieved a measured impedance bandwidth of 330 MHz (13.5%) when tuned to cover ISM band and immersed inside the experimental phantom. The dielectric properties of human tissue may vary due to the dissimilar body shapes, genders, ages, races and etc results in shifting the radiator center frequency. In this circumstance, featuring a higher bandwidth is advantageous as it ensures the antenna performance when small shifts occur in resonant frequency.

Here, the proposed radiator resonating at 2.4 GHz has a compact size of 8.1 × 7.1 × 1.6 mm^3 occupying a volume of 0.09 cm^3 which significantly smaller than those reported in the literature [33, 49, 69, 121]. I have also tuned the proposed radiator geometry to operate over four different standard health care telemetry bands. Following a similar procedure, I carefully reduced their geometry size to guarantee a

high level of performance including the radiation efficiency and impedance bandwidth.

Many factors affect the antenna performance when testing in vivo [51] such as variations in dielectric properties and thickness of the fat and skin layers of experimental vivo models. Furthermore, the realistic factors that may impact during the implantation such as air gap and interstitial fluid needs to be considered in predicting the antenna performance [51, 92, 129-131]. My predictions demonstrate that the proposed DS-PIFAs can perform well when considering the air gaps and interstitial fluids in my calculations. I have also obtained SAR by using an indirect thermal method when the proposed DS-PIFA implanted inside an experimental tissue mimicking phantom.

This chapter is organized as follows: In Section 3.3, I described the configuration of the proposed DS-PIFA, together with parametric studies and antenna calculation performance. Also the working principles of miniaturization and wide bandwidth property are analysed in this section. Section 3.4 presents DS-PIFA Measurements followed by Specific absorption ratio (SAR) in section 3.5. The radio communication link of the proposed antenna including statistical path loss model, link budget and pathloss measurement are given in Section 3.6 whereas in section 3.7 DS-PIFAs performance for different slots arrangement are presented followed by the discussion in Section 3.8.

3.3 Design of Novel PIFA Implantable Antennas

A novel implantable antenna needs to satisfy many requirements which combine the compact size, a light weight, a good radiation efficiency and wider bandwidth to accommodate changes in tissue properties. The proposed geometry promises such a performance while it easily can be tuned to cover desire frequency bands of interest. I propose a modified PIFA type antenna to offer a lower radiated near fields and a lower SAR when implanted inside the body.

The advantage of the proposed implantable Dual slot PIFA is that its structure helps to obtain antenna resonances at two closer resonant frequencies which can help to create wider bandwidth operation. It can also be implanted either under the skin, inside the chest, muscle, small intestine or head, without significant changes in the radiator structure. Moreover, its geometry offers design flexibility so that it can be easily tuned for other bands of frequency such as MICS, Zigbee and WMTS bands by increasing its size by a fixed enlargement factor that is related to the wavelength of operation and optimizing the sizes of the slots and the ground plane. In next section I introduce dual-slot geometry and design a DS-PIFA for operation at 2.4 GHz ISM band and present an adjustment technique to reduce the size of it for patient comfort and system requirement.

3.3.1 Initial Design

The initial design of the proposed antenna structure consists of a patch radiator, a dielectric substrate, a dielectric superstrate, a ground plane, a shorting pin and a feeding point. The top views of the antenna structure with the three main possibility of slots' arrangements are shown in Figure 3-1 a), b) and c). From this figure one can

see the slots are located either on the opposite edges or on the neighbouring edges or the same edge of the top patch.

The antenna design procedure is carried out in three steps. First, a rectangular patch antenna is designed to operate over desired telemetry band when implanted in a homogeneous tissue mimicking numerical phantom. Second, two slots added on geometry purposefully and then following a generalized procedure, shown in Figure 3-2, a model of DS-PIFA with a shorting pin is tuned to operate over desire band when implanted in a multi-layered tissue mimicking numerical phantom. Later, a single layer dielectric thin superstrate is added to the implanted antenna model and the geometrical parameters are varied to obtain resonances at the operating frequency band using the generalized procedure. The model of the antenna with the thin superstrate is then implanted inside a complex human body numerical phantom for more realistic simulations as indicated in Figure 3-3a.

3.3.1.1 Slots Arrangement, Case I:

Based on simulation results when slots are located on two neighbouring sides, as shown in Figure 3-1b, the antenna can be tuned to cover two frequency bands of interest by changing the slot size and position, also adjusting the feeding point and shorting pin location may be needed. However, the maximum impedance bandwidth would be only 5% which is not my interest for this work. However, from the research perspective, it is valuable to do my research fully and investigate the effects of the antenna's geometry parameters for each individual case including case I. Therefore, I will discuss and publish my study outcomes for this case at the end of this chapter.

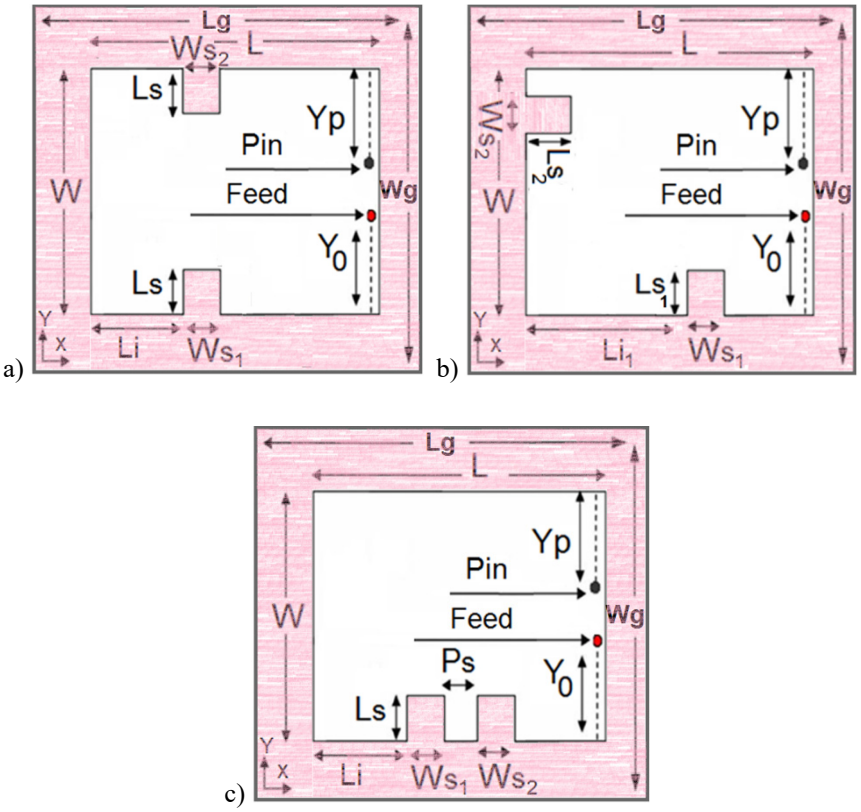

Figure 3-1: Top views of proposed DS-PIFA geometry with different slot position (a), (b) and (c).

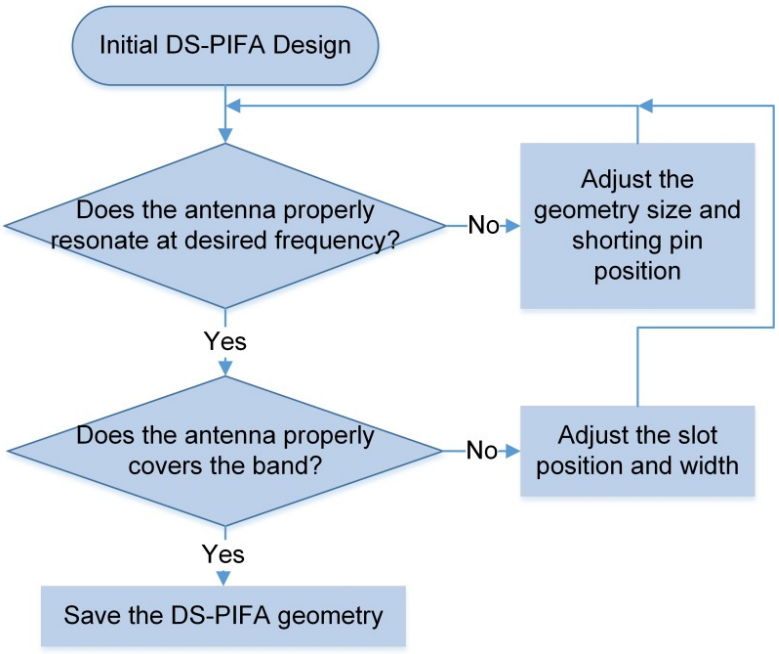

Figure 3-2: Flowchart for initial antenna design methodology.

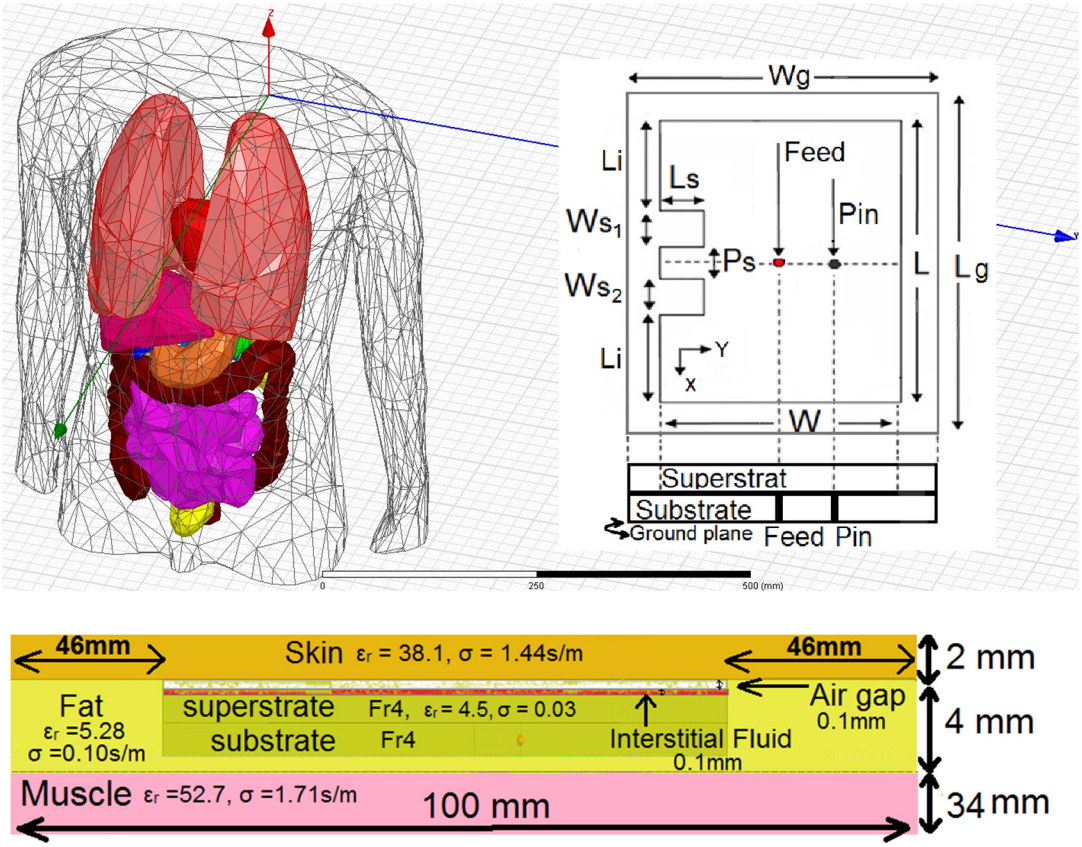

Figure 3-3: Simulation set up in numerical mimicking phantoms, a) 3D complex human body model, b) Side view of layered Block and Cylindrical phantoms.

3.3.1.2 Slots Arrangement, Case II:

The DS-PIFA geometry is also suitable for wearable applications when slots are located in opposite edges of the radiator as shown in Figure 3-1a. It occupies a small volume of 1.5 cm^3 when resonating at 2.4 GHz without superstrate at a close distance to human body numerical phantom. The antenna has a ground plane in the back, moreover, its radiation pattern is balloon shaped in broadside direction so that the radiated power passing through the human body is minimum. However, this slot arrangement does not show an acceptable performance for biomedical implantable applications when compared with the slot arrangement in Figure 3-1c. However, this slot arrangement could be employed for body-worn applications such as wireless capsule endoscopy system.

3.3.1.3 Slots Arrangement, Case III:

When both of the slots are located on the same edge, the radiator shows a remarkable performance for implantable applications. Figure 3-1c shows the top view of the proposed implantable DS-PIFA geometry for which the dimensions of the rectangular-shaped patch as well the two radiating slots are the key parameters for antenna operation. In addition, the relative location of the shorting pin with respect to the position of the coaxial feed can play a major role in obtaining good matching within the chosen band. The antenna structure resonates at two close frequencies. The lower resonant frequency is mainly due to the current distribution around the slots which is affected by the feed position. The higher resonant frequency is determined by the patch width W as well as the incremental extension Δw of the PIFA. The interaction between two close (higher and lower) resonant frequencies can be achieved by adjusting the slots and shorting pin position to create a wideband operation.

For optimum performance, my empirical studies revealed that the feeding position, Y_f, be positioned on the central vertical line at a height approximately equal to 0.6 W from the bottom edge. Additionally, my numerical investigations indicated that to improve the radiation efficiency of the implanted antenna when $1<L/W<2$. The proposed design with L = 1.15 W has provided a calculated radiation efficiency of 2.5% when implanted inside the tissue mimicking numerical phantom.

To mimic antenna implantation into the different locations inside the body such as under the skin, inside the chest, muscle, small intestine or head, the proposed DS-PIFA is immersed inside an inhomogeneous multi layered complex human body phantom using HFSS™ [132] as depicted in Figure 3-3a. The model is an adult male patient standing on its feet along z axis. It consists of over 300 body parts to represent

bones, muscles and organs. It has accuracy at the millimetre level and a frequency dependent material properties database is included. This model can provide accurate results however, it is not memory and computational time intensive.

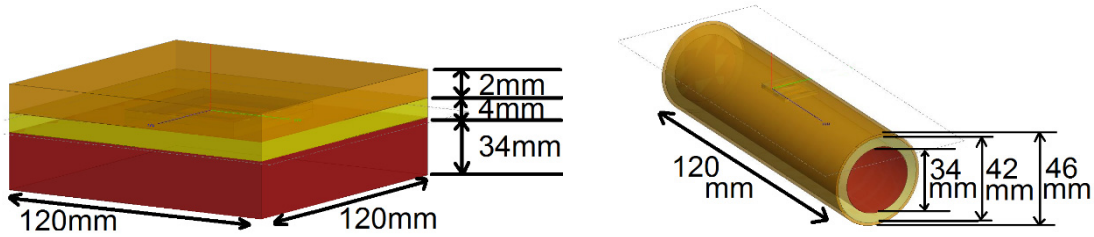

Figure 3-4: Simulation set up in numerical mimicking phantoms, a) Multi-Layered Block phantom, and b) Cylindrical phantom.

For empirical optimization, I need to obtain results faster and hence a smaller phantoms either using the cylindrical multi-layered geometry or layered rectangular block geometry are also employed as shown in Figure 3-4. Based on my calculations, the diminutions provided for both of the layered models in Figure 3-4 are appropriate for higher frequency analysis such as 2450 MHz, however, the thickness provided for each layer is proper for all the frequency bands of interest. For the lower frequency bands such as 400 MHz the diminutions have to be increased carefully by considering the wave length. The antenna is embedded into the fat layer under the skin and above the muscle and the performance calculated using FEKO^{TM} [133]. The x-y plane cut of the calculation set up, showing the proposed antenna positioning inside the layered Block and cylindrical numerical mimicking phantoms, is illustrated in Figure 3-3b. The thickness of air gap layer and interstitial fluid are ideally assumed to be zero at this stage of design. The cylindrically shaped multi-layered phantom was used to mimic antenna implantation inside the arm whereas the layered rectangular block phantom was used to mimic implantation under the chest skin. Later to verify the

antenna performance inside the human body in different locations such as head and small intestine, the complex human body has been employed.

Following the my generalized procedure, shown in Figure 3-2, I could successfully tune the geometrical parameters of DS-PIFA to make the antenna operates over a variety of frequency bands such as MICS band at 400 MHz, Zigbee at 868 MHz and WMTS band at 1430 MHz. The initial designs performed fairly well inside the human tissue numerical phantom. A parametric analysis is then conducted in order to quantify the effects of the different antenna geometric parameters and to empirically optimize its design. The antennas' size and properties are tabulated in Table 3-1.

TABLE 3-1
DS-PIFAS SIZE AND CHARACTERISTICS OVER DIFFERENT MEDICAL FREQUENCY BANDS

Freq. Band MHz	Resonant Freq. MHz	Band width MHz	Radiation efficiency	Patch Size	Antenna volume mm^3
2400	2400	260	2.65%	17 × 19	1296
1430	1430	148	2.7 %	21.2 × 23.1	1458
868	868	56	2.8%	22.6 × 24.2	1680
400	400	24	2.9%	25 × 27	1840

3.3.2 Parametric study

I have conducted detailed parametric study to investigate the effects of each geometrical parameter of the DS-PIFA on the resonant frequency with an aim to further size reduction. To achieve this I followed a generalized procedure as shown in Figure 3-5. I applied this procedure for all of the DS-PIFAs operating over the different frequency bands and could reduce their physical size significantly. Here, the effects of the feed and shorting pin positions, width and lengths of the slots while fixing other antenna parameters were also investigated. I have also employed two types of

substrates such as Fr4 and Rogers 3210 to investigate the effect of dielectric materials for DS-PIFA structure.

During the miniaturization process, I simulated using FEKO™ [133] to calculate not only the radiator resonant frequency but also other properties of antenna such as fractional bandwidth and radiation efficiency at every step mainly to make sure that implantable antenna design requirements are fulfilled. I have also calculated the surface current flow to see how the currents are changing when the antenna size is reduced.

Figure 3-6 shows the calculated surface current distribution on three different prototypes of proposed implantable DS-PIFAs. The plot in the Figure 3-6a shows that the path of the current flow is in the same direction in both of the left and right arms. These currents flow into and merge with the current in the middle arm. This could be primarily responsible for exciting the fundamental radiation mode that is resonant within the 2.4 GHz ISM band. When compared to currents in middle arm, the currents on the left and right arms travel a longer path along the outer edge of the slots and excite the lower side of frequency band. The current in the middle arm although primarily flows in direction opposite to those in other arms, however, there is no significant current cancelation.

The current distribution would get perturbed by reducing the radiator size (as shown in Figure 3-6b thus leading to changes in antenna radiation properties. However, I found that by adjusting the feeding and shorting pin position I successfully forced the surface current effectively flows all over the radiator surface in the same manner as initial design as shown in Figure 3-6c. This will helps to keep the radiation performance close to the design requirements.

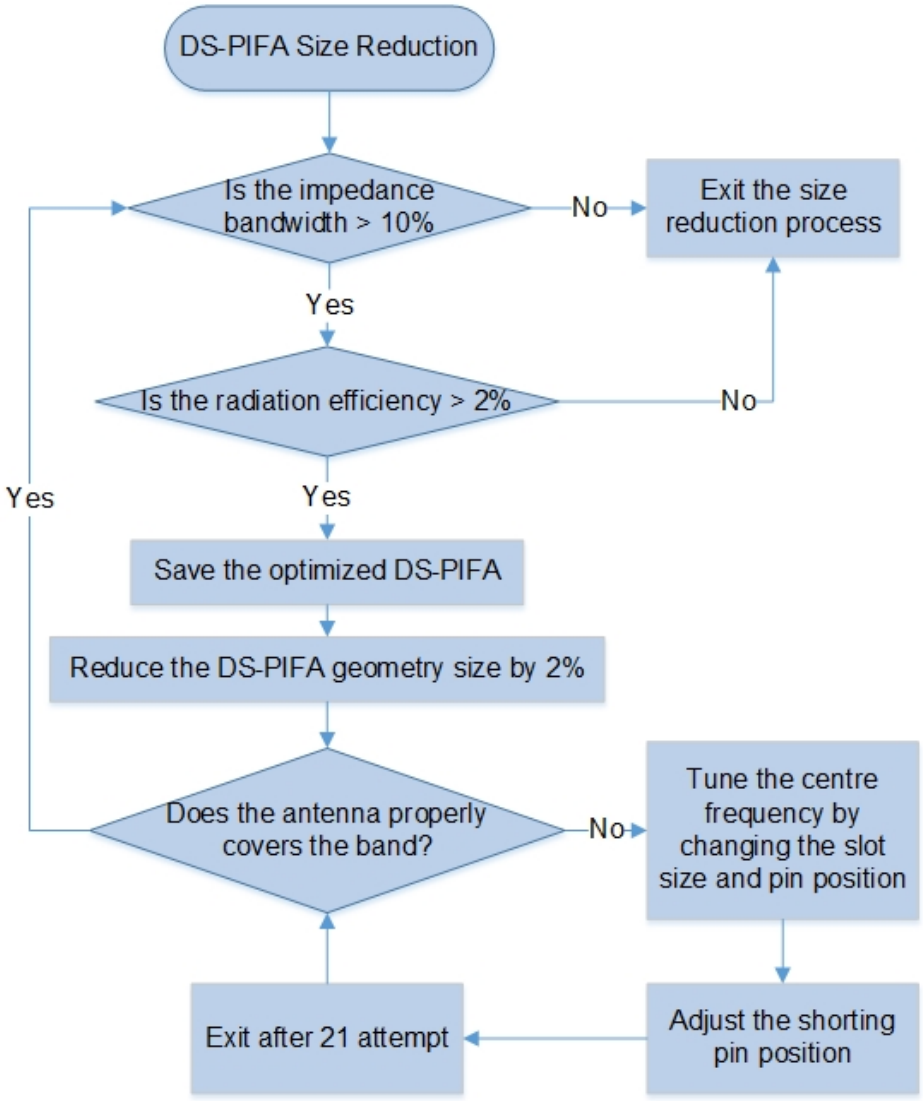

Figure 3-5: The method followed for DS-PIFAs size reduction.

My studies revealed that by reducing the slot lengths while at the same time placing the feed and shorting pin at appropriate locations, follow the generalized procedure shown in Figure 3-5, one could sucsessfully reduce the antenna size without affecting the resonance within 2.4 GHz ISM band.

The intial size obtained for the DS-PIFA operateing at 2.4 GHz is Lg = 27 mm, Wg = 30 mm, L = 17 mm, W = 19 mm and h = 1.6 mm. Reduction of the slot length resulted in the corresponding increase in the metallization area of the antenna. I found

that I could miniaturize the antenna size by reducing the metallization while maintaining the resonant frequency to fall within the ISM band. Thus, a significant reduction in the physical size of the antenna from its initial size was achieved by reducing the lengths of the slots and placing the feed and the pin at proper locations as shown in Figure 3-6d. However, compare to the new radiator size (W (7.1 mm) × L (8.1 mm)), the ground plane size (Wg (14 mm) × Lg (16 mm)) is still large so that further parametric studey is necessary to investigate the fesiblity of ground plane size reduction while keeping the negative effects on the radiation performance minimum.

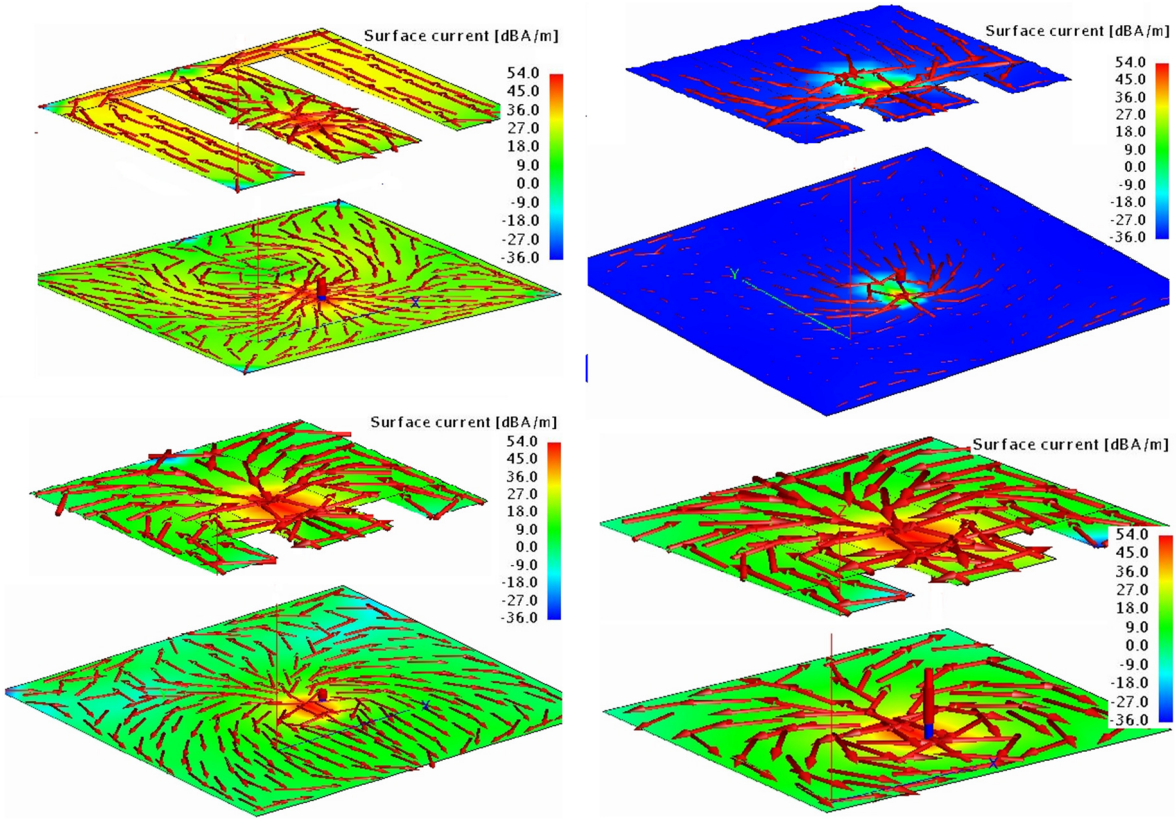

Figure 3-6: The surface current distribution at 2.45 GHz (top view), a) first prototype (b) perturbed surface current (before adjusting feeding and pin position), c) miniaturized prototype, d) miniaturized size with smaller ground plane.

It is well known that the ground plane size has a significant effect on radiation bandwidth of PIFA structure [134]. Here, I have considered seven different size of ground plane for proposed DS-PIFA to gain insight into how the ground plane causes fractional bandwidth variations. I have concluded that by decreasing the width Wg and length Lg of the ground plane size with a fixed ratio the fractional bandwidth may increase. Moreover, by increasing the ground plane dimension the bandwidth will drop slightly. Figure 3-7 shows the effects of the ground plane size variation on antenna performance from the aspect of the bandwidth and helps to choose the best size.

I have also monitored how the surface currents effected by ground plane size variation. Figure 3-6d shows the surface current distribution for the proposed miniaturized implantable antenna. From this figure one can see the currents in left and right hand arms still flowing in the same path as the initial design even though the slots length have been reduced significantly. These currents merge the surface current on main arm and flow towards the shorting pin.

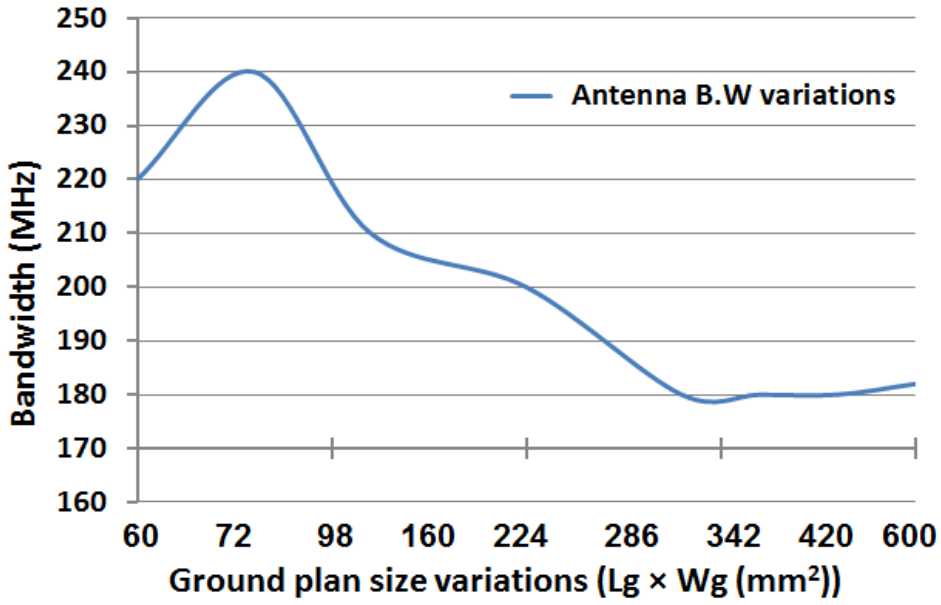

Figure 3-7: Ground plane size variation versus antenna bandwidth.

Furthermore, I found that by increasing or reducing the slot widths, one could tune the resonant frequency as shown in Figure 3-8 without changing the antenna structure or size. This feature demonstrates the flexibility of the proposed antenna geometry concerning practical implementation.

The finalized dimensions of the proposed DS-PIFA, operating over ISM band, are Lg = 9 mm, Wg = 8 mm, L = 8.1 mm, W = 7.1 mm and h = 1.6 mm, thus, a 90% reduction in the physical size of the antenna from its initial size was achieved by reducing the lengths of the slots and placing the feed and the pin at proper locations as shown in Figure 3-6d. The size comparison with similar types of antennas reported in the literature is provided in Table 3-2. I have also performed further parametric study, followed the generalized procedure, to make sure that I have proposed the smallest size possible for DS-PIFAs that cover ZigBee, MICS and WMTS bands having a reasonable fractional bandwidth and radiation efficiency using FR4. The antennas' size and properties are tabulated in Table 3-3. Referring to the Tables 3-2 and 3-3, one can see an 80% antenna size reduction for WMTS, 58% antenna size reduction for ZigBee and 39% antenna size reduction for MICS band achieved, compare to the initial size for the proposed DS-PIFAs, by reducing the lengths of the slots and placing the feed and the pin at proper locations.

Table 3-2
SIZE COMPARISON OF PROPOSED DUALSLOT PIFA

Patch Shape	Freq. Band MHz	Type	Radiation efficiency	Vol. mm^3
[49]	2400	Slot dipole	0.14%	550
[33]	2400	Annular slot	1.2 %	440
[69]	2400	Spiral antenna	0.55%	620
[121]	2400	Cavity loaded	-	127
This work	2400	Dual Slot PIFA	2.5%	115

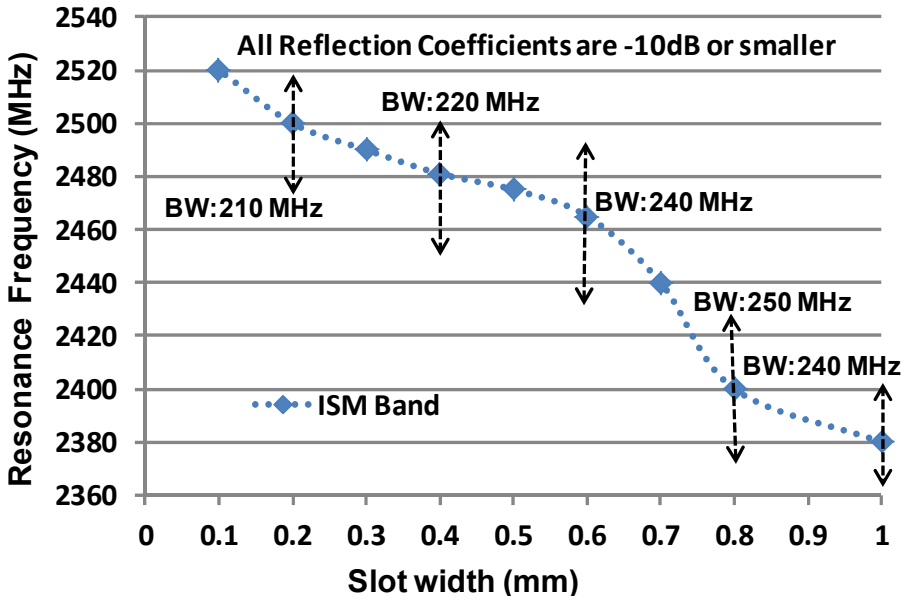

Figure 3-8: Dual-slot PIFA: The effects of reducing the slot width.

To investigate the effect of substrate dielectric material on DS-PIFAs performance I also employed Rogers 3210. This substrate has a lower conductivity for higher frequencies compare to FR4. However, I purposefully chose a higher permittivity to reduce the antenna size further. This substrate has a thickness of 0.64 mm and ε_r of 10. By using DS-PIFA design procedure shown in Figure 3-2, I could successfully redesign DS-PIFAs for my frequency bands of interest using Rogers 3210. To reduce DS-PIFAs size further, I used a similar approach as mentioned above and applied the similar method shown in Figure 3-5. This generalized procedure, helps to tune and reduced the size of my proposed structure to operate over different bands when implanted in a multi-layered tissue mimicking numerical phantom. The antennas' size and properties are tabulated in Table 3-3. Further size reduction of 69% for antenna covering ISM band, 76% for antenna covering WMTS band, 78% for antenna covering ZigBee and 66% for antenna covering MICS band achieved by employing dielectric materials with higher permittivity.

TABLE 3-3
MINIATURIZED DS-PIFAS SIZE AND CHARACTERISTIC OVER DIFFERENT MEDICAL FREQUENCY BANDS

Freq. Band	Resonant Freq. MHz	Dielectric material	Band width MHz	Radiation efficiency	Antenna dimensions	Vol. mm^3
ISM	2400	Fr4	240	2.42%	9 × 8 × 1.6	115
ISM	2400	R.3210	160	1.85%	8 × 7 × 0.64	35.9
WMTS	1430	Fr4	125	2.5 %	13 × 14 × 1.6	291
WMTS	1430	R.3210	105	1.9%	10 × 11 × 0.64	70.4
ZigBee	868	Fr4	60	2.55%	20 × 22 × 1.6	705
Zigbee	868	R.3210	45	2%	15 × 16 × 0.64	153.6
MICS	400	Fr4	25	2.65%	27 × 26 × 1.6	1123
MICS	400	R.3210	20	2.1%	25 × 24 × 0.64	384

3.3.3 Antenna Performance

Beside the resonant frequency and fractional bandwidth, I have also considered the antenna radiation efficiency during the design and calculations. The radiation efficiency of the 2.4 GHz miniaturized DS-PIFA, including superstrate, is 2.5% when immersed inside layered block model. As expected, the calculated efficiency is low due to the presence of lossy tissues. However, the calculated efficiency is higher than the reported results for similar class of antennas in the literature [33, 49, 69, 121]. I have considered a trade-off based on the antenna miniaturization and efficiency to have the maximum radiated power.

The antenna may have a proper reflection coefficient over the ISM band, however, it will not radiate effectively if the input power trapped into the antenna loss mechanism. I could successfully keep the radiation resistance dominant compare to the loss resistance over the antenna structure by adjusting the antenna size and the feeding position to keep the surface current flows uniformly over the radiator.

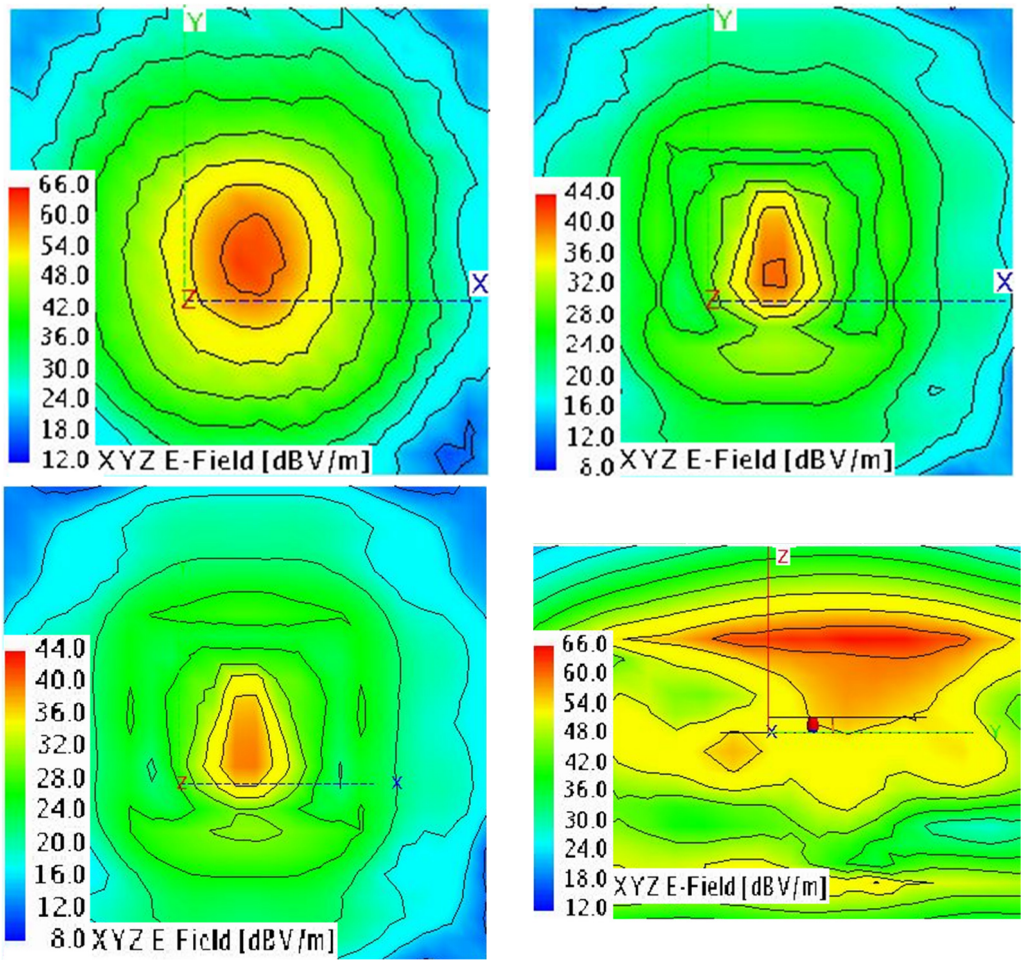

Figure 3-9: The electric near field distribution (top view), a) outside the numerical phantom, b) inside the skin layer, c) inside the muscle layer and d) side view.

To calculate the antenna efficiency excluding surrounding lossy environment and have a better understanding of its performance I set the dielectric properties of the tissue phantom equal to lossless media, however, the antenna did not resonate at the same frequency band due to the changes in surrounding media dielectric properties. To solve this issue, I have calculated losses per media of the numerical phantom so that I could provide the 2.4 GHz miniaturized DS-PIFA efficiency excluding surrounding lossy environment which is 64.77% including superstrate. I have also investigated the effect of the slots' width variation on efficiency and losses for the 2.4 GHz miniaturized DS-PIFA, the results are tabulated in Table 3-4.

TABLE 3-4
LOSSES IN DS-PIFA AND NUMERICAL PHANTOM AT 2.4 GHZ (IN MILI-WATT).

Slot width	1mm	0.8mm	0.6mm	0.4mm	0.2mm
Radiated power	0.10	0.128	0.11	0.1	0.08
Input power	5.2	5.2	5.2	5.2	5.2
Human tissue losses	3.24	3.24	3.22	3.2	3.21
Antenna efficiency	64.2%	64.77%	63.8%	63.4%	63.2%
Total efficiency	2.1%	2.5%	2.1%	2%	1.7%

Antenna efficiency = **(**Radiated power + Human tissue losses**)** / Input power

The electric near field distribution on x-y planes at 2.45 GHz are shown in Figure 3-9a and Figure 3-9b where the x-y planes are located 20 mm above the skin and 2 mm above the antenna inside the skin respectively. (x-y plane shows top view and is parallel with antenna and skin surface). From this figure, one can see that electric near field intensity is much higher at outside of the human body model therefore the absorbed power would be less inside the body.

Moreover, to provide more precise understanding of the distribution of the electric near field inside and outside of the human body, a y-z plane cut at 2.45 GHz is also provided as shown in Figure 3-9d. This figure shows the electric near field intensity is lower inside the human body model and it is mainly focused outside the body with the peak levels. The reduced electric near field yields in reduced power absorption and lower SAR (as defined by equation 3.1). Thus, the radiated power is increased accordingly. As a result, the antenna radiation efficiency and gain are increased.

Furthermore, I have considered the effects of tissue environment as possible affecting factors during the implantation in my calculations. This would be beneficial when my research goes to the next step from vitro to vivo which increase my perception about the antenna performance in more realistic circumstances.

TABLE 3-5
VARIATIONS OF TISSUE ENVIRONMENT DURING IMPLANTATION.

Thickness variations in mm	Air gap layer			Interstitial Fluid layer		
	0.1	**0.3**	**0.5**	**0.1**	**0.3**	**0.5**
Efficiency%	1.8	1.6	1.4	1.8	1.7	1.5
Bandwidth (MHZ)	280	280	270	280	260	250
Resonance freq. GHz	2.42	2.44	2.46	2.42	2.39	2.38

TABLE 3-6
VARIATIONS OF TISSUE ENVIRONMENT DURING IMPLANTATION.

Variations / Effects	Skin thickness (mm)		Skin εr		Fat thickness (mm)		Fat εr	
	1.5	**2.5**	**34**	**42**	**3**	**5**	**4.5**	**6.5**
Efficiency%	2.5	2.1	2	2.5	2.3	2.3	2.1	2.4
Bandwidth (MHZ)	230	290	260	280	260	260	280	270
Resonance freq. GHz	2.37	2.44	2.37	2.48	2.39	2.42	2.37	2.46

As reported in [51] there is a substantial discrepancy between measurement (using rats) and simulation results on reflection coefficient without considering factors affecting the antenna performance in vivo. Therefore, I have investigated the possible factors such as possible air gap layer and interstitial fluid ($\varepsilon_r = 70$) between the antenna and skin. I also anticipate that other contributing factors such as variation of dielectric properties and thickness of the fat and skin should also be considered in calculations. Consequently, I added air gap and interstitial fluid layers with different thickness in calculations and incorporated aforementioned parameters. Figure 3-10 shows simulation environment for possible air gap layer and interstitial fluid when immerse the DS-PIFAs on FR4 substrate inside the human body numerical phantom. The results on efficiency, resonant frequency and bandwidth are tabulated in Table 3-5 and 3-6. These results indicate that the proposed antenna can cover the ISM band in above mentioned situations which is a noticeable achievement.

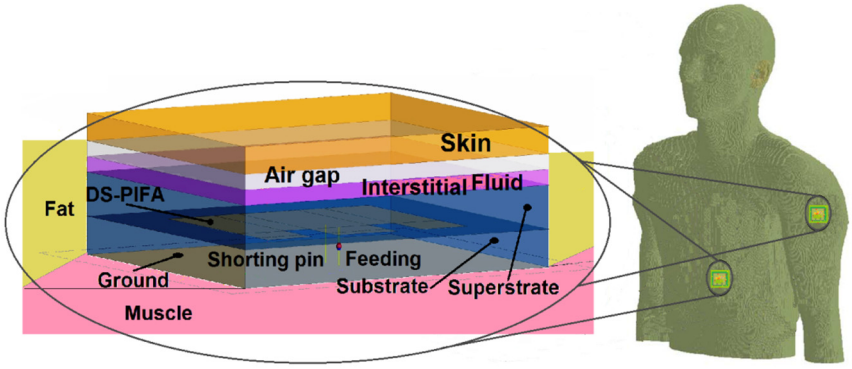

Figure 3-10: Simulation environment for possible air gap layer and interstitial fluid when implant DS-PIFAs in human body.

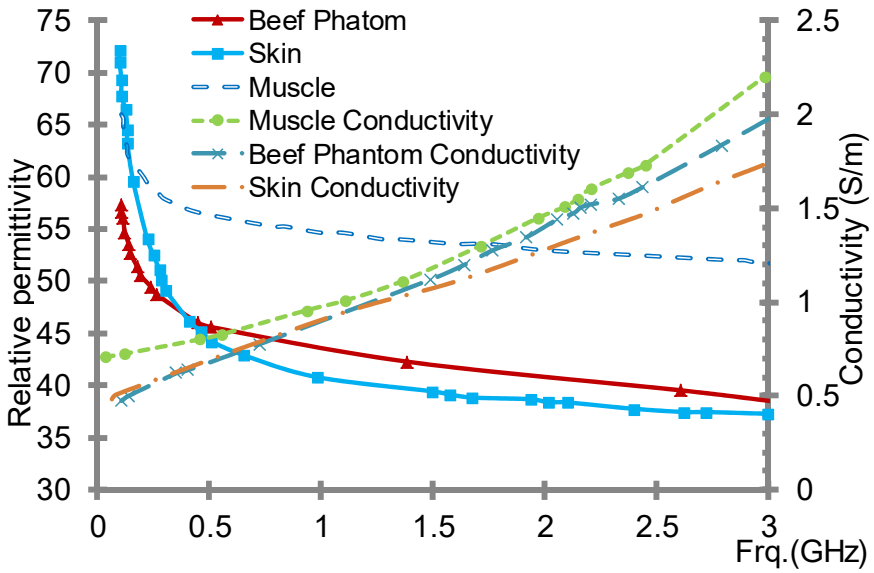

Figure 3-11: comparison of relative permittivity and conductivity of the beef phantom with published data in skin and muscle.

3.4 DS-PIFA Measurements

In order to verify the performance of the implanted antenna when placed inside human body, I have developed a phantom which is prepared with beef. The conductivity and dielectric constants of the experimental phantom were measured by using dielectric probe kit and Agilent E5071C network analyser from 100 MHz to 3 GHz when the experimental phantom was placed in a plastic container of size 120 × 120 × 45 mm^3. A good agreement with the desired dielectric properties [135] was observed, comparison of relative permittivity and conductivity of the beef, skin, and

muscle are shown in Figure 3-11. It can be found that the permittivity of beef phantom is closer to human skin which is useful as the antenna is close to skin. The measured result on reflection coefficient when the antenna (including superstrate) was immersed in experimental phantom shows a good agreement with calculated result using complex human body as shown in Figure 3-12. The Measurement set up and the miniaturised DS-PIFA prototypes on Fr4 and Rogers 3210 for MICS 400 MHz, ZigBee 868 MHz, WMTS 1430 MHz and ISM 2.4 GHz are shown in Figure 3-13.

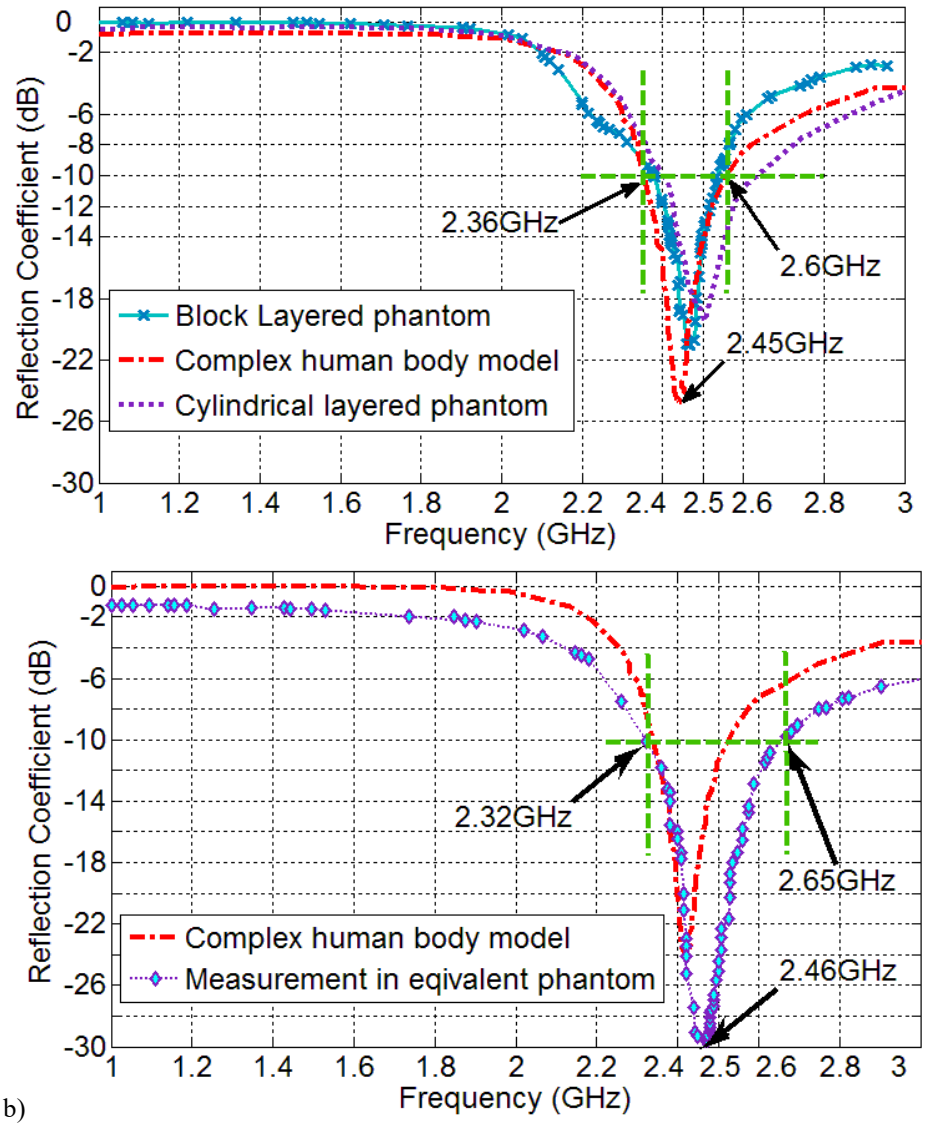

Figure 3-12: Reflection coefficient of Dual-slot PIFA: a) Calculated using Complex human body model, block Layered and cylindrical Layered phantoms, b) Measured vs. Calculated using Complex human body model.

The DS-PIFA has a measured bandwidth of 330 MHz (13.5%) which is significantly valuable when considering slight changes in dielectric properties of human tissue due to the dissimilar body shapes, genders, ages and etc. These changes in dielectric properties may shift the resonant frequency. Hence, the proposed antenna bandwidth could guarantee ISM band coverage for a variety of patients' tissue.

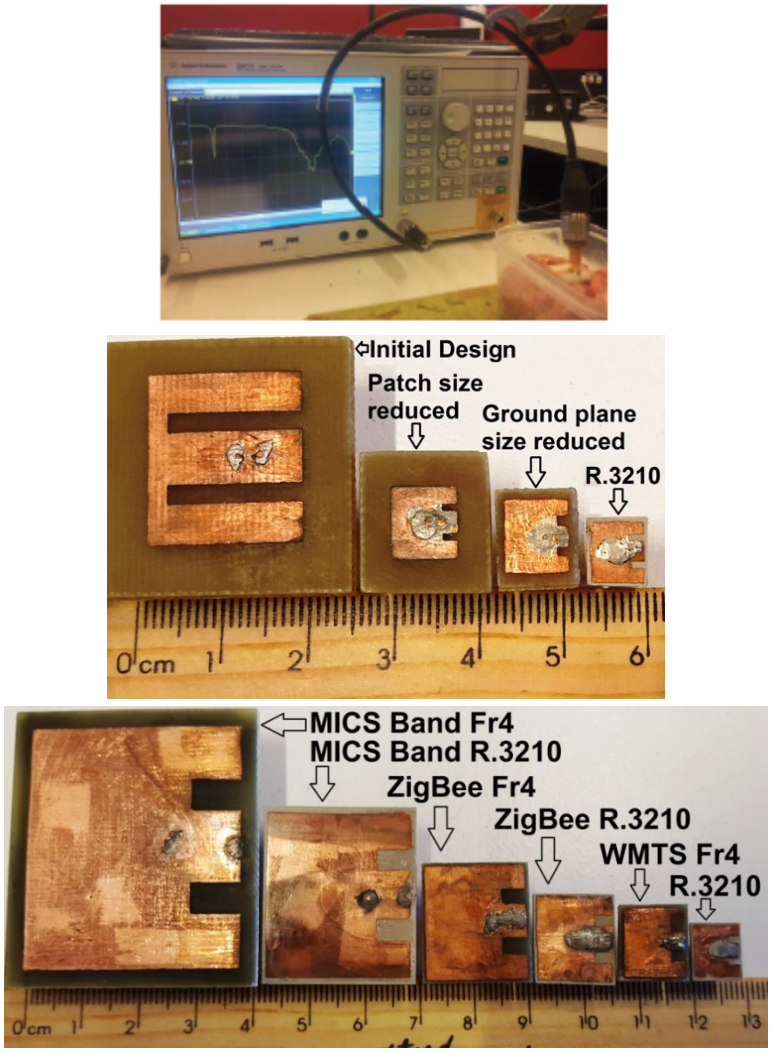

Figure 3-13: Measurement set up and Dual-Slot PIFAs prototype on FR4 and Rogers 3210 substrate for different frequency bands.

I have also used the experimental phantom to verify the performance of the proposed implantable DS-PIFAs for Medical Implant Communication Service (MICS) 400 MHz, Wireless Medical Telemetry Service (WMTS) band at 1430 MHz and Industrial, Scientific, and Medical (ISM) band at 2.4 GHz. The prototype antennas covering these four different standard biomedical bands are printed either on FR4 or Rogers 3210 and covered with superstrate layer with the same dielectric materials as substrate.

Figure 3-14 illustrates the Dual-slot PIFA covering ISM at 2400MHz using Rogers 3210 substrate and results on reflection coefficient of Calculated using block layered and homogeneous human tissue numerical mimicking phantoms versus measured inside the experimental phantom.

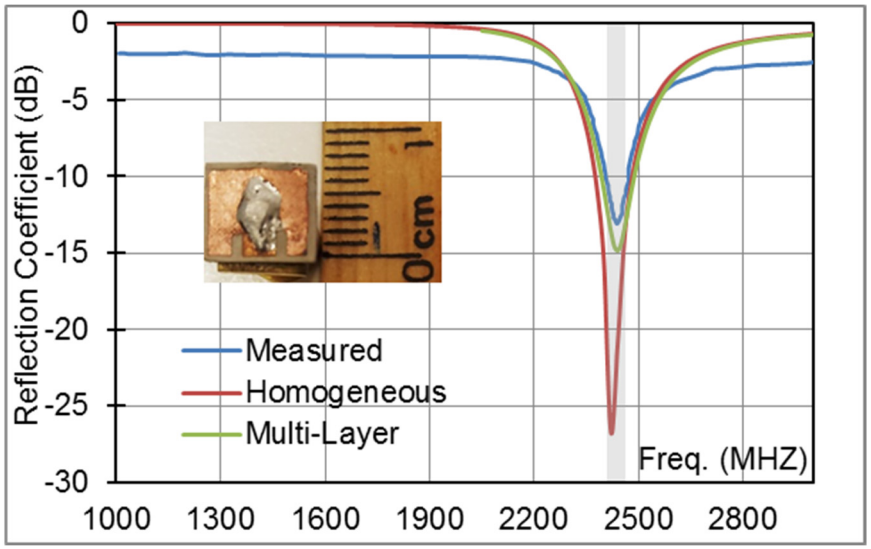

Figure 3-14: Reflection coefficient of Dual-slot PIFA covering ISM at 2400MHz using Rogers substrate: Calculated using block layered and homogeneous human tissue numerical mimicking phantoms versus Measured inside experimental phantom.

Dual-slot PIFAs covering WMTS band at 1400 MHz using FR4 and Rogers substrate, along with results on reflection coefficient for each antenna prototype, are

shown in Figure 3-15 and Figure 3-16 respectively. From these figures one can see the measured results on reflection coefficient when the antennas (including superstrate) were immersed, one by one, in experimental phantom show a good agreement with calculated results using block layered and homogeneous human tissue numerical mimicking phantoms.

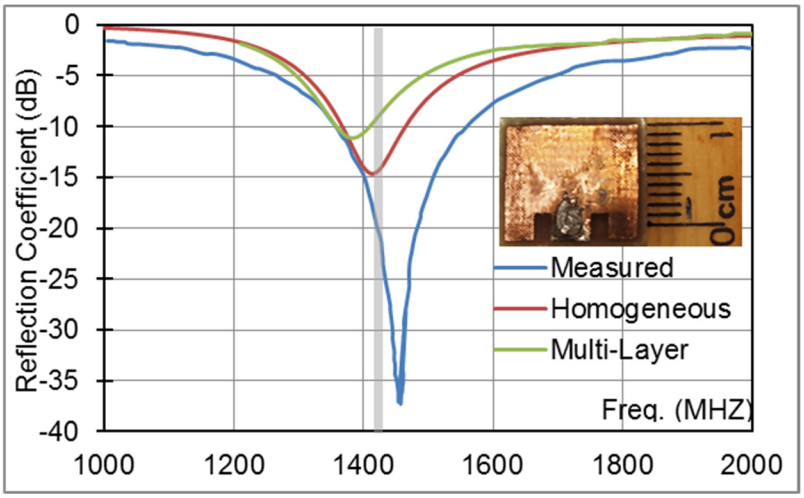

Figure 3-15: Reflection coefficient of Dual-slot PIFA covering WMTS at 1400MHz using FR4 substrate: Calculated using block layered and homogeneous human tissue numerical mimicking phantoms versus Measured inside experimental phantom.

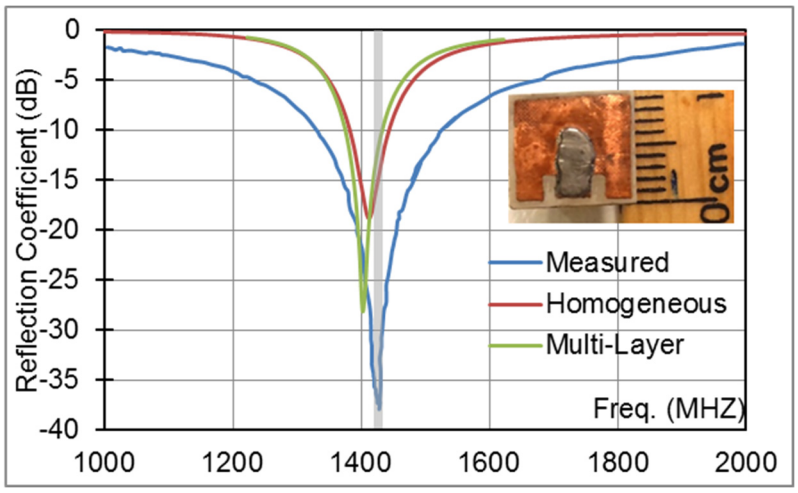

Figure 3-16: Reflection coefficient of Dual-slot PIFA covering WMTS at 1400MHz using Rogers substrate: Calculated using block layered and homogeneous human tissue numerical mimicking phantoms versus Measured inside experimental phantom.

Figure 3-17 and Figure 3-18 illustrate the Dual-slot PIFAs covering Zigbee at 868 MHz using FR4 and Rogers 3210 substrate and results on reflection coefficient of Calculated using block layered and homogeneous human tissue numerical mimicking phantoms versus measured inside the experimental phantom. The measured results on reflection coefficient when the proposed implantable antennas (including superstrate) were immersed, one by one, in experimental phantom show a good agreement with calculated results.

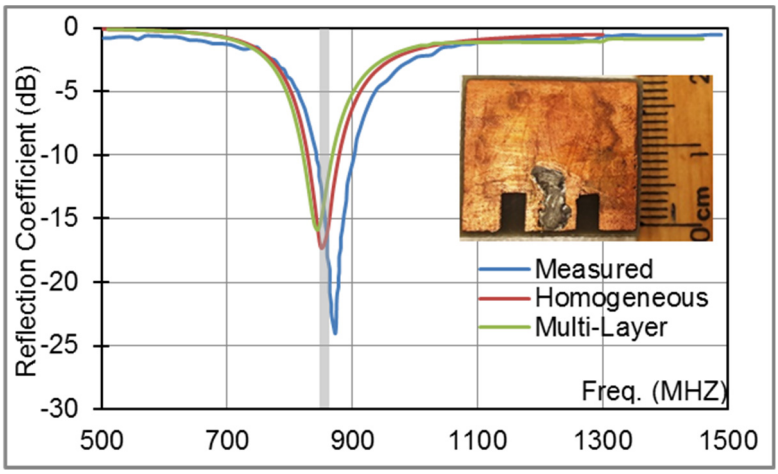

Figure 3-17: Reflection coefficient of Dual-slot PIFA covering Zigbee at 868MHz using FR4 substrate: Calculated using block layered and homogeneous human tissue numerical mimicking phantoms versus Measured inside experimental phantom.

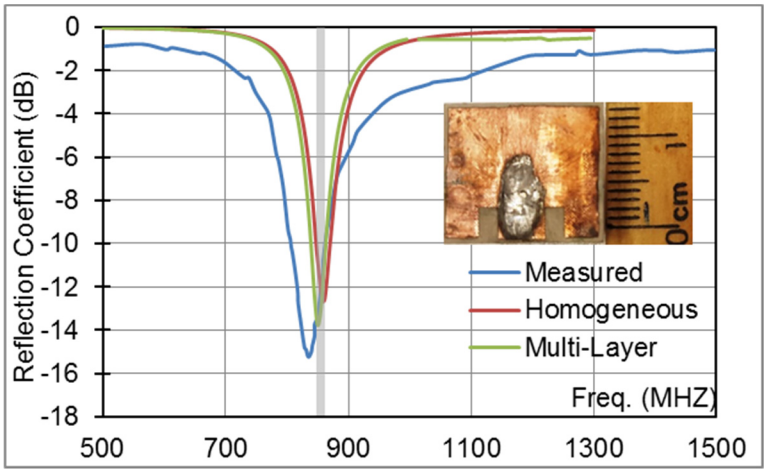

Figure 3-18: Reflection coefficient of Dual-slot PIFA covering Zigbee at 868MHz using Rogers substrate: Calculated using block layered and homogeneous human tissue numerical mimicking phantoms versus Measured inside experimental phantom.

Dual-slot PIFAs covering MICS band at 400 MHz using FR4 and Rogers substrate, along with results on reflection coefficient for each antenna prototype, are shown in Figure 3-19 and Figure 3-20 respectively. From these figures one can see the measured results on reflection coefficient when the antennas (including superstrate) were immersed, one by one, in experimental phantom show a good agreement with calculated results using block layered and homogeneous human tissue numerical mimicking phantoms.

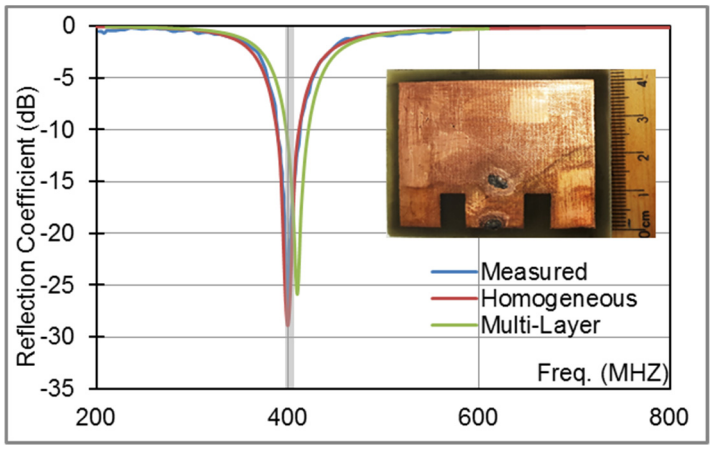

Figure 3-19: Reflection coefficient of Dual-slot PIFA covering MICS band at 400MHz using FR4 substrate: Calculated using block layered and homogeneous human tissue numerical mimicking phantoms versus Measured inside experimental phantom.

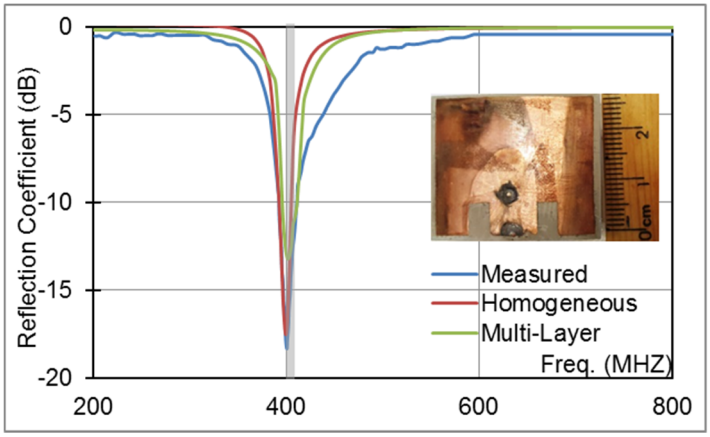

Figure 3-20: Reflection coefficient of Dual-slot PIFA covering MICS band at 400MHz using Rogers substrate: Calculated using block layered and homogeneous human tissue numerical mimicking phantoms versus Measured inside experimental phantom.

3.5 Specific Absorption Ratio (SAR)

For wireless implantable active biotelemetry devices, radiated power limits are determined to avoid over heating of the biological tissue. Human body absorbs the EM energy when exposed to Electromagnetic field. This may results in raised tissue temperature which depend on the exposed power and operating frequency. The temperature increment of human body by RF energy can be defined using SAR and the bio-heat transfer equation. Here, to comply with the maximum spatial average SAR limitations, 1.6 W/kg per 1 gram averaging [12], I have conducted the SAR measurement to determine the maximum input power for the proposed antenna resonating at 2450 MHz.

Conventionally, an electric field probe scanning technique is used as a practical method for SAR evaluation which can be quite expensive. Alternatively, optical fiber thermal sensors are used to measure SAR [136], however, in this method the radiator location is outside the human body phantom as the main aim was to measure SAR of mobile handsets. Here, I use optical fiber thermal sensor for implantable devices when the antenna is located inside the human body mimicking phantom.

This method is a simple measurement technique for measuring the temperature rise in an equivalent human tissue experimental phantom caused by electromagnetic energy absorption radiated by implanted antenna. I have used optical fiber thermal sensor as there is a concern that a metal wire connected to the thermoelectric thermal sensor could disturb the electromagnetic field in the phantom. In addition, the SAR can be stably evaluated over a wide range of frequency bands as the optical thermal sensors do not show frequency dependence, so that suitable for primary testing of an electric field probe scanning system. The relationship between the temperature rise

and the SAR in an equivalent human tissue phantom is given by bio heat transfer equation [136, 137]:

$$\rho.C\frac{\partial T}{\partial t} = K\nabla^2 T + \rho.SAR \tag{3.1}$$

Here, T is the temperature in the phantom (in kelvins), K is the thermal conductivity of the phantom (in watts per meter kelvin) and t is the elapsed time (in seconds), C is the specific heat of the phantom (in joules per kilogram kelvin) which is 3400 (J/kg.k) and ρ is the density of the phantom (in kilograms per cubic meter) which is 1060 (kg/m^3).

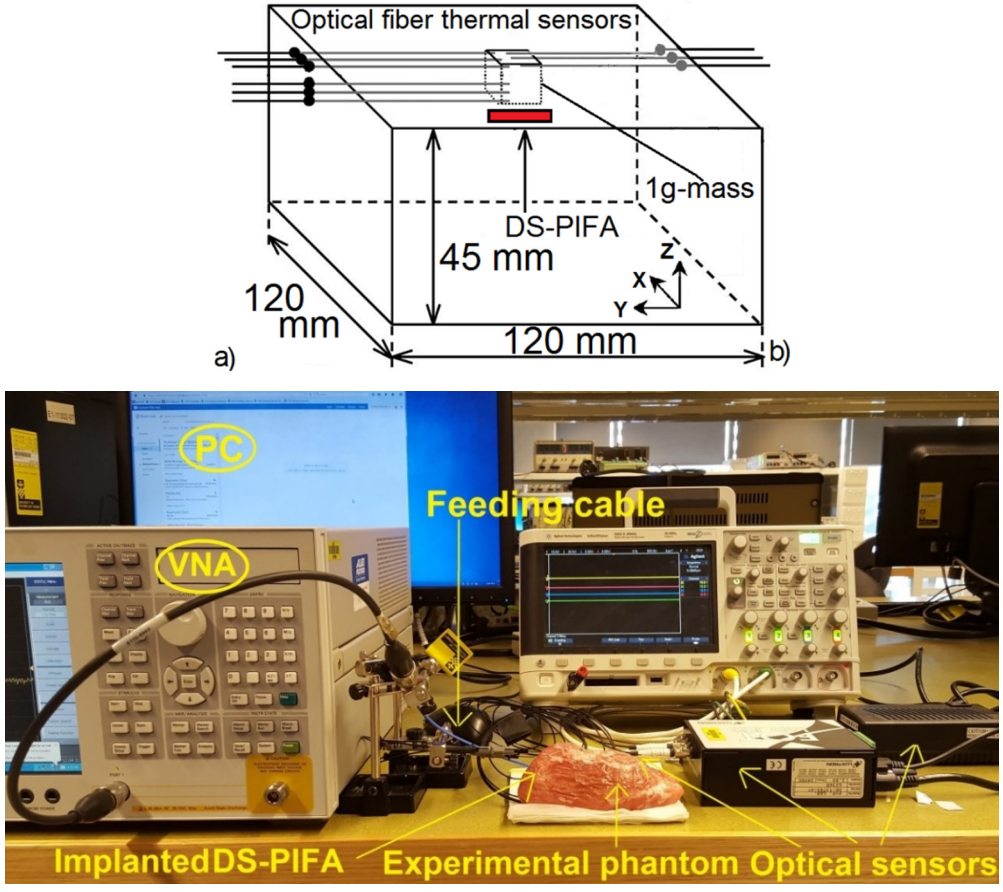

Figure 3-21: a) SAR measurement diagram using optical fibre thermal sensors. b) SAR measurement setup for Dual-slot PIFA on FR4 substrate.

Since the thermal diffusion is low in my experiment the equation (3.1) could be simplified. Here, to evaluate 1-gram average SAR measurment at multiple points are needed to estimate the temperature rise within the experimental phantom. Figure 3-21a shows optical thermal sensors arranged in a 3-D cubic lattice network completly covering the 1-gram mass to measure ΔT in the experimental cubic phantom. If the density of the mimicking phantom material is close to 1000 kg/m^3, then the side lengths of a 1-g mass cube are approximately 10 mm [136]. Consequently, optical fibre thermal sensors are arranged in a 3-D network by choosing 18 temperature measurement points to evaluate 1-g SAR. The sensors are located at .5 and 1.5mm under the skin with 5mm intervals over the X-Y plane parallel with radiator surface.

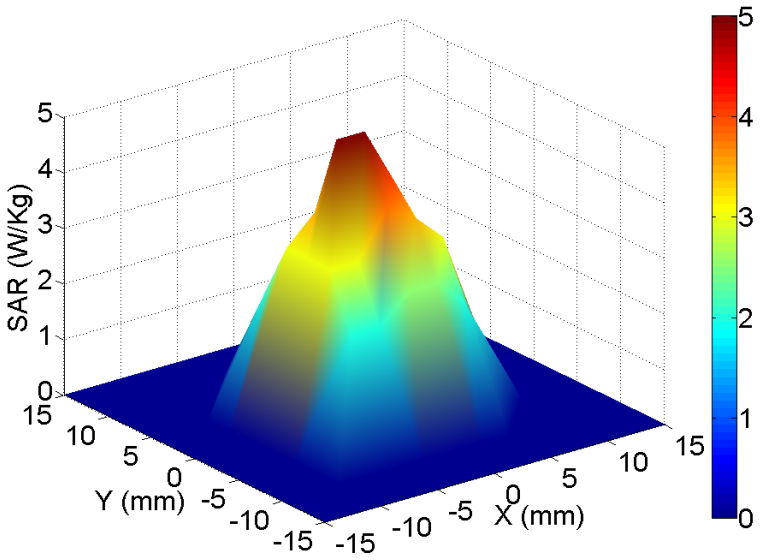

Figure 3-22: Measured 1g-SAR: Miniaturized Dual-Slot PIFA at 2.4 GHz.

I have employed Luxtron FOT Lab Kit and STM and STB optical thermal sensors (from Luxtron, Ltd) to measure temperature rise in the experimental phantom due to radiation. These optical fibres are made from polymer, and their measurement uncertainty is ±0.05C at room temperature.

The SAR measurement setup for DS-PIFA using optical fibre thermal sensors is shown in Figure 3-21b. The input power was set to 10dBm (10mw) at 2450 MHz and the equivalent phantom was exposed to microwaves up to 30 minutes while the thermal sensors measured the resulting temperature rise in the mimicking phantom. Figure 3-22 shows the 1-g SAR values using indirect SAR measurement. The calculated 1-g SAR for the input power level of 10dBm would be 5.2w/kg while the measured result indicates 4.8w/kg for 1-g SAR with the same input power. Figure 3-22 reveals that 1-g SAR is above the limitation [138] so that the input power must be set to less than 3dBm (2mw) to satisfy 1-g SAR regulation.

Furthermore, the 1g-SAR calculations have been carry out for seven different miniaturized DS-PIFAs cover four different standard biomedical bands such as MICS band, Zigbee, WMTS band and ISM band tabulated in Table 3-7. To verify the calculated SAR results, SAR measurements have been conducted for seven different miniaturized DS-PIFAs which could cover four different standard biomedical bands such as MICS band, Zigbee, WMTS band and ISM band printed either on FR4 or Rogers 3210.

The input power was set to 10 dBm (10 mw) at MICS, Zigbee, WMTS and ISM bands. The equivalent phantom was exposed to microwaves up to 30 minutes while the thermal sensors measured the resulting temperature rise in the mimicking phantom. The measured temperatures and simplified form of equation (3.1) are used in a Matlab code to estimate the SAR. The SAR values are calculated in every five minutes step to monitor the SAR variations. The results on 1-g SAR for all the seven miniaturized DS-PIFAs are tabulated in Table 3-7.

3.6 Biotelemetry and Wireless Communication Link

Understanding of electromagnetic wave propagation within tissues is very useful for the design of implantable wireless system as it helps to optimize physical layer design and therefore, achieve improved performance [139]. To obtain realistic channel characteristics, propagation measurements are required with antennas implanted in human bodies. However, for medical implants in the human body, this could pose additional, ethical and practical constraints. Here, to study RF propagation from implanted antenna, I employ a 3D virtual simulation model which will be described later.

TABLE 3-7
MEASURED SAR OVER STANDARD BANDS FOR HEALTH CARE TELEMETRY SYSTEMS

Bands / Timing		Measured SAR for DS-PIFAs using FR4 and Rogers 3210						
		MICS FR4	**MICS ROGERS**	**Zigbee FR4**	**Zigbee ROGERS**	**WMTS FR4**	**WMTS ROGERS**	**ISM ROGERS**
1	**After 10 minutes**	3.5W/Kg	3.7W/Kg	3.8W/Kg	3.9W/Kg	4.0W/Kg	4.1W/Kg	4.5W/Kg
2	**After 15 minutes**	3.5W/Kg	3.8W/Kg	3.9W/Kg	3.9W/Kg	4.1W/Kg	4.3W/Kg	4.6W/Kg
3	**After 20 minutes**	3.6W/Kg	3.8W/Kg	3.9W/Kg	4.0W/Kg	4.2W/Kg	4.5W/Kg	4.8W/Kg
4	**After 25 minutes**	3.6W/Kg	3.9W/Kg	4W/Kg	4.1W/Kg	4.3W/Kg	4.5 W/Kg	4.9W/Kg
5	**After 30 minutes**	3.7W/Kg	3.9W/Kg	4W/Kg	4.1W/Kg	4.4W/Kg	4.6W/Kg	4.9W/Kg
Total		3.7W/Kg	3.9W/Kg	4W/Kg	4.1W/Kg	4.4W/Kg	4.6W/Kg	4.9W/Kg
Calculated		3.9W/Kg	4.1W/Kg	4.1W/Kg	4.3W/Kg	4.6W/Kg	4.7W/Kg	4.8W/Kg

In this section, I employ the miniaturized implantable DS-PIFA which operates over ISM band at 2.45 GHz, and occupies a volume of only 92 mm^3 with a compact size of 8.1×7.1×1.6 mm^3. The antenna provides a reasonably moderate radiation efficiency of 2.5% when immersed inside a human tissue mimicking numerical phantom. Moreover, the proposed PIFA has a measured bandwidth of 330MHz (13.5%).

3.6.1 Statistical Path Loss Model

The path loss in dB at distance d can be statistically modeled by:

$$PL(d) = P_t - P_r = PL(d_0) + 10n\log(\frac{d}{d_0}) + X_{\sigma dB} \quad (3.2)$$

where d is the Tx-Rx distance, $d_0 \leq d$, is a reference distance, X is a zero mean log-normally distributed random variable representing the random fading effects caused by layered tissue medium, receiver environment and antenna gains in different directions etc. [47, 139]. The path loss exponent is $n = 2$ for free space propagation, while for indoor propagation n is environment dependent. Since the human body represents a highly lossy medium, much higher value for the path loss exponent can be expected.

In this study, the wireless power link was simulated using FEKO™ [133]. The simulation environment is shown in Figure 3-23. The calculated values of $|S_{12}|$ obtained at various receiver locations surrounding the body implanted transmitter are used to calculate the pathloss $|S_{12}|^2$ = Pt/Pr. Moreover, in my calculations polarization mismatch was not considered and both Rx and Tx antennas are assumed to be perfectly impedance matched.

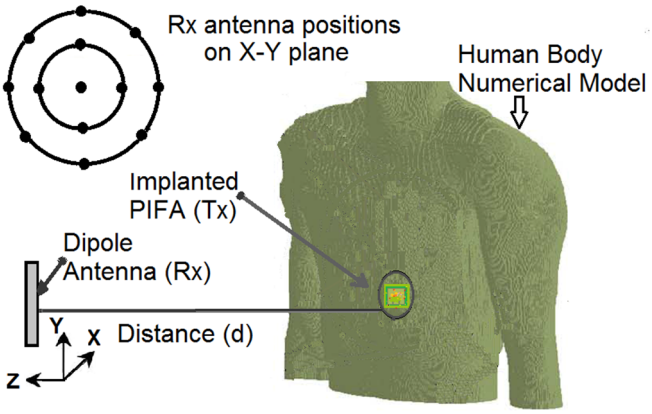

Figure 3-23: Simulation environment of the wireless power link.

In my simulation environment, I have used half-wavelength dipole antennas as receiver antennas with gain of 2.15 dB. Thirteen Rx antennas are arranged in concentric circles surrounding the body implanted PIFA as shown in Figure 3-23. The radius of circles are 150 mm, 250 mm respectively located at the xy-plane as shown in the same figure. For the characterization of the communication link, the proposed PIFA implanted inside a multi-layered numerical phantom acts as a Tx antenna. The position of the Tx antenna was fixed under the skin while the Rx antennas were positioned at various distances to calculate the pathloss. The distance (d) between Tx and Rx is varied along the Z axis from 50mm to 8000 mm to calculate the pathloss. The estimated path loss as a function of Tx-Rx separation is shown in Figure 3-24 in which the solid line indicates the mean value.

3.6.2 Pathloss Measurement

To verify the accuracy of simulated statistical path loss model, I have arranged a measurement set up as shown in Figure 3-25. In the set up I have used a monopole antenna as receiver antennas with gain of 1.25 dB. The Rx antenna has been connected to VNA via a 7 meter low loss coaxial cable. I have measured and considered the cable

loss in my measurement results. The proposed DS-PIFA employed as Tx antenna when implanted inside the same experimental phantom I used in previous section.

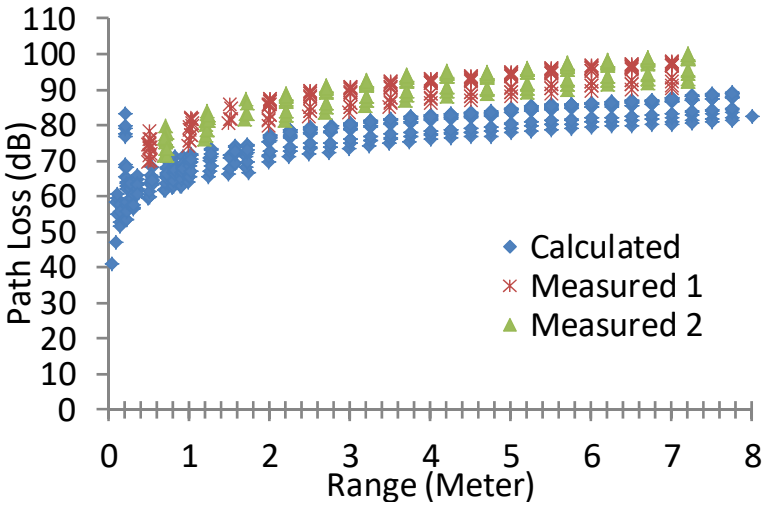

Figure 3-24: Calculated and Measured pathloss variation for Rx and Tx separation.

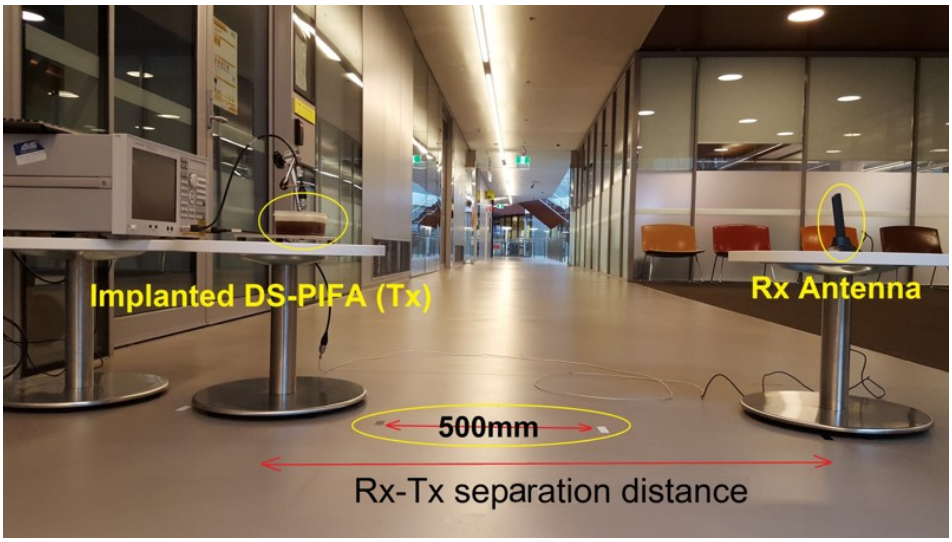

Figure 3-25: Pathloss measurement inside the UTS FEIT Building (Building 11).

The position of the Tx antenna was fixed under inside the phantom while the Rx antenna was positioned at various distances to measure the pathloss. The distance (d) between Tx and Rx is varied from 0.50 m to 7 m to measure the pathloss along the black and white labels positioned with 0.5m intervals. The orientation of Rx antenna

has been varied when measuring S_{12} at each position to record the maximum value and also repeated the measurements 10 times to collect more data. The estimated path loss as a function of Tx-Rx separation is shown in Figure 3-24 in which the solid line indicates the mean value. The mean value of the measured path loss is almost 10 dB greater than the mean value of simulated path loss in different distances.

I have also calculated the estimation of the path loss exponent by using equation (3.2) and data provided by Log-distance path loss experimental model. I have solved the equation respect to n by using measured path loss data and minimum mean square (MMSE) method which results a path loss exponent of 2.86 for the environment showed in Figure 3-25.

3.6.3 Link Budget

I used a link budget to evaluate the required and available power for bio-medical data transmission. To carry out the link budget calculations, the Rx was placed at a distance of 1 m from the human body phantom surface while the Tx was placed under the skin layer. Here, the separation between the Tx and Rx was chosen to be 1m. The input power to the implanted antenna was set to 25 μW at 2.45 GHz ISM band according to European Research Council (ERC) regulation [11]. The parameters selected for developing the link budget of the communication environment are tabulated in Table 3-8. The minimum required power to guarantee the implanted antenna performance in the far field region can be calculated using standard formulas [30].

$$\text{Re}quired\ \ C/N_0 = \frac{E_b}{N_0} + 10\log(R) - G_c + G_d \tag{3.3}$$

$$Link\ \ C/N_0 = P_t - L_{Txfeed} + G_t + G_r - L_t - L_{Rxfeed} - N_0\ , \tag{3.4}$$

$$N_0 = 10\log(k) + 10\log(T_i) \quad (dB/Hz) \tag{3.5}$$

$$T_i = T_0(NF - 1) \quad (K) \tag{3.6}$$

where P_t is the input power, L_{feed} is the antenna feeding loss, R is the bit rate, d is the distance between Tx and Rx antennas, G_t is the gain of the Tx antenna, G_r denotes the gain of the Rx antennas and E_b is the energy per bit and N_0 is the noise power spectral density [139]. Utilizing the data in Table 3-8 along with (3) and (4), the obtainable and required C/N_0 can be calculated, respectively.

TABLE 3-8
PARAMETER VALUES: LINK BUDGET CALCULATION FOR A SEPARATION DISTANCE OF 1 M BETWEEN THE TX AND THE RX ANTENNAS.

Transmission		***Receiver***	
Freq.	2.45GHz	Rx antenna gain G_r	2.15dBi
Tx power P_t	25μW	Temperature T_0	293K
Tx power P_t	-16dBm	Receiver NF	3.5dB
Feeding loss L_{Txfeed}	0dB	Feeding loss L_{Rxfeed}	0dB
Tx antenna gain G_t	-12dBi	Boltzmann constant K	1.38×10^{-23}
Propagation		***Signal Quality***	
Noise power density N_0	-199.70 dBm/Hz	E_b/N_0 (ideal PSK)	9.6dB
Noise power density N_0	4.0×10^{-21}	Bit rate *R*	2Mb/s
Free space loss L_f	52dB	Bit error rate	1×10^{-5}
PL	65dB	Coding gain Gc	0dB
Distance	1m	Fixing deterioration G_d	2.5dB
link C/N_0	**118.7dB/Hz**	**Required C/N_0,**	**75.1dB/Hz**

For a distance of 1 m between the Tx and the Rx, the obtainable C/N_0 was 118.7 dB/Hz which exceeds the required C/N_0 of 75.1 dB/Hz. Hence, wireless communication is feasible. As the gains of Tx and Rx antennas have already been included in pathloss calculations, I did not consider them for this calculation again.

3.7 DS-PIFAs Performance with Different Slots Arrangement, Case I: (Slot Position on Two Neighbouring Sides)

Figure 3-26 shows the slot arrangement for DS-PIFA case I. In this case, one of the slots is located on the left side of the radiator while the other one is located on the bottom edge. The shorting pin position is close to the centre of the patch and the feeding point location is 5 mm away from the bottom edge along with the shorting pin. The antenna geometry printed on Fr4 substrate is tuned to resonate at 1100 MHz when immersed inside the human body. The length and width of the radiator are 0.43λ and 0.38λ respectively. To obtain a good impedance bandwidth, I considered different locations for shorting pin position. I observed that the antenna achieves proper impedance bandwidth when the shorting pin is located close to the centre of the patch. Poor impedance matching appears when the pin is located close to the top or bottom edge of the patch.

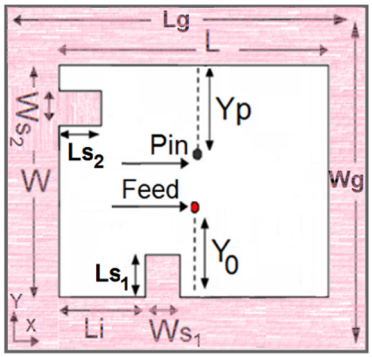

Figure 3-26: DS-PIFA slot position, Case I, on two neighbouring sides, left and bottom.

To investigate the effect of the slots' position on DS-PIFA resonance frequencies, first I changed the location of the vertical slot, in multiple steps, from the left side of the patch to the right side as shown in Figure 3-27. Later, I changed the horizontal slot position from top of the patch to the bottom in seven steps. I concluded that by changing the vertical slot location from the left side of the patch to the right, the centre frequency increases slightly while fractional bandwidth remains the same. On the other hand, by changing the horizontal slot position from top of the patch to the bottom, the centre resonant frequency decreases. This feature is useful to tune the antenna centre resonance frequency when designing the DS-PIFA for a specific biotelemetry band.

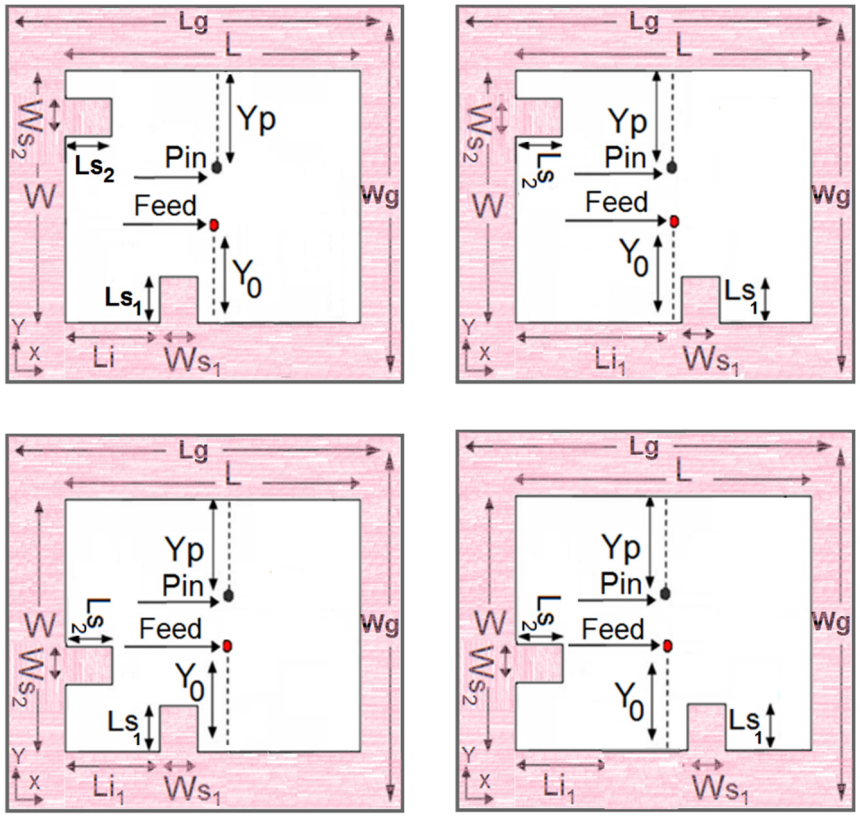

Figure 3-27: Different slots' location for DS-PIFA (Case I, Slot position on two neighbouring sides).

To investigate the effects of the slot size on the resonant frequency, first, I increased the length of the horizontal slot, Ls_2, and then the length of the vertical slot, Ls_1, was increased. The initial size of the both of the slots is 0.1λ. I conclude that by increasing the Ls_2 up to 0.25λ the resonant frequency remain about 1100 MHz and there is no second resonant, however, by increasing Ls_2 more than 0.25λ a second resonance may appear. When Ls_2 is equal to 0.3λ the first resonance drops to 990 MHz and the second resonance reduces to 1810 MHz. I observed that both of the resonance frequencies decreasing gradually when I increase the Ls_2 slowly up to 0.41λ, as shown in Figure 3-28. My proposed DS-PIFA structure is capable to resonate at two different frequencies, the lower resonance is determined by the size of the antenna structure and the second one is determined by the slots' length. When Ls_2 is equal to 0.41λ the antenna resonate at 830 MHz and 1600 MHz.

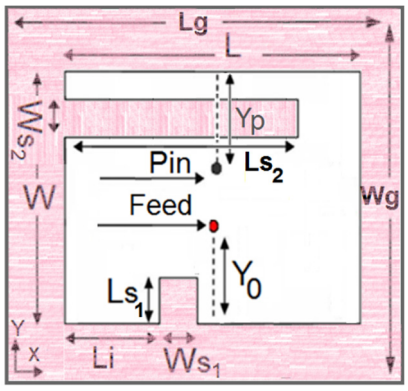

Figure 3-28: DS-PIFA, Case I: Horizontal slot length variation.

Here, I have reduced the initial size of the vertical slot to 0.065λ (2.88 mm). I have observed that by increasing the Ls_1 up to 0.22λ (9.88 mm), as shown in Figure 3-29, the resonant frequency remains around 1100 MHz with 50 MHz fractional bandwidth. In this case, there is no second resonant, however, by increasing Ls_1 more than 0.22 λ a second resonance may appear.

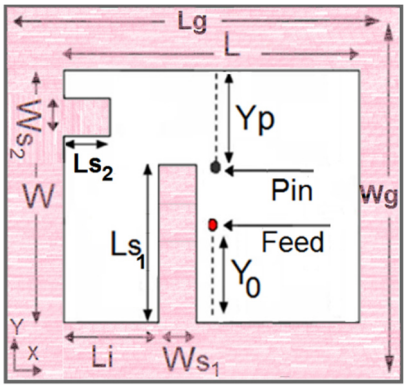

Figure 3-29: DS-PIFA, Case I: Vertical slot length variation.

When Ls_1 is equal to 0.25λ the first resonance drop to 1000 MHz and the second resonant decreases to 1700 MHz. I observed that both of the resonance frequencies decreasing gradually when I increase the Ls_1 up to 0.36λ (15.9 mm) slowly. When Ls_1 is equal to 0.29λ (12.88mm) the antenna resonate at 940 MHz and 1560 MHz. Here, the lower resonance is determined by the size of the antenna structure and the second one is determined by the slots' length.

Moreover, to cover medical telemetry bands such as MICS band, I increased the size of the structure by incremental coefficient which fixed later to a constant factor of two, this exclude the Fr4 physical and electromagnetic properties. The new length and width of the patch are 0.31λ (38.4 mm) and 0.27λ (33.6 mm) respectively. The length and width of the ground plane are 0.48λ (58.4 mm) and 0.44λ (55.3 mm) respectively. The antenna now resonate at 400 MHz and 828 MHz, however, the 400 MHz resonance does not satisfy my expectation for minimum reflection coefficient which is -10dB. The shorting pin used in the proposed structure helps to improve the impedance matching.

I considered twenty different locations to improve the reflection coefficient. Yet only a few locations for the shorting pin could improve the reflection coefficient

significantly. When the pin placed in these locations, the resonant frequency decreased, hence, it needs to be re-tuned. To overcome this issue I reduced the size of the structure to shift-up the lower frequency. The new length and width of the patch are 0.3λ (36.48 mm) and 0.26λ (31.92 mm) respectively. The antenna now operates over the MICS band at 400 MHz, in spite of that, the second resonance appear at 730 MHz and needs to be tuned to cover Zigbee band at 868 MHz. To adjust the upper band I increased the Ls_2 length gradually while Ls_1 has a length of 0.24λ (29.3 mm) as shown in Figure 3-30. When Ls_2 has a length of 0.3λ (35.3 mm), the antenna resonates at 400 MHz and 868 MHz. To find the optimum shorting pin location to achieve a good 50 Ω impedance match, 25 simulations have been conducted using block layer human body numerical phantom.

Since the antenna ground plane plays an important role in PIFA type antenna, I have also studied the effect of the ground plane size reduction on antenna performance. My studies indicate that when ground plane size reduced gradually to 0.31λ (38.4 mm) for length and 0.27λ (33.6 mm) for width, the both lower and higher resonant frequencies shift-down to 390 MHz and 800 MHz while the bandwidth of higher resonant increases by 2%.

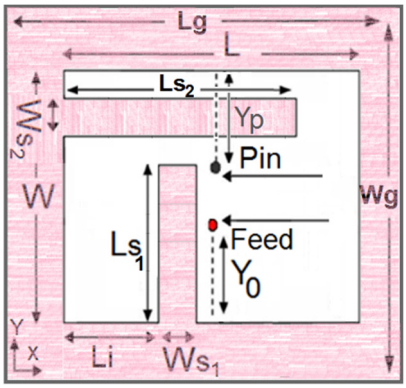

Figure 3-30: DS-PIFA, Case I: Horizontal and vertical slots length variation.

To cover other medical telemetry bands such as ISM band I reduced the size of the structure by incremental coefficient which fixed later to a constant factor of 0.7, this exclude the Fr4 physical and electromagnetic properties. The new length and width of the patch are 0.38λ (13.44 mm) and 0.34λ (11.76 mm) respectively. The radiator resonates at 2400 MHz and covers the ISM band fully, the antenna also resonates at 1360 MHz and has a fractional bandwidth of 50 MHz, yet this is not the band of interest. Therefore, I reduce the size of the structure further to shift-up the lower resonance frequency and cover the WMTS band at 1430 MHz. I may also adjust the length of Ls_1 to tune the higher frequency to operate over ISM band. The new length and width of the patch to cover the WMTS band are 0.34λ (11.9 mm) and 0.3λ (10.4 mm) respectively. I have also adjusted the length of the Ls_1 to 0.28λ (9.8 mm) to cover the ISM band. The structure now operates over two standard biomedical telemetry bands.

I have also investigated the effect of changing length of Ls_2 increasingly when Ls_1 is 0.26λ (9 mm) and antenna resonate at 2400 MHz and 1360 MHz. Here, I used my previous design when the patch size is 0.38λ (13.44 mm) by 0.34λ (11.76 mm). I observed that by slowly increasing the Ls_2 up to 0.23λ (10.2 mm), both of the resonance frequencies shifting-up gradually. When Ls_2 is 10.2 mm the radiator resonate at 1388 MHz and 3060 MHz. When I increase the length of Ls_2 from 10.2 mm to 13 mm slowly, both lower and higher resonant frequencies decrease gradually to 1180 MHz and 2730 MHz respectively. Here, I increased the length of Ls_1 further while Ls_2 is 13 mm, depicted in Figure 3-31. I observed that both of the resonant frequency shifted-down slightly. In this subsection, I have demonstrated the proposed geometry features including easy tuning to cover different biotelemetry bands and capability to operate over two bands of interest.

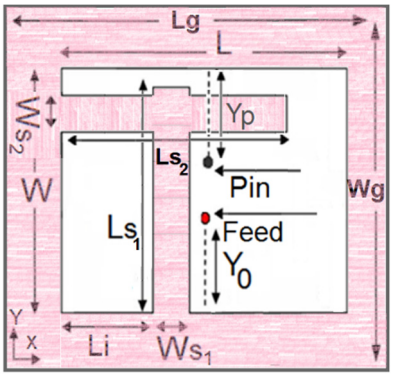

Figure 3-31: DS-PIFA, Case I: Extended vertical slot length variation.

3.8 Discussion

This chapter presented a class of miniaturized implantable DS-PIFA for biomedical telemetry applications. The proposed simple antenna geometry can be tuned, using presented tuning techniques, to resonate at different biotelemetry bands such as Medical Implant Communication Service (MICS) at 400 MHz, Zigbee at 868 MHz, Wireless Medical Telemetry Service (WMTS) band at 1430 MHz and Industrial, Scientific, and Medical (ISM) band at 2450 MHz. To miniaturize the antenna structure physical size, I have investigated the effect of antenna geometry parameters on radiator performance using empirical parametric studies. The design of highly compact DS-PIFAs, operating over a variety of standard biotelemetry bands, printed either on FR4 or on Rogers substrate is also reported. To validate antenna performance in more realistic tissue environment, I have also considered possible affecting factors such as air gap layer and interstitial fluid during the implantation in my calculations. I have also employed bio heat equations and optical fibre thermal sensors to establish an indirect method to conduct SAR measurement for the implantable antennas and verify SAR calculation. Proposed DS-PIFAs exhibit smaller size, good radiation efficiency and wider impedance bandwidth suitable for biomedical implant communications.

CHAPTER – 04

4. TRANSMITTER AND RECEIVER ANTENNAS FOR INGESTIBLE WIRELESS CAPSULE ENDOSCOPY SYSTEMES

4.1 Introduction

In this chapter, miniaturized wideband antennas are presented for ingestible wireless capsule endoscopy microsystems. The proposed antenna, operating over the Medical Implant Communication Service (MICS, 401- 406 MHz) band, is suitable to be integrated to an ingestible wireless capsule to perform as the transmitter antenna. The planar antenna is first designed to resonate at 400 MHz and later optimized for enhanced bandwidth and then was modified into a folded antenna to fit inside the miniature ingestible capsule. Finally, to support the structure and increase the ease of fabrication, the antenna is printed on a dielectric substrate and its wide band performance is validated. For the antenna design, two tunning strips connected to a loop are introduced to excite a new resonance in addition to the main resonance at MICS band, mainly for bandwidth enhancement of 200%. To verify the wide bandwidth performance, the measured impedance characteristics of the proposed antenna are obtained using VNA and an experimental tissue mimicking phantom. Moreover, a 400 MHz compact CP-PIFA is also presented as receiving base station

antenna for wireless capsule endoscopy systems. The antenna covers MICS band fully, has a compact size and circular polarization to enhance the low-level signal reception. The antenna has also been employed as an element in a body-worn conformal array, worn close to human body, for receiving the transmitted pictures of the small intestine took by the capsule. This data can also be used to determine capsule's position inside the human body. To verify the performance of the proposed body-worn antenna (including the conformal array) measurements are carried out using experimental phantom. I have also evaluated the calculated Specific Absorption Rate (SAR) by using a measured temperature rise inside a small intestine mimicking phantom.

4.2 Background Review and Motivation

The majority of the gastrointestinal tract related cancers are curable at early-stage, therefore, timely detection and diagnoses of cancer related to gastrointestinal track are extremely important, yet, the features and complexity of the digestive system restricts the operation of the current examination techniques [62, 64, 70, 71]. The colon and rectum at the bottom of the GI tract can be examined by using traditional Colonoscopy. Gastroscopy also may be used to examine the upper gastrointestinal tract. Small intestine which exists between the rest of the digestive system has an average length of seven meters and is highly convoluted, hence, the two above mentioned conventional techniques are not useful to examine any abnormalities in the small intestine.

Moreover, the special imaging techniques such as Computed Tomography or MRI are less useful to diagnose the diseases in the small intestine. To overcome these issues, a non-invasive cable free technique known Wireless Capsule Endoscopy has been proposed. The ingestible small size capsule includes a digital camera, a wireless transmitter including an antenna, light and power sources [54, 67]. When a patient gulps the capsule, it travels through the GI tract about eight hours, takes approximately sixty thousand color images and instantly transmits them to the base station body-worn receivers where antennas are worn on the patient's skin.

The capsule antenna needs to perform a key role in transmitting of the pictures as the quality of the signal detected by body-worn receiver depends mostly on the antenna performance inside the human body. The human body can be treated as lossy dielectric media for electromagnetic wave propagation which absorbs the wave energy, hence, the received signal power decreases significantly. Furthermore,

transmitting a number of quality real-time images needs a good power source which is constrained by room available inside the capsule.

Therefore, the transmitter antenna for wireless capsule endoscopy ideally has to have the following features: (i), the antenna structure has to be less sensitive to the variation of dielectric properties of human body tissue especially the GI tract, (ii), the resonator has to resonate within a standard frequency band such as MICS band and must provide extra fractional bandwidth to compensate shifting in center frequency, transmit high resolution images and huge number of data, third, for the patient comfort the antenna has to be small while its radiation efficiency has to remain reasonable. The enhancement of the antenna efficiency would facilitate the battery power saving and high data rate transmission.

Multi-band and wide-band implantable antennas with different configurations have been reported in the literature [31, 54, 67-69, 140-143]. A π-shaped PIFA antenna was presented for wideband performance using two meandered strips to excite dual resonant frequencies [141]. However, it occupies a high volume of 791 mm^3, needs further size minimization for implantation. To reduce the occupied volume, a stacked antenna with a reasonable bandwidth is proposed in [140], however, lower profile would be preferred for capsule endoscopy. Conformal configuration is another way property for capsule endoscopy design [68, 69] beside printed patches on dielectric materials. Printed implanted antenna on the wall of a capsule proposed in [64, 70], this reduces the occupied volume by the antenna inside the capsule and save the space for implanting the necessary sensors and electronic circuits. However, these antennas are more sensitive to surrounding environment variation results in frequency shifting. Flexible substrates are also employed to introduce a patch loaded with a complementary split-ring resonator in [65], covering the ISM band at 2.4 GHz. A

multilayer miniaturized circularly polarized helical antenna for capsule endoscope systems is presented in [67] operating over ISM band. The ISM 2400 MHz is not suitable for communication deep inside the human body compare to MICS 400 MHz as it leads to higher absorption loss.

My proposed antenna structure covers the lower required frequency band, i.e. MICS band and has also extra fractional bandwidth to compensate for the frequency shift due to dielectric body effects so that it can transmit high resolution images. Furthermore, the proposed antenna has a less sensitivity to variation of dielectric properties of human body tissue especially GI tract and has a small size to save more room within the capsule so that other components can be accommodated.

For capsule endoscopy systems, the body worn receiver antennas, are called base station antennas, have an important role in the detection of the received power from the capsule when transmitting from inside the body. As the GI tract is a curved non-linear track, the capsule orientation changes frequently during its journey which results in polarization mismatch, therefore, employing Rx antennas with circular polarization would help to overcome this issue. This will help to guarantee a reliable communication link between the capsule and the body worn base station. The received signal can be used to localize the capsule position in the digestive system but for this application an array of antennas are required at base station which are positioned at different location on the skin. The array element needs to resonate within the MICS frequency band for this application. Moreover, it must also satisfy the patient comfort, hence, the array element needs to be small in size and has planar geometry while at the same time keeping its radiation efficiency to be as high as possible. The human body effect on the base station array must be considered as the distance between the antenna array and human body is minimum.

Multiple-band body-worn textile antennas and wideband on-body antennas with different configurations have been reported in the literature [144-150]. An extremely low profile slot patch antenna for on body wireless biosensor is proposed in [78] for the medical body area network (MBAN). It has a size of 70 mm × 25 mm × 1 mm, which is compact and is able to maintain its flexible sensor structure and at the same time enhance its radiation efficiency by locating the proposed antenna at the top of the sensor as a sensor cover layer. A general design of the coplanar waveguide excited IIFA, traditionally excited by a microstrip is presented in [81]. This coplanar excitation permits the bandwidth improvement up to 50% by exciting a new antenna resonance with the help of ground plane. However, the antennas given in [22, 23] can cover only the ISM band at 2.4 GHz. PIFA type antenna with different configuration has also been used for wireless body area network (WBAN) applications [79, 80], however, the occupied volume is large and the polarization is not circular.

In this chapter, I present transmitter loop antennas with bandwidth enhancement and compact PIFA with circular polarization for wireless capsule endoscopy systems. The presented two novel antennas, operating over the MICS band at 400 MHz which have miniaturized geometry and occupy a very small volume, and have improved radiation efficiency and low SAR. In addition, I design base station conformal arrays for body worn receiver using four and six element of CP-PIFA. These CP-PIFA arrays are designed to be kept close to human body to act as receiver and transfer data to capsule to help to diagnose the GI tract diseases.

4.3 Modelling of Human GI Tract Environments

To mimic antenna implantation into different locations inside the body such as GI tract, the chest, muscle or small intestine, the proposed loop antenna is immersed inside an inhomogeneous 3-D multi layered complex human body model using HFSS™ [132]. The numerical model chosen is that of an adult male patient lying on a table. It consists of over 300 body parts to represent bones, muscles and organs. It has accuracy at the millimetre level and frequency dependent material property database is also included. This model can provide accurate results, however, it is not memory and computational-time intensive. For initial empirical antenna optimization, I employed cylindrically shaped multi-layered numerical phantoms, as well as layered-block phantoms. The layer arrangement and antenna position inside the numerical phantom is shown in Figure 4-1. The antenna is embedded into the muscle layer (where the multilayer phantom dielectric properties are close to that of small intestine) under the skin and fat layers and then the antenna performance calculated using FEKO™ [133]. The thickness of air gap layer and interstitial fluid are ideally assumed to be zero at this stage of design. Later to verify the antenna performance inside the human body in different locations such as small intestine, the complex human body HFSS™ [132] has been employed as shown in Figure 4-2.

4.4 Compact Tx Antenna to Fit into Capsule Comportment

The transmitter antenna is one of the active components inside the ingestible capsule and has to be integrated with other electrical components viz. biosensors, LED, camera, electronics, insulation and batteries, for the wireless capsule endoscope system. The passive and active components inside the endoscopy capsule may contain

many conducting materials, so it is necessary to study the antenna performance in presence of these components.

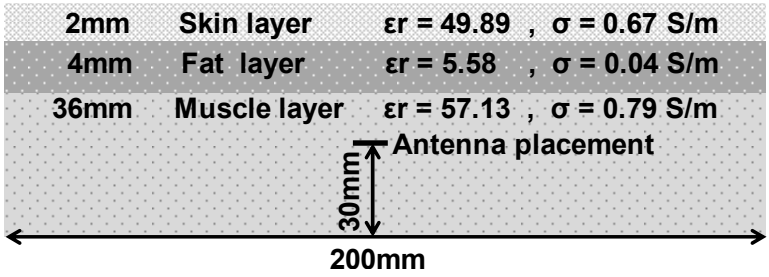

Figure 4-1. Simulation setup: Block-layered arrangement.

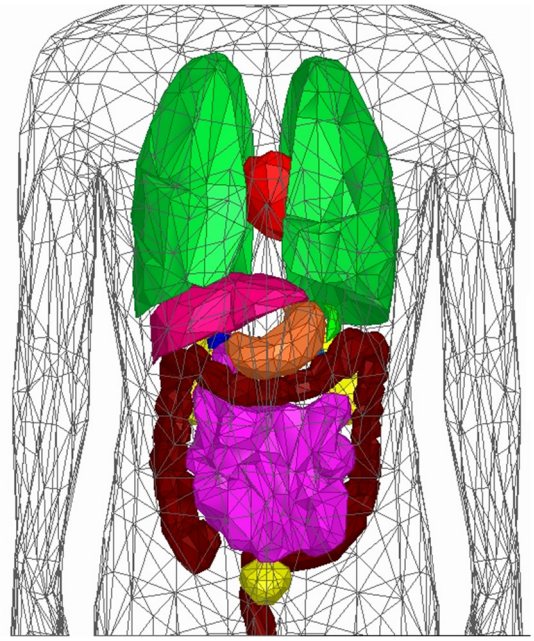

Figure 4-2. HFSS simulation setup: Complex human torso with GI tract.

Figure 4-3. shows the proposed antenna inside the capsule housing along with the placement of all the necessary components for the sensor control, data processing, communication and power supply. The optical dome is filled with air and the transceiver, battery pack and other electrical components are modelled to be perfectly electric conductors in the simulations, to determine antenna performance.

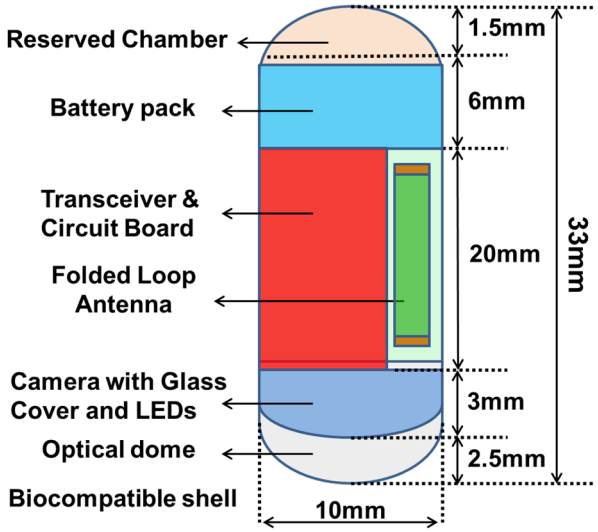

Figure 4-3. Implanted sensor conception: Folded co-planar loop antenna inside the capsule for endoscopy systems. Maximum dimensions are indicated. Placements of battery and electronics are indicated to estimate the overall volume occupancy.

Moreover, biocompatible insulation must embed the implantable device to avoid adverse tissue reaction [151]. The insulation also protects the electronics against the possible short circuits due to highly conductive human body tissues [152, 153]. The endoscopy capsule is generally coated with various biocompatible materials such as, Silastic MDX4-4210 Biomedical-Grade Base Elastomer ($\varepsilon_r = 3.3$, $\tan\delta = 0.01$) [51], Polyethylene ($\varepsilon_r = 2.25$, $\tan\delta = 0.001$) [64] and PEEK (Polyetheretherketones, $\varepsilon_r = 3.2$, $\tan\delta = 0.01$) [69].

The effective dielectric constant of the biocompatible coating can affect the resonant frequency of implanted antenna. The centre frequency may also vary for different thickness of the biocompatible coating material. Studies reported in [48, 152] establish that different methods of coating results in different coating thickness which significantly affects the implantable antenna resonant frequency. In this chapter, for the modelling, PEEK is chosen as the material for capsule shell and biocompatible coating. I keep the thickness of the PEEK to be 0.05 mm as it has minimum effect on the proposed Tx antenna based on my HFSS™ [132] simulations.

4.5 Wideband Folded Co-planar Loop Antenna

The ingestible endoscopy capsule system while traveling through the GI tract take thousands pictures of the GI tract and transform them using the antenna and transceiver placed in the capsule in real time. The small sized capsule system needs to transfer thousands of high resolution images using minimum power during eight hours of its journey inside the GI tract before it comes out naturally human excretion [62, 71]. Furthermore, different electromagnetic properties of the surrounding environments may vary the tuning of narrowband antennas. Therefore, to sustain the ongoing data transfer of the wireless endoscopy system, wideband performance is desirable for the radiator installed inside the capsule. Moreover, the radiator inside the capsule must fulfil the system requirements such as low profile and compact size.

Here, I proposed a novel wide band printed folded co-planar loop antenna for capsule endoscopy systems. Generally small transmitting loop antennas are very useful when the space is limited [154]. The proposed small loop antenna has also got a very desirable property related to robustness in performance when located close or inside the human body. Human body acts as a lossy dielectric media to electromagnetic waves. The conductivity part of the dielectric content absorbs energy from the radiated electric fields, which may severely degrade the antenna efficiency. For dipoles the electric fields are particularly strong in the near field [154] and so its performance is affected significantly by the presence of human body. However, since the human body is non-magnetic, there is no significant effect due to magnetic fields. For the loop antennas, the magnetic fields are strong in the near field and ultimately support the antenna radiation. This property makes loop antenna ideal candidate for use in human body. The loop antenna radiation, which is predominantly due to

magnetic fields, do not get affected when they are placed close or inside the human body. Therefore, they can provide a lower SAR and higher radiation efficiency for biomedical implantable and ingestible applications.

The proposed loop antenna structure is designed to operate over the MICS band. Figure 4-4 shows the top view of the proposed antenna geometry when it is unfolded. The resonator structure consists of a copper loop strip, size reduced ground plane, a pair of tuning strip lines and dielectric substrate. The loop in the proposed structure is designed to have only one turn which is based on experiments reported in the literature [154] as well as my calculations. I found that increasing the number of turns will reduce the radiation efficiency. Increasing the number of turns in a loop increases the inductance and the loss resistance.

On the other hand, when used for lower frequencies, it may require several turns to obtain the desired resonance. To overcome this issue, I have employed a pair of tuning strip lines to increase the electric length so that a resonance at lower resonant frequency can be obtained. In addition, these strips help to support the folded co-planar loop structure. This technique is different from meandering technique which may leads to current cancelation in close branches resulting in poor performance. Inserting tuning strip lines will also excite the second resonance that is close enough to the first resonance so that a wider bandwidth can be achieved.

The occupied area of the proposed miniaturized unfolded co-planar loop antenna measures 20 mm × 11 mm which is quite small. However, based on the maximum size of the capsule, it only could be fitted in the center of cylindrical capsule causing space constraint for other electronics and optical components within the capsule. To overcome this issue, I have folded the loop as shown in Figure 4-5. To minimize the

folding effects on the antenna performance, the position of tuning lines has been adjusted. The new folded co-planar loop now has a small volume of 266 mm^3, 20 mm × 5 mm × 2.66 mm and operates over the MICS band with wide bandwidth.

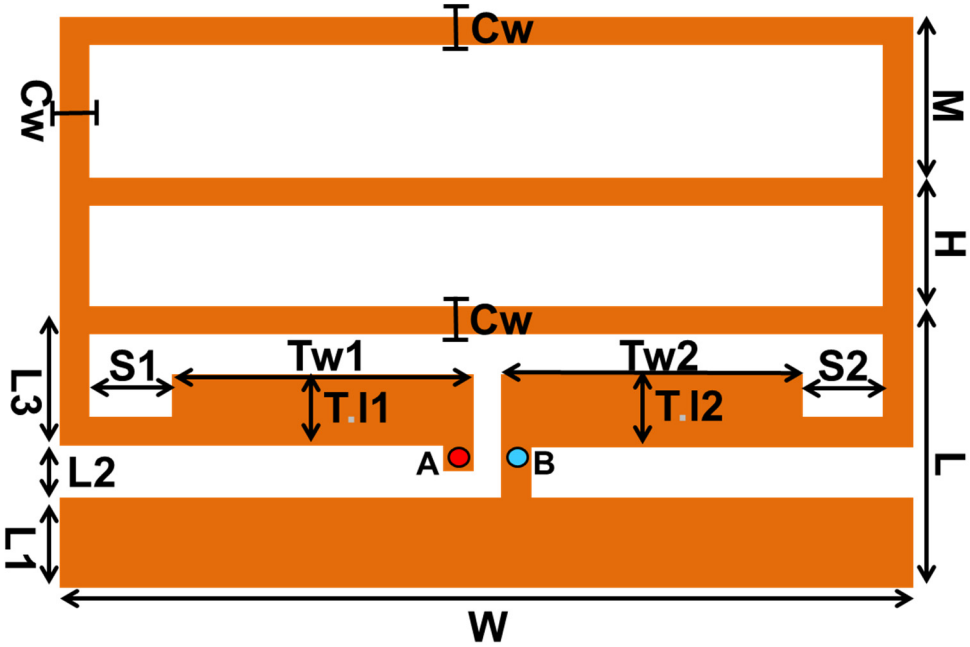

Figure 4-4. Wide band Tx loop antenna geometry: Unfolded version.

4.5.1 Technique for Improved Antenna Design

A well-designed capsule loop antenna is required to maintain two of the following characteristics at the same time:

-- Small size (in term of wavelength).

-- Radiation Efficiency.

-- Wide impedance bandwidth.

It is difficult to satisfy them all simultaneously. In other words, small transmitting loop antennas sacrifice bandwidth for small size and efficiency. The more efficient they are, the narrower the fractional bandwidth would be. Having a wide bandwidth and a small antenna reduces the antenna efficiency. Using a dummy load may help to satisfy the entire three requirement and yet the feeding line becomes a part of the antenna system and this may increase the size of the antenna. However, by employing tuning strip lines, dielectric substrate, rectangular matching elements and modifying the structure size, I successfully achieved an antenna design that fulfil the entire three requirement.

The tuning strip lines help to reduce the size and increasing the -10dB fractional bandwidth as explained beforehand. Employing the dielectric substrate reduces the electrical size of the antenna further and the rectangular matching elements enhance the impedance matching and support the wideband impedance bandwidth. The loop antennas generally have a low radiation resistance and its input impedance has a high inductive reactive component. Hence, it is difficult to match their low impedance to a 50-ohm coaxial line transmitter [154]. Here, to solve this issue, a pair of rectangular matching elements is placed near the feeding port to match the impedance and broaden the impedance bandwidth of the resonator. Total length of the folded co-planar loop strip from A to B is about 54.5 mm, close to the half of the wavelength of the MICS band center frequency at 403 MHz inside the human body. The antenna is fed by a 50 ohm semi rigid coaxial cable. The center conductor of the cable launches the signal from the left-side strip terminal A at the feed point and the outer conductor of the cable is affixed to the right-side strip end B which terminates to the ground plane.

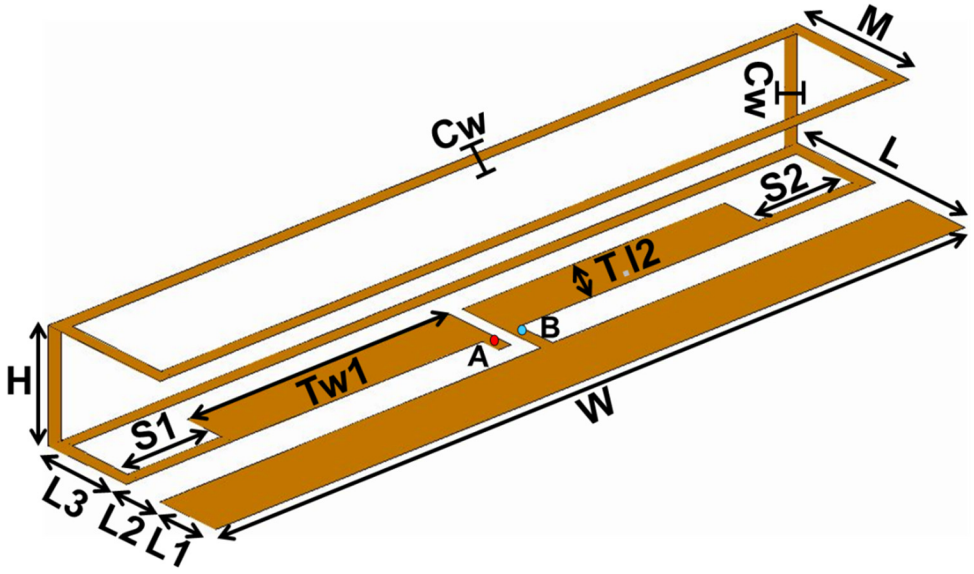

Figure 4-5. Wide band Tx antenna geometry: folded co-planar loop.

Dense packaging is required to reduce volume of the endoscopy capsule. Hence, the antenna feeding point is placed in a small predefined area to minimize the constraints. The feeding point is located at the top of the transceiver so that only a very short coaxial cable can be used as the feeding cable.

4.5.2 Design of Printed Folded Co-planar Loop Antenna

Since available space in the wireless capsule endoscopy system is extremely limited, so introducing a very compact antenna is highly significant. Here, I could successfully reduce the structure size of the folded co-planar loop significantly by printing it on a dielectric superstrate.

In the previous section, I have folded the loop antenna structure, as shown in Figure 4-5, to reduce the occupied area. However, the loop strip has a very narrow width so that the resonator structure needs to be supported and its fabrication can be quite expensive. Furthermore, it is important to also reduce the antenna height to

decrease the occupied volume further. To achieve these, I have employed dielectric substrate and by folding the loop backwards, as shown in Figure 4-6. Moreover, the height of the loop antenna structure needs to reduce to that of the superstrate height.

I used an FR4 substrate with ε_r of 4.5, loss tangent of 0.02 and thickness of 1.6mm, to print the folded co-planar loop antenna that now occupies a total volume of 160 mm^3 which is 40% smaller than the folded model. Moreover, the printed radiator is now easy to fabricate and the substrate also acts as support structure. The actual process of antenna manufacturing has to be taken into account in order to avoid extremely tight tolerances and to maximize the repeatability of the fabrication process. The detailed parameters of the proposed Tx antenna are given in Table 4-1.

I have also preformed parametric study to make sure that the smallest size possible has been achieved for the proposed printed loop antenna which covers the MICS band fully with wideband fractional bandwidth and reasonable radiation efficiency. I have also employed Rogers 3210 substrate to investigate the effect of substrate dielectric material on the performance of the printed loop antenna. The size and performance comparisons with similar types of antennas reported in the literature are tabulated in Table 4-2.

TABLE 4-1
DETAILED DIMENSION OF THE PROPOSED PRINTED FOLDED CO-PLANAR LOOP ANTENNA
(UNIT: MILLIMETERS)

Parameter	Value	Parameter	value	Parameter	value
H	2.66	Tw1	7	L1	0.33
L	5	Tw2	7	L2	1
W	20	Tl1	1.33	L3	2.4
S1	2.5	Tl2	1.33	CW	0.33
S2	2.5	M	3.33		

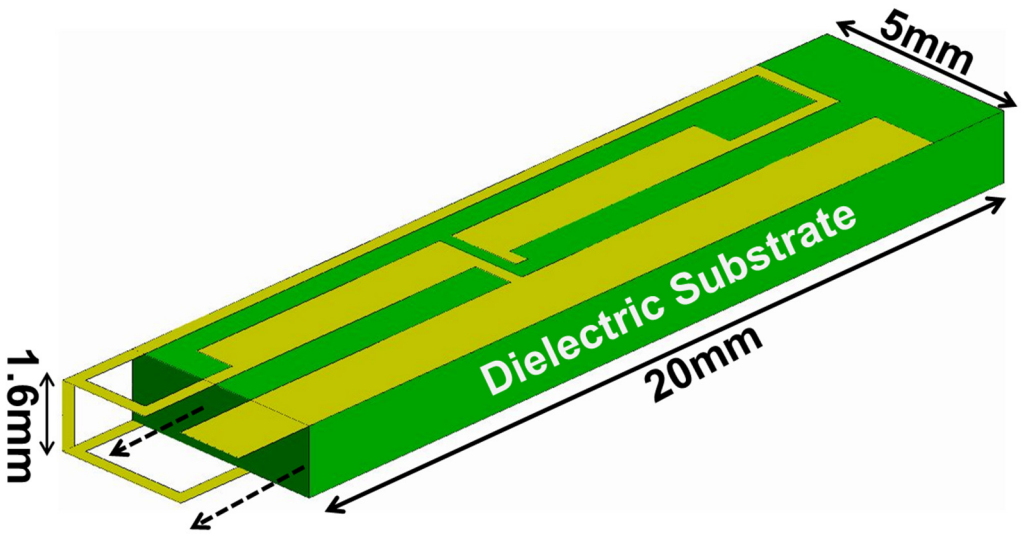

Figure 4-64. Wide band Tx antenna geometry: Printed folded co-planar loop antenna.

On the top side of the substrate, a ground plane of width 1.6 mm and length 20 mm is printed which can be use as the system ground plane for the capsule electronics. The feeding strip ports, matching elements and a tuning strip lines are all printed on same side of the FR4 substrate, but the rest of the loop is printed on the opposite side. Here, I need to connect the two printed conductors on two side of the FR4 together by using two narrow conductor strips as shown in Figure 4-6.

I studied and compared both printed and folded co-planar loop antennas performance inside the numerical phantom of the GI tract. To mimic the antenna implantation into the small intestine, the proposed Tx antenna was immersed inside an inhomogeneous multi layered complex human body phantom using HFSS™ [132]. The Results on VSWR of Folded Co-planar Loop antenna and Printed Folded Co-planar Loop antenna are compared in Figure 4-7. It reveals that both antennas cover the MICS band fully and show wide band performance. Reducing the antenna height and printing on FR4 substrate shifted up the lower edge of the band width by 10 MHz, however, both antennas have a VSWR of ≤ smaller than 2 up to frequency 1100 MHz.

The printed version has a radiation efficiency of 0.92% inside the body which is 0.03% lower than the original version.

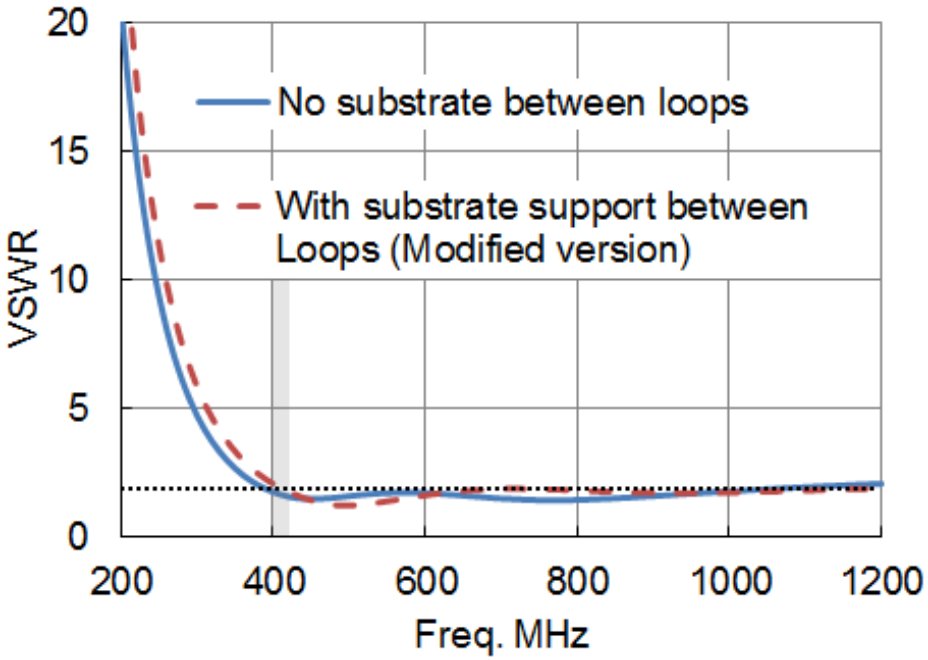

Figure 4-7. VSWR comparison of folded and modified loop antennas.

TABLE 4-2
SIZE AND PERFORMANCE COMPARISON OF THE PROPOSED TX ANTENNA

Ref.	Frequency MHz	Antenna Type	Fractional Bandwidth	Vol. mm^3
[1]	1400	Meandered dipole Conformal	5%	29.2 x 5
[2]	400	Outer-Wall Loop Conformal	65%	17 x 4
[3]	500	Spiral antenna	21%	392.5
[4]	450	Spiral antenna	14%	235.5
[5]	400	Meandered dipole	37.8%	329
[6]	2400	Helical antenna	26%	299
This work	400	Folded antenna	175%	266
This work Modified	400	Printed folded antenna	175%	160

The Surface current distribution for the proposed printed folded co-planar loop antenna at 403 MHz is shown in Figure 4-8. The main current is limited in the closed loop pattern and feed port area so that the current on the ground plane is low. This would be beneficial for the capsule application. As the capsule travels through the GI tract, the human body proximity effect may lead to the current variation and degrading the antenna performance. In this case the resonating currents are spread out over the system ground plane resulting poor radiation efficiency and shifting down the resonate frequencies. The proposed printed folded co-planar loop antenna is a good candidate for the capsule endoscopy system since the current induced on the ground plane is small.

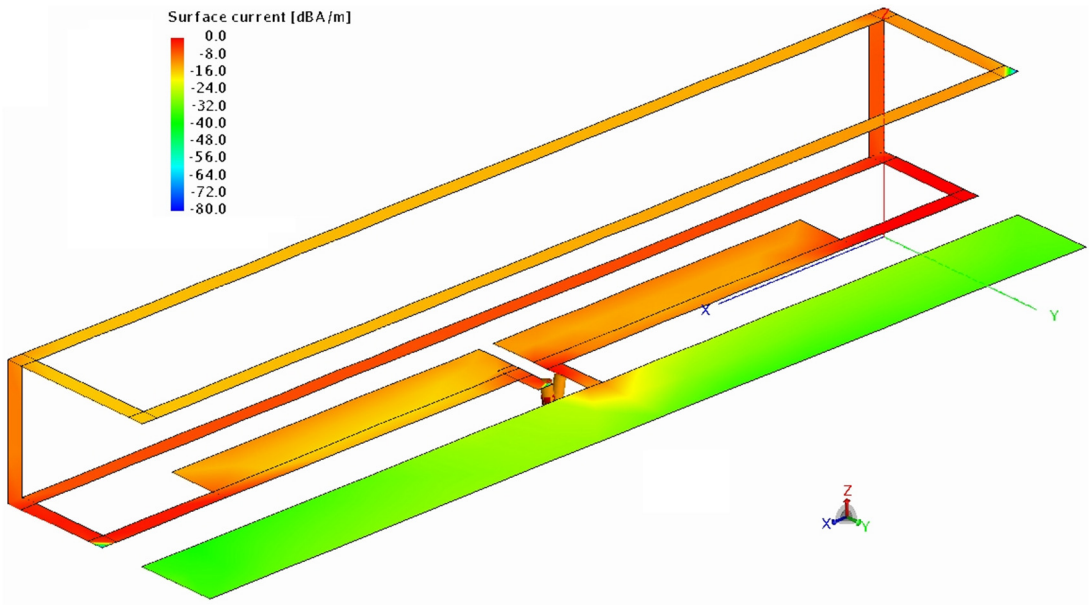

Figure 4-8. Surface current distribution for the folded co-planar loop antenna.

4.6 Measurements for the Proposed Antenna

The printed folded loop antenna prototype, used as capsule transmitter, is shown in Figure 4-9. The prototype antenna is printed on FR4 substrate and operates over the MICS band at 400 MHz. This figure shows the bottom and top views of printed loop antenna are connected to the coaxial cable. The measurement setup is also shown in Figure 4-10. Here, in order to verify the performance of the implanted antenna when placed inside the human body, I have developed a meat phantom that is prepared using beef. The conductivity and dielectric constants of the experimental phantom were measured by using dielectric probe kit from 100 MHz to 3 GHz.

The comparison of relative permittivity and conductivity of the beef, skin and small intestine are shown in Figure 4-11. The measured result on reflection coefficient, when the printed folded loop antenna was immersed in the experimental phantom, shows a good agreement with calculated results obtained using complex human body model as shown in Figure 4-12.

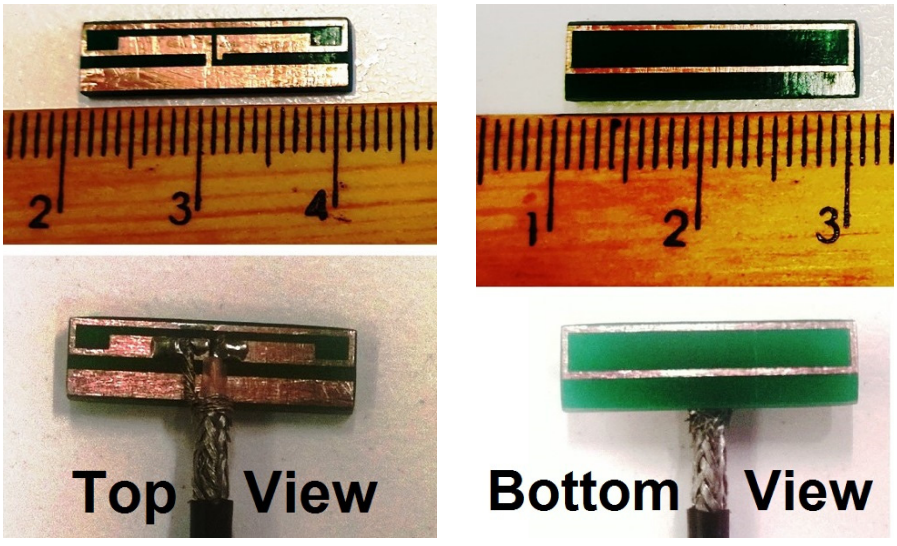

Figure 4-9. Transmitter antenna on FR4: Top view and bottom view.

Figure 4-10. Measurement setup for Transmitter antenna on FR4.

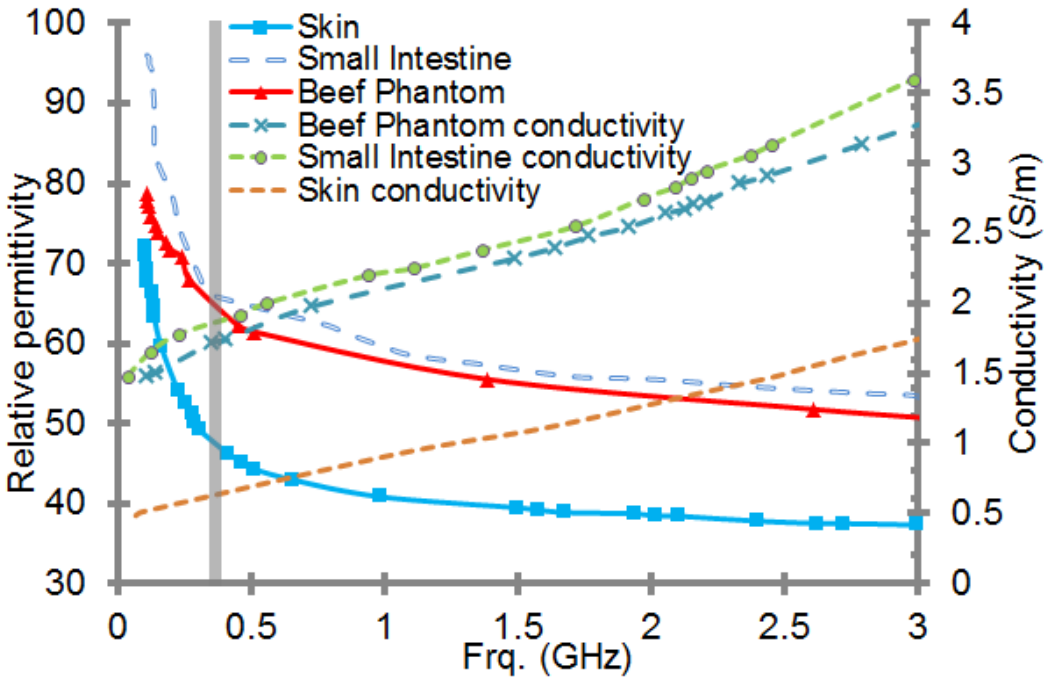

Figure 4-11. The comparison of relative permittivity and conductivity of the experimental phantom, skin and small intestine.

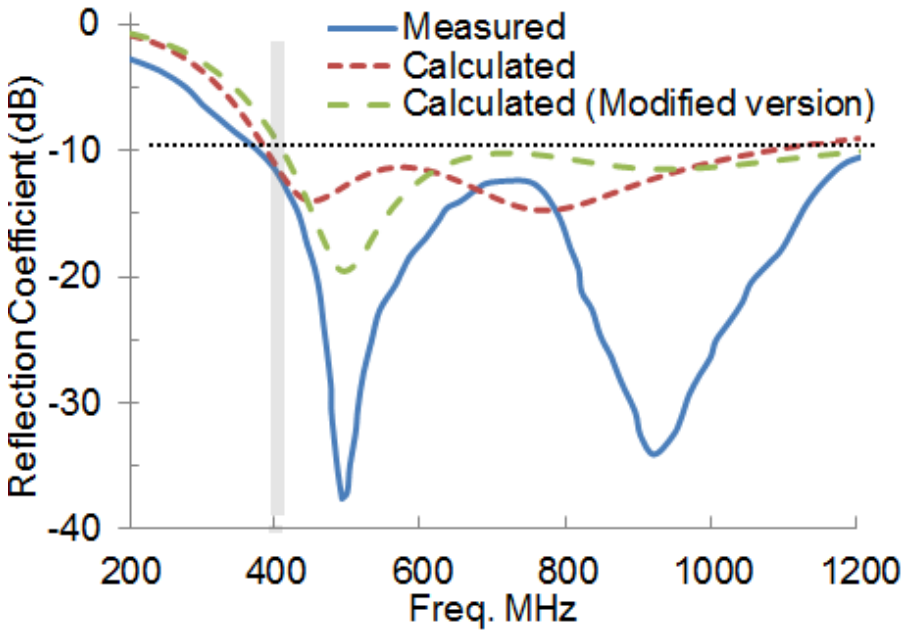

Figure 4-12. Reflection coefficient comparison: calculated versus measured.

4.6.1 SAR Measurements

To calculate 1-g SAR, due to the loop antenna radiation, inside the small intestine, complex human body model is employed as shown in Figure 4-2. There are challenges in measuring SAR inside the human body. Conventionally, an electric field probe scanning technique is used as a practical method for SAR evaluation which can be quite expensive. In this work, optical fiber thermal sensors are employed to measure temprature raise and indirectly obtain SAR. The advantages of using an optical fiber thermal sensor is that it will not disturb the electromagnetic field within the mimicking phantom. This method also may be employed over a wide frequency range as it is frequency independent. Here, I have modified the optical method introduced in [136] to measure SAR when the device is located inside the human body mimicking phantom. This method first measurs the temperature rise in the experimental phantom caused by absorption of the electromagnetic radiation from the Tx printed loop

antenna. The relationship between the temperature rise and the SAR in an equivalet human tissue phantom is given by [136]:

$$p.c\frac{\partial T}{\partial t} = K\nabla^2 T + p.SAR \tag{4.1}$$

Here, T is the temperature in the phantom (in kelvins), K is the thermal conductivity of the phantom (in watts per meter kelvin) and t is the elapsed time (in seconds), C is the specific heat of the phantom (in joules per kilogram kelvin) which is 3400 (J/kg.k) and ρ is the density of the phantom (in kilograms per cubic meter) which is 1060 (kg/m^3).

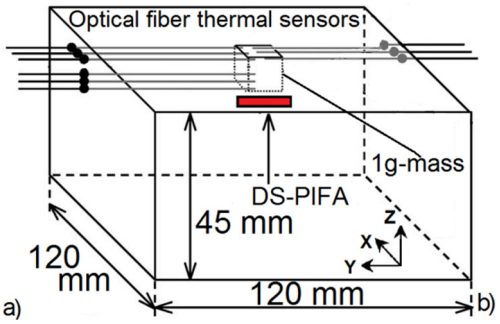

Figure 4-13. Schematic of optical fibre sensors arrangement for 1g-SAR measurement.

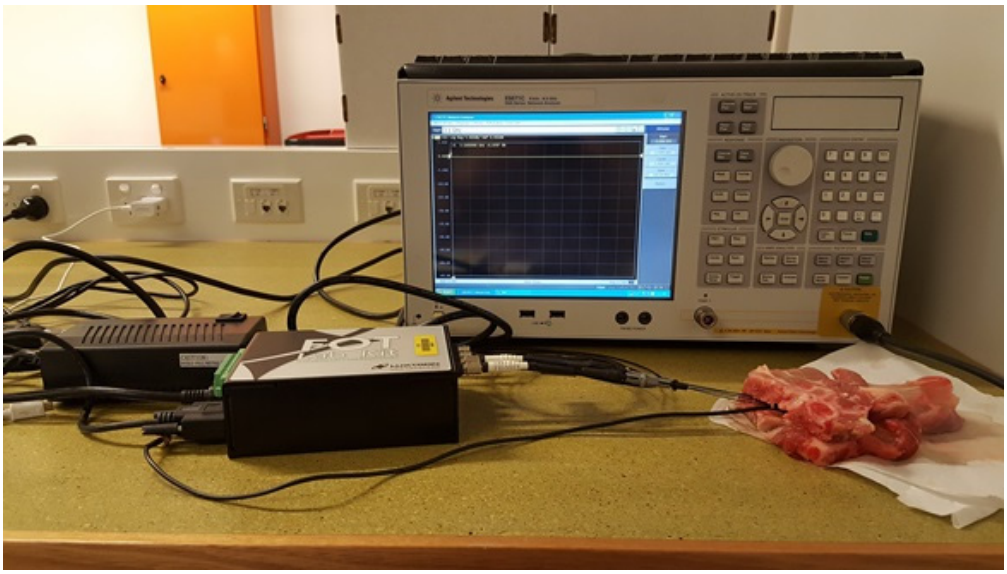

Figure 4-14. 1g-SAR measurement setup using optical fibre sensors arrangement.

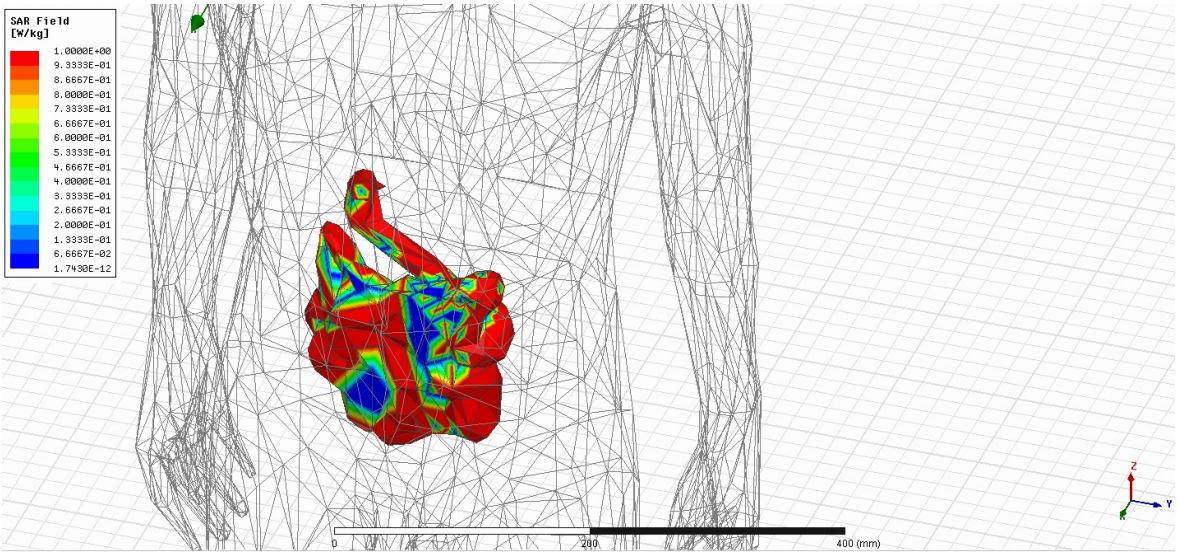

Figure 4-15. SAR calculation for transmitter antenna inside the small intestine.

Equation (4.1) could be simplified when the thermal diffusion is low. In addition, to evaluate 1-gram average SAR measurements at multiple points are needed to estimate the temperature rise within the experimental phantom. Figure 4-13 shows the optical thermal sensors arranged in a 3-D cubic lattice network that completely covers the 1-gram mass to measure ΔT in the experimental cubic phantom. This arrangement for the optical fibre thermal sensors is similar to the same arrangement I used in Chapter 1. As the density of the phantom material is around 1000 kg/m^3, the side lengths of a 1-g mass cube are approximately 10 mm, so that, optical fibre thermal sensors should be arranged in a 3D network by choosing 18 temperature measurement points to evaluate 1-g SAR. The optical sensors are placed at depth of 0.5 and 1.5 mm under the skin with 5 mm intervals over the X-Y plane parallel with radiator surface. Here, I have employed Luxtron FOT Lab Kit and STM and STB optical thermal sensors (from Luxtron, Ltd) to measure temperature rise in the experimental phantom due to radiation.

The input power for the antenna was set to 10dBm (10mw) at 400 MHz and the equivalent phantom was exposed to antenna radiation up to 30 minutes while the

thermal sensors measured the resulting temperature rise in the mimicking phantom. The SAR measurement setup is shown in Figure 4-14. The calculated 1-g SAR for the input power level of 0dBm would be 1w/kg, as shown in Figure 4-15, while the measured result indicates 4.8w/kg for 1-g SAR with 10dBm input power. This measurement result reveals that 1-g SAR is above the limitation with 10dBm input power so that the input power must be set to less than 3dBm (2mw) to satisfy 1-g SAR regulation.

4.7 Body-worn Antenna for Base Station Array

The video data radiated by the ingested capsule is received by a base station of receivers whose antennas are worn on the body of a patient. Hence, the base station antennas play a very important role for disease diagnosis. The receiving antenna for the wireless capsule endoscopy system has to be body-worn antenna type and must have low profile, electrically small size and good impedance bandwidth when placed close to the human body. Moreover, it must satisfy the patient comfort and safety. Furthermore, the Rx antenna should have circular polarization (CP) to minimize the polarization mismatch. Usually the capsule Tx antenna is designed for liner polarization, on the other hand, the orientation of the wireless capsule, while traveling inside the small intestine region, changes frequently, so that, the chance of polarization mismatch is high. In this case, employing receiver elements featuring circular polarization is important to improve the overall system performance by detecting linearly polarized transmitted signals that are radiated by capsule undergoing different orientations inside the body.

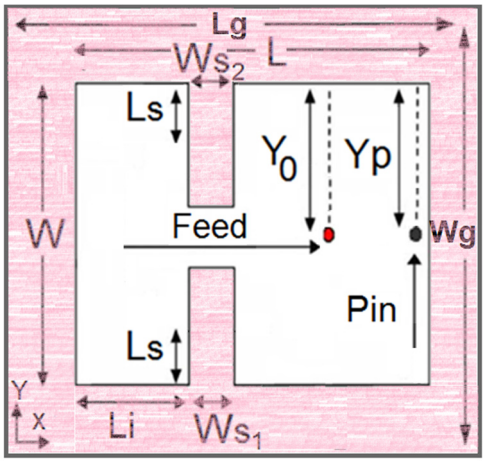

Figure 4-16. Geometry of proposed receiver antenna.

Here, I propose a compact CP-PIFA element suitable for array of base station receivers useful for wireless endoscopy systems. I first investigate the performance of a single CP-PIFA element and then employ it to form an array of receiving base station antennas for capsule endoscopy system. The proposed geometry, shown in Figure 4-16. resonates at the desired frequency bands when structure size is modified and shorting point location is adjusted. The antenna structure consists of a printed radiator patch, a ground plane, a substrate, a shorting pin and a feeding port.

4.7.1 Numerical Phantoms for Simulations

The proposed receiver antenna performance has to be evaluated in presence of the human body numerical phantom while the capsule transmitter is placed inside the small intestine. To perform these calculations, I used the full human body of HFSS™ [132] same as the one used in pervious sections. This frequency dependent human body model is a complex inhomogeneous multi layered numerical phantom with a high accuracy to the millimetre level.

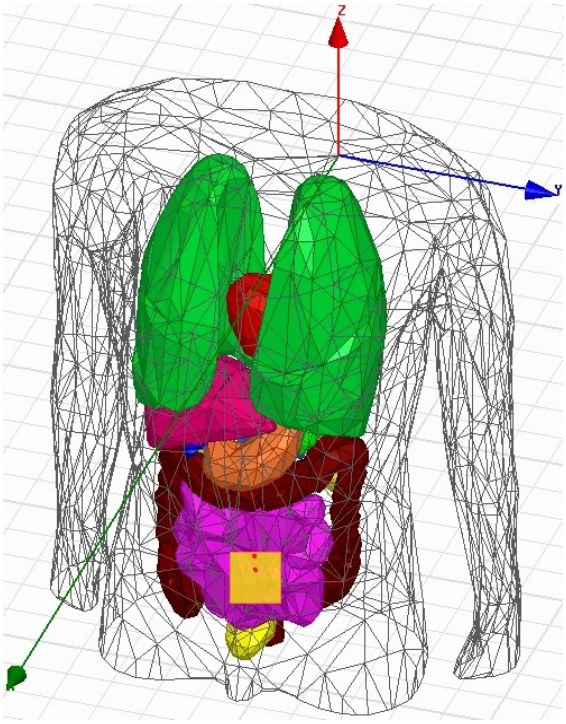

Figure 4-17. Simulation setup: CP-PIFA placed close to the Complex human torso.

To quickly optimize the antenna design, I have performed initial simulations using multi-layer block model shown in Figure 4-1. Finally, the proposed compact CP-PIFA was placed very close and in front of the HFSS complex body model to validate its performance.

4.7.2 Design Procedure of Compact CP-PIFA

The body-worn antenna design procedure is carried out in three steps. Firstly, a rectangular patch antenna is designed to operate over MICS band at 400 MHz when placed very closely to a multi-layer tissue mimicking numerical phantom. Secondly, two slots are added on to the patch purposefully and simultaneously the geometrical parameters are varied to obtain resonance at the operating frequency band. Later the model of the CP-PIFA with a tuned shorting pin is placed closely to the skin of complex human body HFSS model for a precise simulation as shown in Figure 4-17.

For the proposed CP-PIFA the length and width of the patch determine the resonant frequency while proper shorting pin position improves the impedance matching. The advantage of the proposed receiving antenna is that its structure can be miniaturized and can be retuned easily by adjusting the slots' position and size. It can also provide circular polarization over MICS band. Moreover, the antenna simple geometry offers design flexibility so that it can be easily tuned for other bands of interest such as ISM band. This can be achieved by reducing the geometry size using a fixed reduction factor, that is related to the wavelength of operation, and optimizing the sizes of the slots and the ground plane.

To radiate circular polarization, antenna should have surface current distribution with two orthogonal components. Here, I have inserted two opposite slots in the CP-PIFA geometry to perturb the surface current distribution and support two orthogonal component viz. x and y components of currents as shown in Figure 4-18. These orthogonal currents produce circular polarization even when the antenna is placed close to the human body model in free space. Figure 4-19 shows the presented receiver antenna axial ratio performance when it is placed close to complex human body model using HFSS™ [132]. From this figure one can see that the receiver antenna has circular polarization characteristic over its operating band.

Furthermore, these two symmetrical slots on the planar patch of proposed CP-PIFA make the surface currents propagate over a longer path along the slots' edge so that the radiator resonates at lower frequencies. This feature significantly helps to reduce the size of the CP-PIFA geometry and make the antenna to be electrically small. By moving the slot position to the left and right sides of the patch, the center frequency is found to be shift up and down. This is useful when the fine tuning of antenna resonant frequency is needed. One may also adjust the center resonance frequency by

changing the slot' length, however, this may deteriorate the axial ratio greater than 3dB which results in poor circular polarization. This may have significant negative effect on received signal quality and degrade overall system performance.

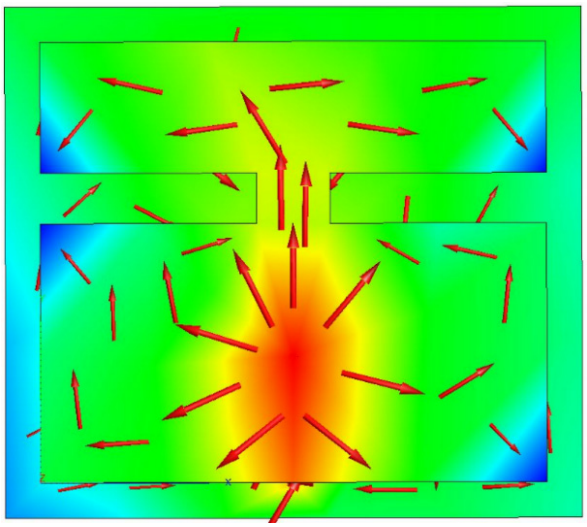

Figure 4-18. Receiver element surface current distribution at 403 MHz.

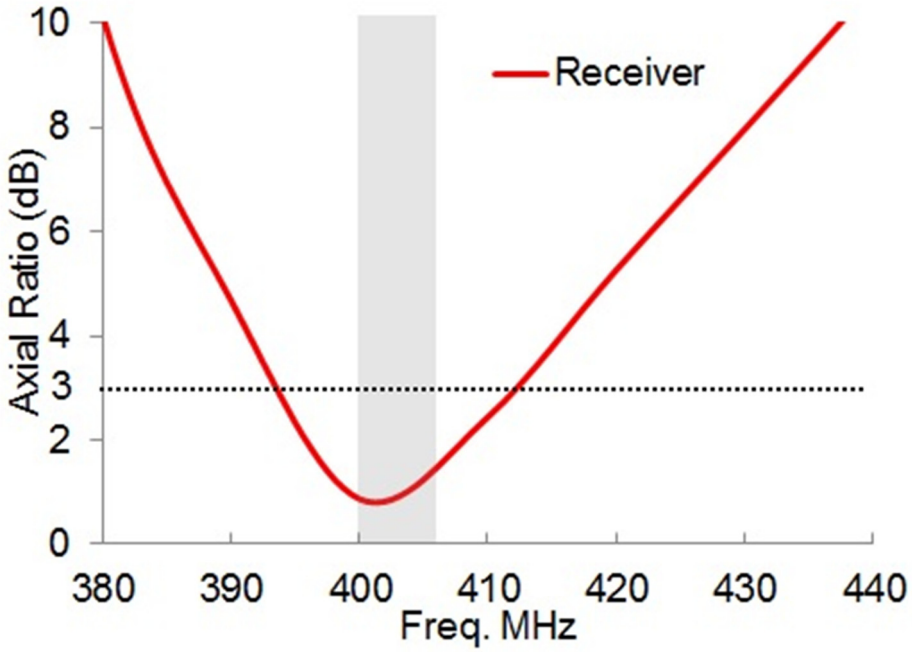

Figure 4-19. Receiver antenna axial ratio (A.R).

For PIFAs, it is well known that increasing the size of the ground plane will help to increase the antenna bandwidth, however, it increases the size of the antenna structure simultaneously. Hence, in this chapter, I chose the ground plane size to be minimum. The detailed parameters of the proposed base station antenna element are given in Table 4-3. The calculated radiation efficiency for the both of the proposed transmitter printed loop antenna and the receiver CP-PIFA base station antenna are tabulated in Table 4-4. To calculate radiation efficiency I have employed the complex human body numerical phantom of HFSS™ [132].

TABLE 4-3
DETAILED DIMENSION OF THE PROPOSED CP-PIFA (UNIT: MILLIMETERS)

Parameter	Value	Parameter	value	Parameter	value
Ls1	15	Li1	10	Yp	2
Ls2	15	Li2	10	Y_0	10
W	36	Wg	40	Ws1	4
L	32	Lg	36	Ws2	4

TABLE 4-4
SIZE AND PERFORMANCE COMPARISON OF THE PROPOSED CP-PIFA RX ANTENNA

Reference	Freq. Band	Type	Bandwidth	Vol. mm^3
[40]	400 MHz	Folded meandered dipole	10%	4320
[41]	400 MHz	Circular patch	3%	742
[42]	400 MHz	Fractal antenna	2%	6208
[43]	2400 MHz	Button antenna	4%	6806
This work	400 MHz	Compact CP-PIFA	5%	893

TABLE 4-5
RADIATION EFFICIENCIES OF PROPOSED ANTENNAS IN THIS CHAPTER

Radiator Type	Operating Frq Band	Calculated Efficiency
Tx Folded loop antenna	MICS	0.92% at 400MHz
Rx CP-PIFA	MICS	64% at 400MHz

To further miniaturize the overall size of antenna structure the presented body-worn antenna and reduce mutual coupling effect, I have employed low loss Rogers 3210 substrate with dielectric permittivity of 10.2, loss tangent of 0.0027 and thickness of 0.64 mm. The aim is to reduce the substrate loss as R.3210 substrate has a lower loss tangent at 400 MHz than substrate FR4. The proposed base station antenna can cover MICS band fully, has electrically small size, can radiate circular polarization and has good radiation efficiency. It has also simple geometry, low profile and less weight. The size and performance comparisons with similar types of antennas reported in the literature are tabulated in Table 4-5. The Rx antenna geometry shown in Figure 4-16. has a total size of 40 mm × 36 mm for the ground plane, has a width of 36 mm and length of 32 mm for the top patch. The slots' length and width are 15 mm, 4 mm respectively and the feeding point is located 4 mm away from the shorting pin.

4.7.3 Measurements on Compact CP-PIFA

The compact CP-PIFA prototype, shown in Figure 4-20, resonates at 400MHz with the total patch length of 40mm and width of 36mm. The top patch and the ground plane are printed on both the sides of the Rogers 3210 substrate and the feeding point is connected to a coaxial cable trough the SMA connector. Figure 4-20 also illustrates the measurement setup where the antenna is placed very close to experimental meat phantom. To verify the proposed antenna performance when it is placed very close to the human body, I employed a similar meat phantom that is discussed in section 3.6. The conductivity and dielectric constants of the experimental phantom are also measured to validate its electromagnetic characteristics. The measured result on reflection coefficient, when the compact CP-PIFA was placed very close to the

experimental phantom, shows a good agreement with the calculated results obtained using complex human body numerical phantom as shown in Figure 4-21. The measured and calculated results on S_{12}, where the proposed printed loop antenna acting as the transmitter and the proposed CP-PIFA acting as receiving element are also compared in Figure 4-21.

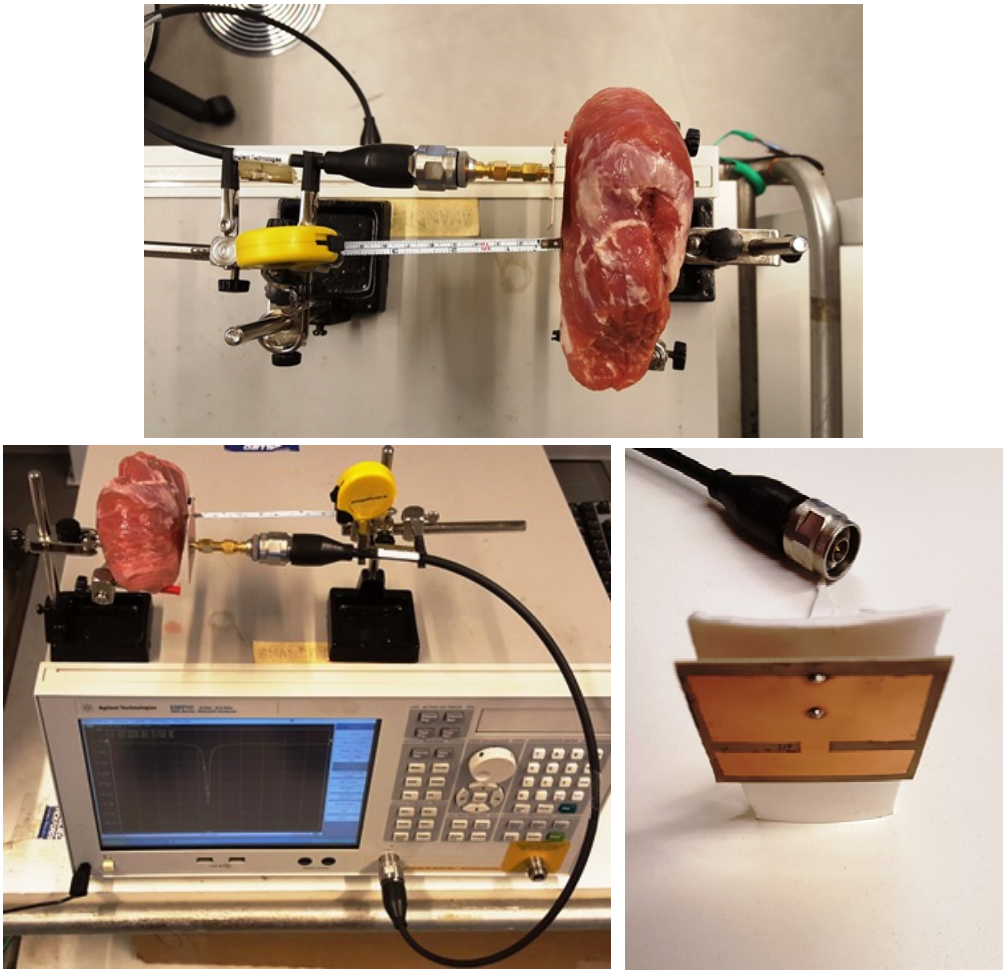

Figure 4-20. Receiver antenna: prototype and measurement setup.

To verify the circular polarization characteristic of the proposed receiver body worn base station antenna, I placed the Tx antenna inside the experimental phantom at three different orientations viz. vertical, horizontal and +45° slant using complex

human body model. I observed maximum variation of 1.6dB for S_{12} over the MICS band confirming that the CP-PIFA has good circular polarization properties. The compact CP-PIFA has a measured bandwidth of 20 MHz and provides circular polarization over the complete MICS band which is significantly valuable when considering slight changes in dielectric properties of human tissue/skin and variation of capsule orientation inside the human GI tract.

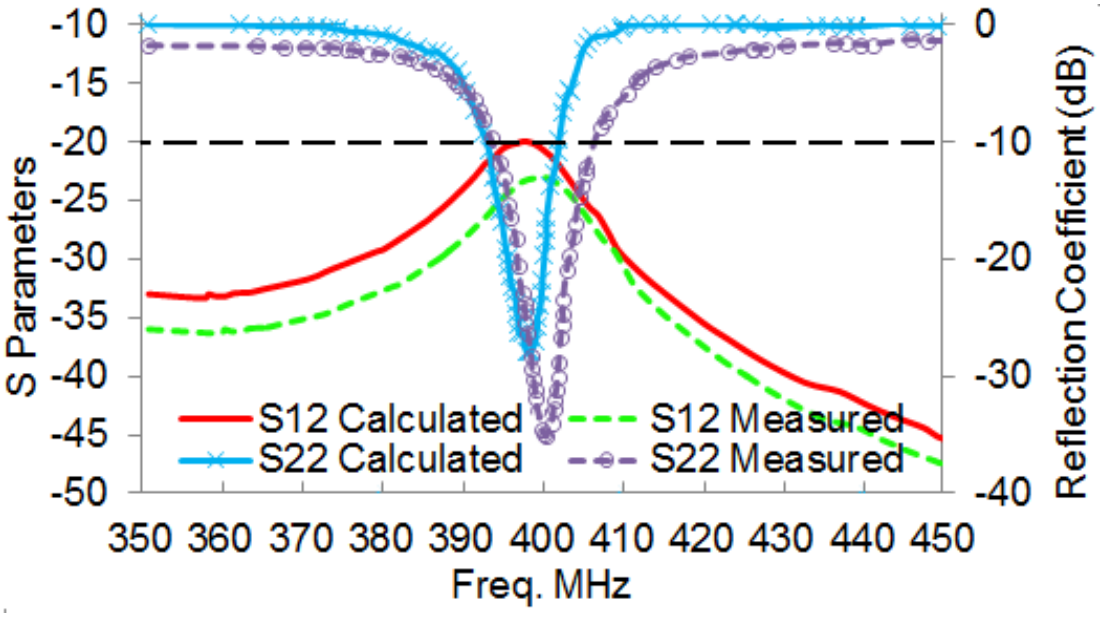

Figure 4-21. The reflection coefficient and S parameter comparison for CP-PIFA receiver antenna: Measurement versus simulation.

4.8 Receiver Array for Wireless Endoscopy Systems

For wireless capsule endoscopy system, receiver unit collects and records the images transmitted by the transmitter inside the capsule. The receiver recording unit is connected by wires to the base station array consisting of several Rx antenna elements worn very close to patient skin in different locations over the abdomen. The wireless links using high frequencies are commonly used due to the advantages such as higher data rate, small size electronics and antenna, however, these links suffer from

higher path loos and higher tissue penetration losses. Therefore, in order to provide reliable wireless communication link and minimize the losses, the receiving array must be placed very close to the skin of human body. On the other hand, human body acts as a lossy media to electromagnetic waves and has deleterious effects on antenna array performance. Hence, the effect of the human body has to be considered during the array design and antenna placement.

4.8.1 Numerical Phantoms for Simulation

The Rx antenna array performance has to be evaluated in the presence of the human body numerical phantom while the transmitter folded loop antenna is placed inside the small intestine of the phantom. The system requirement is that the Rx array has to cover complete MICS band fully when it is quite close to the human body. To achieve this, I have modified the antenna size as given in Table 4-3 in such a way to make it resonate at 400 MHz. To perform these calculations, I used the same HFSS™ [132] numerical phantom that I discussed in pervious sections. This frequency dependent human body model is a complex inhomogeneous multi layered numerical phantom with a high millimetre level accuracy. To accelerate the array performance validation, I have conducted initial calculations using cylindrical multi-layer block model. Finally, the proposed array of compact CP-PIFA was placed very close to the complex body phantom to validate its performance.

4.8.2 Antenna Array Design

I propose a conformal array of CP-PIFA receiving elements for the capsule endoscopy receiving base station. The compact CP-PIFA presented in previous section is chosen as the array antenna element. For initial design, I have employed a four-element array and a homogeneous cylindrical numerical phantom as shown in Figure 4-22. The transmitter printed loop antenna is placed inside the small intestine mimicking phantom while the receiver antennas are positioned very close to the body skin in all the front, back, left and right direction of the human body. I have already considered the influence of human body when designing the single antenna.

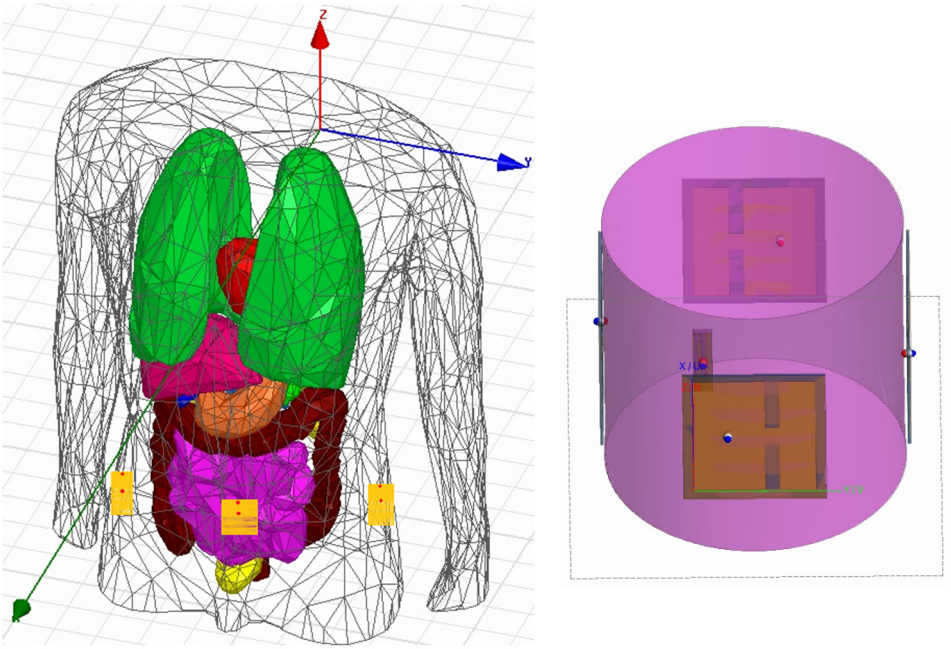

Figure 4-22. Simulation setup to calculate antenna performance: The HFSS complex human body numerical model and simplified cylindrical homogeneous human tissue phantom.

However, when using multiple antenna elements to form an array, the effect of mutual coupling must be considered for optimum performance. Mutual coupling may change the current distribution on antenna surface and alter the antenna's radiation

pattern as well. Mutual coupling can also degrade the antenna efficiency as well as axial ratio. To reduce the effects of mutual coupling and adjust the resonant frequency, I have optimized the length width and position of the two rectangular slots inserted into the top patch previously. These two symmetrical slots on the planar patch make the surface currents travel a longer path along the slots' edge so that the radiator resonates at lower frequencies. This will help to compensate the center frequency up shift due to the mutual coupling effect. Thus the modification, shown in Table 4-6, are made to retune the antenna resonance at 400 MHz.

Furthermore, the effect of mutual coupling can be reduced by increasing the displacement between the elements, however, this may change the array radiation pattern in undesirable way. Therefore, the spacing between the elements has to be adjusted in such a way to optimize system performance. The proposed Rx antenna has electrically small size of $0.053\lambda \times 0.048\lambda$ so that the distance between elements can be reduced without undergoing the mutual coupling effect. This will allow to increase the number of array elements at different location on the body. Increasing the number of receiving array elements result in robust communication link as more antennas receive transformed data. Thus, I have increased the number of the array element to six. The receiver antennas are placed around the skin close to the abdomen. The proposed array arrangement is shown in Figure 4-22, in which the proposed array, having circular polarization, can receive transformed data from all directions around the body when connected to a wearable receiver. It also increases the sensitivity of the received signal for a better signal transmission.

TABLE 4-6
DETAILED DIMENSION OF THE PROPOSED CP-PIFA (UNIT: MILLIMETERS)

Parameter	Value	Parameter	Value	Parameter	value
Ls1	15.5	Li1	11	Yp	2
Ls2	15.5	Li2	11	Y_0	10
W	36	Wg	40	Ws1	4.4
L	32	Lg	36	Ws2	4.4

4.8.3 Measurements

To verify the array antenna performance when it is placed close to the human body, I employed a larger meat phantom for experimentation which is similar to the one I prepared in section 1.7.3. The experimental phantom, in this case, has a size of 400mm × 200mm × 400mm. The conductivity and dielectric constants of the experimental phantom are measured, using dielectric probe, to validate its electromagnetic characteristics. The antenna array prototype, consists of six compact CP-PIFAs, is shown in Figure 4-23. In the measurement setup, the CP-PIFA Rx antennas are placed very close to the experimental phantom, to mimic the real situation.

The measured result on reflection coefficient, when the array placed very close to the experimental phantom, shows a good agreement with calculated result using the HFSS numerical complex human body phantom. The measured and calculated results on s-parameters for the proposed printed loop transmitter antenna and CP-PIFA receiving elements are also compared in Figure 4-24. The magnitude of the received signal is related to the path loss which can be used to localize the transmitter location inside the human body.

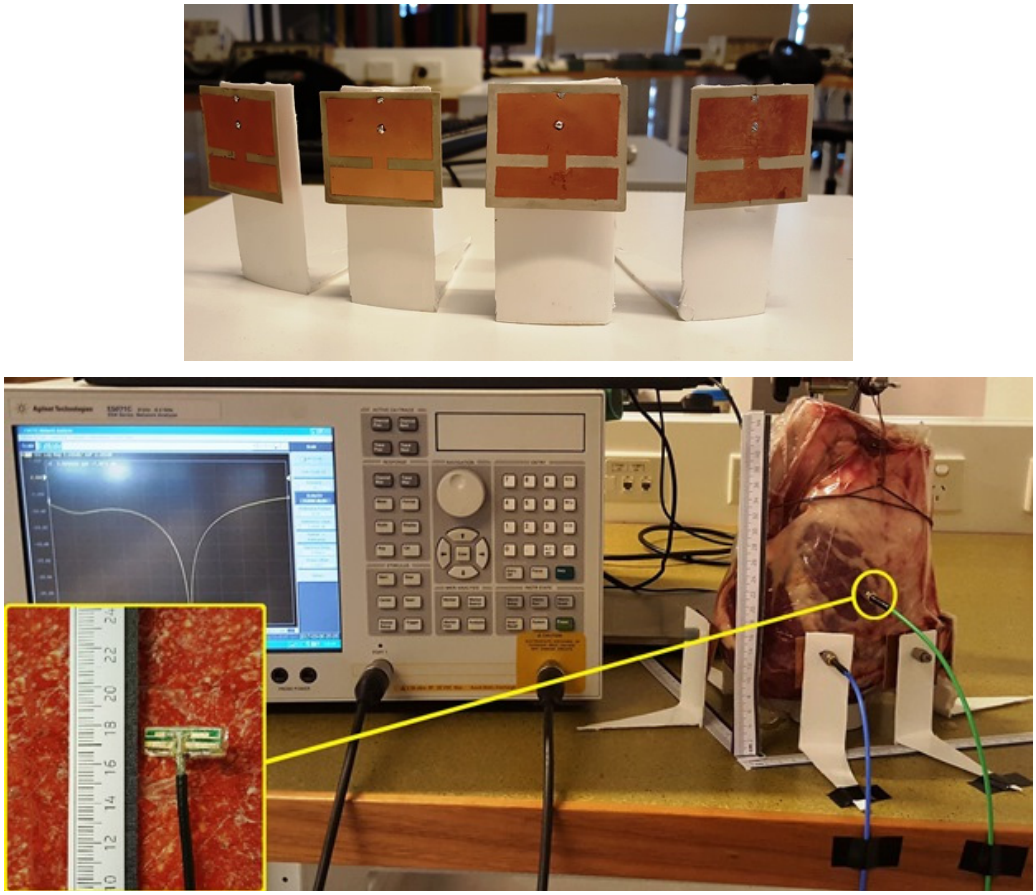

Figure 4-23. Receiver array element prototypes and measurement setup.

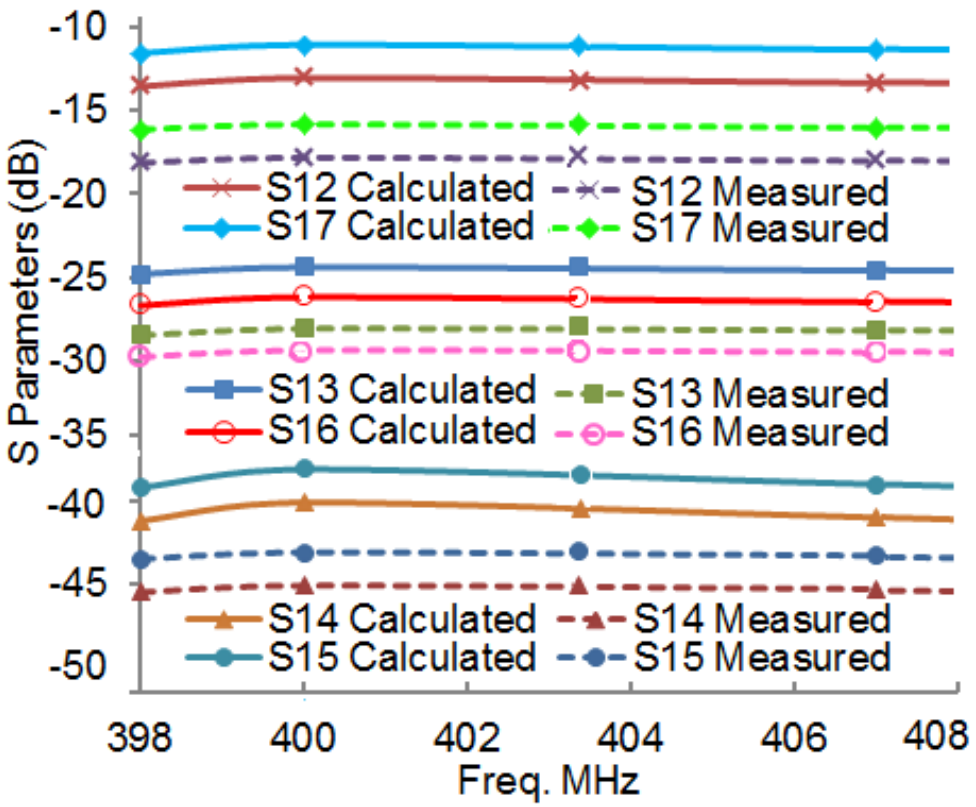

Figure 4-24. Power received at six receiver ports.

4.9 Development of Path Loss Model for Heterogeneous Human Body Based on Received Signal Data

In-body and On-body wireless communication experience loss in the form of absorption and attenuation. Therefore, introducing a path loss (PL) model is necessary to identify these losses in measurements and simulations using mimicking phantoms. Here, the path loss model is mainly concerned with ingestible wireless capsule when transmits video data of the GI tract. In this application, as the capsule travels through GI tract, it is surrounded by different tissue environment with different electromagnetic properties. The path loss model is calculated based on 3-D electromagnetic numerical phantom and the results will be validated with measured data obtained using meat phantom. Developing a path loss model will help to understand the effects of the dielectric properties of the surrounding human body tissues and the power attenuation. Simulations are further extended for different locations and orientations of the capsule transmitter antenna inside the small intestine operating in MICS band. Furthermore, path loss in homogeneous numerical phantom is computed and compared with the path loss obtained using realistic model having heterogeneous tissues. To obtain numerical data, I use two different set of receiving antennas, CP-PIFA and insulated dipole antennas, as base station receiving antennas. The printed loop antenna is used as the capsule transmitter antenna.

4.9.1 Setup for Homogeneous Body Tissue: Insulated Dipoles

Initially I have investigated the wave propagation at 400 MHz in human small intestine tissue with relative permittivity of 64 and conductivity of 1.35 S/m. I have developed identical dipoles where each dipole arms are perfect electric conductors

(PEC) made with radius of 1 mm covered with an insulation made of polytetrafluoroethylene (εr = 2.1 and σ = 0 S/m). I have employed dipole antennas for this study as they have a simple structure and also simple to analyse. The advantage of insulated dipoles over the bare dipoles is that the insulation prevents the leakage of conducting charges from the dipole and reduces the sensitivity of the entire surface current distribution with respect to the electrical properties of the ambient medium. This feature makes insulated dipoles useful for on-body wireless wideband communication [89]. Simulations are performed using a 3-D electromagnetic solvers including FEKO and HFSS.

The wavelength of the EM wave is affected by the medium in which it propagates which must be considered when designing implantable antennas for biomedical applications. The effective wavelength of propagation in a lossy medium such as a small intestine is given by,

$$\lambda' = \frac{2\pi}{\beta'} \tag{4.2}$$

Here, λ' is the wavelength of the signal in a lossy medium and β′ is the phase constant of the signal in a medium having a relative permittivity of ϵ_r and a conductivity of σ,

$$\beta' = \omega \sqrt{\frac{\mu\epsilon_r}{2}\left(\sqrt{1+\left(\frac{\sigma}{\omega\epsilon_r}\right)^2}+1\right)} \tag{4.3}$$

where, μ is the permeability, which could be taken as unity since human body is considered as non-magnetic medium. To develop a path loss model, initially, a homogeneous small intestine numerical phantom, shaped cylindrically as shown in Figure 4-25, has been used. It has a height (*H)* of 300 mm, diameter (*D)* of 260 mm, dielectric constant of 64 and conductivity of 1.35 S/m at 400 MHz.

I employed 36 insulated dipole antennas which are placed around and very close to the homogeneous cylindrical phantom as illustrated in Figure 4-25. The dipoles separating is 66 mm and all are equidistant from each other and arranged in three rings with 12 antennas in each ring. The printed loop is immersed inside the cylinder to act as capsule transmitter antenna and half wavelength dipoles provides the opportunity to investigate the path loss feature. The Tx and Rx antennas are separated by a distance up to 260 mm.

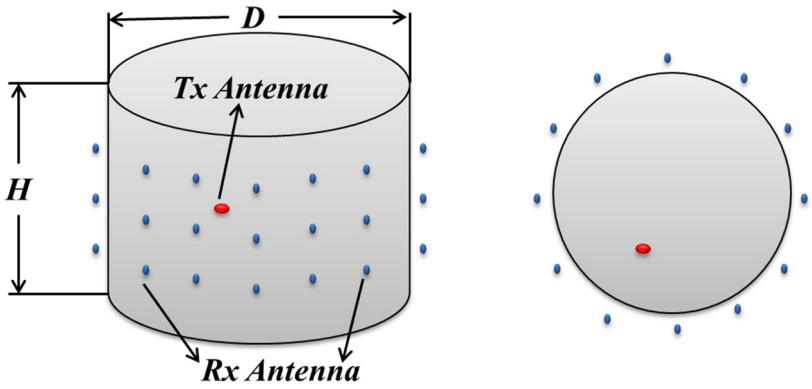

Figure 4-25. Side View (left) and Top View (right) of the Simulation Setup using dipoles as receivers and printed loop antenna as transmitter.

For the receiver and transmitter antennas having a separating distance d, in free space, the received power can be derived using the Friis' Free Space Propagation law [155], given by

$$P_r(d) = \frac{P_t G_t G_r}{L}\left(\frac{\lambda}{4\pi d}\right)^2 \tag{4.4}$$

where, $P_r(d)$ is the received power, P_t is the transmitted power, G_r is the receiver antenna gain, G_t is the transmitter antenna gain, d is the distance between the receiver and transmitter antennas and L accounts for the miscellaneous system losses. For ideal situations, the miscellaneous system loss, L, can be neglected (L = 1).

Assuming a reference receiver antenna is located in the far-field of the transmitter antenna at a distance, d_0, such that $d_0 < d$, where d is taken as the maximum distance between the receiver and transmitter. I can rewrite equation (4.4) to accommodate d_0 as follows:

$$P_r(d) = P_t G_t G_r \left(\frac{\lambda}{4\pi d_0}\right)^2 \left(\frac{d_0}{d}\right)^2 \tag{4.5}$$

where, λ is the wavelength of the transmitted signal in meters.

When using the logarithmic scale, the path loss defined as the difference between the effective transmitted power and the received power. Therefore, I get:

$$\frac{P_t}{P_r} = \left[\frac{G_t G_r}{L}\left(\frac{\lambda}{4\pi d}\right)^2\right]^{-1} \tag{4.6}$$

Converting equation (4.6) into logarithmic scale, I get:

$$PL_{[dB]} = 10\log\frac{P_t}{P_r} = -10\log\frac{G_t G_r}{L}\left(\frac{\lambda}{4\pi d}\right)^2 \tag{4.7}$$

Using equation (4.5) into equation (4.7) I can obtain path loss as:

$$PL(d)_{[dB]} = P_{t[dB]} - P_r(d)_{[dB]} = -\left[10\log\frac{G_t G_r}{L}\left(\frac{\lambda}{4\pi d_0}\right)^2 + 10\log\left(\frac{d_0}{d}\right)^2\right]$$

or,

$$PL(d)_{[dB]} = P_{t[dB]} - P_r(d)_{[dB]} = -\left[-PL(d_0)_{[dB]} - 10\log\left(\frac{d}{d_0}\right)^n\right] \tag{4.8}$$

where, the path loss exponent $'n'$ signifies how the received power is decreased which is environment specific.

For a two port network, the path loss can also be expressed in the terms of the scattering (*S*) parameters. For a pair of receiver and transmitter antennas, the S_{21}

parameter is the ratio between a wave coming out of port-2 and a wave going into port-1 and can be written as [156],

$$S_{21} = \frac{V_2^-}{V_1^+} \tag{4.9}$$

where, V_1^+ is the voltage value of the wave entering to the first port and V_2^- signifies the voltage value of the wave coming out from the second port. Assuming the ports to be impedance matched, equation (4.9) can be expressed in terms of power as,

$$|S_{21}|^2 = \frac{P_r}{P_t}$$

or,

$$\frac{1}{|S_{21}|^2} = \frac{P_t}{P_r} \tag{4.10}$$

Converting equation (4.10) to logarithmic scale,

$$-10\log|S_{21}|^2 = -20\log|S_{21}| = 10\log\frac{P_t}{P_r}$$

or,

$$-|S_{21}|_{[dB]} = P_{t[dBm]} - P_{r[dBm]} \tag{4.11}$$

Therefore, from equations 4.6 and 4.9, path loss is equal to,

$$PL_{[dB]} = -|S_{21}|_{[dB]} \tag{4.12}$$

The $|S_{21}|_{[dB]}$ data is collected for each of the 36 transmitter receiver pairs while setting up the numerical calculation using FEKO™ [133]. Figure 4-26 shows the

scatter plot of the path loss data as a function of distance *d* for the insulated dipole obtained from the calculation using the numerical phantom illustrated in Figure 4-25.

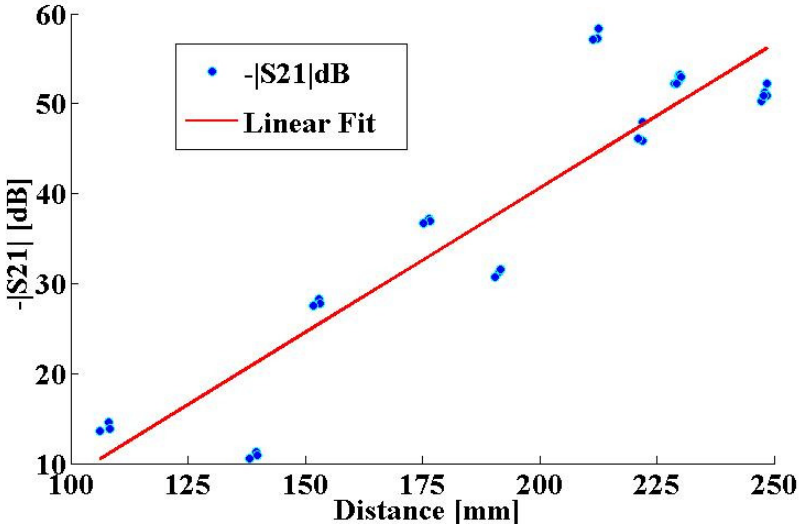

Figure 4-26. Scatter Plot of Path Loss Data.

4.9.1.1 Path Loss Model

The calculated results in the previous section are used to develop a PL model as a function of distance when a 400 MHz transmitter capsule antenna is placed inside a small intestine. The pass loss model developed using calculated data may be represented as follows:

$$PL|_{dB} = \alpha_1(10loge^2)l + K_1|_{dB} \qquad for\ l \geq l_m \tag{4.13}$$

$$PL|_{dB} = \alpha_2(10loge^2)l + K_2|_{dB} \qquad for\ l \leq l_m \tag{4.14}$$

where l is distance in millimeter, l_m (mm) is a distance where the mutual coupling reduces significantly between the Tx and Rx antennas, α_1 and α_2 (1/mm) are the

attenuation constants and $K_1|_{dB}$ and $K_2|_{dB}$ are constants. This model includes two regions, region one, where $l \geq l_m$, and region two where $l \leq l_m$. In the first region, there is very little mutual coupling between the Rx and Tx. Region 2, the Tx antenna is very close to the receivers with a separation varying from 0 to 6.25 cm. In this region, when Tx and the Rx are placed closely, the mutual interaction can affect the impedances due to the mutual coupling. As mentioned earlier, in the other region, mutual coupling effect is low and the input impedance of both of the Tx and the Rx remain constant. The parameter values in (4.13) and (4.14) can be obtained by employing least square error method. However, to develop a more realistic path loss model, more data using realistic numerical phantom are required. In next section, to obtain more realistic data, I have employed a complex heterogeneous human body phantom and also changed the Tx antenna location and orientation inside the small intestine phantom.

4.9.2 Setup for Inhomogeneous Body Model: Half-Wavelength Dipoles

For realistic simulations, I have employed an inhomogeneous 3-D multi layered tissue phantom using HFSS™ [132]. The numerical model is an adult male patient consists of over 300 body parts to represent bones, muscles and organs. It has high accuracy in tissue size and use frequency dependent material property database. For different tissues ε_r has a variation of $5 \leq \varepsilon_r \leq 75$ and σ may vary between $0.3\ S/m \leq \sigma \leq 3.5\ S/m$ for calculations in MICS band. To determine the influence of ε_r and σ on path loss, simulations are carried out using the insulated dipole antenna explained in the previous section.

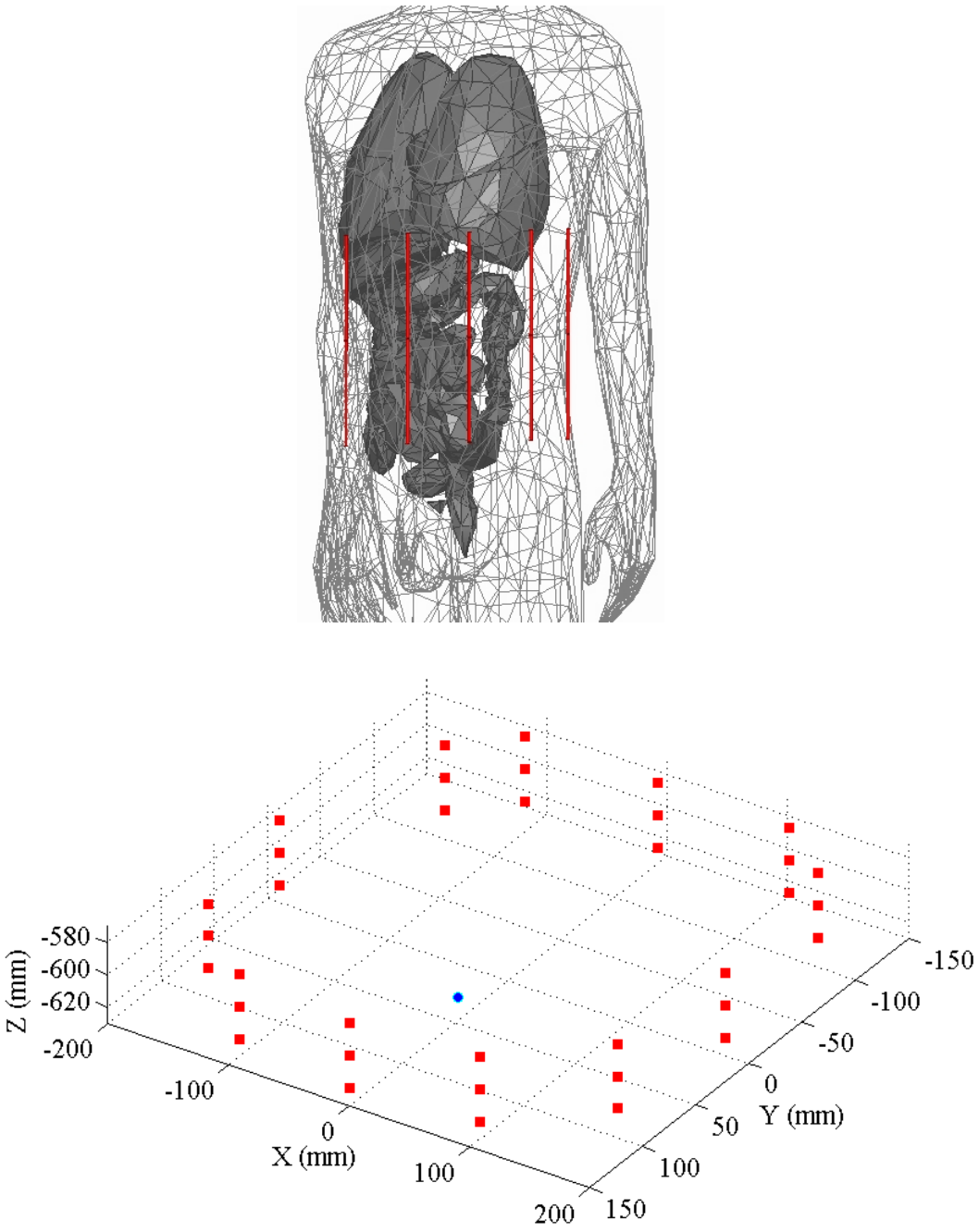

Figure 4-27. Setup for calculating scattering parameters data using half-wavelength dipoles as receiver. a) Complex human body phantom, b) The position of Rx antennas (in red) and Tx antenna (in blue) around the body model.

Here, the printed folded loop antenna placed inside the small intestine phantom as the capsule transmitter and the insulated half wavelength dipole antenna array is employed as base station receiver array placed close to human body. The dipoles are made to resonate at 400 MHz. I found that the dipole antennas in the array resonate at

400 MHz when length of the dipole, L_1 = 24 cm, is equal to half the wavelength in a medium whose dielectric properties are the combination of the dielectric properties of insulation and the human tissue medium. The dipole arms diameter (t_1) are set to 1 mm and the diameter of the insulation layer (t_2) is 1.5 mm. The setup for collecting the $|S_{21}|_{[dB]}$ data is as illustrated in Figure 4-27. The receivers are arranged in three rings surrounding the body with 12 antennas in each ring. A total number of 36 receivers are used to collect the data for a single position of the capsule. Using more Rx antennas in each ring can introduce mutual coupling resulting in an impaired performance in the desired band.

The *S*-parameter calculated and $|S_{21}|_{[dB]}$ data is collected for each of the 36 Tx-Rx pairs using the HFSS inhomogeneous complex human body model. Figure 4-28 shows the scatter plot of the calculated path loss as a function of distance *d* between the insulated dipole array and capsule transmitter placed inside the GI tract phantom.

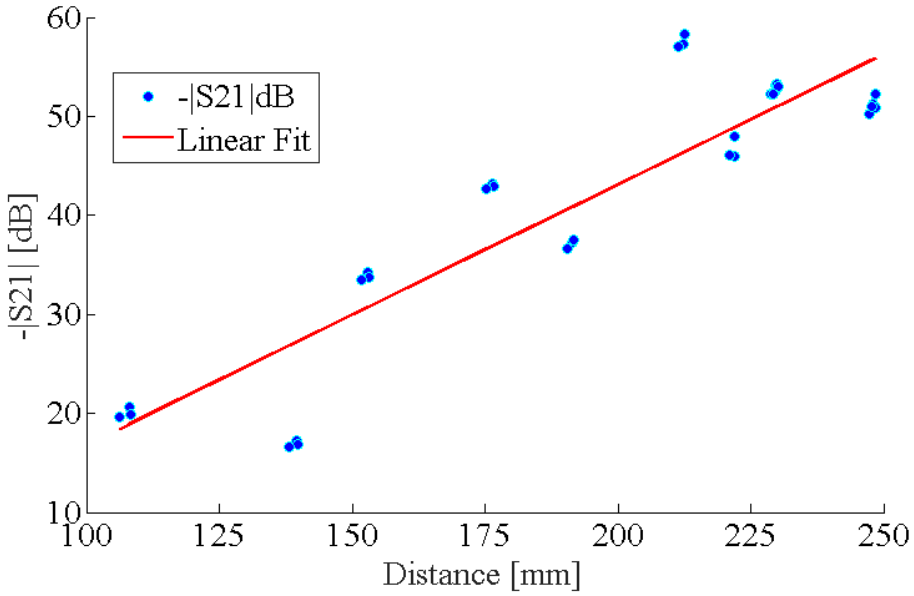

Figure 4-28. Scatter Plot of Path Loss Data.

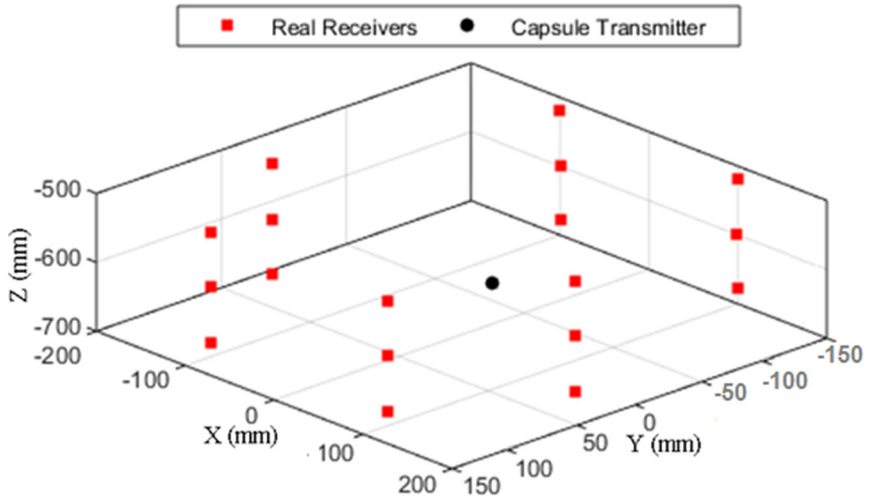

Figure 4-29. Setup for calculating scattering parameters using CP-PIFA as array antenna receiving element. Rx arrays are placed in three rings consisting of six CP-PIFAs each (total of 18 antennas).

4.9.3 Path loss calculation using compact CP-PIFA as receiver antennas

A practical base station receiver array for wireless capsule endoscopy system has to be small and compact to satisfy patient comfort and safety, so that the size and the number of the Rx antennas must be minimum at the same time collecting transmitted data effectively. The insulated dipoles can be long to be used in a practical base station array for wireless endoscopy. To be more realistic, I employed the proposed the CP-PIFA and the printed loop antenna as Rx and Tx antennas. Here, the number of Rx antennas are reduced to six placed in one ring around the complex numerical body phantom. The eighteen receiver antennas have been distributed in three rings with a spacing of 36 mm between each rings to minimize potential mutual coupling, the antenna arrangement for the simulation set up is depicted in Figure 4-29. The $|S_{21}|_{[dB]}$ data was collected by placing the proposed printed folded co-planar loop antenna acting as capsule Tx antenna within the small intestine phantom. The position of transmitter antenna was changed to multiple locations and the received fields are collected for a precise path loss modeling for each and every position.

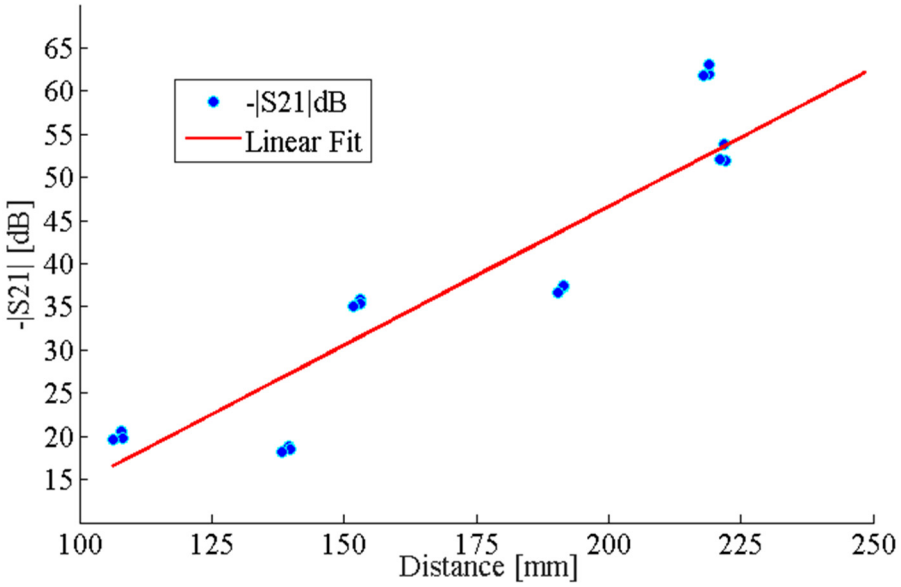

Figure 4-30. Scatter Plot of Path Loss Data.

A scatter plot of the path loss data as a function of distance *d* between Tx antenna (printed loop) and CP-PIFAs is shown in Figure 4-30. Form this plot, one can observe that the path loss varies from 15 dB to 63 dB. The small intestine is a meandering structure and has winding path through which the wireless capsule travels and while it is moving, the orientation of the capsule may change frequently. Here, I try to simulate these conditions in the mimicking phantoms. To test the robustness of the designed Tx and Rx antennas and improve the path loss calculation, the orientation of the Tx antenna is shifted by 90° while the orientation of the Rx array antennas are fixed. Them, the $|S_{21}|_{[dB]}$ data is collected, the path loss values are calculated and compared with the previous results. I have observed that the new results show a good agreement with previous results. This calculation shows that the functioning of the transmitter antenna is not affected by its orientation and receiving antennas are able to establish a communication link with the wireless capsule even its orientation is changed. This has also been verified for many different positions of the transmitter as shown in Figure 4-31.

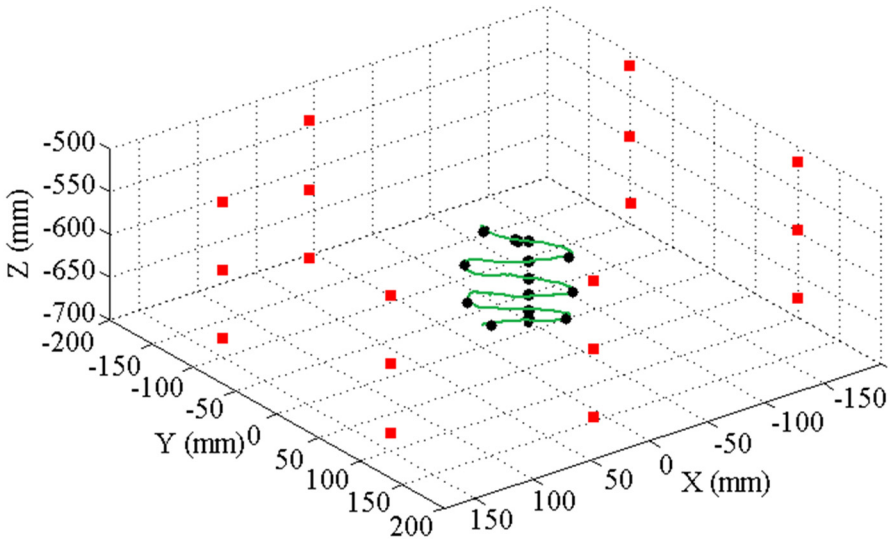

Figure 4-31. Setup for calculating scattering parameters for the different positions of transmitter and receiver antennas. Rx arrays are placed in three rings consisting of six CP-PIFAs each.

4.9.4 Experimental Validation

In order to verify the calculation results experimental work have been conducted using Agilent E7051C vector network analyzer to measure the scattering parameters, $|S_{11}|_{dB}$ and $|S_{21}|_{dB}$, between transmitter and receiver antennas. The experimental setup is shown in Figure 4-23 using a meat phantom whose approximate dimensions are 400 × 260 × 400 mm.

The fabricated printed loop antenna is employed as the Tx antenna and which is fed using a coaxial cable connected to the VNA after being embedded inside the experimental meat phantom. For the base station receiving antenna array, a six-element array of CP-PIFAs is fabricated and each of the elements are placed around the experimental phantom to form the receiving array. The six Rx antennas are kept parallel to the phantom at a height of 150 mm around and at a minimum distance to the surface of experimental phantom and the Tx antenna is embedded inside the meat phantom. For the different position, the $|S_{21}|_{[dB]}$ data was measured at each receiver antenna at 400 MHz and then used for path loss calculation.

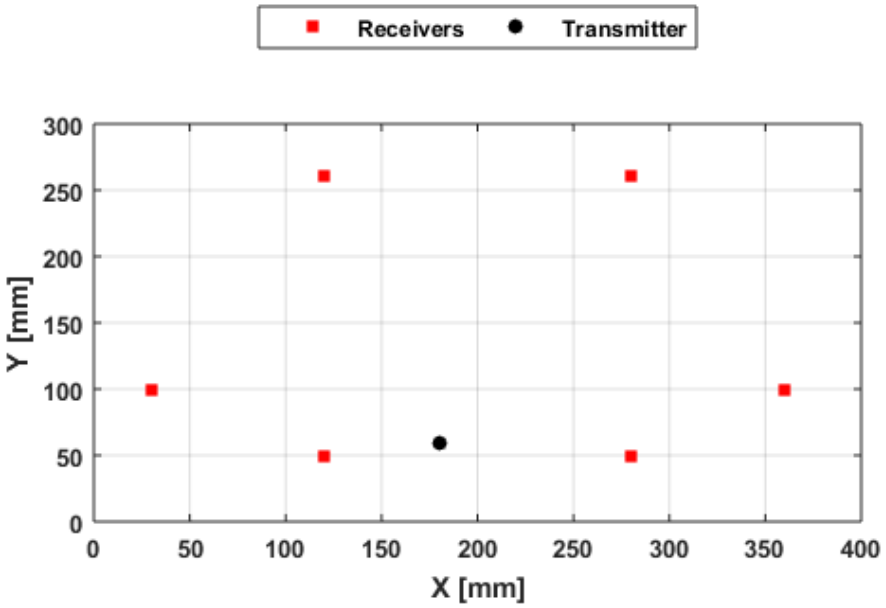

Figure 4-32. Setup for collecting the $|S_{12}|_{[dB]}$ measured data for the proposed Tx and Rx antennas. Total of six receiver antennas are used.

Setup for collecting the $|S_{12}|_{[dB]}$ measured data using a total of six proposed CP-PIFA is shown in Figure 4-32. A scatter plot of the path loss for different distance between Tx and Rx antennas is illustrated in Figure 4-33 and is linearly fit for one transmitter position.

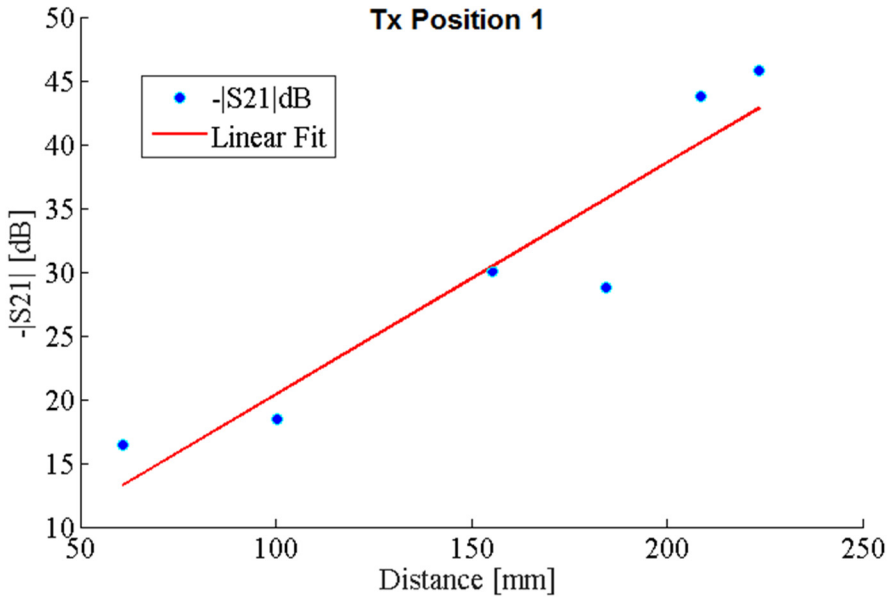

Figure 4-33. Path loss data for Tx antenna position-1 inside the meat phantom. The lowest path loss recorded is around 15 dB while the highest is around 45dB.

More measured data has been collect by repeating the experiment for three separate positions of the transmitter antenna. For each measurement, the transmitter antenna position inside the experimental phantom is moved by steps of 50 mm from position-1. The measured data in $|S_{12}|_{[dB]}$ for the Tx Position-1, 2 and 3 appear to be very similar. Setup for collecting the $|S_{12}|_{[dB]}$ measured data for three different location of Tx antenna is shown in Figure 4-34.

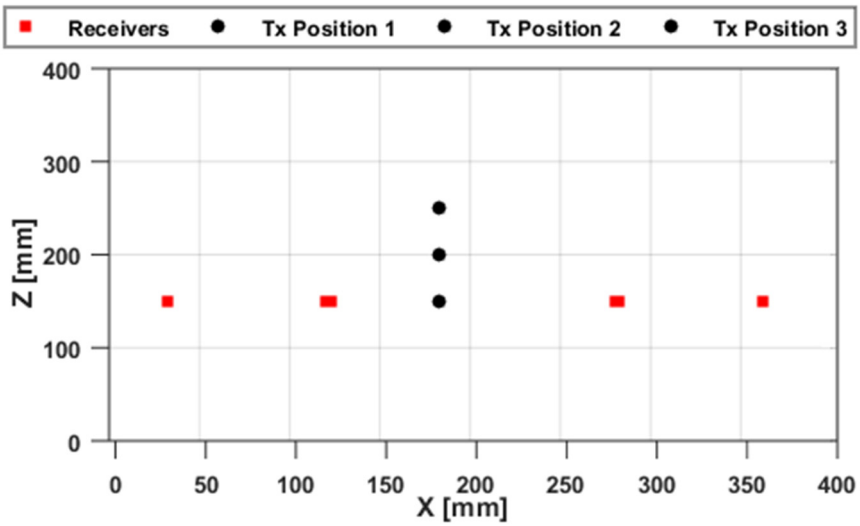

Figure 4-34. The side view of the measurement setup for the $|S_{12}|_{[dB]}$ data collection using the array of six compact CP-PIFAs for three different positioning of Tx antenna.

The path loss data can be used to localize the transmitter. To estimate the ingestible wireless capsule location with a high level of accuracy, it is necessary to place the array of receiving antennas in such a way that the signals transmitted by the capsule, which is traveling through the entire area within the GI tract, are covered. This will help to record the signals transmitted from various positions without missing any of the signals. I could cover the entire area in the experiment using only six compact CP-PIFAs in the receiving array. The signal quality of received data confirms that the radiation performance of the proposed antennas are appropriate for this application.

4.10 Discussion

A printed loop antenna with bandwidth enhancement is presented for ingestible wireless capsule endoscopy systems operating over the MICS band. The antenna is folded and printed on FR4 substrate to miniaturize the antenna geometry. The printed antenna fits inside the endoscopy capsule, occupies a very small volume of 160mm^3, and has a bandwidth enhancement of 200%. I have also evaluated the calculated SAR by using an indirect thermal method to measure the SAR inside the mimicking phantom. Moreover, a compact CP-PIFA is also presented as receiver base station antenna for wireless capsule endoscopy systems. The antenna covers MICS band fully, has a compact size and circular polarization to enhance the low-level signal reception. The antenna has also been employed to form a conformal array placed closely to human body to communicate with wireless capsule.

I have also carried out empirical path loss model for homogeneous and heterogeneous human tissues using numerical models and equivalent experimental phantom. I employed proposed printed folded co-planar loop antenna as transmitter and compact CP-PIFA as array receiving elements. To validate the calculations with measurement, conformal array of six CP-PIFAs and a meat phantom with approximate size of 400 × 260 × 400 mm were employed. To examine the robustness of the designed Tx antenna and the accuracy of the developed path loss, the orientation of the capsule shifted by 90° while the orientation of the Rx antennas are fixed. I concluded that the functioning of the transmitter antenna is not affected by its orientation and receiving antennas are able to establish a communication link with the wireless capsule. This was also verified for a couple of different positions of the capsule within the numerical and experimental phantom.

CHAPTER – 05

5. MINIATURIZED ANTENNAS FOR HEAD IMPLANTABLE DEVICES

5.1 Introduction

THis chapter presents implantable miniaturized single slot planar inverted-F antennas (SS-PIFAs) and folded oval loop antennas for head implantable biomedical applications. I have used a simple geometry to propose miniaturized SS-PIFAs that can operate over a variety of biotelemetry frequency bands. Every presented SS-PIFA is carefully tuned to cover either of Medical Implant Communication Service (MICS) 400 MHz, Zigbee at 868 MHz, Wireless Medical Telemetry Service (WMTS) band at 1430 MHz and Industrial, Scientific, and Medical (ISM) band at 2.4 GHz. To satisfy the wideband antenna requirement for head implant devices, I have presented a compact folded oval loop antenna covering MICS band up to 1 GHz. The radiator is first designed and optimized in planar form and then by introducing two tunning strips connected to an oval loop, a new resonance is excited in addition to the main resonance. This leads to bandwidth enhancement of 200%. The comprehensive knowledge gained in previous chapters (three and four) helped us to design both SS-PIFAs and folded oval loop antennas.

I have also investigated the effects of the antenna geometry parameters on radiation performance using empirical parametric studies to further reduce the size of the

antennas. Following the systematic process, I could successfully achieve the design for compact folded oval loop antennas and miniaturized SS-PIFAs. The impedance characteristics of the proposed antennas were measured using experimental tissue mimicking phantoms. Moreover, I have compared the calculated SAR with measured SAR obtained by using an indirect thermal method inside the mimicking phantom.

5.2 Background Review and Motivation

Monitoring and controlling of the increased Intracranial Pressure (ICP) are necessary for the treatment of the people suffering from the head injuries (e.g., traumatic brain injury (TBI)) and diseases of the brain such as hydrocephalus. The increased Intracranial Pressure is the pressure inside the human body skull, which contains the human brain, blood and cerebrospinal fluid (CSF) [157, 158]. ICP is an important factor for the management of different cerebral disorders and trauma. It is one of the key indicator of the brain tissue and cerebral vascular status. People suffering from craniocerebral trauma due to the skull injury as well as patients facing neurological disorders such as hydrocephalus need monitoring of ICP for their medical management. Increased ICP may lead to permanent damage to the patient's brain or cause disability or even death.

During the neurosurgical procedure, a compact intracranial pressure monitoring device can be implanted inside the cranium to facilitate future ICP measurement. A key component of this is the antenna which facilitate the wireless communication for the device. A planar inverted F antenna (PIFA) operating at 2450 MHz is presented in [35] for intracranial pressure (ICP) monitoring systems. Comparative studies carried out in [94] for short dipole and loop antennas implanted inside the head for different

frequency bands. Furthermore, the communication link performance of a small loop antenna operating at MICS band is characterized when placed under the scalp for ICP monitoring [93]. However, head implantable antenna design, regardless of the operating frequency band, faces major challenges including miniaturization, improved radiation performance and bandwidth enhancement. In general, due to the high dielectric loss, caused by the human body, the total radiation efficiency of the implanted antennas decreases. On the other hand, for the head implantable antennas, the overall structure size has to be small. The smaller size and lower efficiency coupled with lower radiation power can lead to a shorter communication range.

To overcome these issues, many head implantable antennas including planar and non-planar structures, such as annular slot antenna and miniaturized stacked type antennas are proposed [159, 160]. Arye Rosen et al. [33] developed and verified an embedded compact wireless ICP sensor, including a new radiator and packaging preparation. The proposed annular slot antenna has a size of 20 × 22 mm which is large for head implants systems. The radiator has small efficiency of 0.5% – 1.0% depending on the coating thickness. Gosalia et al. [97] employed a pair of small microstrip planar patch antennas and analyzed a data telemetry link at two standard frequency bands of 1.45 GHz and 2.45 GHz for retinal prosthesis. Soontornpipit et al. [45, 48], who investigated the performance of serpentine and spiral antennas at 402–405 MHz, have also evaluated microstrip patch antennas for implantable biomedical applications. However, all of these planar antennas are limited by their larger volume and not appropriate for practical ICP monitoring devices.

On the other hand, for non-planar radiating structures, further size miniaturization reported in the literature [56, 57, 59] by using vertically stacked radiating patches and multilayer structures to increase the path length of the current

flow. Stacked PIFA radiators having very compact volume of 32.7 mm^3 were also reported in [160], however the radiation efficiency is low. Nikita et al. [36] proposed a miniaturized stacked antenna with a radios of 4 mm operating over the MICS band. The two vertically stacked circular meandered patches are printed separately on an alumina substrate with 0.25 mm thickness. The proposed antenna achieves a significant reduction in size compared to previous work reported in the literature, however, the radiation efficiency is only 0.8% which is still low. Hence, there is a need for compact sized implantable antennas with improved radiation efficiency.

On the other hand, different standard telemetry bands such as MICS (433 MHz), WMTS (1400 MHz) and ISM (2450 MHz) are allocated to communicate with the head implanted devices. However, the above cited antennas are not proper for re-tunning the resonant frequency to cover other standard telemetry bands rather than the principle ones. Employing a tunnable and simple antenna geometry, which can resonate over standard telemetry bands, reduces the system cost and antenna design complexity significantly.

Scalp implantable loop and short dipole antennas, operating at 402 MHz, 915 MHz, 1575 MHz and 2450 MHz, reported in [94]. However, only the radiation patterns and gains of the proposed antennas compared while neither effective antennas size nor physical size of the antennas are scaled to each band of frequency. Circular miniaturized scalp implantable PIFA type antennas for integration with head implanted medical devices covering MICS (402 – 405 MHz) and ISM (433.1 – 434.8, 868 – 868.6 and 902.8 – 928 MHz) bands are presented in [47]. To verify the simulation results an antenna prototype, operating at MICS band, is fabricated and tested, however, other frequency bands are missed for verification and no

measurement results provided. Moreover, the proposed structure can not be modify to cover higher standard frequency bands.

In this chapter, I propose a class of miniaturized PIFAs, suitable for scalp implantable devices, with a simple geometry capable to resonate at different frequencies when tuned. I present a compact Single Slot PIFA with enhanced radiation efficiency which is capable of operating over several standard telemetry bands such as MICS band at 400 MHz, Zigbee at 868 MHz, WMTS band at 1430 MHz or ISM band at 2450 MHz. The proposed SS-PIFA when embedded inside the computational human tissue phantom, achieved a radiation efficiency of 1.9% at 2450 MHz which is higher than previously reported works in the literature [33, 48, 93, 97, 159, 160]. The antenna structure involves full ground plane on the back of the antenna which minimized the back lobe radiation to protect the brain from electromagnetic wave radiation. Here, the proposed radiator resonating at 2.4 GHz has a compact size of 5 × 7 × 1.6 mm^3 occupying a volume of 0.056 cm^3 which significantly smaller than those reported in the literature [33, 48, 93, 97, 159, 160]. I have also tuned the proposed radiator geometry to operate over four different standard health care telemetry bands. Following a similar procedure, I carefully reduced their geometry size to guarantee a high level of performance including the improved radiation efficiency and impedance bandwidth.

The dielectric properties of human tissue may vary due to the diversity in body shape, gender, age, race, etc which results in shifting the radiator center frequency. In this circumstance, featuring a higher bandwidth is advantageous as it ensures the antenna performance when small or large shifts occur in resonant frequency. Also, transmitting data with a higher rate needs a wider bandwidth. Therefore, I have also used the printed folded coplanar loop antennas concept demonstrated in chapter two

and present a compact folded oval loop antenna operating from 400 MHz up to 1000 MHz. The proposed wideband antenna is small enough to be integrated with head implant devices for application such as brain wave sensing for the paralyzed, stroke rehabilitation, brain edema evolution monitoring, pressure monitoring, RFIDs and position tracking. For the proposed wideband head implantable antenna, enhanced bandwidth of 200% achieved by employing two tunning strips connected to the folded oval loop. Here, new resonances are excited besides the main resonance to escalate the bandwidth.

Additionally, the proposed SS-PIFA is capable of resonating at multiple standard telemetry bands which makes it possible to implant it in different part of the human body such as arm, leg, scalp or under the chest. Using multiple band antennas may reduce the physical size of the multi-function systems since the system may not require more than one antenna. In the literature, dual band two layers slot antenna [161], dual band microstrip patch antenna [31, 127] and compact dual band implantable antennas [51, 162] operating at MICS and ISM bands have been proposed for implantable medical devices. Employing dual band antenna enable the system to shift between two modes i.e., wakeup and sleep to save more energy and extend the overall lifespan of the device. Serpentine patch antenna and PIFA with an open-end slot on the ground plane are proposed in [163] and [164] respectively. The proposed dual band antennas, resonating at 400 MHz and 2450 MHz, has a compact size 8.75 mm × 7.2 mm × 0.5 mm and 19.8 mm × 19.4 mm × 0.635 mm respectively. However, no comparison with other frequency bands was reported in these papers.

Differentially fed dual-band implantable antennas are also proposed in [165-167]. These differential antennas can be simply integrated with differential circuitries and eliminate the loss caused by the matching circuits and baluns. The proposed

antenna in [166] resonates at two center frequencies of 433.9 MHz and 542.4 MHz and can be employed for fully implantable neuro micro-systems. The antenna dimensions are 27 mm × 14 mm × 1.27 mm and occupies 480.06 mm^3 which is quite large for scalp implantation. Moreover, the antenna covers only one standard telemetry band.

A triple band stacked spiral antenna presented in [34] covering ISM band at 2.45 GHz and MICS band at 402 MHz and 433 MHz. The prototype of the π-shape stacked antenna with the volume of 254 mm^3 is fabricated using Roger 3210 substrate. However, the measurement results do not agree fully with simulations. Most recently, an implantable triple band antenna was proposed in [168, 169] , resonating at 402 MHz, 1450 MHz and 2450 MHz. The antenna has an overall size of 20.5 mm × 31 mm × 0.05 mm occupying a large area, and printed on polyamide flexible substrate. However, it can be wrapped around the electronics but redesigning may be needed to compensate the wrapping effect. To cover Mics band (401-406 MHz and 433-434 MHz), WMTS band (1427-1432 MHz) and ISM band (2400-2485 MHz) S-shaped quad-band PIFA is proposed in [170] for implantable biotelemetry. The antenna is composed of three substrates and a superstrate, layer 1involves S-shaped radiator, layer 2 and layer 3 consist of two twin radiators of spiral structures. The proposed PIFA occupies a compact volume of 10 × 10 × 2.45 mm^3, however, its radiation efficiency is low (1.1% at ISM band, 0.9% at WMTS band and 1.2% at MICS band) since stacked structure also adopted to reduce the antenna size.

In this chapter, an implantable triple band SS-PIFA antenna is also presented for biomedical applications. The miniaturised antenna, operating over in 433MHz MICS band, 1430MHz WMTS band and 2450 MHz ISM band, is compact in size and occupies a volume of 0.9 cm^3. The antenna characteristics are verified using

experimental phantom; and the measured results agree reasonably well with the calculated results using anatomically realistic numerical human tissue phantoms.

This chapter is organized as follows: In Section 5.3, I described the configuration of the proposed SS-PIFA, together with parametric studies and calculation of antenna performance. Also, the working principles of miniaturization and wide bandwidth property are analysed in this section. Section 5.4 presents SS-PIFA measurements followed by Specific absorption ratio (SAR) in section 5.5. Folded oval loop antenna and its performance for scalp implants are given in Section 5.6 whereas in section 5.7 the triple band configuration for the proposed SS-PIFA including experimental results are presented followed by the discussion in Section 5.8.

5.3 Single Slot PIFA Design and Performance

The proposed geometry is a modified PIFA type antenna, providing a lower radiated near fields and a lower SAR when implanted inside the body. The presented antenna structure has a compact size, light weight, good radiation efficiency and reasonable bandwidth to accommodate changes in tissue properties. Moreover, it can easily be tuned to cover the desire frequency bands of interest, such as MICS, Zigbee WMTS and ISM bands by increasing its size by a fixed adjustment factor that is related to the wavelength of operation and optimizing the sizes of the slot and the ground plane.

The radiator is mainly designed for head implantable devices such as ICP monitoring systems, but can also be used under the skin, inside the chest, or muscle without significant changes in the radiator structure. Compare to the Dual Slot PIFAs introduced in chapter 1, the SS-PIFA has a smaller size but lower radiation efficiency

and impedance bandwidth. The advantage of the proposed implantable Single Slot PIFA is being printable on different substrates based on the system requirements and its structure size can be miniaturized easily as required, for head implants. In next section I introduce Single Slot geometry, design a SS-PIFA operating at ISM band, 2450 MHz, and demonstrate the miniaturization procedure for patient comfort and system requirement.

5.3.1 Design Procedure

The proposed antenna structure consists of a patch radiator, a dielectric substrate, a dielectric superstrate, a ground plane, a shorting pin and a feeding point. The top view of the antenna structure with the main possible slot arrangement is shown in Figure 5-1. The antenna design procedure was carried out in three steps. First, a rectangular patch antenna was designed to operate over desired telemetry band when implanted in a homogeneous tissue mimicking numerical phantom. Second, a single slot added on radiator geometry and then following a generalized procedure, shown in Figure 5-2, a model of SS-PIFA with a shorting pin was tuned to operate over the desired frequency band when implanted in a multi-layered tissue mimicking numerical phantom. At this stage, both shorting pin and feeding point must be placed on the right edge of the top patch to achieve the desired resonance characteristics. Later, a single layer dielectric thin superstrate was added to the implanted antenna model and the geometrical parameters were varied to obtain resonance at the operating frequency band using the generalized procedure. The model of the antenna with the thin superstrate was then implanted inside an anatomically realistic complex human body model for a precise simulation as shown in Figure 5-3a.

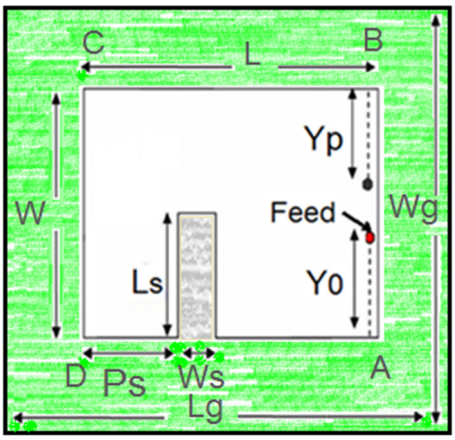

Figure 5-1: Top view of SS-PIFA geometry.

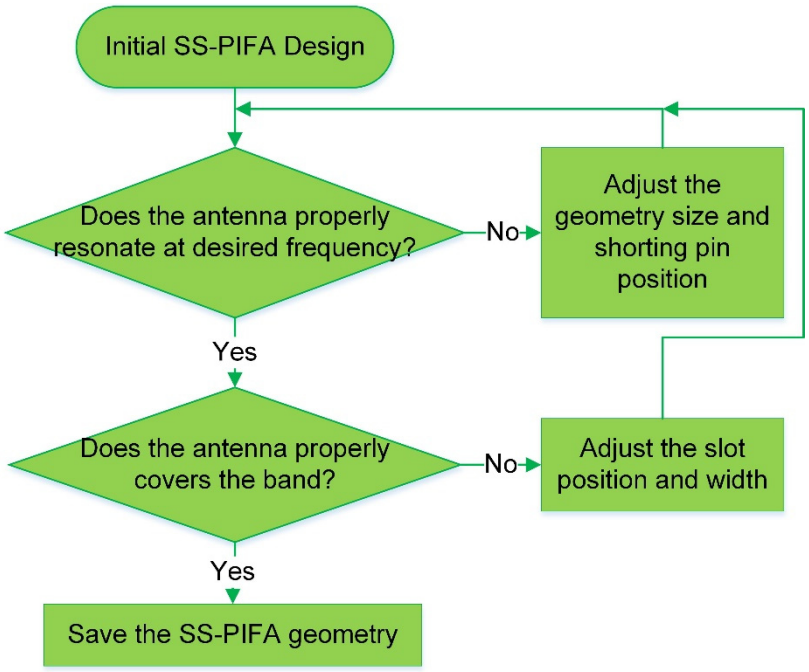

Figure 5-2: The initial antenna design flowchart.

Figure 5-3a also illustrates the presented SS-PIFA structure for which the dimensions of the rectangular-shaped patch as well the radiating slot are the key parameters for antenna operation. Based on simulation results when the slot is located at bottom edge and both the feeding point and the shorting pin are place on the right edge of the top patch the radiator shows a remarkable improvement in performance for implantable applications.

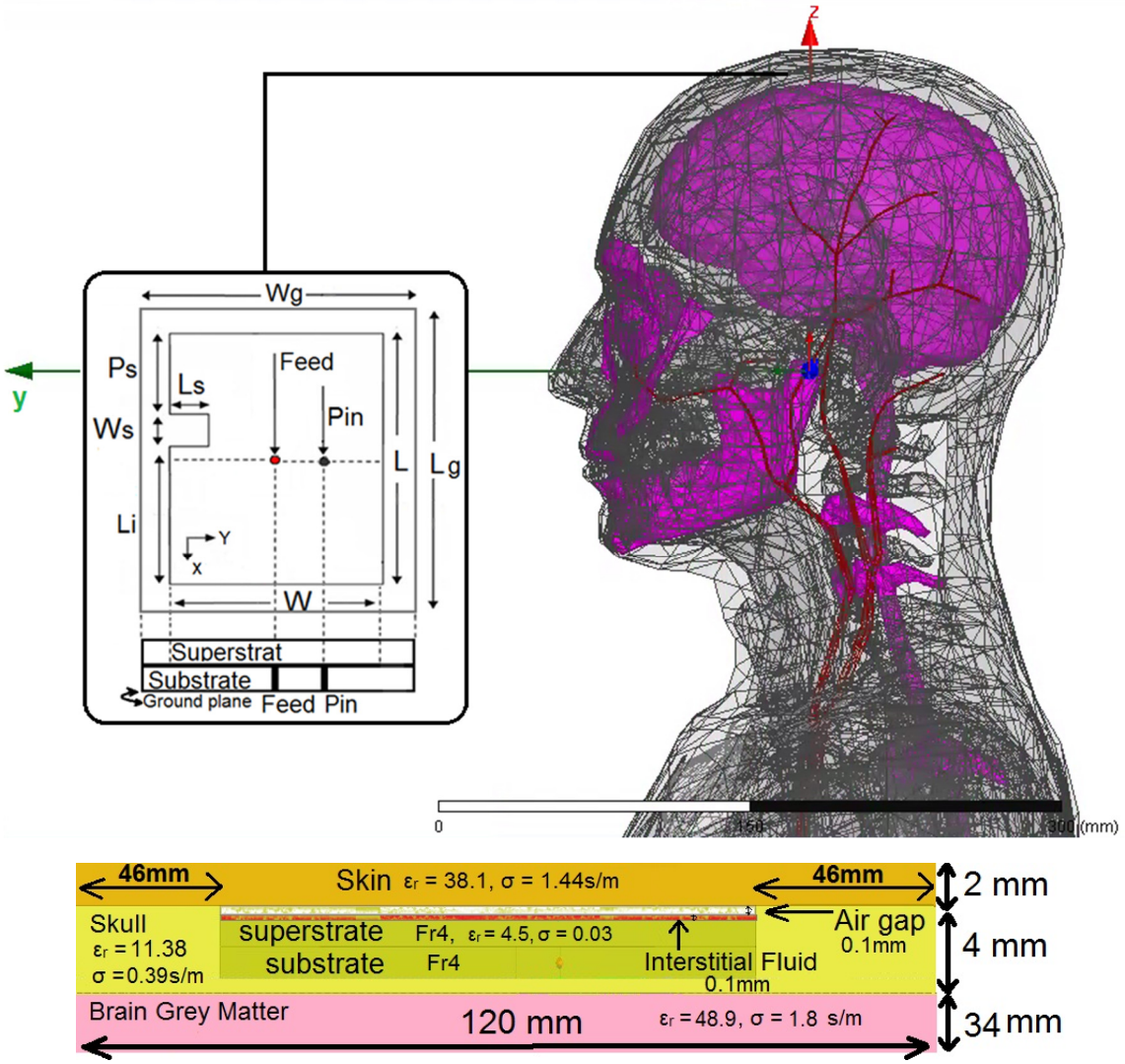

Figure 5-3: Simulation set up in numerical mimicking phantoms, a) 3D complex human head model, b) Side view of layered block and cylindrical phantoms.

In addition, the relative location of the shorting pin with respect to the position of the coaxial feed can play a major role in obtaining good matching within the chosen band. The main resonant frequency may be determined by the patch width W as well as the current distribution around the slot which is affected by the shorting pin position. The antenna can be tuned to cover other frequency bands of interest by changing the size of the patch and the slot. Readjustment of the feeding point and the slot location as well as slot position may be needed.

For optimum performance, my empirical studies shown that the feeding position, Y_f, must be positioned on the right edge of the patch with an approximate distance of 0.16 W from the bottom edge as shown in Figure 5-4. In addition, my numerical investigations indicated that to improve the radiation efficiency of the implanted antenna, W/L must be greater than 1.1 but smaller than 2.2. The calculated radiation efficiency when W = 1.57 L and the antenna resonating at 2450 MHz while immersed embedded the tissue mimicking phantom is 1.9% which is reasonably good for scalp implants. The full ground plane, slightly larger than the top patch, and the balloon shaped broadside radiation pattern of the SS-PIFA minimize the radiated power passing through the human head.

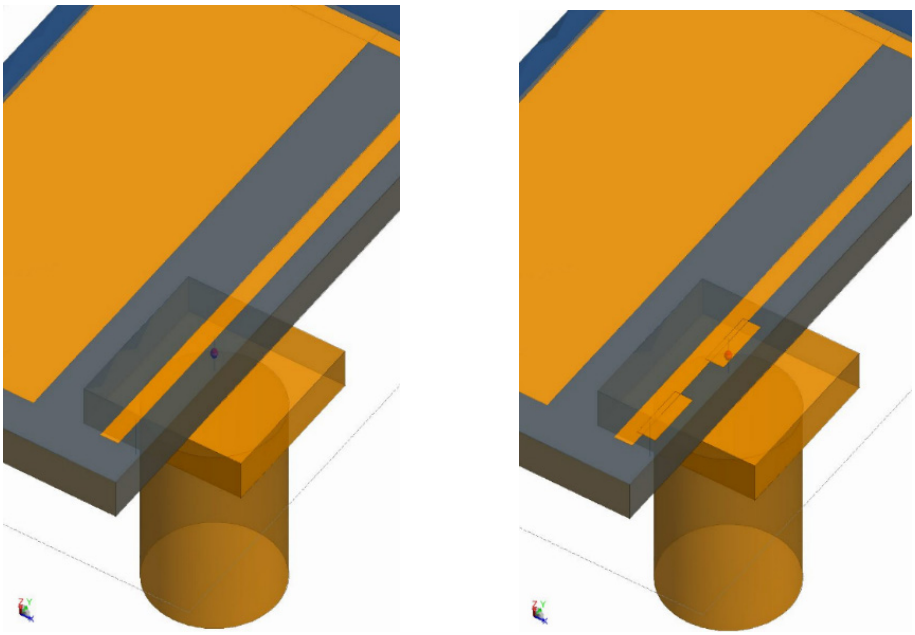

Figure 5-4. Single Slot PIFA structure.

5.3.2 Calculation Environment

To mimic the antenna implant inside the human head the proposed SS-PIFA was immersed inside an inhomogeneous multi layered complex human body phantom using HFSS [132] as shown in Figure 5-3a. The model is an adult male patient standing on its feet along z axis. It consists of over 300 body parts to represent bones, muscles, veins and organs, some of them are highlighted for a better understanding. It has an accuracy in the order of millimetre and a frequency dependent material properties database is included. This model can provide accurate results, without being memory and computational time intensive.

To carry out empirical optimization, it is required to obtain the results rather quickly. Hence, smaller human tissue mimicking phantoms viz. spherical and cylindrical multi-layered model or layered block model were also employed. Each model consists of three different tissue layers representing skin, cortical bone (skull) and brain grey matter. The dielectric properties for these tissue layers when antenna resonating at 2450 MHz are illustrated in Figure 5-3b. Based on my calculations, the dimensions provided for the layered models, shown in Figure 5-5b, are appropriate for higher frequency analysis such as 2450 MHz. Also, the thickness provided for each layer is appropriate for all the frequency bands of interest. For the lower frequency bands such as 400 MHz the effective wave length has to be considered and the dimensions have to be increased carefully. The dielectric properties of the different layers for the human body head are tabulated in Table 5-1.

The proposed antenna was embedded under the skin above the brain grey matter and its performance calculated using FEKO^{TM} [133]. The x-y plane cut of the calculation set up, showing the proposed antenna positioning inside the multi-layer

spherical mimicking phantom, is illustrated in Figure 5-3b. This setup is similar when using layered block and cylindrical numerical phantoms. The thickness of the air gap layer and interstitial fluid are ideally assumed zero at this stage of the design. The spherical model has been employed to mimic the SS-PIFA implantation inside the human head. The cylindrically shaped multi-layered phantom can be used to simulate antenna embedding inside the arm whereas the layered rectangular block phantom was used to mimic implantation under the chest skin. Later to verify the antenna performance inside the human body in different locations such as head and small intestine, the complex human body has been employed.

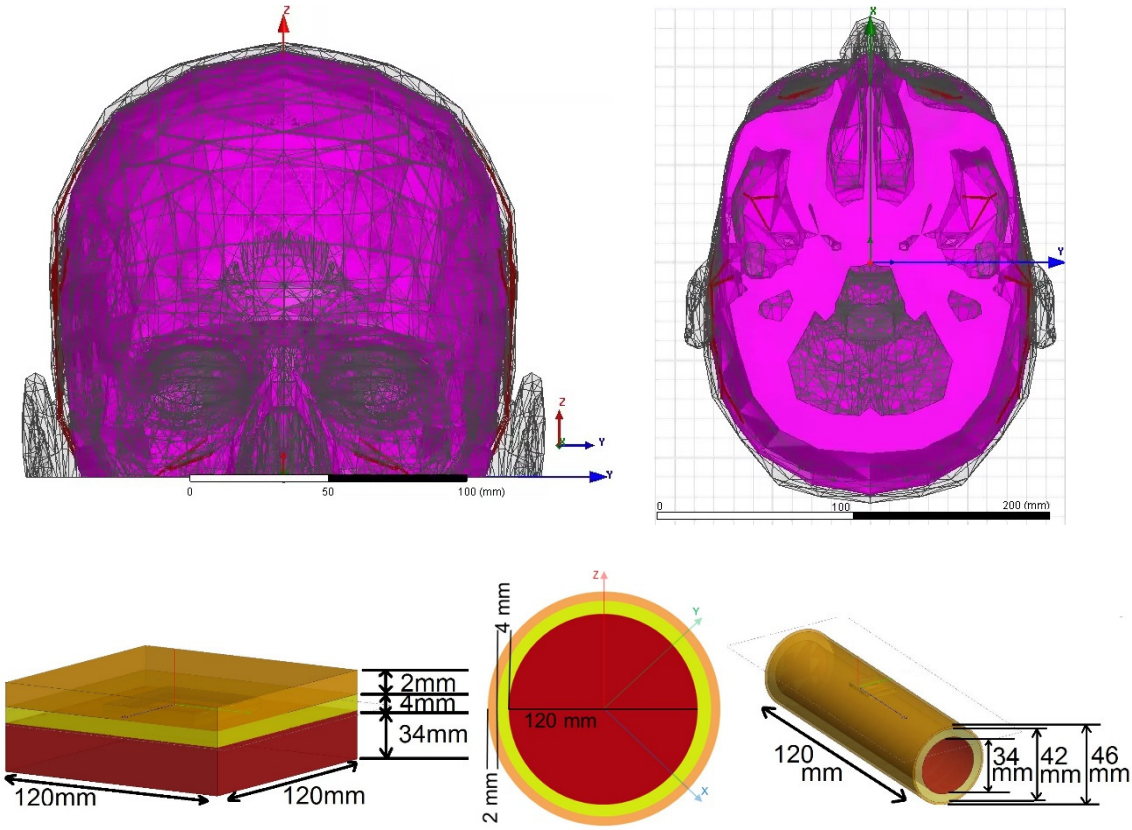

Figure 5-5: Simulation set up in numerical mimicking phantoms, a) 3D complex human head model, b) Side view of Multi-Layered Block, Multi-Layered Spherical and cylindrical phantoms.

Following the generalized procedure, shown in Figure 5-2, I could successfully tune the geometrical parameters of SS-PIFA to make the antenna operating over a variety of frequency bands such as MICS band at 400 MHz, Zigbee at 868 MHz and WMTS band at 1430 MHz. The antennas' size and properties are tabulated in Table 5-2. The initial designs performed well inside the human tissue numerical phantom. Later parametric analysis was carried out in order to quantify the effects of the different antenna geometric parameters and to empirically optimize its design.

TABLE 5-1
HUMAN HEAD TISSUE DIELECTRIC PROPERTIES FOR DIFFERENT MEDICAL FREQUENCY BANDS

Tissue	*MICS Band 400 MHz*		*ZigBee 868 MHz*		*WMTS Band 1430 MHz*		*ISM Band 2450 MHz*	
	ε_r	σ	ε_r	σ	ε_r	σ	ε_r	σ
Skin (Scalp)	46.74	0.689	41.58	0.856	44.51	1.066	42.85	1.591
Dura	46.65	0.827	44.51	0.951	43.40	1.162	42.03	1.668
Brain Grey Matter	57.39	0.738	52.88	0.929	50.86	1.199	48.91	1.807
Cortical Bone (Skull)	13.10	0.090	12.48	0.139	12.01	0.2186	11.38	0.394
Brain White Matter	42.05	0.445	38.99	0.581	37.57	0.776	36.16	1.215
Cerebrospinal Fluid	70.97	2.252	68.71	2.399	67.71	2.691	66.24	3.457
Spinal Cord	35.39	0.447	32.63	0.565	31.35	0.7288	30.14	1.088
Lens	48.14	0.669	46.63	0.784	45.76	0.9896	44.62	1.504
Vitreous Humor	69.00	1.529	68.91	1.627	68.72	1.847	68.20	2.478
Muscle	57.11	0.797	55.11	0.932	54.03	1.164	52.72	1.738
Fat	5.58	0.04	5.49	0.052	5.39	0.065	5.28	0.10
Eye sclera	57.66	1.005	55.36	1.155	54.12	1.409	52.62	2.033
Cartilage	45.45	0.587	42.77	0.768	41.05	1.068	38.77	1.755

TABLE 5-2
SS-PIFAS SIZE AND CHARACTERISTIC OVER DIFFERENT MEDICAL FREQUENCY BANDS

Freq. Band MHz	*Resonant Freq. MHz*	*Band width MHz*	*Radiation efficiency*	*Patch Size mm^2*	*Antenna volume mm^3*
2400	2450	175	1.9%	17 × 10	682
1430	1430	108	1.8 %	21 × 12	760
868	868	40	1.8%	23 × 12.6	875
400	400	18	1.9%	25 × 14	985

5.3.3 Parametric Study

To minimize the antenna size, I have conducted detailed parametric study and investigated the effects of each geometrical parameter of the SS-PIFA on the resonant frequency. The generalized procedure, illustrated in Figure 5-6, has been used to reduce the size of the proposed antenna. This procedure has also been applied to all of the designed SS-PIFAs operating over MICS, ZigBee and WMTS bands and reduced the antenna physical size significantly. Here, the effects of the feed and shorting pin positions, width and length of the slot while fixing other antenna parameters were also investigated. I have also employed two types of substrates such as Fr4 and Rogers 3210 to investigate the effect of dielectric materials for SS-PIFA structure.

To maintain the optimum performance for the presented antenna, throughout the miniaturization process, I observed not only the radiator resonant frequency but also other antenna performance indicators such as fractional bandwidth and radiation efficiency. This is necessary to make sure that implantable antenna design requirements are fulfilled at each and every step. I have also calculated the surface current flow to observe how the currents are changing when the antenna size is reduced.

My studies revealed that by increasing the slot lengths and moving its position gradually towards the right edge of the antenna while at the same time placing the feed and shorting pin at appropriate locations on the right edge, as shown in Figure 5-4, one could sucsessfully reduce the antenna size without affecting the resonance within 2.4 GHz ISM band. The intial size obtained for the SS-PIFA resonating at 2450 MHz is Lg = 23.4 mm, Wg = 18.2 mm, L = 17 mm, W = 10 mm and h = 1.6 mm. Increasing the slot length resulted in increasing the current flow path. I identified that the antenna

can be miniaturize by increasing the length of the current flow path while maintaining the resonant frequency to fall within the ISM band. So that, a significant size reduction in physical size of the antenna achieved compare to its initial size. For the PIFA type antennas, the ground plane size has a significant effect on radiation bandwidth [134]. Based on my experience with DS-PIFA, I have considered different size of ground plane for SS-PIFA to identify the best ground plane which maximize the fractional bandwidth. I have concluded that by choosing the size of the ground plane slightly bigger than the patch, i.e. 0.5 mm for the width *Wg* and length *Lg* of the ground plane, the maximum bandwidth can be obtain.

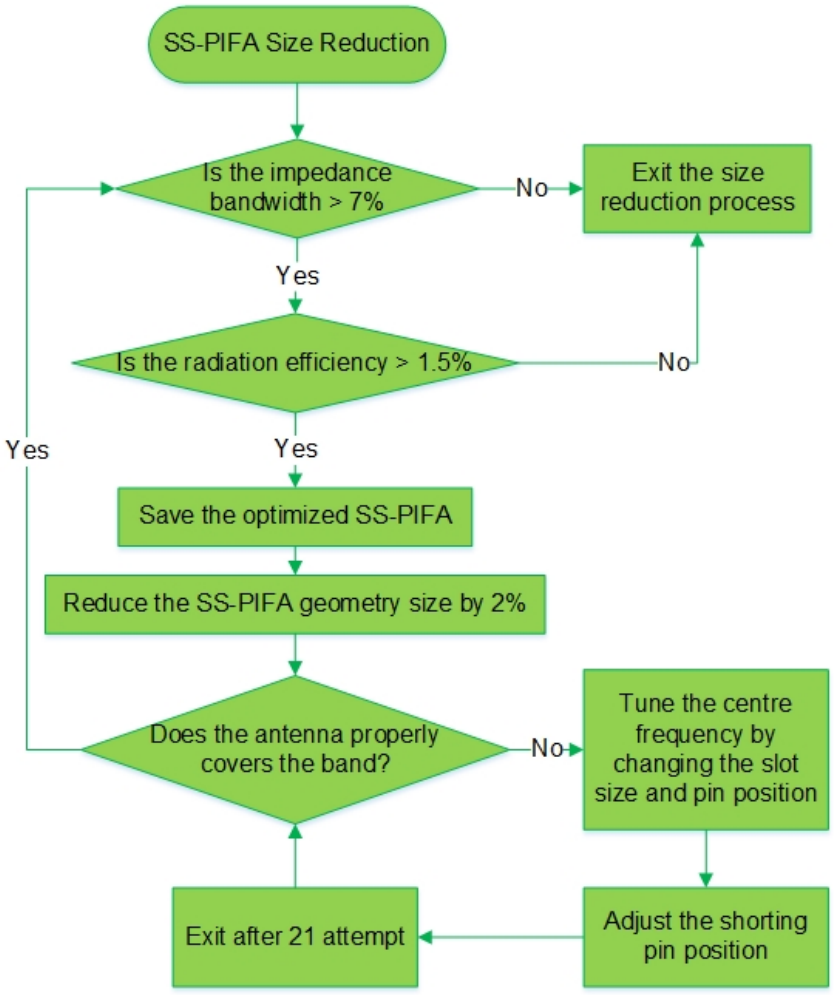

Figure 5-6: The SS-PIFAs size reduction flowchart.

Furthermore, I found that by increasing or reducing the slot widths, one could tune the resonant frequency as shown in Figure 5-8 without changing the antenna structure or size. This feature demonstrates the flexibility of the proposed antenna geometry useful for practical implementation.

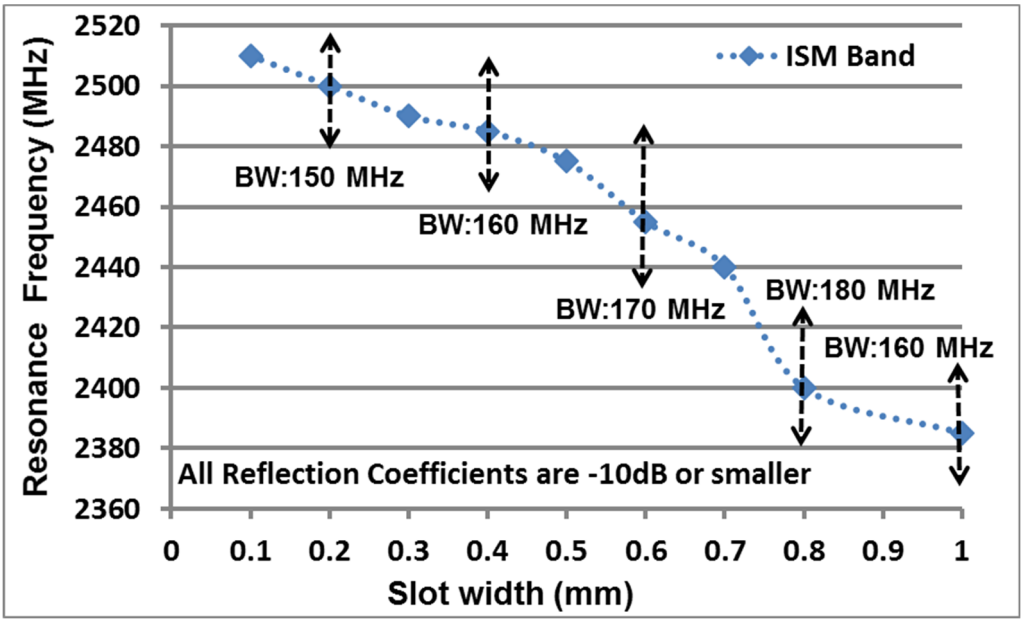

Figure 5-7: Single slot PIFA: The effects of reducing the slot width.

The finalized dimensions of the proposed SS-PIFA, operating over ISM band, are $Lg = 5$ mm, $Wg = 7$ mm, $L = 4$ mm, $W = 5$ mm and $h = 1.6$ mm. Here, 92% physical size miniaturization gained for the presented antenna compared to its original size. The size comparison with similar types of antennas reported in the literature is provided in Table 5-3. I have also performed further parametric study, followed the generalized procedure, to make sure that I have proposed the smallest size possible for SS-PIFAs that cover ZigBee, MICS and WMTS bands having a reasonable fractional bandwidth and radiation efficiency using FR4. The antennas' size and properties are tabulated in Table 5-4. Referring to the Tables 5-2 and 5-4, one can see 89% antenna size reduction

for WMTS, 86% antenna size reduction for ZigBee and 60% antenna size reduction for MICS band achieved, compare to the initial size for the proposed SS-PIFAs, by reducing the lengths of the slots and placing the feed and the pin at proper locations.

To investigate the effect of substrate dielectric material on DS-PIFAs performance I also employed Rogers 3210. This substrate has a lower conductivity for higher frequencies compared to FR4. However, I purposefully chose a higher permittivity to reduce the antenna size further. This substrate has a thickness of 0.64 mm and ε_r of 10. I could successfully redesign SS-PIFAs, using the design procedure shown in Figure 5-2, for my frequency bands of interest employing Rogers 3210. To miniaturize SS-PIFAs, I used a similar approach as described above and applied the similar method shown in Figure 5-6. This generalized procedure, helps to tune and reduced the size of my proposed structure to operate over different bands when implanted in a multi-layered tissue mimicking numerical phantom. The antennas' size and properties are tabulated in Table 5-4. Further size reduction of 76% for antenna covering ISM band, 72% for antenna covering WMTS band, 69% for antenna covering ZigBee and 66% for antenna covering MICS band achieved by employing dielectric materials with higher permittivity.

TABLE 5-3
SIZE COMPARISON OF PROPOSED SINGLE SLOT PIFA

Patch Shape	Freq. Band MHz	Type	Radiation efficiency	Area mm^2
[5]	400	Loop antenna	0.84%	14 × 14
[8]	2400	Annular antenna	1.1 %	20 × 22
[9]	2400	Patch antenna	0.85%	6 × 6
[10]	400	Microstrip antenna	1.2%	19.6 × 20.6
This work	2400	Single Slot PIFA	1.8%	7 × 5

TABLE 5-4
MINIATURIZED SS-PIFAS SIZE AND CHARACTERISTIC OVER DIFFERENT MEDICAL FREQUENCY BANDS

Freq. Band	Resonant Freq. MHz	Dielectric material	Band width MHz	Radiation efficiency	Antenna dimensions mm^3	Vol. mm^3
ISM	2450	Fr4	240	1.8	5 × 7 × 1.6	56
ISM	2450	R.3210	160	1.65%	4 × 6 × 0.64	15.4
WMTS	1430	Fr4	125	1.7 %	6 × 8 × 1.6	76.8
WMTS	1430	R.3210	105	1.55%	5 × 7 × 0.64	22.4
ZigBee	868	Fr4	60	1.7%	7 × 11 × 1.6	123.2
Zigbee	868	R.3210	45	1.5%	6 × 9.5 × 0.64	36.5
MICS	400	Fr4	25	1.8%	12 × 20 × 1.6	384
MICS	400	R.3210	20	1.6%	10 × 18 × 0.64	115.2

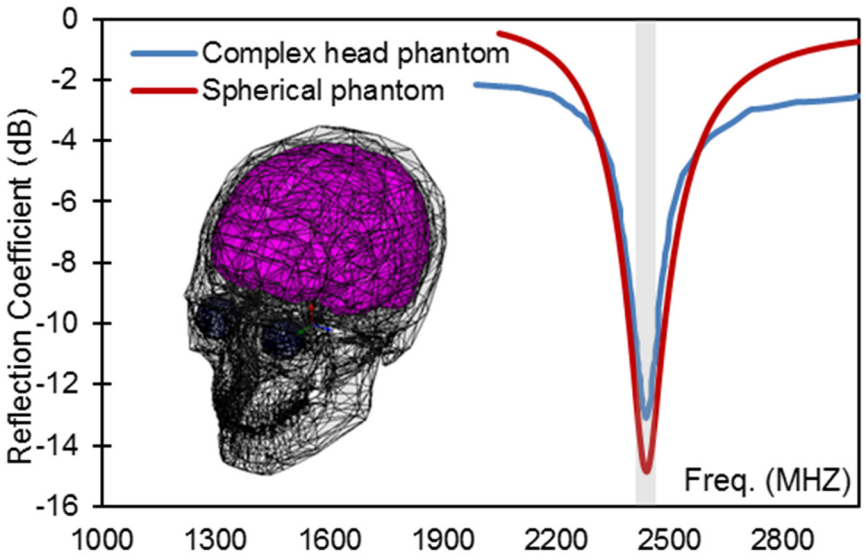

Figure 5-8: Reflection coefficient of Single slot PIFA covering ISM band when immersed inside the multilayer spherical numerical phantom and the complex human body head phantom.

5.3.4 Antenna Performance

The proposed SS-PIFA performed well when implanted inside the head and could cover the ISM band fully with a good impedance bandwidth margin. **Error! Reference source not found.**Figure 5-8 shows the reflection coefficient results of the miniaturized SS-PIFA resonating at 2450 MHz when immersed inside the multilayer spherical numerical phantom and the inhomogeneous multi layered complex human

body phantom using HFSS. The radiator patch is printed on FR4 substrate and, provides an impedance band width of 170 MHz which is sufficient to satisfy the required bandwidth for a variety of the implantable systems.

I have also considered a trade-off based on the antenna miniaturization and efficiency to have the maximum radiated power. Compared to the loss resistance over the antenna structure, I could successfully maintain the radiation resistance dominance by adjusting the antenna size and the feeding position to keep the surface current flow uniform over the radiator. The radiation efficiency of the 2450 MHz miniaturized SS-PIFA, including superstrate, is 1.9% when immersed inside the spherical multi-layer numerical head phantom using FEKO. As expected, the calculated efficiency is low due to the presence of lossy tissues. However, the calculated efficiency is higher than the reported results for similar class of antennas in the literature [33, 48, 93, 97, 159, 160]. I have calculated the losses per media of the numerical phantom and then estimated the antenna radiation efficiency, excluding surrounding lossy environment, which is 61.25% including superstrate. This helps to develop a better understanding of antenna performance alone. I have also investigated the effect of the slot width variation on efficiency and losses for the 2450 MHz miniaturized SS-PIFA and, the results are tabulated in Table 5-5.

TABLE 5-5
LOSSES IN SS-PIFA AND NUMERICAL PHANTOM AT 2.45 GHZ (IN WATT).

Slot width	1MM	0.8MM	0.6MM	0.4MM	0.2MM
Radiated power	0.00010	0.00011	0.00009	0.00008	0.00006
Input power	0.0055	0.0055	0.0055	0.0055	0.0055
Human tissue losses	0.00326	0.00326	0.00326	0.00326	0.00326
Antenna efficiency	61%	61.25%	60.85%	60.7%	60.35%
Total efficiency	1.65%	1.9%	1.8%	1.7%	1.55%

Antenna efficiency = **(**Radiated power + Human tissue losses**)** / Input power

5.4 SS-PIFA Measurements

The antenna prototype is then fabricated using Fr4 substrate and etching technique. The antenna prototype operating over MICS band, 400 MHz, ZigBee band, 868 MHz and ISM band, 2450 MHz, are depicted in Figure 5-9. However, the top patch geometry has a very thin conductive arm as shown in Figure 5-4. Since the etching technique is a simple low cost technique with low level of accuracy it is not a suitable method for printing very thin conductor tracks. For the first attampt, using etching method, I could not to validate the calculation results so that I have employed the PCB machinary and printed the propose SS-PIFAs with high level of accuracy. For the secound attempt, I could successfully verify the calculated results as demonstrated below.

The Measurement set up and the miniaturized SS-PIFA prototypes printed on Fr4 for MICS 400 MHz, ZigBee 868 MHz, WMTS 1430 MHz and ISM 2450 MHz are shown in Figure 5-9 and Figure 5-10 respectively. In order to verify the performance of the implanted antenna when placed inside human body, I have developed a phantom that is prepared with minced beef (80 % meat and 20% fat). The conductivity and dielectric constants of the experimental phantom were measured by using dielectric probe kit and Agilent E5071C network analyser from 100 MHz to 3 GHz when the experimental phantom was placed in a plastic container of size 140 × 140 × 50 mm^3. A good agreement with the desired dielectric properties [135] was observed, comparison of relative permittivity and conductivity of the experimental phantom, skin, and coritical bone (skull) are shown in Figure 5-11. It can be found that the permittivity of minced beef phantom is closer to the human skin which is useful as the antenna placment is close to the scalp.

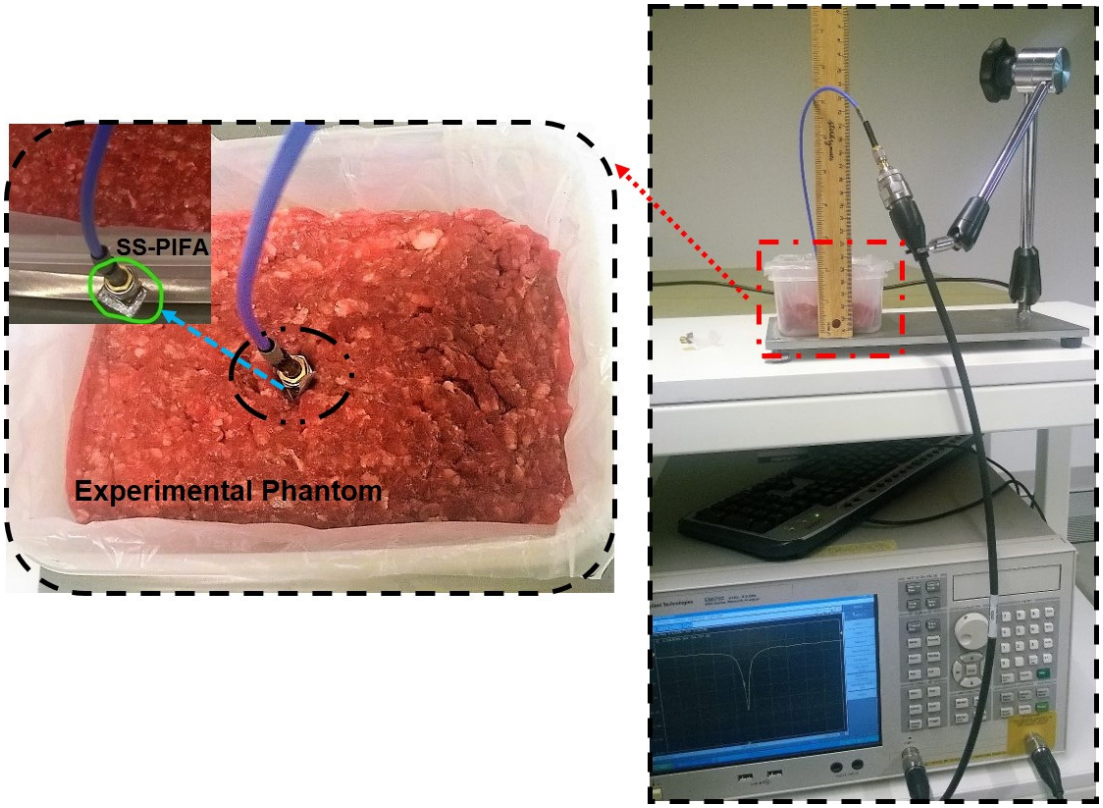

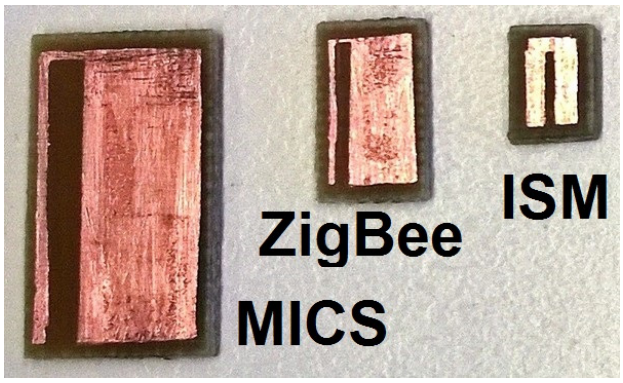

Figure 5-9: Measurement set up and Single Slot PIFAs prototype, using etching technique, on FR4 substrate for different frequency bands.

The SS-PIFA, operating over Industrial, Scientific, and Medical (ISM) band at 2450 MHz, has a measured bandwidth of 190 MHz (7.8%) which is significantly valuable when considering slight changes in dielectric properties of human tissue due to the dissimilar body shapes, genders, ages and etc. These changes in dielectric properties may shift the resonant frequency. Hence, the proposed antenna bandwidth could guarantee ISM band coverage for a variety of patients' tissue.

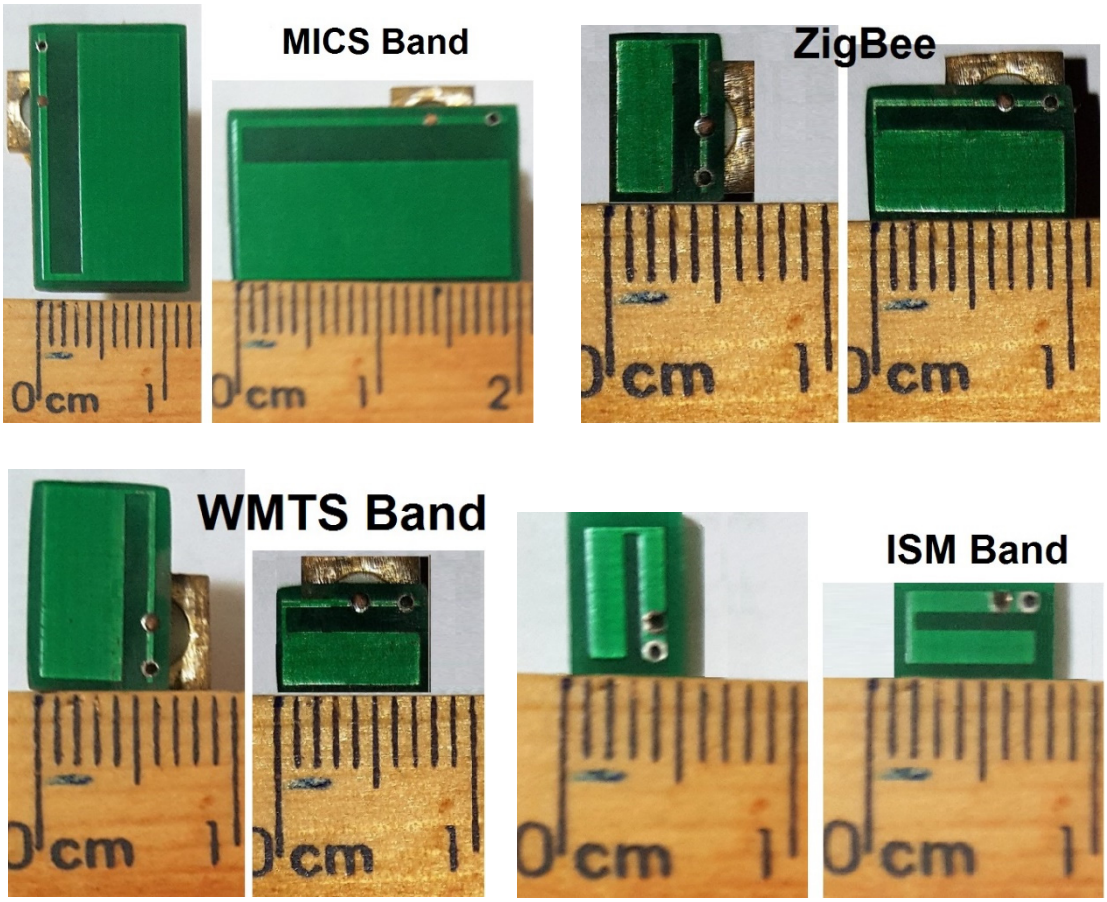

Figure 5-10: Single Slot PIFAs prototype on FR4 substrate for different frequency bands of interest.

The measured result on reflection coefficient when the antenna (including superstrate) was immersed in experimental phantom shows a good agreement with calculated result using complex human body as shown in Figure 5-12. Slight discrepancies are noticed which are within the uncertainty range imposed by the fabrication inaccuracies such as soldering and dependency of Fr4 permittivity on operating frequency.

I have also used the experimental phantom to verify the performance of the proposed implantable SS-PIFAs for Medical Implant Communication Service (MICS) 400 MHz and Wireless Medical Telemetry Service (WMTS) band at 1430 MHz. The antenna prototypes are covered with the superstrate layer with the same dielectric materials as substrate, Fr4.

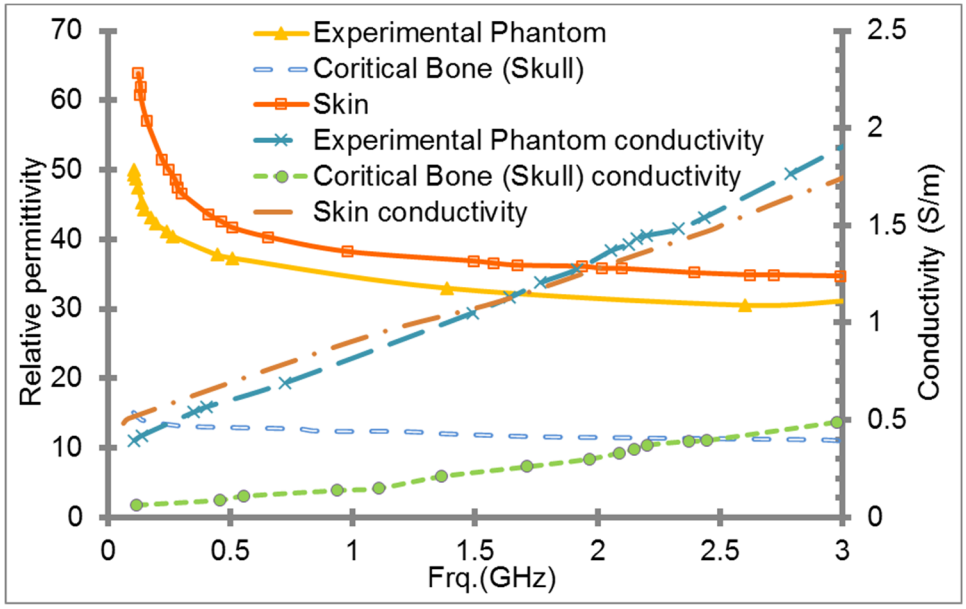

Figure 5-11: comparison of relative permittivity and conductivity of the beef phantom with published data in skin and muscle.

The results on reflection coefficient for each of the antenna prototypes, resonating at different standard telemetry bands, is also shown in Figure 5-12. The comparison is attained using computational inhomogeneous multi-layer complex human head mimicking phantom versus measured inside the experimental phantom. From this figure, one can see the calculated results on reflection coefficient show a good agreement with measured results when the antennas including superstrate immersed, one by one, in the experimental phantom.

5.5 Specific Absorption Ratio (SAR)

To measure the SAR for the proposed miniaturized SS-PIFA resonating at 2450 MHz I have employed the similar method I used in previous chapters. This method is a simple measurement technique for measuring the temperature rise in an equivalent human tissue experimental phantom caused by electromagnetic energy absorption radiated by implanted antenna.

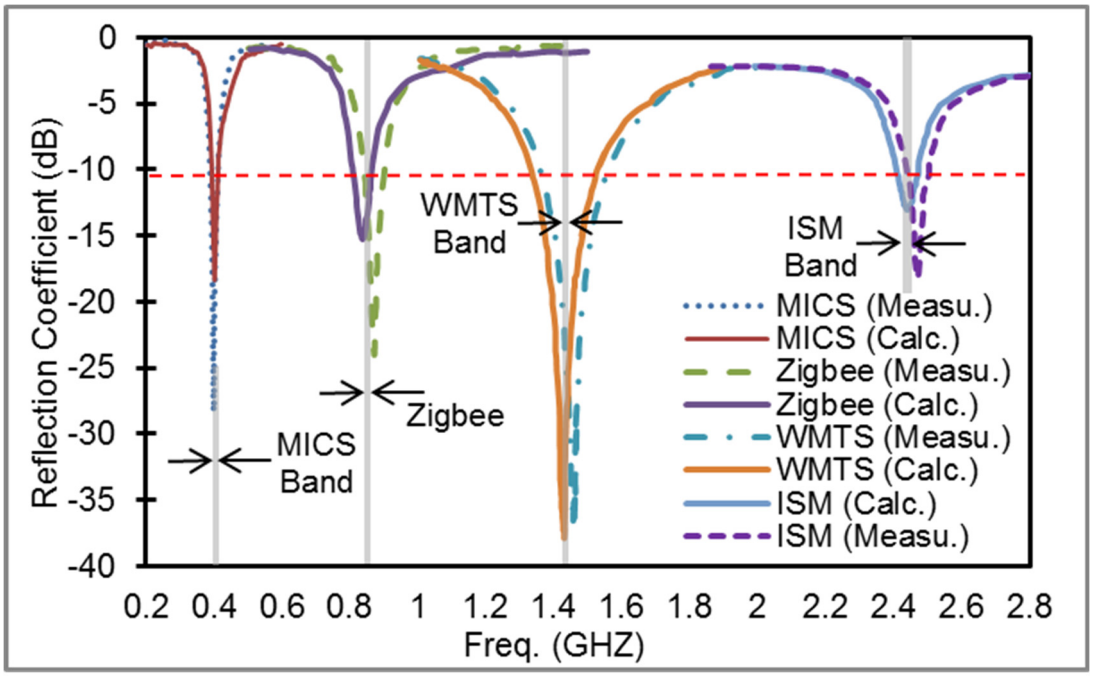

Figure 5-12: Reflection coefficient of Single slot PIFA: a) Calculated using Complex human body model, block Layered and cylindrical Layered phantoms, b) Measured vs. Calculated using Complex human body model.

I have used optical fiber thermal sensors to minimize the metal wire thermal sensors disturbing the electromagnetic field in the phantom. Moreover, the SAR can be stably evaluated over a wide range of frequency bands as the optical thermal sensors are frequency independent. The relationship between the temperature rise and the SAR in an equivalent human tissue phantom is given by [136, 137]:

$$\rho.C\frac{\partial T}{\partial t} = K\nabla^2 T + \rho.SAR \tag{5.1}$$

Here, T is the temperature in the phantom (in kelvins), K is the thermal conductivity of the phantom (in watts per meter kelvin) and t is the elapsed time (in seconds), C is the specific heat of the phantom (in joules per kilogram kelvin) which is 3400 (J/kg.k) and ρ is the density of the phantom (in kilograms per cubic meter) which is 1060 (kg/m^3).

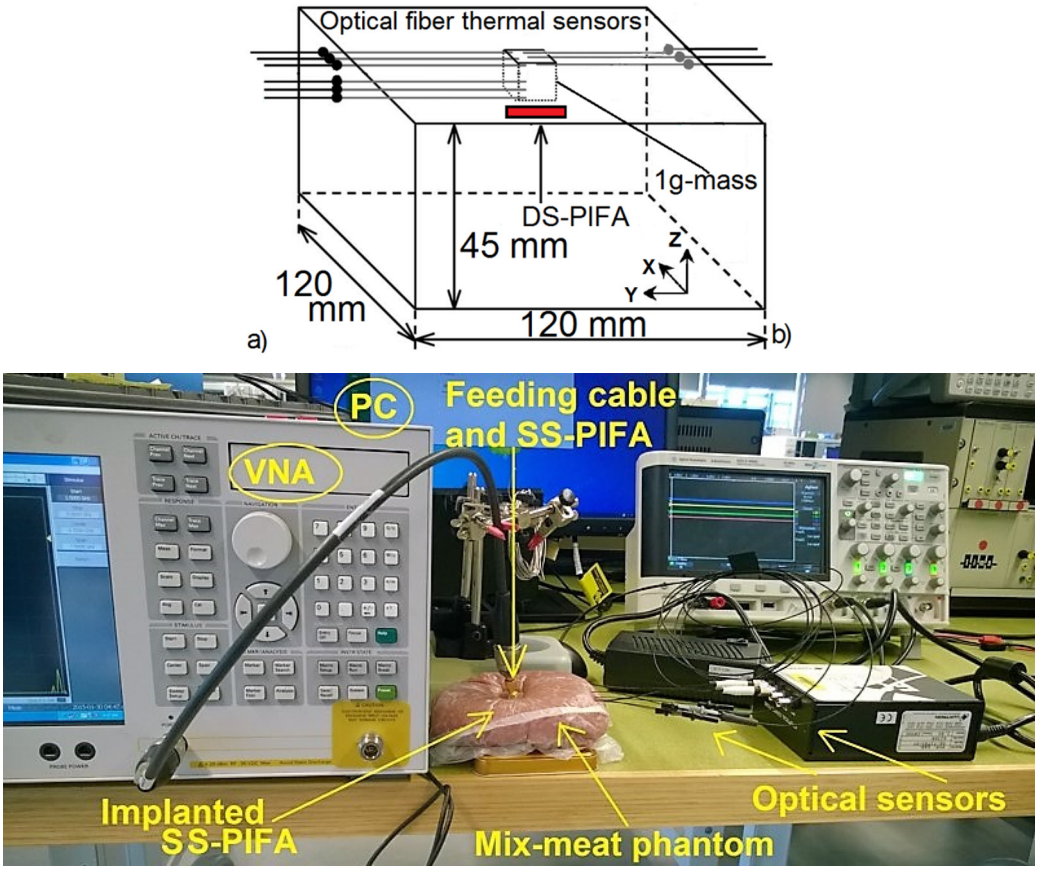

Figure 5-13: a) SAR measurement diagram using optical fibre thermal sensors. b) SAR measurement setup for Single slot PIFA on FR4 substrate.

The equation (1) could be simplified when the thermal diffusion is low. In addition to evaluating 1-gram average SAR multiple points are needed to measure the temperature rise in the experimental phantom [136]. Figure 5-13a shows optical thermal sensors arranged in a 3-D cubic lattice network completly covering the 1-gram mass to measure ΔT in the experimental cubic phantom. If the density of the mimicking phantom material is close to 1000 kg/m^3, then the side lengths of a 1-g mass cube are approximately 10 mm [136]. Consequently, optical fibre thermal sensors are arranged in a 3-D network by choosing 18 temperature measurement points to evaluate 1-g SAR. The sensors are located at 0.5mm and 1.5mm under the skin with 5mm intervals over the X-Y plane parallel to radiator surface.

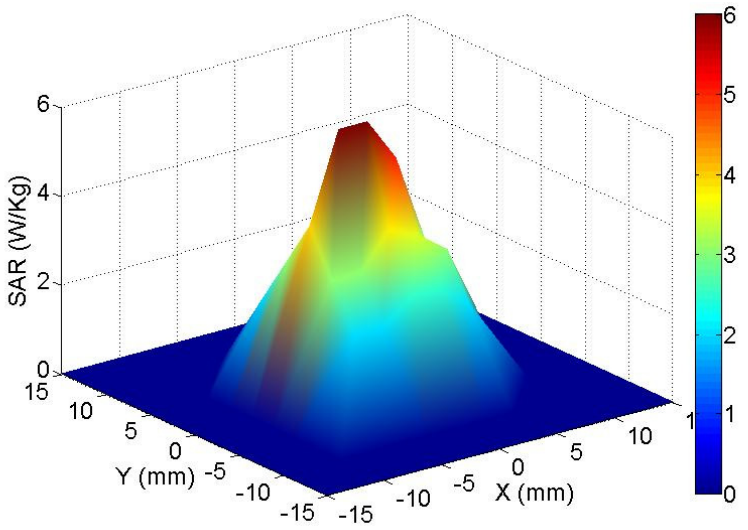

Figure 5-14: Measured 1g-SAR: Miniaturized Single Slot PIFA at 2450 MHz.

The SAR measurement setup for SS-PIFA using optical fibre thermal sensors is shown in Figure 5-13b. I have employed Luxtron FOT Lab Kit and STM and STB optical thermal sensors (from Luxtron, Ltd) to measure temperature rise in the experimental phantom due to radiation. These optical fibres are made from polymer, and their measurement uncertainty is ±0.05C at room temperature. The input power was set to 10 dBm (10mw) at 2450 MHz and the equivalent phantom was exposed to microwaves up to 30 minutes while the thermal sensors measured the resulting temperature rise in the human tissue mimicking phantom. Figure 5-14 shows the 1-g SAR values using indirect SAR measurement. The calculated 1-g SAR for the input power level of 10 dBm would be 5.8 w/kg while the measured result indicates 5.4 w/kg for 1-g SAR with the same input power. Figure 5-14 reveals that 1-g SAR is above the limitation [138] so that the input power must be set to less than 3 dBm (2 mw) to satisfy 1-g SAR regulation.

Additionally, the 1g-SAR calculations have been carried out for three different miniaturized SS-PIFAs covering three different standard biomedical frequency bands

such as MICS band, Zigbee and WMTS band as tabulated in Table 5-6. To verify the calculated SAR results, SAR measurements have also been conducted for the presented miniaturized SS-PIFAs. The input power was set to 10 dBm (10 mw) at MICS, Zigbee, WMTS and ISM bands. The equivalent phantom was exposed to microwaves up to 30 minutes while the thermal sensors measured the resulting temperature rise in the mimicking phantom. The measured temperatures and simplified form of equation (1) are used in a Matlab code to estimate the SAR. The SAR values are calculated in five minutes step to monitor the SAR variations. The results on 1-g SAR for all the four miniaturized SS-PIFAs are tabulated in Table 5-6.

TABLE 5-6
MEASURED SAR OVER STANDARD BANDS FOR HEALTH CARE TELEMETRY SYSTEMS

Bands / Timings		MICS	Zigbee	WMTS	ISM
1	**After 10 minutes**	3.7w/kg	4w/kg	4.4w/kg	4.9w/kg
2	**After 15 minutes**	3.8w/kg	4.1w/kg	4.5w/kg	5.1w/kg
3	**After 20 minutes**	4w/kg	4.2w/kg	4.6w/kg	5.3w/kg
4	**After 25 minutes**	4.1w/kg	4.3w/kg	4.8w/kg	5.4w/kg
5	**After 30 minutes**	4.1w/kg	4.4w/kg	4.9w/kg	5.4w/kg
Total		4.1w/kg	4.4w/kg	4.9w/kg	5.4w/kg
Calculated		4.5w/kg	4.8w/kg	5.4w/kg	5.8w/kg

5.6 Folded Oval loop

The compact folded oval loop antenna covering MICS band up to 1 GHz proposed to satisfy the wideband antenna requirements for head implant devices. Wideband performance is desirable to assure the ongoing and steady operation of the system, which may be affected by variation of the electromagnetic properties of the surrounding environments that influences the tuning of narrowband antennas. This feature also can facilitate a higher data transfer rate [54, 62, 171, 172].

The magnetic fields of the loop antennas are strong in the near field [154] and ultimately support the antenna radiation. Therefore, they tend to be much more robust in terms of performance when they are placed in close proximity of or inside the human body. As a result, they can provide a lower SAR and higher radiation efficiency for head implants. Figure 5-15 shows the top view of the proposed antenna geometry when it is not folded. The resonator structure consists of a copper loop oval strip, size reduced oval ground plane and a pair of tuning strip oval lines. The antenna design concept is similar to the transmitter antenna design concept presented in chapter 2. Here, the oval shape is preferred to avoid vertexes (sharp edges) that may cause tissue injuries.

For loop antennas, several turns may be required to obtain the desired resonance at lower frequencies. On the other hand, increasing the number of turns in loop antenna increases the inductance and the loss resistance resulting in reduced efficiency. To overcome this issue, I have employed a pair of tuning strip lines to increase the electric current path length for lower resonant frequency and also support the folded loop. This technique is different from meandering technique which may lead to current cancelation in close branches results in poor resonant performance. Inserting tuning

strip lines also excites the second resonance, close enough to the first one for supporting a wider bandwidth performance. This escalates the bandwidth up to 200%.

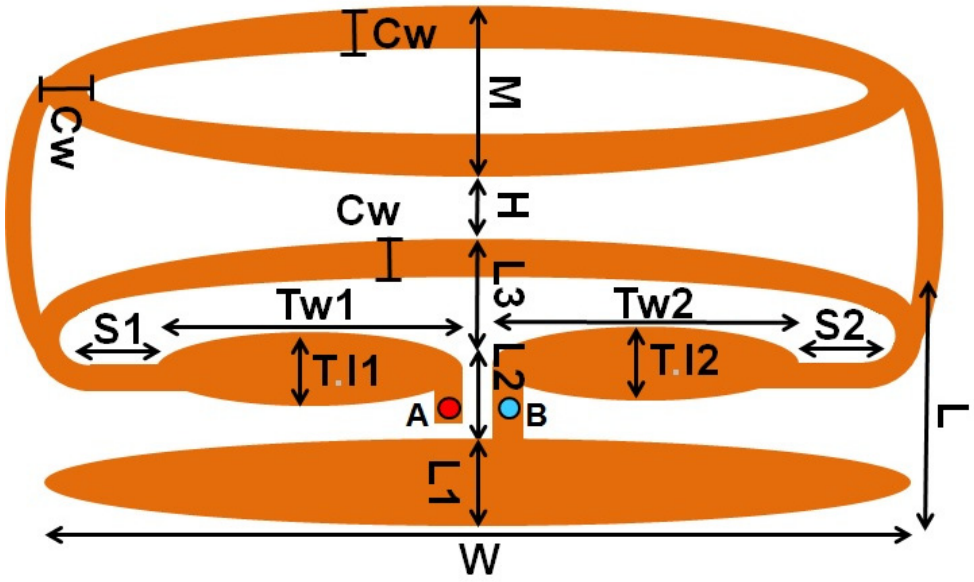

Figure 5-15. Wide band oval loop antenna geometry: Unfolded loop.

The presented radiator fulfils the head implant system requirements such as compact size, low profile and cost effective. The occupied area of the proposed loop antenna measures 22 mm × 12 mm which is a small size. To reduce the size of the antenna further, I have folded the loop as shown in Figure 5-16. To minimize the folding effects on the antenna performance, the tuning lines position has been adjusted. The presented folded oval loop now has a small volume of 324 mm^3, 20 mm × 6 mm × 2.7 mm, operates over the MICS band and has wide band performance. The proposed wideband folded oval loop antenna is small enough to be integrated with head implant devices for application such as brain wave sensing for the paralyzed, stroke rehabilitation, brain edema evolution monitoring, pressure monitoring, RFIDs and position tracking.

Figure 5-16. Wide band folded oval loop antenna geometry.

It is difficult to match the low impedance of the loop antennas to a 50-ohm coaxial line transmitter [33] since loop antennas generally are highly inductive component to their reactance and have low radiation resistance. Here, to solve this issue, a pair of oval matching elements is placed near the feeding port to match the impedance and broaden the impedance bandwidth of the radiator. Total length of the oval loop strip from A to B is about 57.5 mm, close to the half of the wavelength of the MICS band center frequency at 403 MHz inside the human body. The antenna is fed by a 50 ohm semi rigid coaxial cable. The center conductor of the cable launches the signal from the left-side strip terminal A at the feed point and the outer conductor of the cable is affixed to the right-side strip end B which terminates to the ground plane. The detailed parameters of the proposed Tx antenna are given in Table 5-7. The size and performance comparisons with similar types of antennas reported in the literature are tabulated in Table 5-8.

To mimic the antenna implantation into the scalp, the proposed loop antenna was immersed inside the complex human body mimicking phantom using HFSS

depicted in Figure 5-5. The Results on VSWR of Folded Oval Loop antenna is shown in Figure 5-17, which reveals that the antenna covers the MICS band fully and shows a wide band performance. The antenna has a VSWR of smaller than 2 from 360 MHz up to 1000 MHz. The folded version has a radiation efficiency of 0.95% inside the body which is 0.07% lower than the original version.

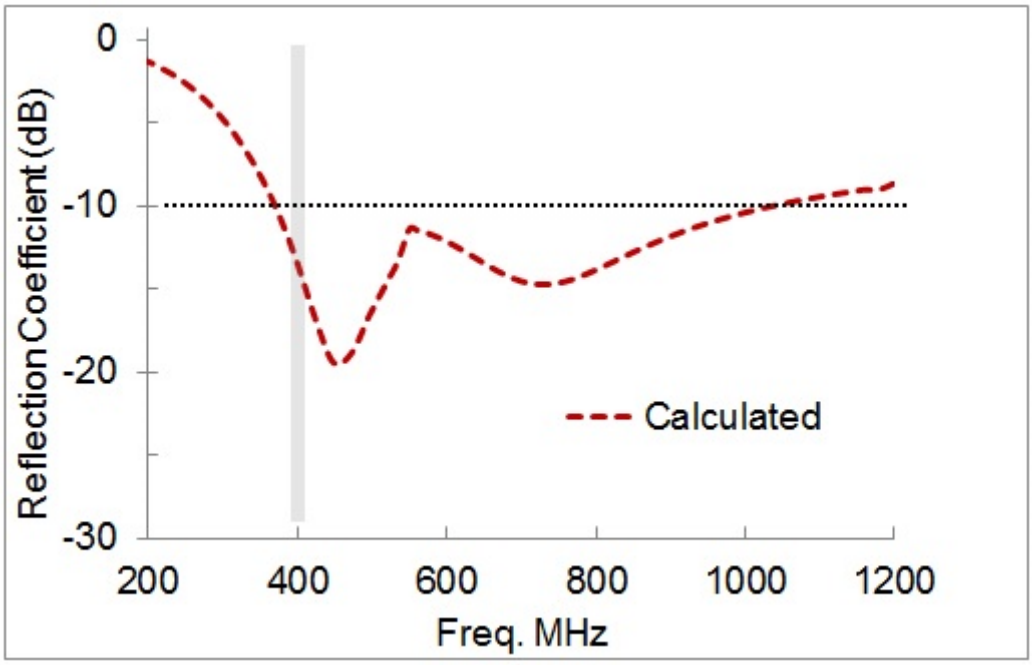

Figure 5-17. Calculated reflection coefficient of compact folded oval loop antenna.

TABLE 5-7
DETAILED DIMENSION OF THE PROPOSED FOLDED OVAL LOOP ANTENNA
(UNIT: MILLIMETERS)

Parameter	Value	Parameter	Value	Parameter	value
H	2.7	Tw1	7	L1	1.9
L	6	Tw2	7	L2	1
W	20	Tl1	1.7	L3	3.1
S1	2.5	Tl2	1.7	CW	0.33
S2	2.5	M	3.4		

The Surface current distribution for the proposed antenna at 403 MHz is shown in Figure 5-18. The main current is limited in the closed loop pattern and feed port area so that the current on the ground plane is small. This would be beneficial when the device implanted inside human body-head, the human body proximity effect may lead to the current variation and degrade the antenna performance. In this case the resonating currents are spread out over the system ground plane resulting poor radiation efficiency and shifting down the resonance frequencies. To avoid degrading antenna performance, the presented Folded Oval loop antenna is a good candidate for the head implant systems since the current induced on the ground plane is small.

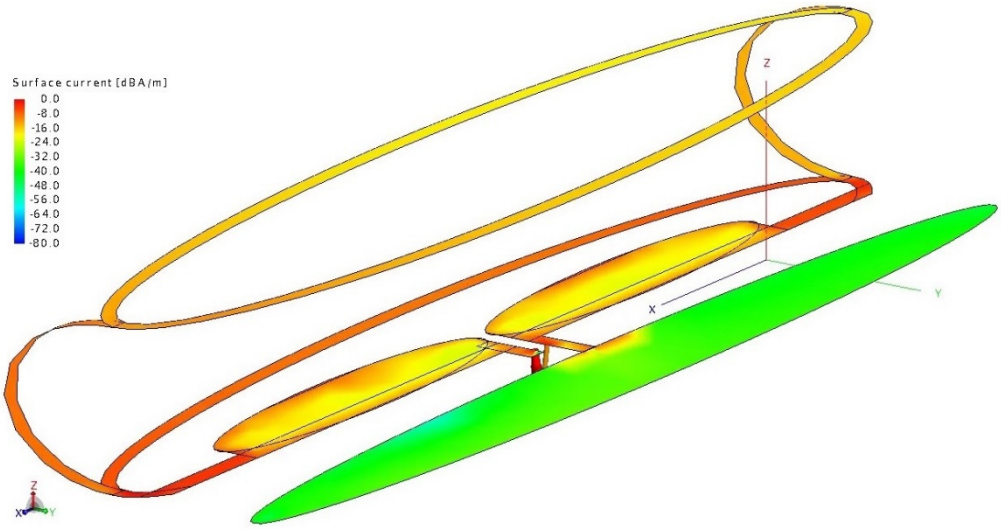

Figure 5-18. Surface current distribution for the folded co-planar loop antenna.

TABLE 5-8
SIZE AND PERFORMANCE COMPARISON OF THE PROPOSED TX ANTENNA

Antenna	Frq. Band	Type	Bandwidth	Vol. mm^3
[39]	400 MHz	Sigma-shaped monopole	68%	80
[38]	400 MHz	Monopole antenna	67.8%	560
[40]	400 MHz	Meandered dipole	37.8%	329
[41]	500 MHz	Spiral antenna	21%	392.5
This work Modified	400 MHz	Folded Oval Loop antenna	150%	324

5.7 Multi Band Single Slot PIFA

Using multiple band antennas may reduce the physical size of the multi-function systems since the system may not require more than one antenna. The presented Single Slot PIFA is capable of resonating at multiple standard telemetry bands and possible to implant it in different part of the human body such as scalp, arm, leg and chest. This section presents the design of a triple band implantable miniaturised SS-PIFA for Medical Implant Communication Service (MICS) band at 433MHz, Wireless Medical Telemetry Service (WMTS) band at 1430 MHz and Industrial, Scientific, and Medical (ISM) band at 2450 MHz. Employing triple band antenna enable the system to switch between different modes i.e., wireless charging, wakeup and sleep to save more energy and extend the overall lifespan of the device [49, 173].

The implanted antenna must fulfil miniaturization requirements and have a good radiation performance when it is implanted inside the human body [30-32]. The prototype of the π-shape stacked antenna with a volume of 254 mm^3 fabricated using Roger 3210 substrate reported in [34] operates over triple frequency bands covering ISM band at 2.45 GHz and MICS band at 402 MHz and 433 MHz. However, the measurement results do not agree fully with simulations. The implantable S-shaped quad-band PIFA is presented in [170] for to cover Mics, WMTS and ISM biotelemetry bands. The PIFA occupies a compact volume of 10 × 10 × 2.45 mm^3, however, its radiation efficiency is low (1.1% at ISM band, 0.9% at WMTS band and 1.2% at MICS band). The proposed triple band Single Slot PIFA has a good radiation efficiency over the biotelemetry bands and occupies a volume less than 1cm^3. The antenna structure miniaturized using a shorting pin and tunning the length of the slot, the overall radiator size is 50% smaller compared to the initial design. I will demonstrate the effectiveness

of employing shorting pin which is placed between the patch and the ground plane so that the antenna is compact in size and resonates over the three chosen bands. The antenna characteristics are verified employing equivalent experimental phantom, the measured results agree reasonably well with the calculated results on numerical multilayered phantoms.

5.7.1 Design of Multi Band Single Slot PIFA

The proposed antenna structure consists of a patch radiator, a dielectric substrate, a dielectric superstrate, a ground plane, a shorting pin and a feeding point. The top views of the antenna structure and the 3D view of it including superstrate are shown in Figure 5-19 and Figure 5-20 respectively. The antenna design procedure was carried out in three steps. First, a rectangular patch antenna was designed to operate over the second desired telemetry band, WMTS, when immersed in a homogeneous tissue mimicking numerical phantom. Second, a single slot added on radiator geometry and then a model of SS-PIFA with a shorting pin was tuned to operate over desire bands when implanted in a multi-layered tissue mimicking numerical phantom. At this stage, both shorting pin and feeding point must be placed on the right edge of the top patch to achieve the desire resonances. Later, a single layer dielectric thin superstrate was added to the implanted antenna model and the geometrical parameters were varied to obtain three resonances at the operating frequency band. The model of the antenna with the thin superstrate was then implanted inside a complex human body model for a precise simulation as shown in Figure 5-3a.

Here, the dimensions of the rectangular-shaped patch as well the radiating slot are the key parameters for antenna operation. Based on simulation results when the

slot is located close to the bottom edge and both of the feeding point and shorting pin are place on the right edge of the top patch the radiator shows an outstanding performance for implantable applications.

By fixing the antenna size and adjusting the relative positions of the feed and shorting pin, I can make the SS-PIFA resonate at all the three chosen frequency bands. Thus, the proposed antenna can be tuned to either multiple bands or a single frequency band. My investigations have revealed that, when the distance between shorting post from the feeding point is >λ/8, the resonance occurs in a single, but lower, frequency. When the shorting post is positioned at a distance of < λ/12 from the feeding point, three different resonant frequencies appear as tabulated in Table 5-9. This feature of the proposed antenna can be useful for applications where two or three different carrier frequencies are employed for implantable communications. Further size reduction has been obtained by employing a properly positioned shorting post so that the antenna resonates at the frequencies of interest when immersed inside phantoms. The locations of the shorting posts depend on the resonant modes and they can modify the impedance of the antenna by introducing inductive effects on input impedance [174].

To determine the antenna's input impedance match, I have obtained the appropriate feeding position by performing numerical experiments using numerical human tissue mimicking phantoms with FEKO^{TM} [133]. The finally designed slot PIFA has a volume of about 0.9 cm^3 when placed inside a numerical phantom and can operate over 433 MHZ MICS band as well as covering 1430MHz WMTS and 2450 MHz ISM bands simultaneously. The overall size of the proposed antenna is 19 × 30 × 1.6 mm, which is quite appropriate for implantable wireless system.

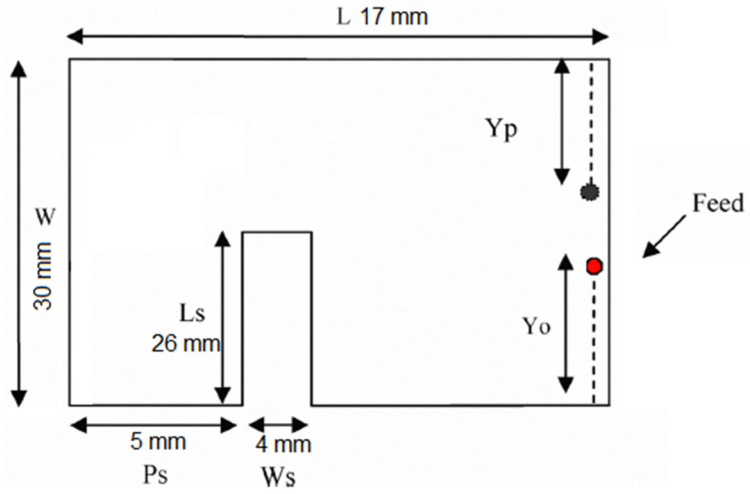

Figure 5-19. Top view of SS-PIFA geometry.

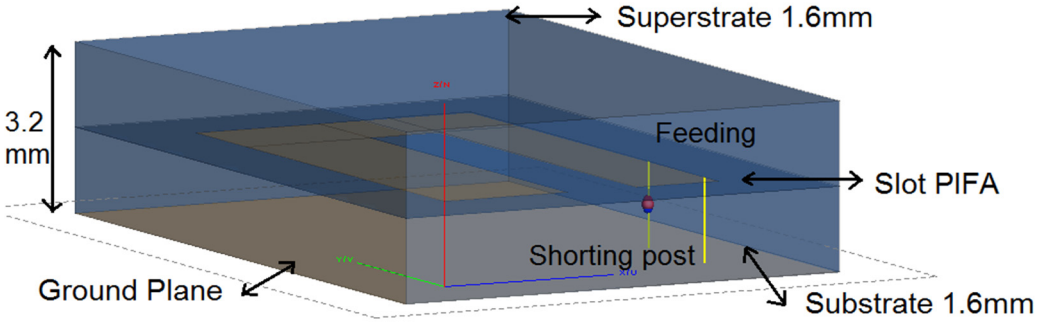

Figure 5-20. Triple band Single Slot PIFA structure.

TABLE 5-9
PROPOSED MULTI BAND SINGLE SLOT PIFA FEATURES

	Band 1.	Band 2.	Band 3.
Centre Frq.	433 MHz	1433 MHz	2450 MHz
Bandwidth	16 MHz	100 MHz	200 MHz
Efficiency calculated	1.6%	2.1%	2.6%
Gain calculated	-10 dBm	-11.5 dBm	-12 dBm

5.7.2 Antenna Performance and Numerical Phantom

Calculations based on homogeneous and inhomogeneous phantoms are employed to design the presented triple band antenna. For simulations, I have used block and cylindrical shaped numerical human tissue mimicking phantoms which employ multiple layers to model the human body effects. The layered rectangular block numerical phantom mimics the implantation under human chest as shown in Figure 5-5b in which the antenna is positioned 2 mm below the skin surface. It is placed in the fat under the skin, parallel to the boundary. The x-y plane cut of the calculation set up, showing the proposed antenna positioning inside the multi-layer spherical mimicking phantom, is illustrated in Figure 5-3b. This setup is similar when using layered block and cylindrical numerical phantoms. The thickness of the air gap layer and interstitial fluid are ideally assumed zero at this stage of the design. For calculations, I used the dielectric properties of skin, fat and muscle as tabulated in Table 5-1 [175]. Moreover, cylindrical shaped multi layered numerical phantom was used for mimicking the antenna implantation inside the human arm. In the cylindrical phantom, the average thickness of each layer is chosen to be 34 mm for muscle, 4 mm for fat and 2 mm for skin respectively. For the lower frequency bands such as 433 MHz the effective wave length is considered and the length of the phantoms is increased to 250 mm. Here, the numerical phantoms are designed using frequency dependent dielectric properties to represent human tissues closely at the required frequency bands.

The initial designs performed well inside the human tissue numerical phantom. Comparison of the results on reflection coefficient obtained in both cylindrical and layered block phantoms, shows that the antenna can resonate over the desired operating frequency bands and the agreement on resonant frequencies is close.

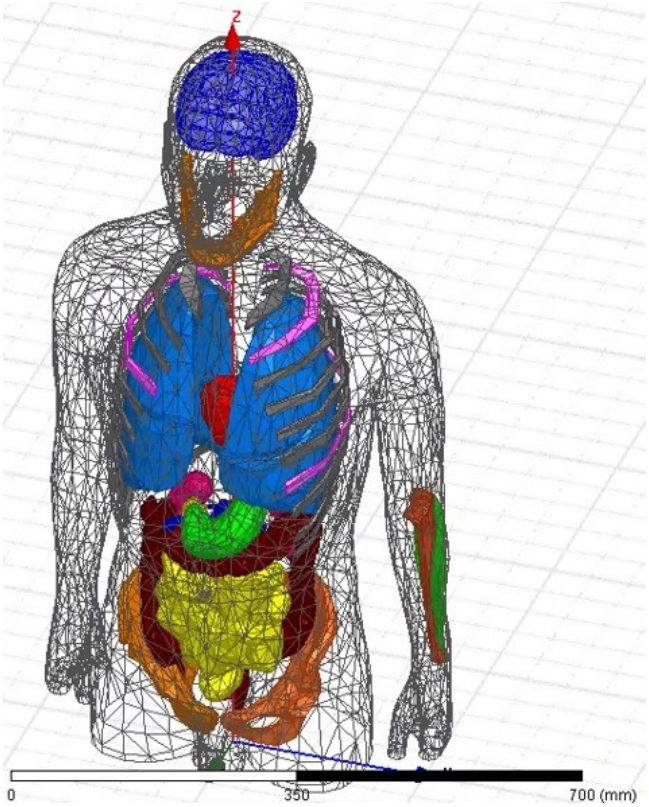

Figure 5-21. Complex human body model.

Later, a model of the antenna with the thin superstrate was then implanted inside a complex human body model for a precise simulation as shown in Figure 5-21. To mimic the antenna implantation inside the human body, the proposed triple band SS-PIFA was immersed inside an inhomogeneous multi layered complex human body phantom using HFSS [132]. The model is an adult male patient standing on its feet along z axis. It consists of over 300 body parts to represent bones, muscles, veins and organs, some of them are highlighted for a better understanding. It has an accuracy at the millimetre level and a frequency dependent material properties database is included. This model can provide accurate results, however, it is not memory and computational time intensive. Later, parametric analysis was carried out in order to quantify the effects of the different antenna geometric parameters and to empirically optimize its design.

Figure 5-22 shows the calculated surface current distribution with FEKO on the proposed slot PIFA. The plot in Figure 5-22a, shows that the path of current flow is in the same direction in both the arms which may be primarily responsible for exciting the fundamental resonant frequency that covers the MICS band. In Figure 5-22b, the current paths are opposite in each arm however, the current in one arm is stronger than the other exciting higher order mode, in this case, corresponds to the resonant frequency at WMTS band.

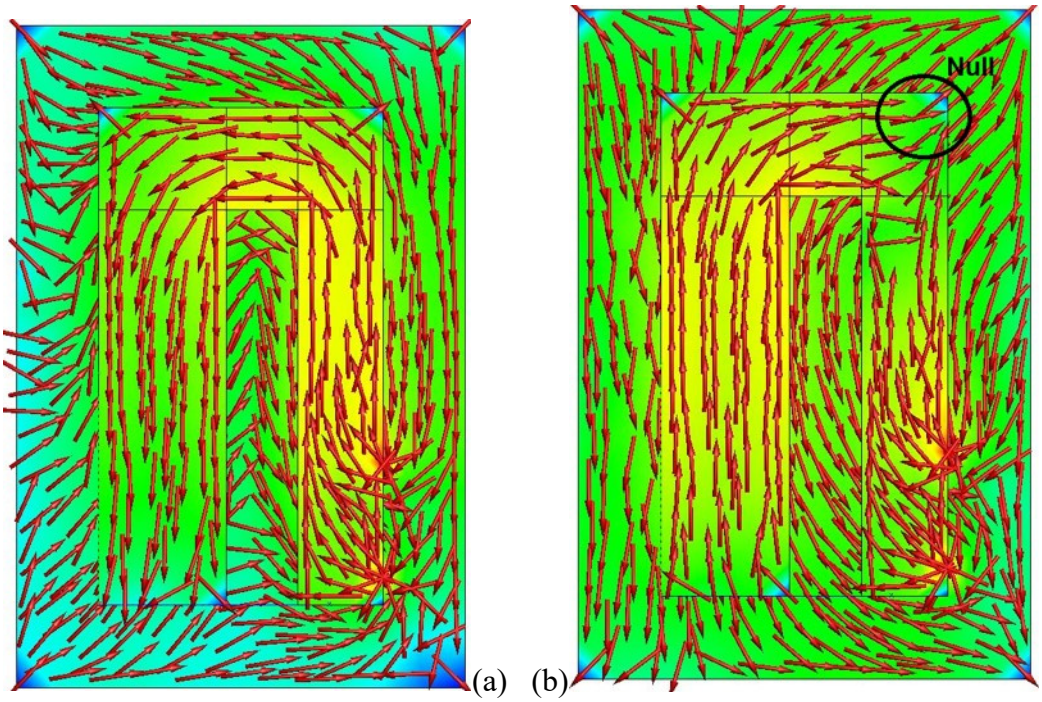

Figure 5-22. Surface current distribution of the proposed antenna at (a) MICS band and (b) WMTS band.

5.7.3 Experimental Results

The dielectric properties of any tissue mimicking experimental phantom must be similar to the realistic human body for obtaining reliable measurements to verify the performance of the implanted antenna. In the literature, pork leg [34] and skin gel

[30] were proposed as tissue mimicking phantoms for multiband operation. However, skin gel can only be used for one special single band and the relative permittivity and conductivities of pork leg [34] is higher than the normal human tissue. Therefore, to measure the performances of the antenna when implanted, I employed pork skin with fat as the experimental phantom. The size of the phantom is 350 × 350 × 5 mm which has provided reasonable measured results over all the three bands. The dielectric properties of the pork skin phantom are measured from 0.1 to 3 GHz by using dielectric assessment probe kit from SPEAG and Agilent E5071C network analyser. A good agreement with the desired dielectric properties [135] was observed between the experimental phantom and skin. It can be found that the permittivity of experimental phantom is closer to the human skin which is useful as the antenna placment is close to the skin layer.

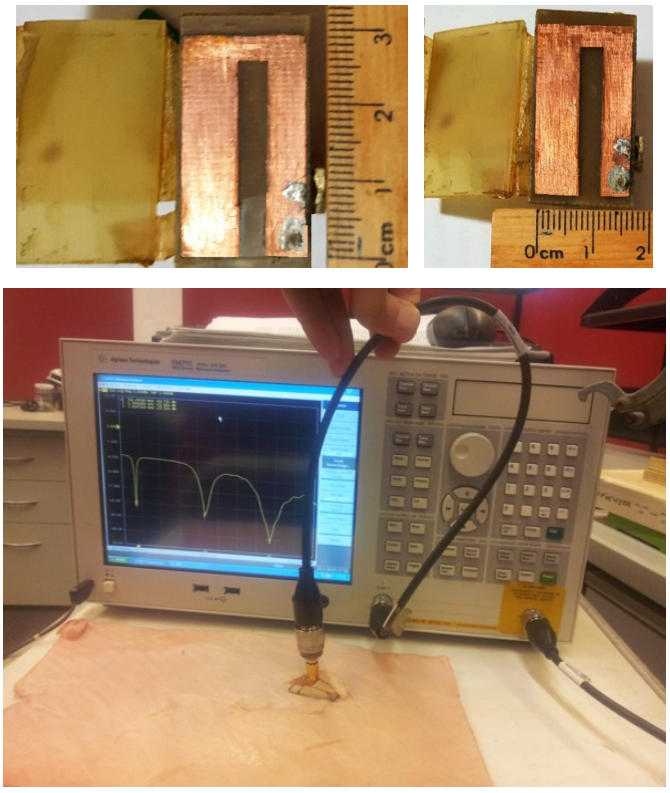

Figure 5-23. Triple band Single Slot PIFA prototype and Measurement set up.

The proposed multi band SS-PIFA fed by a coaxial probe is composed of a single metallic layer and is printed on one side of a FR4 substrate. The substrate thickness is 1.6 mm, and its dielectric constant is 4.7 and loss tangent of 0.0038. A dielectric superstrate having the same dielectric and thickness as that of the substrate is used to cover the antenna. Figure 5-23 shows measurement setup and the prototype of triple band Single Slot PIFA printed on FR4 substrate.

The simulated results on reflection coefficient for the proposed antenna when immersed inside both complex and multi-layered numerical phantoms are compared with the measured results when the antenna is immersed in the pork skin phantom and are shown in Figure 5-24 and Figure 5-25 respectively. From Figure 5-25, one can observe that the antenna has a reflection coefficient of -17dB at 433MHz and has an impedance bandwidth of 16 MHz which is adequate for implanted biomedical applications. In these figures, the measured data obtained using pork skin phantom compares reasonably well with results obtained using complex numerical phantom. The comparison of results shown in Figure 5-24 also demonstrates a good agreement between measured data with simulations on three-layered numerical phantoms. The shifts in center frequencies are attributable to fabrication tolerances, as well as due to possible reflections within multiple layers of the numerical phantoms.

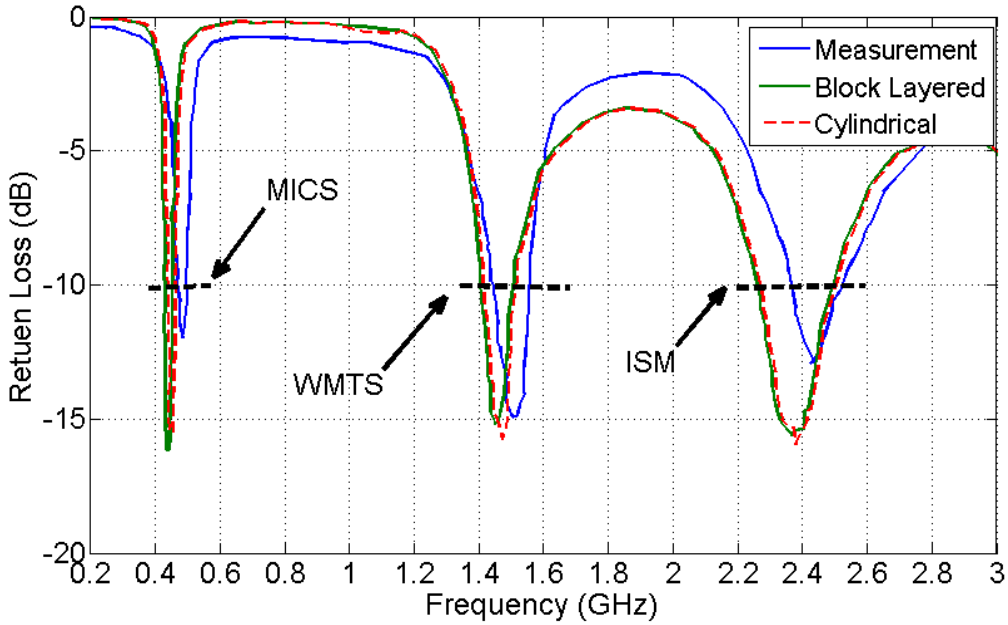

Figure 5-24. Reflection coefficient: Measured in pork skin vs. Simulation in layered block and cylindrical tissue phantoms.

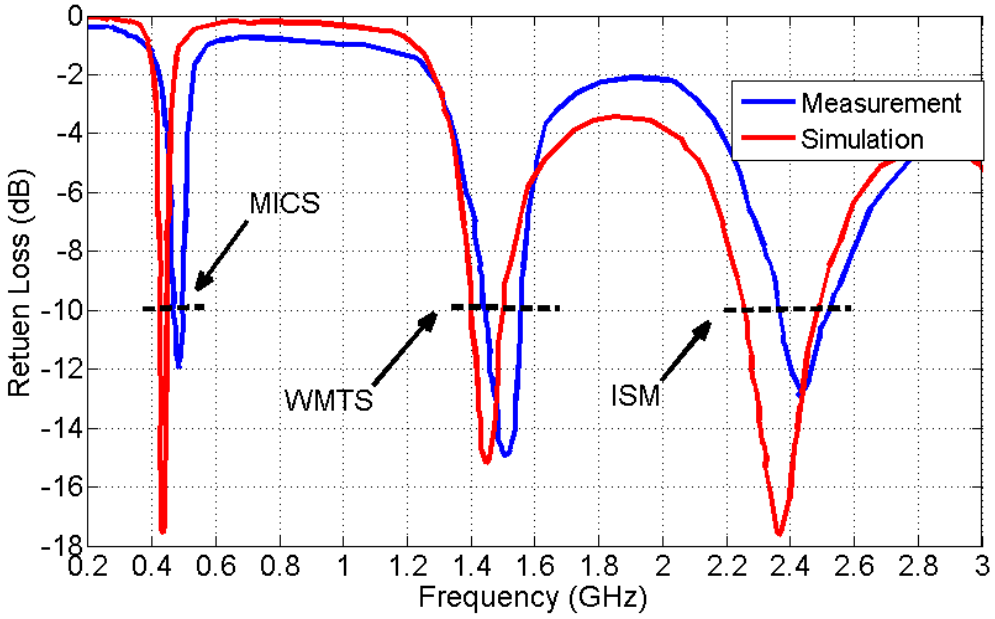

Figure 5-25. Reflection coefficient: Measured in pork skin vs. simulation using inhomogeneous tissue phantom.

5.8 Discussion

In this chapter, I have used a simple geometry to propose a class of miniaturized SS-PIFAs, suitable for scalp implantable devices, which can operate over a variety of standard biomedical frequency bands such as MICS band, Zigbee, WMTS band and ISM band. To miniaturize the antenna size, I have conducted detailed parametric study and investigated the effects of each geometrical parameter of the SS-PIFA on the resonant frequency. Further size reduction of 92% for antenna covering ISM band, 89% for antenna covering WMTS band, 86% for antenna covering ZigBee and 60% for antenna covering MICS band achieved by reducing the lengths of the slots and placing the feed and the pin at proper locations.

Proposed SS-PIFAs exhibits smaller size, good efficiency, standard SAR, and reasonable bandwidth suitable for biomedical head implant applications. For instance, the presented antenna resonating at 2450 MHz has 190 MHz measured bandwidth, good radiation efficiency of 1.8%, a compact size of 5×7 mm^2 and occupies a volume of 56 mm^3. I have also employed bio heat equations and optical fibre thermal sensors to establish an indirect method to carry out SAR measurement for implantable antennas and verify related SAR calculation.

This chapter also present a triple band Single Slot PIFA of size 19×30 mm for implantable biomedical applications. The antenna can cover three bands viz., ISM band (2450 MHz), WMTS band (1427–1432 MHz) and MICS band (433–434 MHz). The proposed implantable antenna exhibits low reflection coefficient, wide band impedance matching and has small size.

This Page Intentionally Left Blank.

CHAPTER – 06

6. NEAR FIELD FOCUSED BODY WORN ARRAY FOR NON-INVASIVE MICROWAVE HYPERTHEMIA

6.1 Introduction

Cancer is a leading cause of death in the western countries, preceded only by cardiovascular diseases. Hyperthermia is a type of cancer treatment, in which the tumor is exposed to elevated temperatures for an adequately long period. Hyperthermia makes the tumor more sensitive to the traditional chemotherapy and radiation therapies without any additional long term side effect. On the other hand, it also helps to reduce the cancer treatment side effects by reducing cytostatic drugs and radiation doses. Clinical studies have also shown doubled cure rates when combining hyperthermia with traditional cancer treatment.

The objective of hyperthermia treatment is to raise the temperature in the tumors to 42 - 44°C for one hour to kill cancerous cells or make them more sensitive to ionizing radiation or chemotherapy. There are three heating techniques for hyperthermia: electromagnetic heating (EM), thermal conduction and ultrasound. EM heating is, due to its versatility, the most developed technique as well as the most frequently used. The heat effect is developed in the target by the transmission of EM energy, using array of antenna, which is adjusted in frequency, time and strength in

order to work together to form a focus in the target. This places high demands on the precision of the system, the near filed focused body worn arrays can provide such a level of accuracy and concentrate the EM energy only on the target.

In this chapter, I present a planar antenna array for non-invasive microwave hyperthermia applications. The proposed near field focused (NFF) array covers ISM 2.45 GHz and consists of 25 miniaturized double slot PIFAs. The array is immersed inside a coupling bolus occupying a volume of 8.3 cm^3 (152 cm^3 including bolus). The proposed NFF array can focus on small target with a size of 10 × 10 mm and has an effective penetration depth up to 55 mm. I have also introduced size reduced NFF array to simplify the feeding network of the applicator and reduce the system cost, this array configuration satisfies system requirements and can focus on small targets.

6.2 Background Review and Motivation

Thermal therapy has mainly two types, Hyperthermia and Ablation [98, 99]. Hyperthermia is a form of cancer treatment involving exposing cancerous tissues to controlled high temperatures which may results in the destruction of cancer cells [100-102]. The hyperthermia can be considered as not only a treatment itself, but also a synergistic method with radiation oncology or chemotherapy [105, 176, 177]. Methods of hyperthermia treatment may differ according to different types of cancer growths. Treatment can be whole-body, regional or local hyperthermia, depending on the extent of the area being treated [103, 104]. Local body hyperthermia treatment may directly apply heat to a fairly small, specific area such as tumors to kill the local cancer cells [114].

Local hyperthermia systems use various heating methods and technologies including radio frequency and microwave, ultrasound waves and direct heat to body. Non-Invasive Local Microwave Hyperthermia (NI-LMH), which is my interest in this work, is a heat treatment serves to enhance the effectiveness of chemotherapy or radiation therapy and leads to gain remarkable results. In clinical trials an extension of doubling the tumors response rate is reported [118, 119, 178, 179] when NI-LMH employed along with these therapies. In biomedical engineering treatment, thermal therapy may be delivered either with moderate temperature between 43 to 45°C for 60 minutes in Hyperthermia system or with high temperature of 50°C for 5 minutes in thermal ablation. To achieve maximum therapeutic effect, the electromagnetic energy must be precisely delivered only onto the tumor volume [105] which is one of the main challenges in NI-LMH systems. By introducing near field focused array antennas [180] for biomedical applications, a new approach attracts lots of interest.

Near field focusing of electromagnetic waves has applications in microwave thermal therapy [106-109] such as microwave hyperthermia and imaging in biomedical systems [106, 107]. Here, the key idea is to generate an appropriate phase for the radiation sources on the antenna aperture (or feeding currents of the array elements) to obtain an in-phase summation of the aperture contributions at specified focal point [181]. The far field radiation region may be determined based on the dimensions of the array and the resonant frequency by $(2L^2/\lambda)$. However, most of the cancerous cells are located in the near field region of the antenna array, so that, an array of antenna performing near field focused radiation is necessary. Employing array of antenna generates a narrow beam radiation pattern for local hyperthermia application results in focusing in small prescribed regions.

Generally, EM antenna technology used for local hyperthermia systems are complex, have high cost and large size results in poor fitting to contoured patient anatomy. The current beam focused antennas categories in two types: 1) planar focused antennas and 2) nonplanar focused antennas. Planar focused antennas mostly include, leaky-wave antennas [182-184], patch array antennas [185, 186] and Fresnel zone antennas [187, 188], whereas, nonplanar focused antennas include reflector antennas [189], dielectric lens antennas [190], parabolic antennas and conical horns with a focalizing lens in front of the antenna aperture. The second category has improved focusing properties, however, they are expensive since more accurate fabrication technology is needed and very difficult to miniaturize them [108]. However, the planar array structure has small size and convenience for treatment and patients plus reasonable cost. These features along with being low profile and lightweight make this class of antennas a realistic option for the NFF array practical design in NI-LMH application.

A near field focused microstrip array for a radiometric temperature sensor introduced in [105], the array has 64 elements and small size, however, since the operating frequency is 12.5 GHz penetration depth is very short. Planer antenna arrays having a beam focused to a small spot in the near field region suitable for microwave industrial inspection presented in [191]. The X-band square arrays employed broadband U-slotted patch antennas with two focal distances of 300 mm and 126 mm. However, both array and its elements are bulky, heavy and occupies considerable volume. Lens antennas operating at the ka-band are used in the near-field region are presented [187]. Although a single antenna is used, however, the overall size is still large and the penetration depth is short.

In the literature, to cure non-deep seated tumors, non-invasive hyperthermia applicators are proposed for heating up the target and destroy it permanently [110-112], these tumors may be located inside the breast, head or neck [113-116]. To obtain superficial and deep focusing properties, non-invasive focused hyperthermia systems using complete ellipsoidal beam-formers are introduced in [117, 118]. Here, different operating frequencies used beside an arrangement of several dielectric matching layers. However, the introduced applicators are not suitable to heat up the deep-seated tumors magnificently.

To conduct the feasibility of employing arrays of multiple antennas to heat up the deeper regions in mimicking human body tissue models, various theoretical studies and laboratory measurements have been carried out [106, 111, 116, 192-195] using different methods such as operating over lower frequency bands which may increase penetration depth but has particular negative effects on system performance. Double discone antenna presented in [119] to deposit electromagnetic energy into the human body head, however, several hot regions observed in the phantom temperature measurements. Non-invasive time multiplexing RF beam-forming technique employed in [106] to heat up selective localized target in the human body numerical model. Here, an array of 134 small antennas positioned around the head and deionized water employed as coupling medium in contact with the head surface. However, for a practical approach, further simplification and optimization of the proposed setup is necessary.

For NI-LMH application one of the main challenges in NFF array design is maximizing the power deposition in a desired small target area and increasing the depth of focus. Recently, design criteria of near field focused antennas have been studied [108], and different methods have been presented in order to optimize

characteristics of these antennas such Levenberg–Marquardt algorithm [109]. However, focusing on small regions is still a challenge as the smallest focusing region reported in [137] is only 30 × 30 mm. Deposition of electromagnetic energy in smaller areas may result in destruction of even smaller tumors and enhance the effectiveness of the Microwave NI-LMH method.

Here, I aim to reduce the size of the focusing area by using optimized array element and higher operating frequency of 2.4 Ghz. However, the penetration depth may reduce when applicator resonate at higher frequencies. Since human body is lossy media to electromagnetic wave propagation [196], microwave hyperthermia systems, especially for the deep located tumors, radiate at lower frequencies such as 400 MHz and 915 MHz bands [106] which allow for higher penetration depth. However, due to the longer wavelength for lower frequencies, these systems have a larger size which is inappropriate to fit the patient anatomy and have a slight heating distinction of tumor location. Therefore, I aim to use higher frequency of 2.45 GHz to reduce the radiator size and have a precise focus on target while keep the penetration depth high enough to heat up the deep seated targets.

6.3 Antenna Design

The application of the NFF planar array applicator is limited only for superficial local hyperthermia due to the low penetration depth [107, 197] when operating over higher frequency bands. Therefore, a proper operating frequency must be chosen based on the treatment need and system requirement. In general, for NI-LMH systems, near field focused array antenna design faces six major challenges and considerations including:

- Ability to heat up both superficial and deep seated tumors
- Capability to focus on smaller regions
- Accurate focusing properties on target with minimum heating distinction of tumor location
- Having minimum number of undesirable hot regions to protect normal cells from generated artificial heat
- Limited number of radiators for having a smaller applicator
- Improved radiation efficiency

Satisfying all of these requirements may necessitate the need to introduce a superlative applicator design as some of these requirements are in contrast such as increasing penetration depth and decreasing applicator size or capability to focus on smaller regions. Therefore, considering a trade-off, based on the treatment essentials, would be inevitable.

In near field focused arrays a maximum of the radiated field may be attain at small area in the array near field region by implementing a proper phase adjustment worthwhile for compensation of the different distance between each source point on the antenna aperture and the focal point. Here, the size of the focused area of a near

field focused planar array depends on the elements arrangement and the array overall size, inter element distance, prescribed focal depth, operating frequency and phase profile at the antenna aperture. By increasing the number of properly excited radiating elements in the array arrangement, the electromagnetic waves can be focused in smaller region, however, focusing on smaller targets is still challenging since additional adverse hot spot may appear when they array arrangement is poor with extra mutual coupling between elements. To achieve a low side lobe level (SLL) characteristic the spacing between two neighboring antennas must be carefully designed to reduce the mutual coupling between array elements, however, this may increase the system size significantly. In 6.3.2 subsection, on the basis of both theoretical analysis and numerical trials, appropriate array arrangement and number of array elements (along with proper values for the above mention design parameters and considerations) have been investigated.

6.3.1 Calculation Environment

To mimic the applicator performance when placed close to the human body, the proposed array was immersed inside an inhomogeneous multi layered complex human body phantom using HFSS [132] as depicted in Figure 6-1. The model is an adult male patient standing on its feet along z axis. It consists of over 300 body parts to represent bones, muscles and organs. It has accuracy at the millimeter level and a frequency dependent material properties database is included. This model can provide accurate results however it is not memory and computational time intensive.

Therefore, for empirical optimization, I need to obtain results faster and hence a smaller numerical multi-layered block model was also employed as shown in Figure

6-2. The simplified numerical tissue model consists of a tumor region with a size of 20 × 20 × 10 mm and a three layered block human body tissue model involving skin, fat, and muscle. The size of the tumor can be varied from the minimum size of the 10 × 10 mm to maximum size of 30 × 30 mm. The dielectric properties of these layers [135] and tumor are tabulated in Table 6-1.

The equivalent phantom is composed with 2 mm of skin, 4 mm of fat, and 80 mm of as muscle. Based on my calculations, the diminutions provided for this numerical model is appropriate for higher frequency analysis such as 2450 MHz, however, the thickness provided for each of the layers are proper for all the frequency bands of interest. For the lower frequency bands such as 400 MHz the diminutions have to be increased carefully by considering the wave length.

The layered rectangular block phantom was used to mimic the RF energy exposure under the chest skin whereas a cylindrically shaped multi-layered phantom can be used to mimic the RF energy exposure inside the arm or leg. Here, the array of antenna was first embedded into the bolus, as shown in Figure 6-2, then the applicator performance calculated using FEKO^{TM} [133] while it is placed close by the skin and above the muscle layer. The bolus pack which is in contact with the skin surface acts as a coupling layer that helps impedance matching to the array and also protect the patient skin from being overheat by cooling effect. The coupling water based bolus pack which is filed with distilled water and silicone emulsion has similar dielectric properties to human body skin at 2.45 GHz. Later the complex human body has been employed to verify the applicator performance exposing RF energy into the human body different tissues such as head, neck and breast.

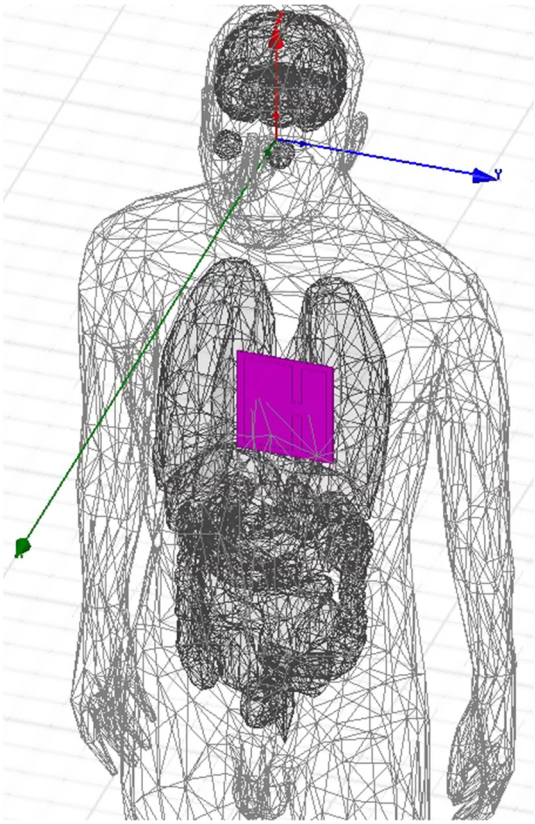

Figure 6-1: Simulation set up in numerical mimicking phantom: 3D complex human body model.

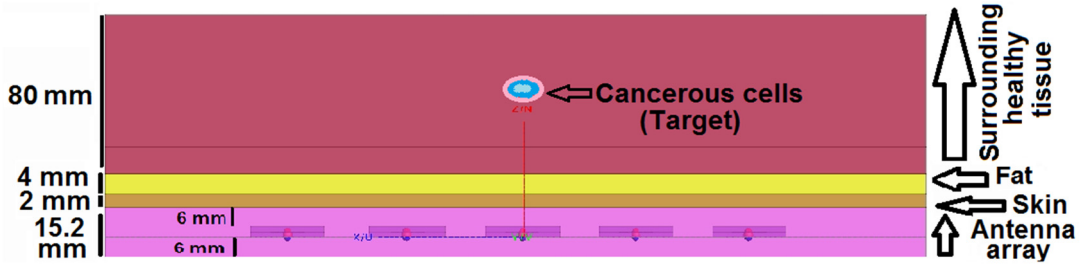

Figure 6-2. Calculation set up for the proposed array inside the bolus close by the multi-layer numerical phantom (side view).

TABLE 6-1
DIELECTRIC PROPERTIES OF HUMAN BODY

	Freq.	Muscle	Skin	Fat	Tumor	Bolus
Permittivity	2.45GHz	52.8	38.1	5.28	51.5	49.5
Conductivity s/m	2.45GHz	1.7	1.44	0.10	1.92	1.6

6.3.2 Specific Absorption Rate (SAR) and Bio-heat Transfer Equation

Electromagnetic field deposit energy into the human body when passing through and this will raise the tissue temperature of the human body. The temperature increment of human body by microwave can be defined from specific absorption rate (SAR) and the bio-heat transfer equation [137, 198]. The bio-heat transfer equation defines pace of the temperature elevation with SAR, blood perfusion, and thermal conductivity, simply, it represents the relationship between the rate of electromagnetic energy absorbed into the human body and the temperature incensement.

$$c\rho\frac{\partial T}{\partial t} = k\nabla^2 T - \rho\rho_b c_b F(T - T_b) + \rho SAR \tag{6.1}$$

where the T is the temperature (°C), tissue density is (ρ) (kg/m^3), t is the time (s), k is the thermal conductivity (W/m.K), c is the specific heat (J/kg.K), ρ_b is the density of the blood (kg/m^3), the F is the blood flow rate (m^3/kg.s), c_b is the specific heat of the blood (J/kg.K), and T_b is the temperature of the blood (°C).

The distribution of absorbed electromagnetic power in human tissue causes temperature elevation whereas blood perfusion and thermal conductivity diffuse the generated heat. The hyperthermia treatment system takes advantage of the different reactions between tumors and normal tissues. When hyperthermia system radiates, healthy tissues could handle the heat since blood circulation spreads the heat over the body to maintain homeostasis. However, the blood flow rate is low inside the tumors and there is no proper distribution of blood vessels to damp the artificial heat. As a result, when heat is continuously accumulated in human body, cancerous cells temperature will increase dramatically compared with healthy cells.

6.3.3 Array Configuration

The excellence and the success of NI-LMH treatment are extremely dependent on the capability to deposit power effectively and thus, to localize the temperature distribution in the tumor region without damaging the surrounding healthy tissues. Near field focused patch array antennas are one of the best options for hyperthermia systems since they can promise the low profile, light weight and low cost radiating arrays. The operation of focusing in these types of antennas is based on controlling the phases of the each element in order to sum in all the phases at focal distance [191, 199, 200]. To reach this goal, a proper phase shift should be applied to the elements in order to compensate the phase differences caused by the distance of each element from the focal point.

Transmission line theory can be used to design the feeding network, the amplitude distributions may be obtain using power dividers with tuned width for the feeding lines. The phase difference may be obtain in various ways. Here, by tuning the length of the feeding lines, (or coax cable connected to each radiating element) the phase distributions realized.

The speed of electromagnetic waves is different form the space when travelling through the coaxial cables, so that the wavelength is also different. The velocity factor (VF) that RF signals travel inside a coaxial cable can be determined by (as the proportion of speed of light):

$$VF = \frac{1}{c\sqrt{LC}} \tag{6.2}$$

where C and L are the distributed capacitance and inductance of the feeding cable (per meter) and the c is the speed of light. The length of the feeding cable to obtain the suitable phase shift for a specific radiating element can be calculated by:

$$C.L = \lambda_g \times \frac{\varphi}{360} \tag{6.3}$$

where $\lambda_g = \frac{VF \times c}{f} = VF \times \lambda$,

λ_g is wavelength in the cable, φ is the required phase shift and f is the operating frequency. When the characteristic impedance (Z_0) and capacitance of the coaxial cable are provided by the manufacturer, V.F can be calculated using:

$$VF = \frac{1}{c \,.\, Z_0} \tag{6.4}$$

where $Z_0 = \sqrt{\frac{L}{C}}$

To study how the array size and its configuration may affect the focusing properties of near field focused arrays for hyperthermia application, I have presented various NFF arrays including four elements NFF linear arrays, sixteen elements NFF circular arrays and two NFF square arrays with size of 4 × 4 and 5 × 5 elements

operating at 2.45 GHz. The performance of these array have been investigated when immersed inside the coupling bolus and placed close by the numerical human body model as shown in Figure 6-2. Here, I assumed a small tumor with a size of 10 × 10 mm located at depth of 50 mm inside the human body that must be heated to kill all the cancerous cells.

I have designed a four element linear array in the rectangular coordinate system located on x axes. The number of elements in this array, separated by distance *d*, are fairly limited so that the overall size of the applicator would be small and the system cost including the feeding network would be less. However, the directivity of this array may not be high enough to focus on small area, therefore, its radiation performance must be evaluated.

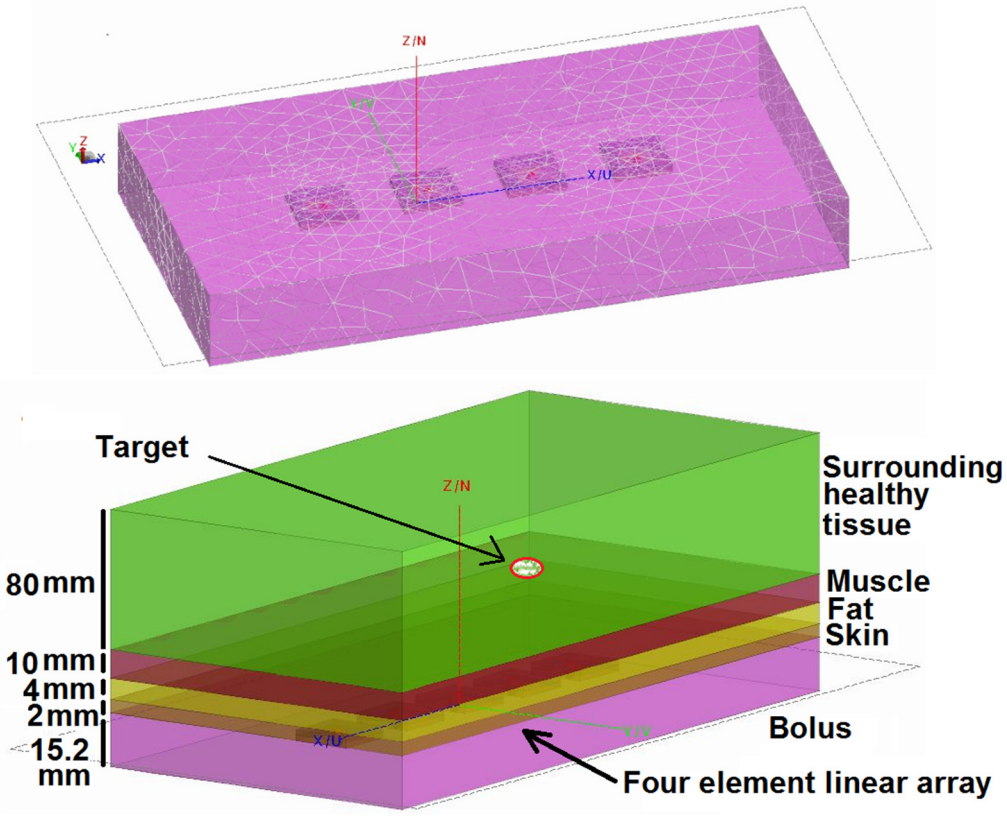

Figure 6-3: a) The presented linear array immersed inside the coupling bolus. b) The applicator package close by the multi-layer block human tissue mimicking phantom.

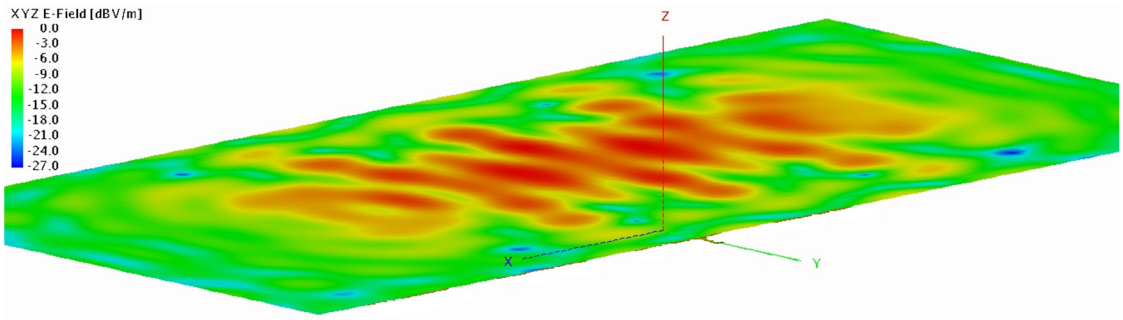

Figure 6-4. E-field distribution of linear array at depth of 5 cm.

The presented linear array has a length of 50 mm ($3\lambda_g$) and immersed inside the coupling bolus as shown in Figure 6-3a. The whole package is placed close by the multi-layer block human tissue mimicking phantom, shown in Figure 6-3b, to focus on the target area. My calculation results, shown in Figure 6-4, reveals that the linear array could not focus on the target effectively, the focusing area is large with a non-geometric shape and not easy to reduce its size.

To overcome this issue, a circular array with a sixteen elements has been designed. The circular array has a radius of 72 mm, located in the x, y plane, and immersed inside the bolus where the elements are distributed equidistantly. The circular array configuration is shown in Figure 6-5 and the angular position of n^{th} element (n = 1, 2, 3, …) can be obtain using $\varphi = 2\pi n/N$ respect to x axes. The simulation results, using multi-layer block human tissue phantom, indicate that circular array could not focus on the tumor precisely at depth of 50 mm as shown in Figure 6-6. It generates Multiple hot spot region with oval shape which are not useful for my presumed scenario. Consequently, I employed the square configuration to investigate its performance when using a similar and same number of radiating elements.

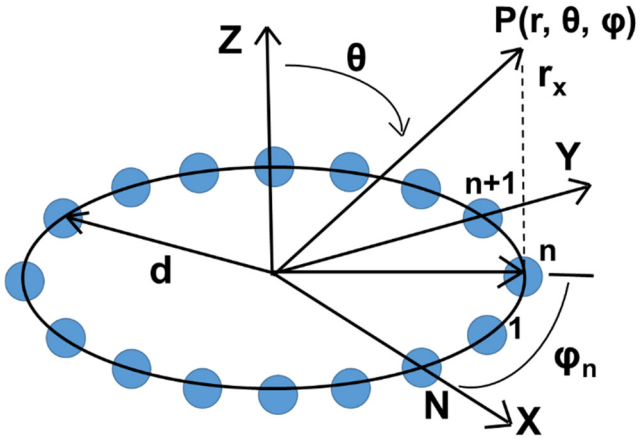

Figure 6-5. Circular array configuration.

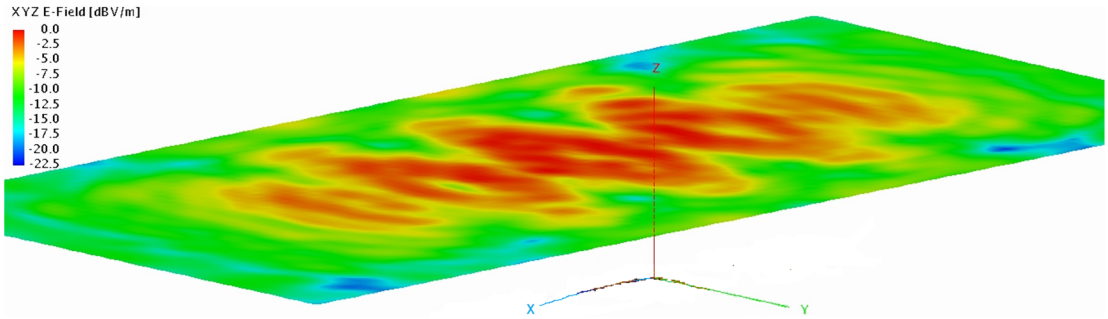

Figure 6-6. E-field distribution of circular array at depth of 5 cm.

Figure 6-7 shows a typical geometry of planar square arrays in the rectangular coordinate system located in the x, y plane. The square array involves N × N active antennas on a rectangular grid. The electric field radiated at the observation point P(x, y, z) by the N × N array can be expressed as [108]:

$$E(p) = \sum_{m=-\frac{N}{2}}^{\frac{N}{2}-1} \sum_{n=-\frac{N}{2}}^{\frac{N}{2}-1} I_{mn} E_{mn}(P) \tag{6.5}$$

where I_{mn} and E_{mn} (P) are the feeding current and the radiated field corresponding to the (m, n)th element of the array, respectively. The (m, n)th element

is located at the point of coordinates (x_m, y_n, 0) with an inter-element distance (d) along both axes, where $x_m = 2(m+1)\, d/2$, $y_n = 2\,(n+1)\, d/2$, the length and width of the array is $L = Nd$. The focal point of my interest is located at F = (0, 0, r_0 (in this case r_0 = 5mm)), along the normal to the array plane. Here, the feeding current amplitude for each active element has been set equal to I_0 (since focal point is located on z axis) and its phase, ϕ_{mn}, can be obtain using:

$$\phi_{mn} = \frac{2\pi}{\lambda}\left[\sqrt{x_m^2 + y_n^2 + r_0^2} - r_0\right] \tag{6.6}$$

to facilitate all the element contributions add in phase at the focal point. It should be noticed that the length differences for setting phases depend on the surrounding environment and the substrate guided wavelength at operating frequency. Here, the radiating array immersed inside the coupling bolus and the elements are printed on the FR4 substrate. The dielectric properties of bolus are tabulated in Table 6-1 and the FR4 substrate has the dielectric permittivity of 4.4 at 2.45 GHz, hence, the calculated λ_{eff} is equal to 16 mm.

To investigate the square configuration performance, a 4 × 4 square array has been designed with the similar and same number of radiating elements used in the circular array. The initial spacing between the radiators set to $\lambda_{eff}/2$ and the required phase shift obtained using (6.2) for the focal depth of 5 cm. The new NFF square array is able to focus on single and smaller area compare to the sixteen elements NFF circular array as shown in Figure 6-8. To study how the size of the square array may affect its near field focusing characteristics, a 5 × 5 square array has been designed.

Here, the proposed array geometry consists of 25 miniaturized microstrip patch antenna resonating at 2.45 GHz. The desired focal area has a depth of 5 cm from the skin surface and has a size of 10 × 10 mm. The initial spacing between elements of antenna array was set to $\lambda_{eff}/2$, the feeding current amplitude has been set equally for each element since the target assumed to be located on the z axis parallel to x-y plane. The initial value of phases for the array feeding network obtained using (6.2) while r_0 value set to 5 cm. Here, empirical studies have been conducted for optimizing the phases' value to adjust the desire depth and focus on single small target area. To reduce the number of side lobes (additional hot spots) mutual coupling has to be minimum. To determine the optimum distance and reduce the mutual coupling effect, I obtain the appropriate seating position by performing systematic numerical experiments with FEKO^{TM} [133] while initially employing block-layered numerical tissue model. Furthermore, to compensate the influence of bolus on array performance and focal point accuracy, the effect of dielectric properties of bolus on effective wavelength has been considered for optimization.

Compared to the 4 × 4 square array, with same focal depth, the 5 × 5 array has improved the focusing characteristic significantly (the array performance discussed in details in section 6.4). I concluded that as the number of antennas increases, more radiated energy may focus to central area of the maximum field intensity plane (this improves the ability to focus on much smaller areas). The x-y plane cut of the calculation set up, showing the proposed array configuration inside the bolus, is also illustrated in Figure 6-9. The finally designed array of antenna has a size of 72 × 72 mm when placed inside a coupling bolus and operates over 2450 MHz. The overall size of the bolus pack is 10 × 10 × 1.52 cm which is quite appropriate for EM antenna hyperthermia systems.

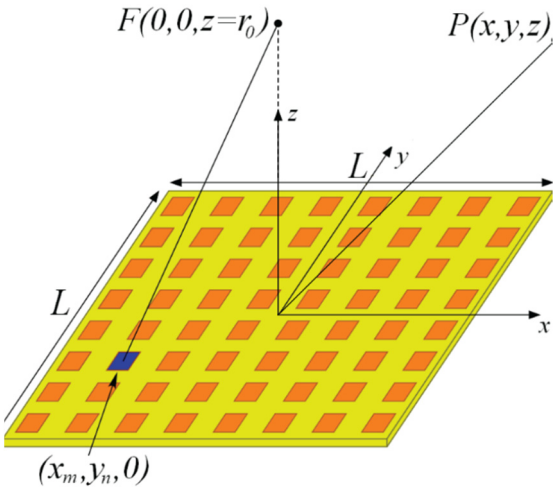

Figure 6-7. A three-dimensional view of the planar square array geometry [108].

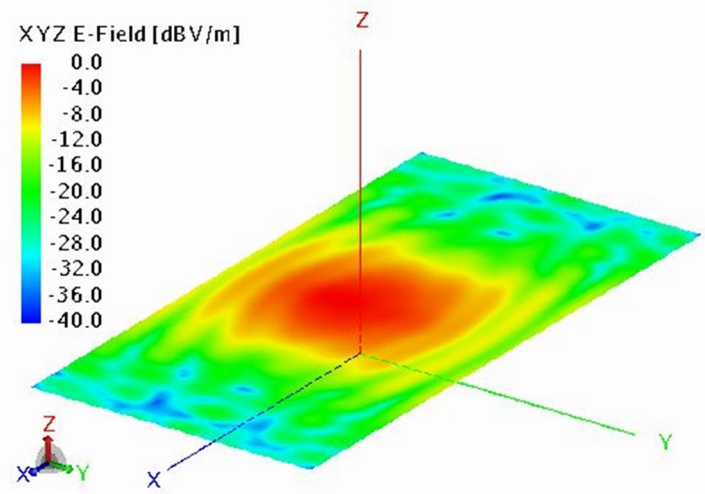

Figure 6-8. E-field distribution of array at depth of 5 cm.

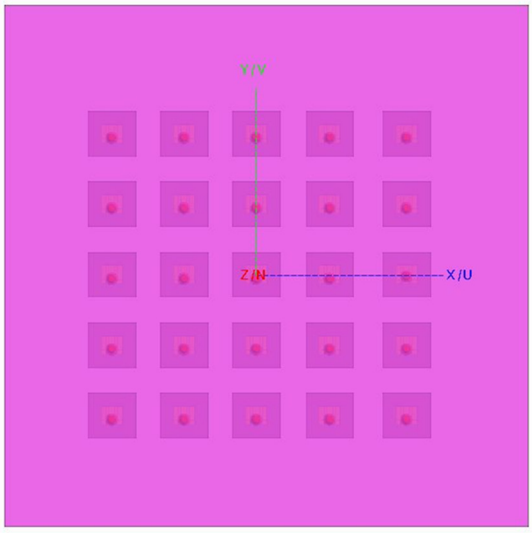

Figure 6-9. Configuration of the proposed array of antenna array inside the bolus (top view).

6.3.4 Technics to Optimize Focusing

Near field focused array of antennas can be employed to focus the electromagnetic energy into the desired spot in the radiating near field (Fresnel) region [105, 108, 187, 191]. However, for medical applications such as noninvasive microwave hyperthermia, it is desired to maximize the energy deposition at a prescribed spot precisely and heat up the unhealthy biological tissue [107, 201]. To achieve this goal and reduce the number of undesired hot spots (minimizing side lobs) an appropriate optimization method is needed to enhance the amplitude and phase of the array feeding network [202, 203].

Consider a hyperthermia system consists of an applicator with N elements radiating array and a receiver antenna. The receiving antenna is for measurement propose only and it is separated by a distance of D from the transmitting array as shown in Figure 6-10. The receiving antenna is placed in the desired position in which radiations need to be maximized. This system, as illustrated in Figure 6-10, forms an N+1 ports network that can be characterized by the scattering matrix as follows [204]:

$$\begin{bmatrix} [j_t] \\ [j_r] \end{bmatrix} = \begin{bmatrix} [S_{tt}] & [S_{tr}] \\ [S_{rt}] & [S_{rr}] \end{bmatrix} \begin{bmatrix} [i_t] \\ [i_r] \end{bmatrix} \tag{6.7}$$

Where

$[i_t] = [i_1, \quad i_2, \quad \dots, \quad i_N]^T$

$[i_r] = [i_{n+1}]$

$[j_t] = [j_1, \quad j_2, \quad \dots, \quad j_N]^T$

$[j_r] = [j_{n+1}]$

are the normalized incident and reflected waves. The subscript "t" denotes the transmitting antenna array; and the subscript "r" represents the receiving antenna. The power transmission efficiency, η, between the antenna array and the receiving antenna is defined as the ratio of the power delivered to the load of the receiving antenna to the input power to the antenna array and can be expressed as:

$$\eta = \frac{|[j_r]|^2 - |[i_r]|^2}{|[i_t]|^2 - |[j_t]|^2} \tag{6.8}$$

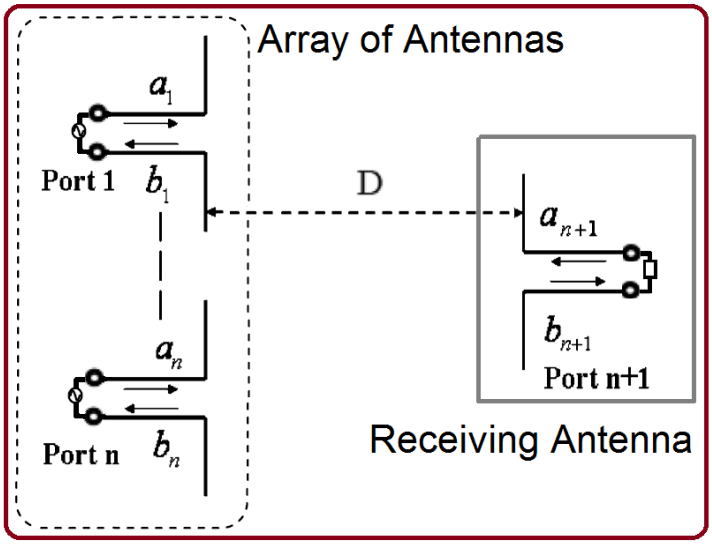

Figure 6-10. Antenna array and receiving antenna separated by distance D.

I have expected the receiving antenna to be matched to maximize the η, so that $[i_r] = 0$. Using (6.3) and (6.4), the maximum power transmission efficiency between the receiving antenna and the radiating array can satisfy the following eigenvalue equation [205]:

$$[K][i_t] = \eta\,[L][i_t] \tag{6.9}$$

Where

$$[K] = [S_{rt}^*]^T [S_{rt}] \tag{6.10}$$

$$[L] = 1 - [S_{tt}^*] [S_{tt}] \tag{6.11}$$

The equation (6.9) may reduce when the entire array of antenna is matched,

$$[K][i_t] = \eta [i_t] \tag{6.12}$$

The largest eigenvalue of equation (6.12) gives the maximum possible value of power transmission efficiency which can be obtain numerically. For the array feeding network, the corresponding eigenvector [a_t] is the optimal distribution of excitation at the antenna array ports. Here, while deriving (6.9) and (6.12), the antenna types and surrounding media are presumed to be arbitrary so that this optimization method can be apply to any arbitrary array of antennas. Since there is only one receiving antenna, equation (6.12) yields only one positive eigenvalue and the rest are zero as the rank of the matrix [k] is one. Hence, the unique non-zero eigenvalue of equation (6.12) provides the maximum power transmission efficiency between the receiving antenna and the antenna array. The corresponding eigenvector gives the optimal excitation for the transmitter antenna array in the sense that the transmitted electromagnetic energy is maximized towards the receiving antenna. To minimize the transmitted electromagnetic energy in the direction of the receiving antenna and generate a null in the desired direction, the eigenvectors corresponding to the zero eigenvalues of equation (6.12) can be used as the optimal excitation distributions for the array of the

antennas. I employ this optimization procedure to optimize the proposed array of Dual Slot PIFAs for NI-LMH system.

6.3.4.1 Feeding Optimization

Here, the goal of the optimization is set to maximize the η, power transmission efficiency, between the receiving antenna and the transmitting array. The optimization procedure for the proposed array antenna can be summarized in three steps as follow:

1) Calculate the scattering parameters of the system involving the receiving antenna and the transmitting array.

2) To achieve the optimum amplitude and phase distribution for the radiating elements the eigenvalue equation (6.12) has to be solved.

3) The optimum amplitude and phase distribution can be used to modify the antenna array feeding network.

The receiving antenna is the same as the element employed to form the active array and the distance, D, is assumed to be 50 mm, the receiving antenna is thus placed at (r, θ, φ) = (50mm, 0, 0). To obtain the scattering matrix for the proposed array configuration the whole system without feeding network was simulated employing the computer aided design (CAD) tools, such as Feko and HFSS. To calculate the scattering parameters, all of the ports are terminated to 50Ω load except one of the ports which is active and connected to the signal source. This will generates the scattering matrix of the whole system.

The optimal excitation distribution for the array elements as well as the maximum power transmission efficiency for the system can be obtained from (6.8) using the computed scattering parameters. For the proposed 5 × 5 rectangular

configuration, the maximum power transmission efficiency between (the only nonzero eigenvalue) is found to be 3.2%. The corresponding optimized distribution of excitations (phase and amplitude), [i_t], are tabulated in Table 6.2.

Here, by varying the location of the receiving antenna, in the Fresnel region of the proposed array, the focal distance could be adjusted. Also, the surrounding environment and the mutual coupling between the array elements have already taken into account when generating and exporting the scattering parameters from the CAD tools. Finally, power dividers with different choices of width for the feeding lines (alternatively use power attenuators) can realize the array elements amplitude. The phase distributions also can be generate by adjusting the length of the feeding lines. The radiating element employed for the proposed NFF arrays, is presented in section 6.3.5 of this chapter.

TABLE 6-2
OPTIMIZED PHASE AND AMPLITUDE DISTRIBUTION OF THE DUAL SLOT PIFA ARRAY

	Colum 1	Colum 2	Colum 3	Colum 4	Colum 5
Row 1	$0.21 \angle -140°$	$0.21 \angle -80°$	$0.20 \angle -60°$	$0.19 \angle -80°$	$0.19 \angle -150°$
Row 2	$0.21 \angle -110°$	$0.21 \angle -60°$	$0.20 \angle -30°$	$0.19 \angle -60°$	$0.19 \angle -100°$
Row 3	$0.20 \angle -80°$	$0.24 \angle -30°$	$0.25 \angle 0°$	$0.24 \angle -30°$	$0.20 \angle -80°$
Row 4	$0.18 \angle -100°$	$0.18 \angle -60°$	$0.20 \angle -30°$	$0.22 \angle -60°$	$0.22 \angle -110°$
Row 5	$0.18 \angle -150°$	$0.18 \angle -80°$	$0.20 \angle -60°$	$0.22 \angle -80°$	$0.22 \angle -140°$

6.3.5 Array Element Design

The Dual Slot PIFA proposed in Chapter 3 has suitable characteristics to be employed as the applicator array element. It has a volume of 0.5 cm^3 when immersed inside the coupling bolus and operates over 2.45 GHz. The antenna has a small size with dimensions of 19 × 17 × 1.6 mm [196]. However, employing twenty five of Dual Slot PIFAs with proper spacing between them, will increase the size of the proposed applicator. Reducing the size of the array element while maintaining its specifications the same, will help to reduce the size of the applicator and enhance its performance. Therefore, I have redesigned and adjusted the antenna geometry with the aim of further miniaturization. Moreover, the protective layer, superstrate, should be removed from the top of the antenna since the package is not implantable inside the human boy. To compensate the effect of removing the protection layer, the antenna size and its geometry parameters need to be adjusted.

Here, I have optimized and miniaturized the Dual Slot PIFA in three steps. First, a model of the antenna with a shorting pin, as shown in Figure 6-11, placed close by the human body numerical phantom and the geometrical parameters of the antenna were varied to obtain resonance at the ISM, 2.45 GHz, band. Second, the antenna immersed inside the bolus equivalent numerical phantom and the antenna structure size adjusted, following the generalized procedure shown in Figure 3-2, to operate over the operating band. Third, empirical parametric studies employed to investigate the effect of the antenna geometry parameters on resonant frequency and patch size reduction. Here, the applicator was placed close by the complex human body model for a precise simulation as shown in Figure 6-1.

I have conducted detailed parametric study to investigate the effects of each geometrical parameter of the Dual Slot PIFA on the resonant frequency with an aim to further size reduction. To achieve this I followed the generalized procedure as shown in Figure 6-12 and could reduce antenna physical size significantly. Here, the effects of the feed and shorting pin positions, width and lengths of the slots while fixing other antenna parameters were also investigated. My studies have indicated that by reducing the slot lengths while at the same time placing the feed and shorting pin at appropriate locations, one could reduce the size of the antenna without affecting the resonance at 2450 MHz. The new antenna size is 8 × 7.7 × 1.6 mm (92 mm^3) and compared to the pervious design with volume of 516 mm^3 in [196] occupies 5.5 times smaller volume. So that the overall size of the 25 element array could be reduced significantly by employing the miniaturized Dual slot PIFA.

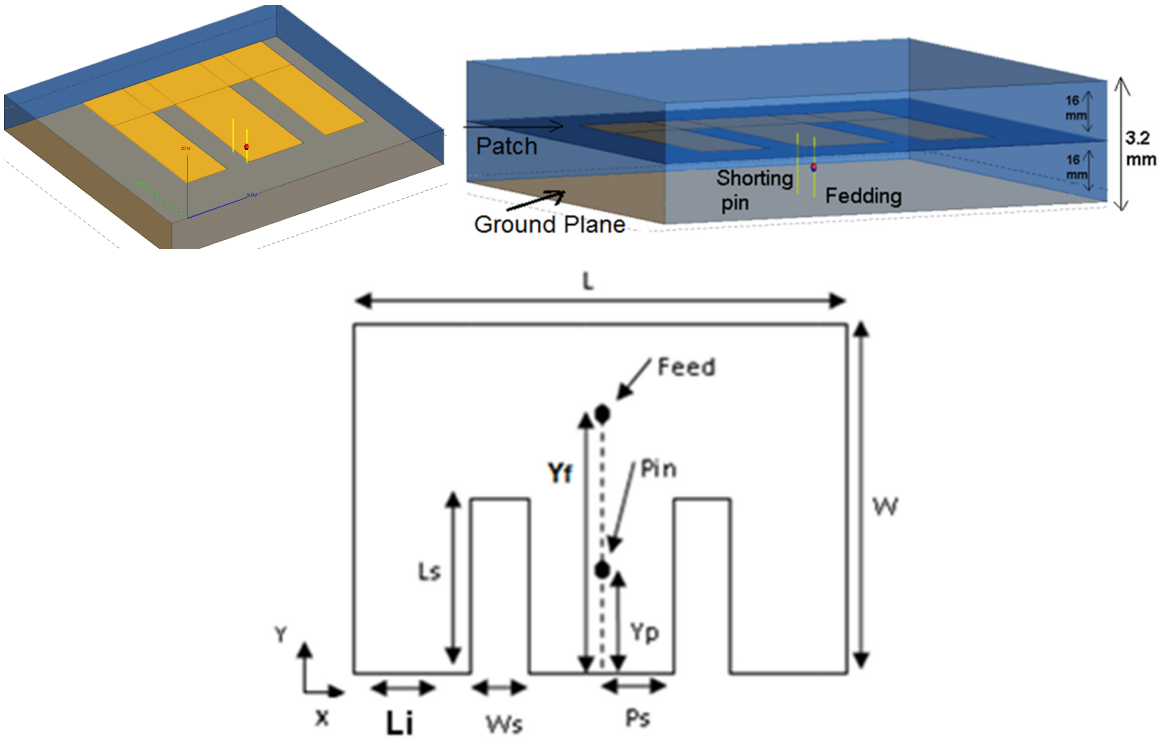

Figure 6-11. Geometry of Dual Slot PIFA.

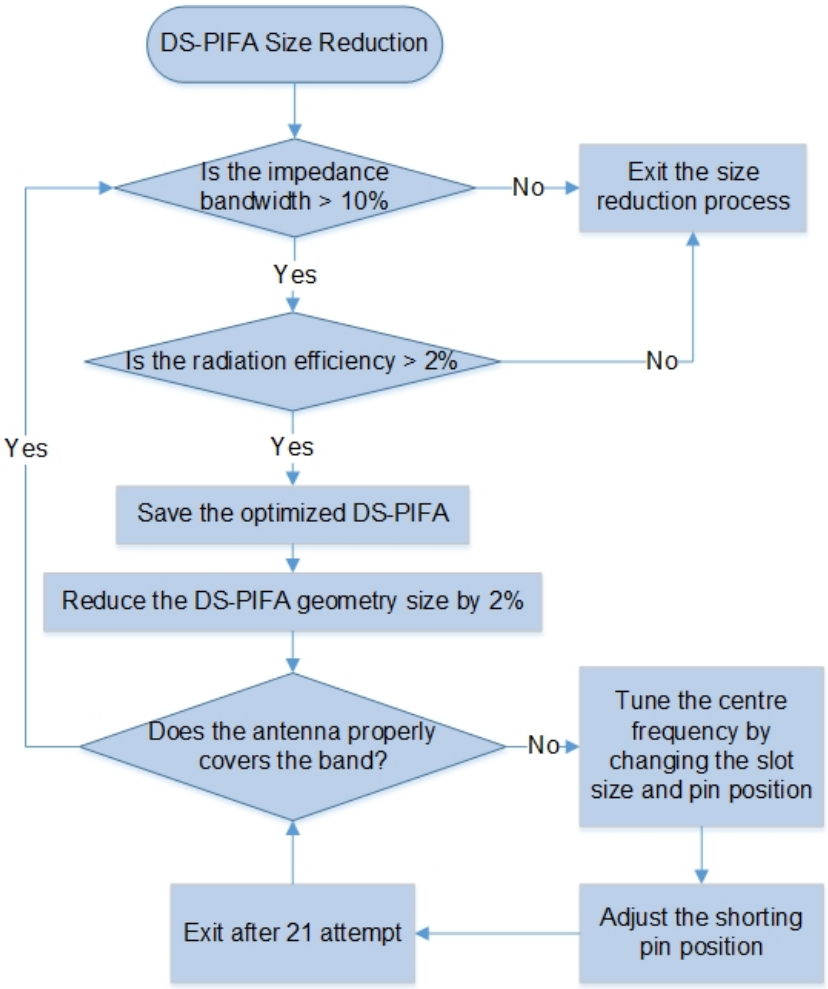

Figure 6-12. The DS-PIFAs size reduction flowchart.

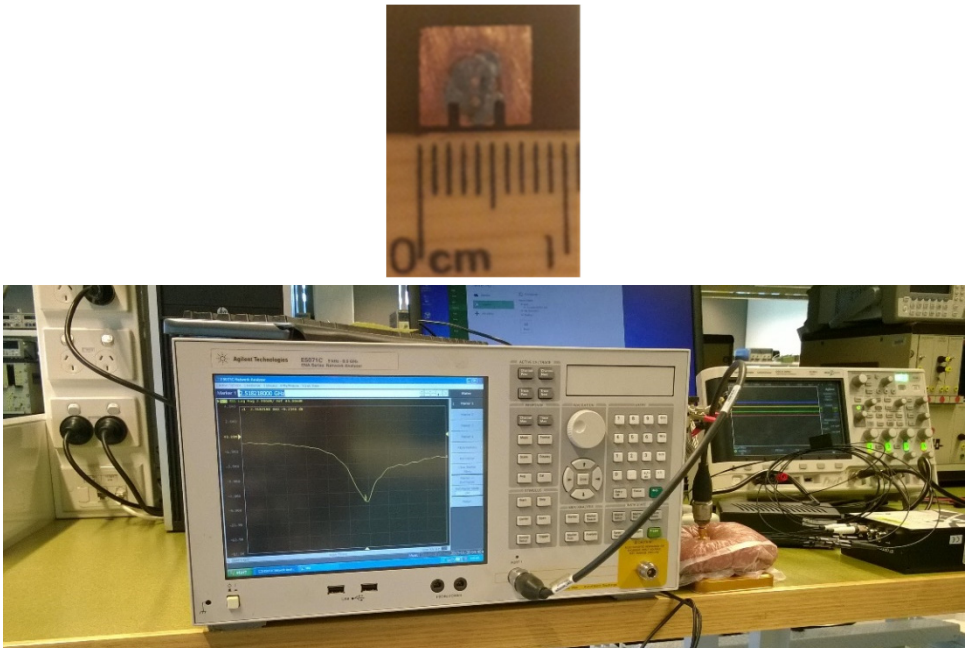

Figure 6-13. Printed Dual Slot PIFA on FR4 substrate and measurement setup.

Figure 6-13 shows the antenna prototype printed on a FR4 substrate and the measurement setup. The measurement set up for the single antenna prototype is the same as the one that I used in section 1.4 with the similar dielectric properties for the solid experimental mimicking phantom (measured again and reported in 4.6 section of this chapter). The prototype of dual slot-PIFA had a single metallic layer and was printed on a single side of a FR4 substrate having a dielectric constant of 4.7, loss tangent of 0.0038, and thickness of 1.6 mm. Figure 6-14 compare the simulated results on reflection coefficient for the proposed antenna when immersed inside homogeneous numerical phantoms were compared with the measured results when the antenna was immersed in the equivalent phantom at 2.45 GHz.

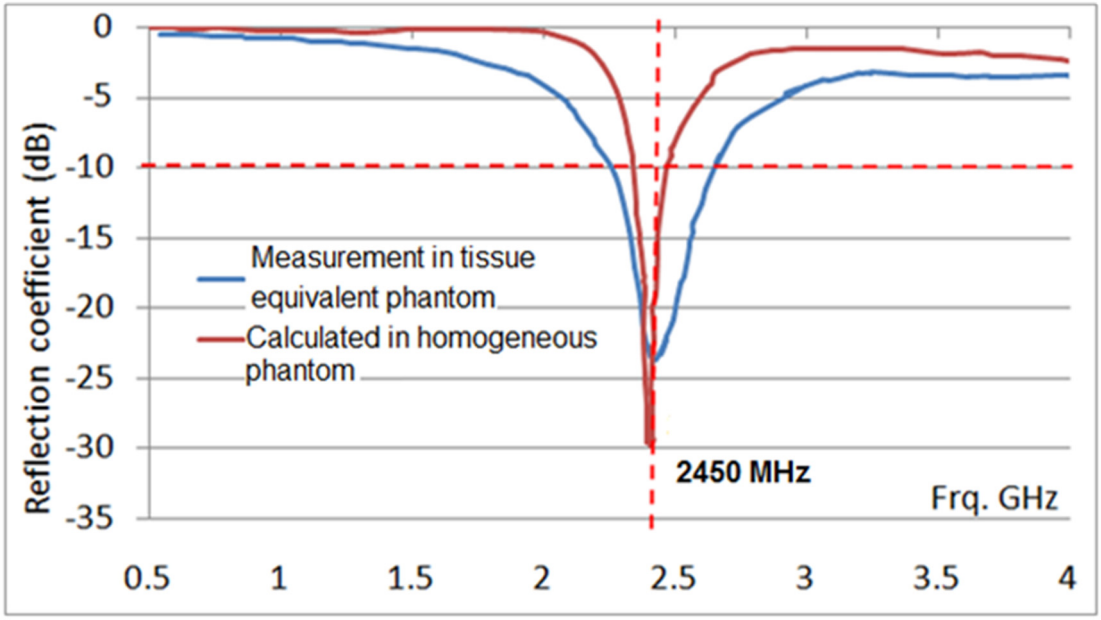

Figure 6-14. Measured vs calculated: Homogeneous numerical phantom.

6.4 Calculation Results

The 5 × 5 Dual Slot PIFA array designed to cover 2450 MHz frequency while able to focus the electromagnetic field in a small area with desire depth to heat the tissue for treatment applications. The desired focal point initially was set for depth of 5 cm from the skin surface.

The E-field information is required to calculate the focusing area that the applicator is able to heat up and determining the effective penetration depth of radiation. Furthermore, the SAR level could be calculated directly from the E-field information so that the temperature rises in the target and the surrounding tissue can be determined. When the heating time duration is 60 minutes, and the total input power for the applicator is 1 Watt, the temperature distribution reaches to the maximum of 46 °C as shown in Figure 6-15. The initial body temperature phantom has 37 °C whereas room temperature is 15 °C. For the ease of tissue modeling and simplicity of calculations, I have neglect the blood flow rate, F, in bioheat transfer equation. The blood flow may reduce the temperature raise inside the target, however, this would be easily compensated by increasing the applicator input power slightly. The exposing time and the total input power for the array must be controlled to prevent heating cells over 47 °C for safety of healthy tissue.

Figure 6-17 shows the E-field distribution of the array at different target depth (20, 30, 40, 50 mm) from the skin surface. A small focused spot of 10 × 10 mm with 20% tolerance is achieved between 20 to 50 mm of depth. Moreover, the calculated temperature rise using SAR demonstrates that an effective penetration depth up to 55 mm depth is achievable as shown in Figure 6-15.

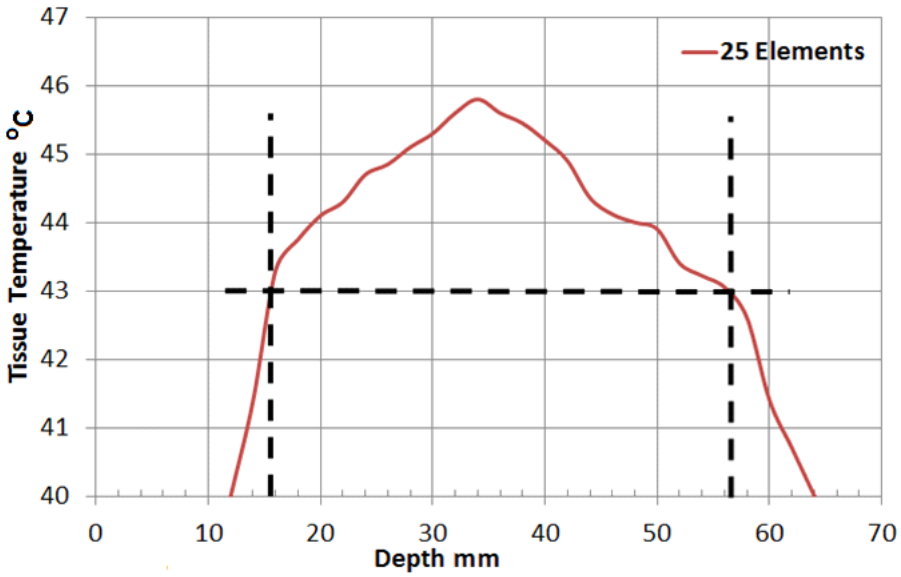

Figure 6-15. Temperature distribution of 5 × 5 planar array.

The 3D normalized SAR distribution of the proposed 5 × 5 array, at the depth of 35 mm from the skin surface, is illustrated in Figure 6-16. This is the depth where the SAR appears at its highest rate and focused at the center along the z axis.

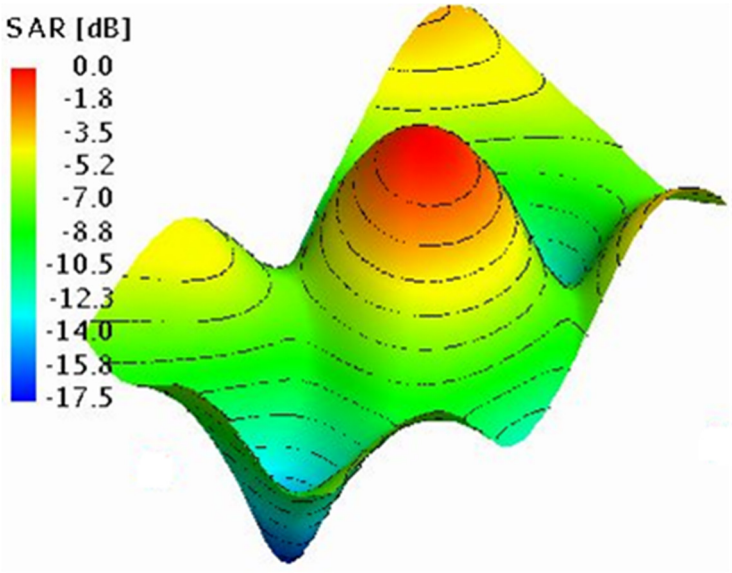

Figure 6-16. Normalized SAR distribution at depth of 3.5 cm.

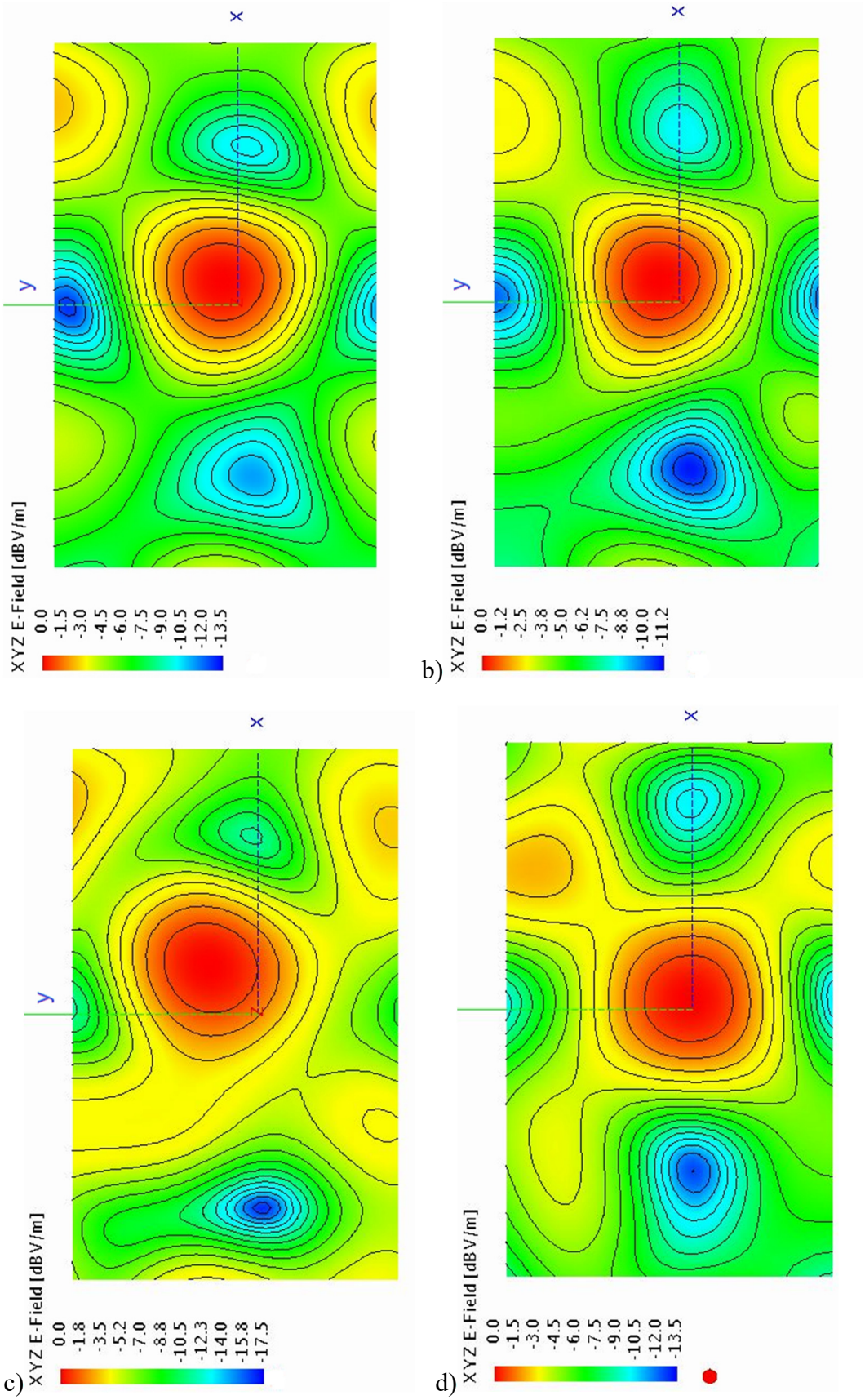

Figure 6-17. E-field distribution of array at different target depth along z axis: a) 20mm, b) 30mm, c) 40mm, d) 50mm from the body surface.

6.5 Antenna Array with Limited Number of Elements for NI-LMH

Arrays consist of a large number of elements are capable to show excellent performance for NI-LMH systems, however, having more elements in array will increase the size of the applicator significantly, it will also increases the size and weight of the bolus results in patient discomfort as shown in Figure 6-18. Moreover, the complexity, cost and weight of the feeding network will also increase remarkably.

Here, to overcome this issue I limit the number of elements from twenty five to nine so that the cost, weight and complexity of applicator and its feeding network reduces considerably. On the other hand, reducing the number of elements decreases the ability to focus on the smaller regions and focal point accuracy. To compensate these weaknesses, I will introduce six new array arrangement consist of maximum nine active and passive elements for NI-LMH application.

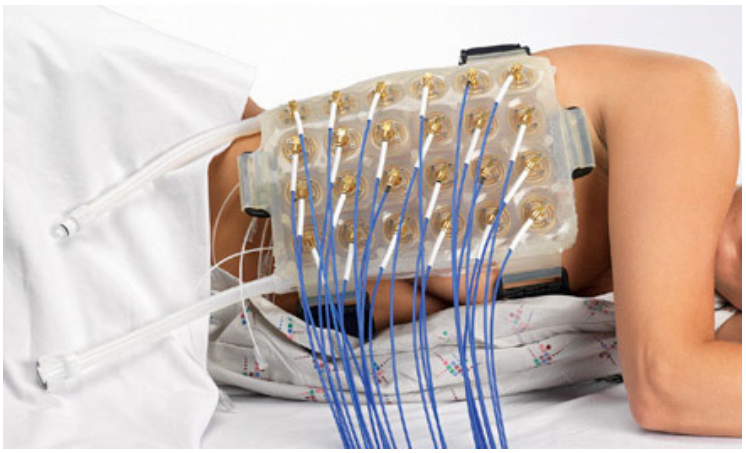

Figure 6-18. Array of antenna (feeding cables included) inside the applicator for NI-LMH.

6.5.1 Square Arrangement

The geometry of the square array is shown in Figure 6-19a. It consists of eight active elements placed on each corner of the square and middle of the opposite sides. The square array has a perimeter of 160 mm and the applicator pack has overall size of 6.5 × 6.5 × 1.52 cm when the array operates over ISM, 2.45 GHz, band. The new applicator was placed closed by the complex human body numerical phantom, as shown in Figure 6-1, to calculate the array performance.

I learned that the square arrangement could not focus on small targets precisely, as shown in Figure 6-20. Therefore, a single parasitic element added to the array at the center of square to improve beam string. The geometry of the square array with parasitic element at the center is shown in Figure 6-19b. I conclude that adding parasitic element helps to improve the accuracy of focal point when heating up the target, however, to have a more precise focusing, more parasitic elements is needed. This will increase the number of antennas and applicator size which is not my interest at this stage so that I use circular arrangement in the next sub section.

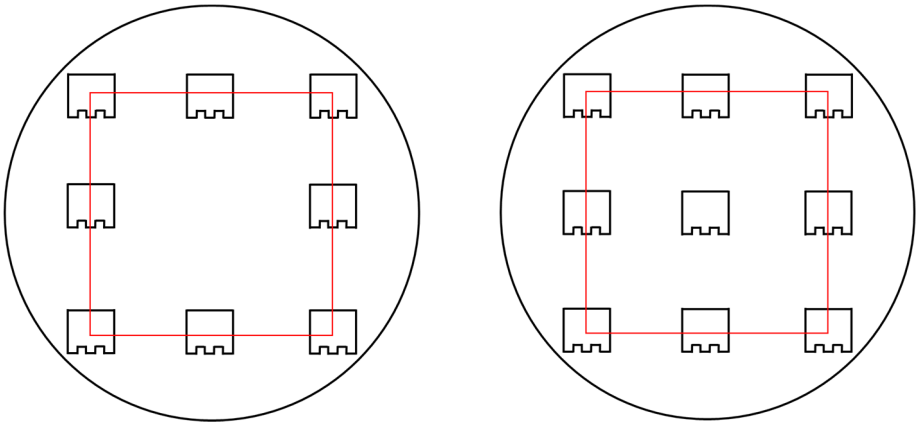

Figure 6-19. Square array arrangement: a) without parasitic antenna, b) with parasitic antenna.

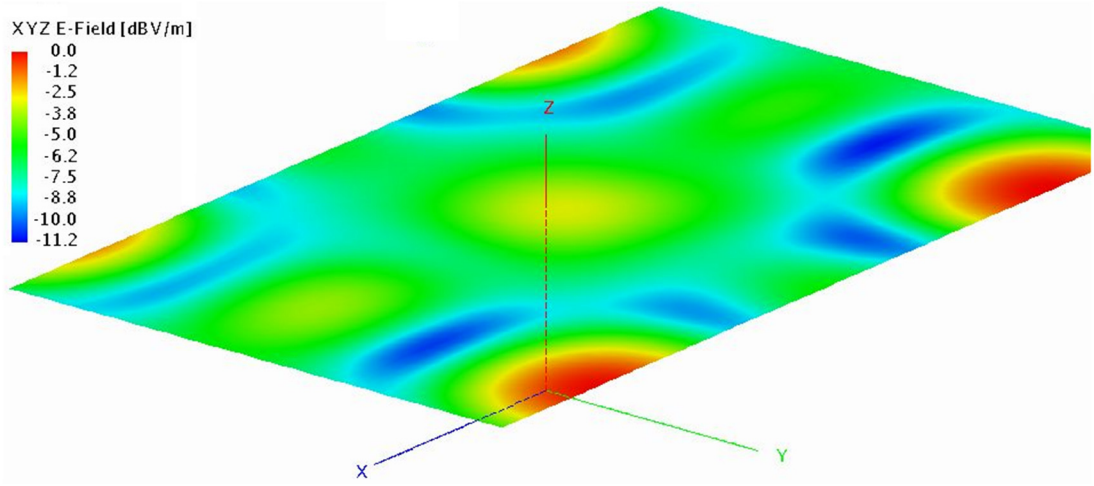

Figure 6-20. E-field distribution of square array arrangement.

6.5.2 Circular Arrangement

Here, I have arranged the eight active antennas in such a way to form a circular array with an aim of more accurate focusing on cancerous cells. The diameter of the circular array is fixed at 55 mm and radiating elements are distributed around the circle equidistantly. The geometry of the proposed circular array, to cover ISM band (2.45 GHz), is shown in Figure 6-21a. The applicator has a size of 7 × 7 × 1.52 cm and placed closed by the complex human body numerical phantom to calculate its performance.

The circular array could focus on smaller targets compare with the rectangular array presented in previous sub section. However, the penetration depth is not deep enough to heat up the deep seated tumor. To deposit the energy in not only superficial tumors but also in the deep seated ones, I added a parasitic element at the center of the circular array, as shown in Figure 6-21b, later I investigated the effects of varying the size of the parasitic element. Here, the gain and directivity of the circular array may be increased up to 12% by changing only the length and width of the parasitic elements by 5%. Adding a parasitic element at the center of the circle helps to focus on the

target more accurately, as shown in Figure 6-22, however, it does not help to heat up deep seated tumors. To overcome this issue, I introduce cross array for NI-LMH in the next sub section.

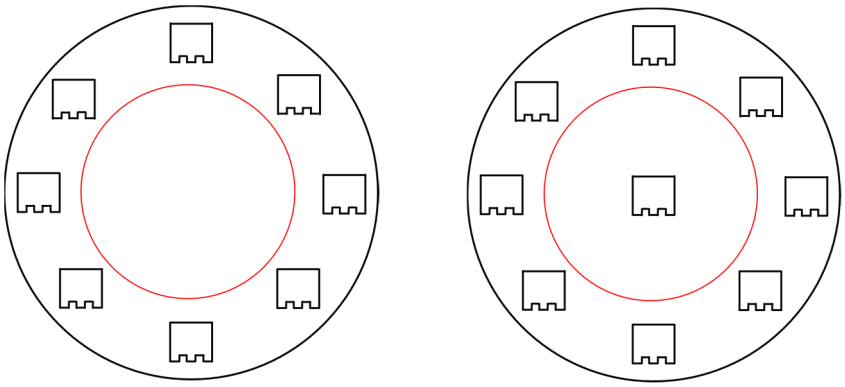

Figure 6-21. Circular array arrangement: a) without parasitic antenna, b) with parasitic antenna.

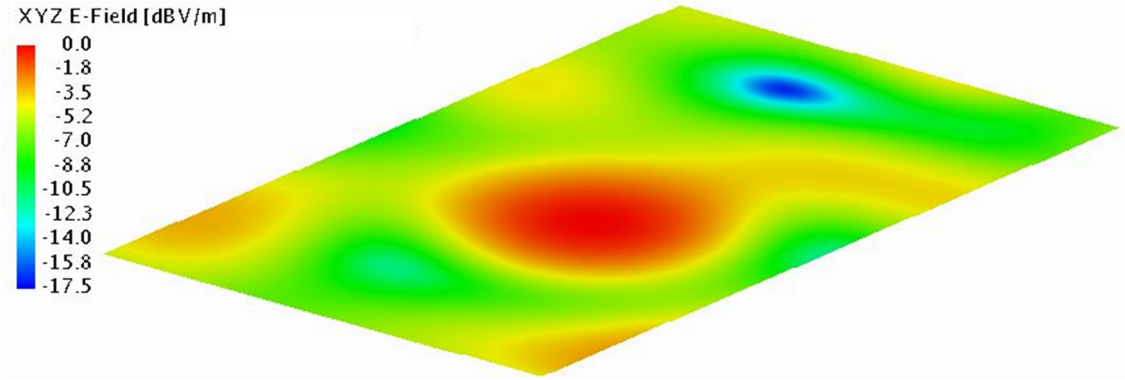

Figure 6-22. E-field distribution of circular array arrangement.

6.5.3 Cross Arrangement

Generally, cross arrangement for printed PIFA arrays perform well when directional beam is needed. In this subsection, I have employed eight active elements to form proposed cross array as shown in Figure 6-23a. Both horizontal and vertical legs of the cross array have a size of 70 mm when array resonate at 2.45 GHz. The new applicator pack has overall size of 8.6 × 8.6cm and was placed closed by the

complex human body numerical phantom to calculate the array performance. The cross array could heat up both superficial and deep seated tumors with minimum number of undesired hot spots, however, the its front to back ratio is low caused the system efficiency reduce significantly. Furthermore, the low front to back ratio may raise safety issues since the cross array radiates backward.

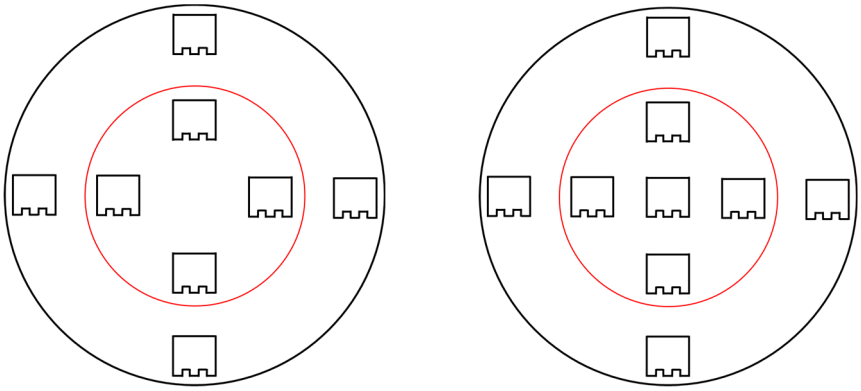

Figure 6-23. Cross array arrangement: a) without parasitic antenna, b) with parasitic antenna.

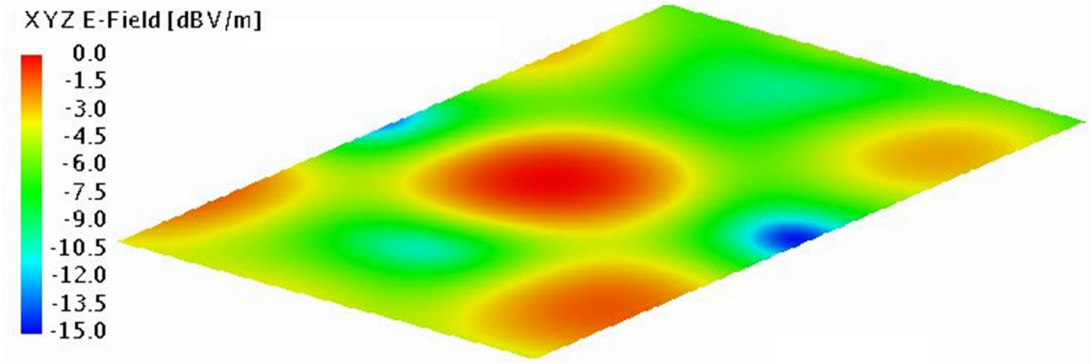

Figure 6-24. E-field distribution of cross array arrangement.

For NI-LMH application when using near filed focusing array, a high front to back ratio is desirable since it indicate that the minimum amount of energy is radiated towards undesired directions. In general, to overcome this issue, the spacing between the antennas are adjusted whit an aim of achieving maximum front to back ratio, rather

than maximum gain in the desired direction. However, this will effect on the applicator performance in a negative way so that the array could not deposit energy in deep seated tumors. Alternatively, I have used a single parasitic element with the same size of the active antennas; the passive antenna positioned at the center of the cross array as illustrated in Figure 6-23b. I concluded that the passive element increase the directivity, acts as a director, and improve the front to back ratio. However, the minimum number of hot spots may increase when employing parasitic element for the cross array as illustrated in Figure 6-24.

6.5.4 Hexagonal Arrangement

The geometry of the hexagonal array is shown in Figure 6-25a. It consists of only five active elements placed on each corner of the hexagonal array. The hexagonal array has a maximum radius of 30 mm and the applicator pack has maximum size of 7 × 7 × 1.52 cm when the array operates over ISM, 2.45 GHz, band. The new applicator was placed closed by the complex human body numerical phantom, as shown in Figure 6-1, to calculate the array performance.

I concluded that the hexagonal array could not focus on cancerous cells accurately, as shown in Figure 6-26, so that a single parasitic element added to the array at the center of the hexagon to improve the beam string. The geometry of the square array with parasitic element at the center is shown in Figure 6-25b. I learned that adding parasitic element improves the accuracy of energy deposition when heating up the target, however, to focus exactly on a specific area more elements needs to be added. This will increase the size of the applicator and does not agree with goals I set at beginning of this section.

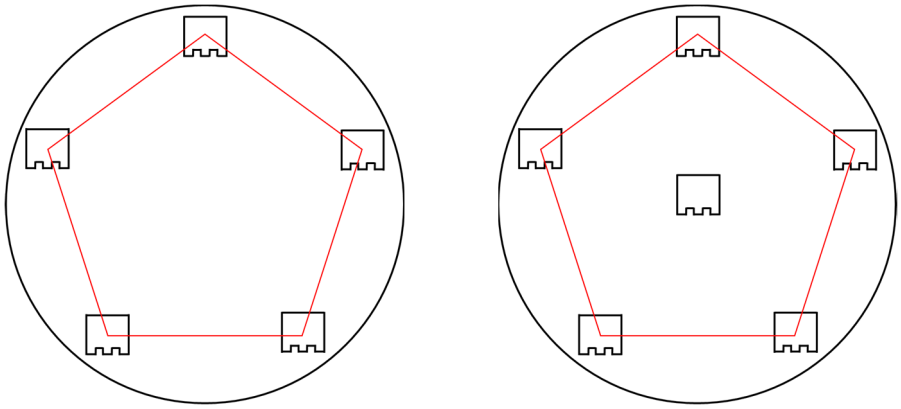

Figure 6-25. Hexagonal array arrangement: a) without parasitic antenna, b) with parasitic antenna.

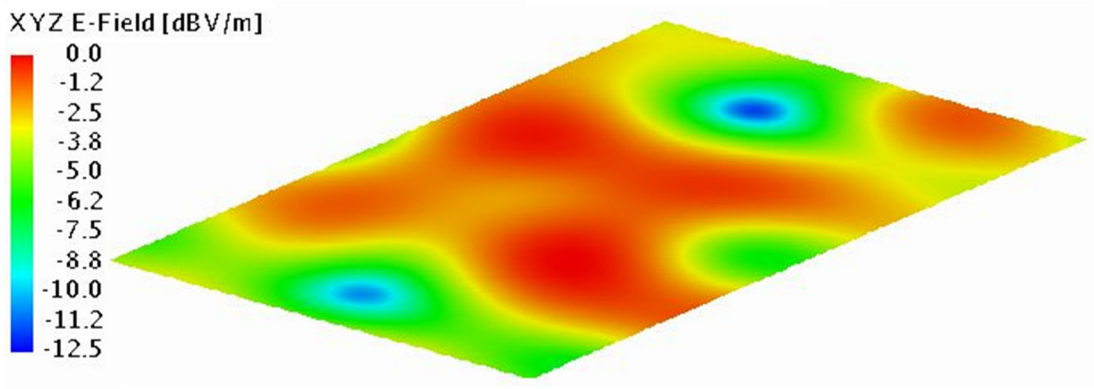

Figure 6-26. E-field distribution of hexagonal array arrangement.

6.5.5 Outer Square & Inner Circular Arrangement

The proposed array arrangement consist of both ring and square arrays with four excited antenna in each. The diameter of the ring array is fixed at 36 mm and the radiating elements are distributed around the ring equidistantly. The square array has a perimeter of 200 mm and the four antennas are placed at four corner of the square. The geometry of the proposed array, covering ISM band (2.45 GHz), is shown in Figure 6-27a. The applicator has a size of 7.2 × 7.2 × 1.52 cm and placed closed by the complex human body numerical phantom to calculate its performance.

I have also employed a single parasitic element at the center of the ring, as illustrated in Figure 6-27b, to increase the accuracy of the focal point focusing on cancerous cells. The proposed nine elements array could focus on smaller targets compare with the previous arrangements proposed in this section and able to heat up both superficial and deep seated tumors. It has also a higher front to back ratio, However, the number of undesired hot spots is not minimum as shown in Figure 6-28.

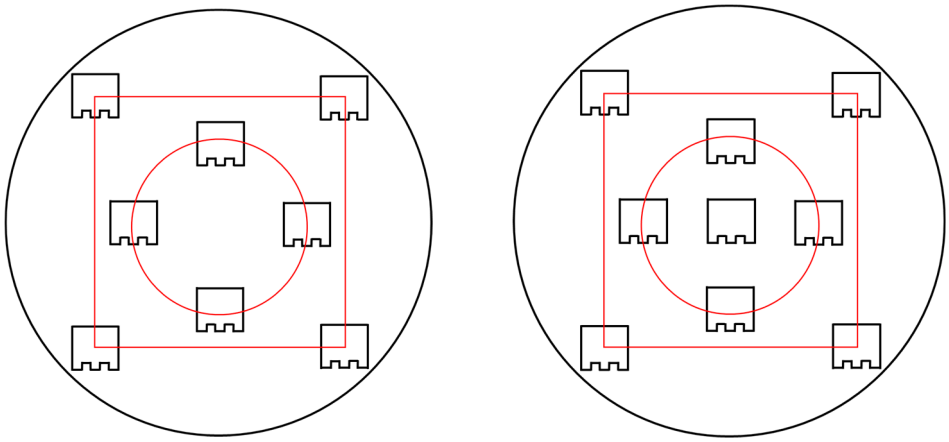

Figure 6-27. Outer Square & Inner Circular array arrangement: a) without parasitic antenna, b) with parasitic antenna.

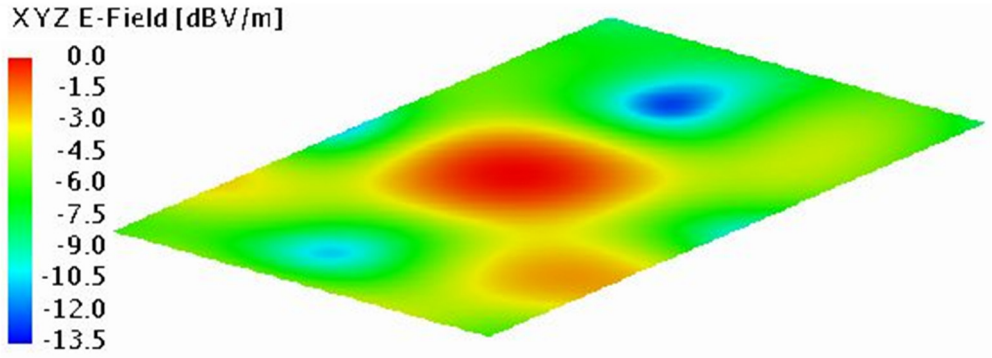

Figure 6-28. E-field distribution of Outer Square & Inner Circular array arrangement.

6.5.6 Outer Circular and Inner Square Arrangement

To reduce the number of undesired hot spot to none, I increase the ring radius and decrease the square perimeter for the previous design. The diameter of the ring array is fixed at 50 mm and the four radiating elements are distributed around the ring symmetrically as shown in Figure 6-29a. The square array has a perimeter of 110 mm and the four antennas are placed at four corner of the square. The geometry of the proposed array, operating over ISM band (2.45 GHz), is illustrated in Figure 6-29a. The applicator has a size of 7.2 × 7.2 × 1.52 cm and placed closed by the complex human body numerical phantom to calculate its performance.

Later, to focus on smaller targets with high level of accuracy, a single parasitic element, with the same size of the active antennas, added to the center of the array as shown in Figure 6-29b and investigated its effect on array performance. Directivity and gain of the proposed array could be increased up to 10% by increasing the length and width of the parasitic elements up to 3%. I learned that adding a parasitic element at the center of the array helps to focus on the target precisely.

The proposed nine elements array could to heat up effectively both superficial and deep seated tumors and capable to focus on smaller targets compare to the previous arrays proposed in this section. It has also a higher front to back ratio and minimum number of undesired hot spots. These features demonstrates that the introduced array is suitable for NI-LMH systems employing near filed focusing arrays. Here, I could successfully reduce the applicator size, complexity of the feeding network and the cost of the system while increasing the patient comfort with limited number of radiators inside the applicator.

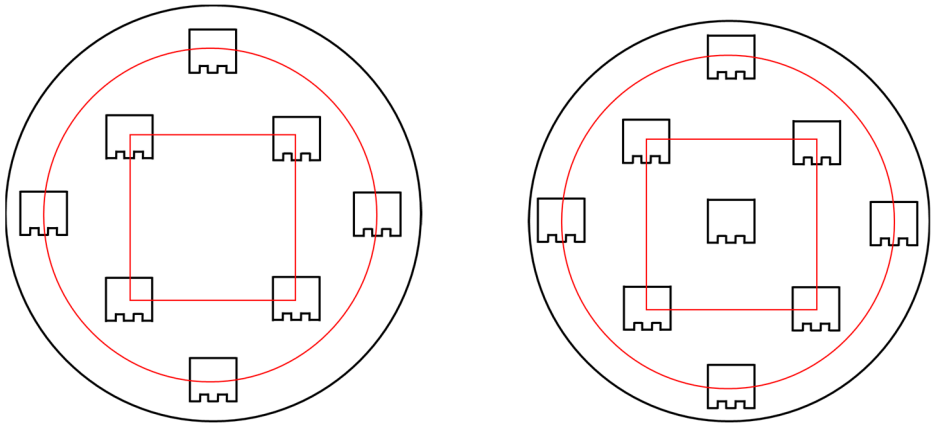

Figure 6-29. Inner Square & Outer Circular array arrangement: a) without parasitic antenna, b) with parasitic antenna.

6.5.6.1 Calculation Results

For the calculations using numerical human body mimicking phantom, the temperature distribution reaches to its maximum of 45.5 °C at depth of 30 mm as shown in Figure 6-30. The total input power for the applicator was set to 1 Watt and the duration of the heating time is 60 minutes. The initial body temperature phantom is 37 °C whereas room temperature is 15 °C. For the ease of tissue modeling and simplicity of calculations, I have neglect the blood flow rate, F, in bioheat transfer equation. The exposing time and the total input power for the array must be controlled to prevent heating cells over 47 °C for safety of healthy tissue. Figure 6-31illustrates the 3D E-field distribution of the proposed nine elements array at depth of 50 mm from the skin surface. A small focused spot of 15 × 15 mm with 15% tolerance is achieved between 20 to 50 mm of depth. Moreover, the calculated temperature rise using SAR demonstrates that an effective penetration depth up to 52 mm depth is achievable as shown in Figure 6-30.

The optimized excitation distribution (phase and amplitude) for the proposed array, using optimization method presented in section 6-3-3, is tabulated in Table 6-3.

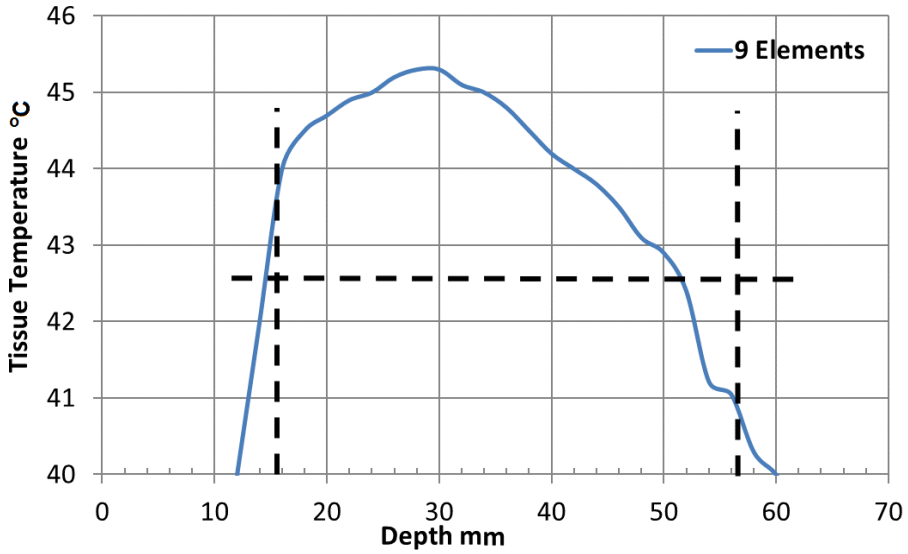

Figure 6-30. Temperature distribution of the nine elements planar array.

TABLE 6-3
OPTIMIZED PHASE AND AMPLITUDE DISTRIBUTION OF THE DUAL SLOT PIFA ARRAY

	Colum 1	Colum 2	Colum 3	Colum 4	Colum 5
Row 1	N/A	N/A	$0.30 \angle -120°$	N/A	N/A
Row 2	N/A	$0.33 \angle -60°$	N/A	$0.33 \angle -60°$	N/A
Row 3	$0.30 \angle -120°$	N/A	$0.00 \angle 0°$	N/A	$0.30\angle -120°$
Row 4	N/A	$0.33 \angle -60°$	N/A	$0.33 \angle -60°$	N/A
Row 5	N/A	N/A	$0.30 \angle -120°$	N/A	N/A

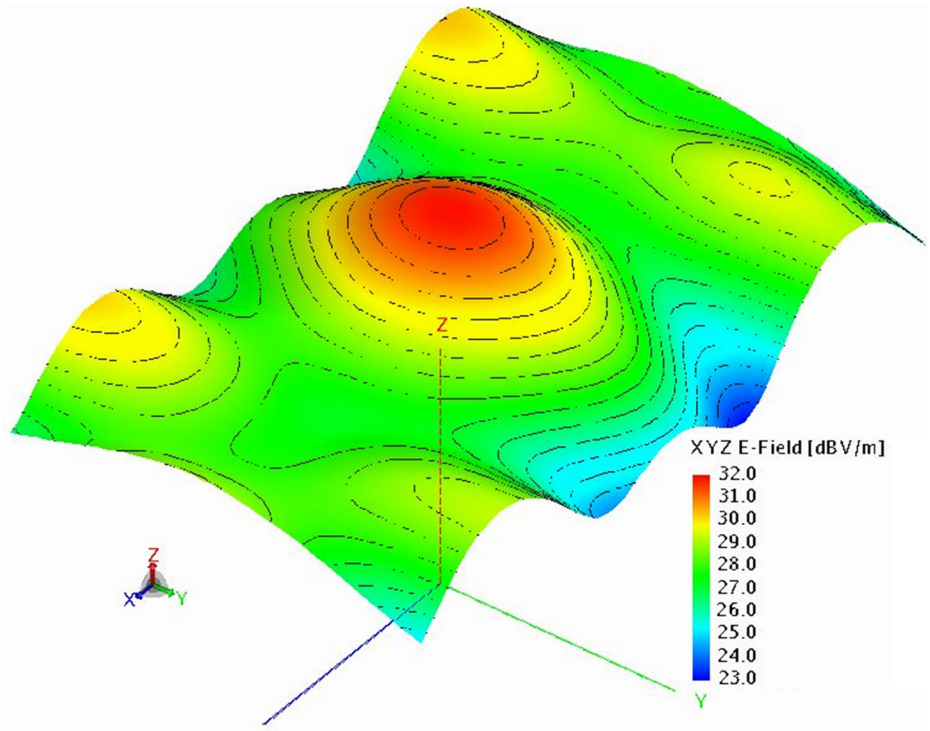

Figure 6-31. E-field distribution of Outer Circular & Inner Square array arrangement at depth of 5 cm.

6.6 Experimental Setup and Temperature Measurement

The proposed NI-LMH system prototype consists of a signal generator, a low noise amplifier (LNA), an eight-channel power divider, coax phase shifters and nine elements NFF array. The temperature rise measurement is configured in four stages illustrated in Figure 6-32. The signal generator delivers a low-power (10 dBm) continuous RF signal at 2450 MHz. The CW signal then amplified with a broadband LNA amplifier (Minicircuits Zx60-83LN+) generating +30 dBm power as planed in stage I. The signal then transmitted into the 8-way power divider (Minicircuits ZN8PD1-63W-S+) and each equally divided channel (signal) is then instantaneously phase-delayed using coaxial feeding cables with proper different length determined in pervious section. Each of the appropriately delayed signals are then used to excite the NFF antenna array immersed inside the coupling bolus as shown in stage II. The applicator transmits the electromagnetic energy to the experimental mimicking phantom with an excitation power of 30 dBm.

The third stage involves the preparation of the equivalent experimental phantom for the human body and the coupling bolus. The one layer equivalent experimental phantom is the same as the one that I used in section 3.4. The dielectric properties for the human tissue experimental phantom and the coupling bolus has been measured (using DAK dielectric probe kit and Agilent E5071C network analyser (from 100 MHz to 3 GHz)) and illustrated in Figure 6-33. The coupling bolus consists of silicone emulsion and distilled water with 15 mm thickness which is placed close by the human body experimental phantom. The thermal information at depth of 3 cm from the phantom surface has been observed at nine different points (in red color) on x-y plane as shown in Figure 6-34. The temperature rise has been measured using optical

thermometer device (Luxtron FOT Lab Kit) as planned at stage IV. The configuration of the temperature measurement set up and the NFF antenna array prototype printed on FR4 substrate (top view and bottom view) are shown in Figure 6-36 and Figure 6-35 respectively. The digital dc power supply employed to supply the voltage bias to the low noise power amplifier and the spectrum analyzer employed to validate the quality of the input signal.

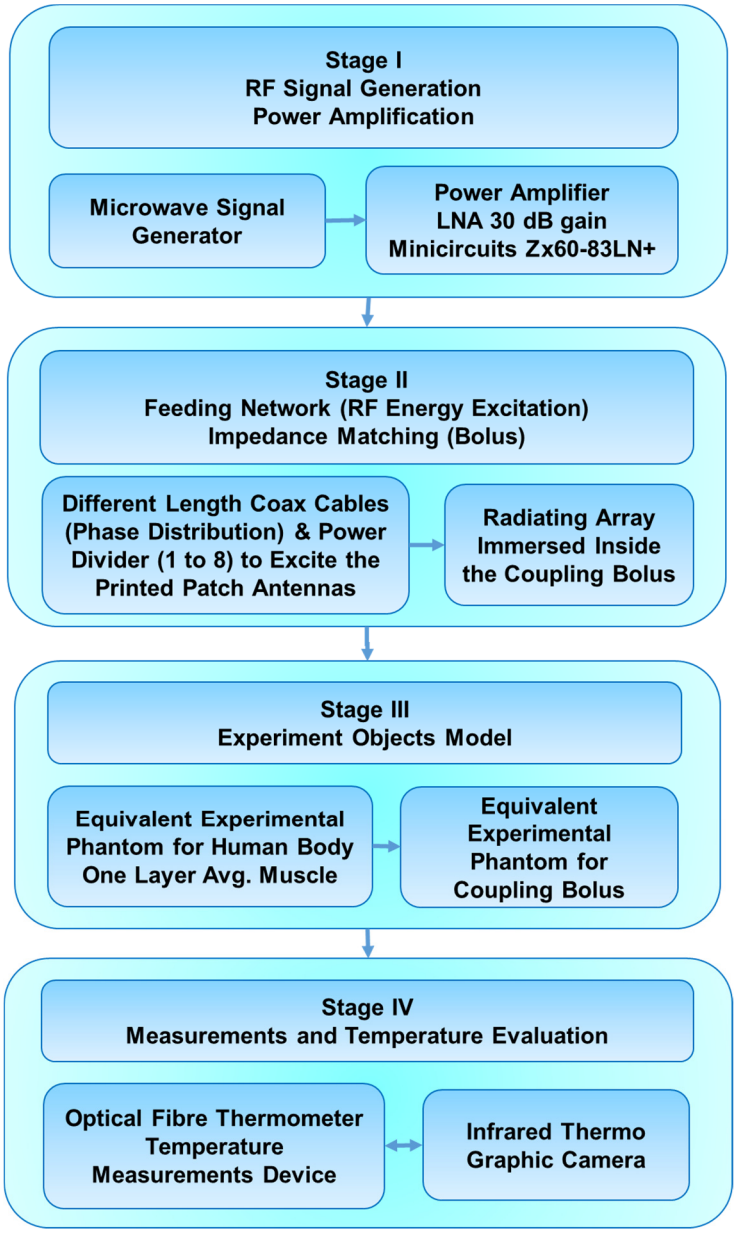

Figure 6-32. Temperature raise measurement block diagram.

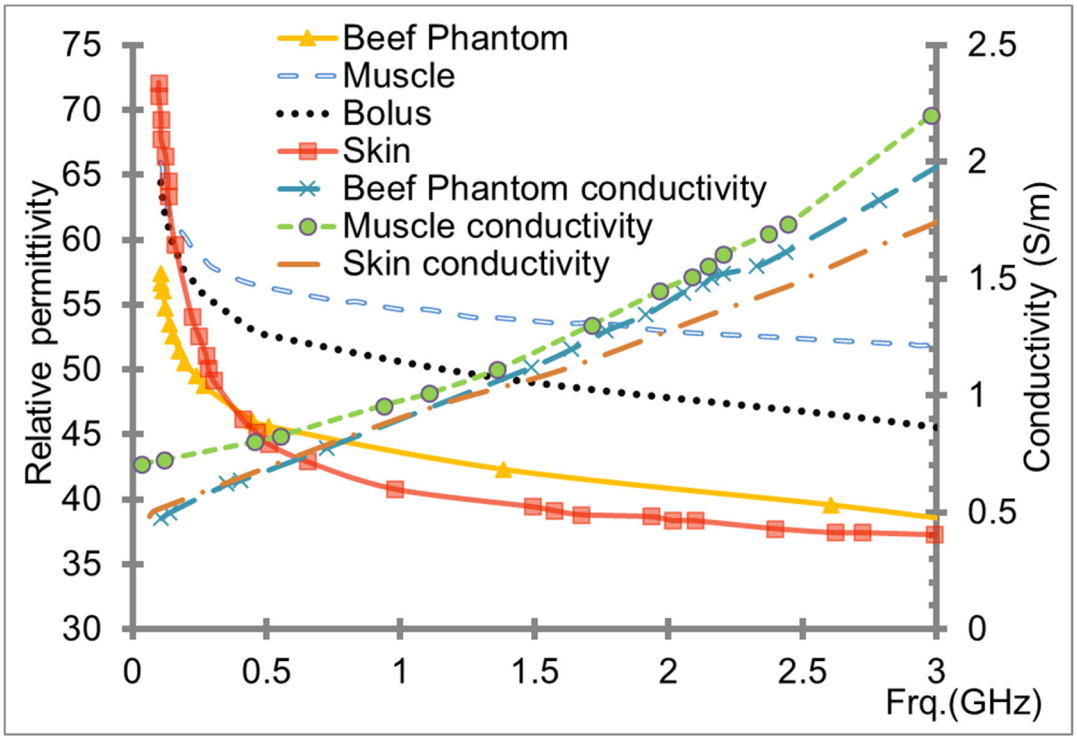

Figure 6-33. Ccomparison of relative permittivity and conductivity of the beef phantom with published data in skin and muscle.

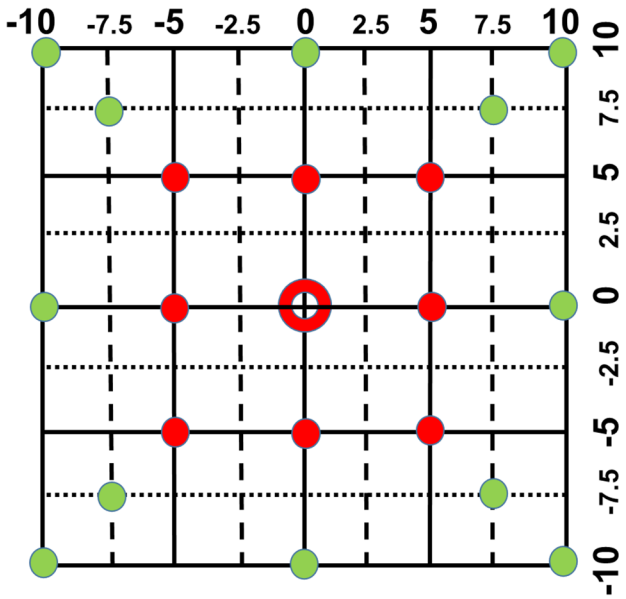

Figure 6-34. Temperature measurement points at depth of 3 cm from the phantom surface on x-y plane: a) desired hot spot in red, b) surrounding tissue and boundary points in green.

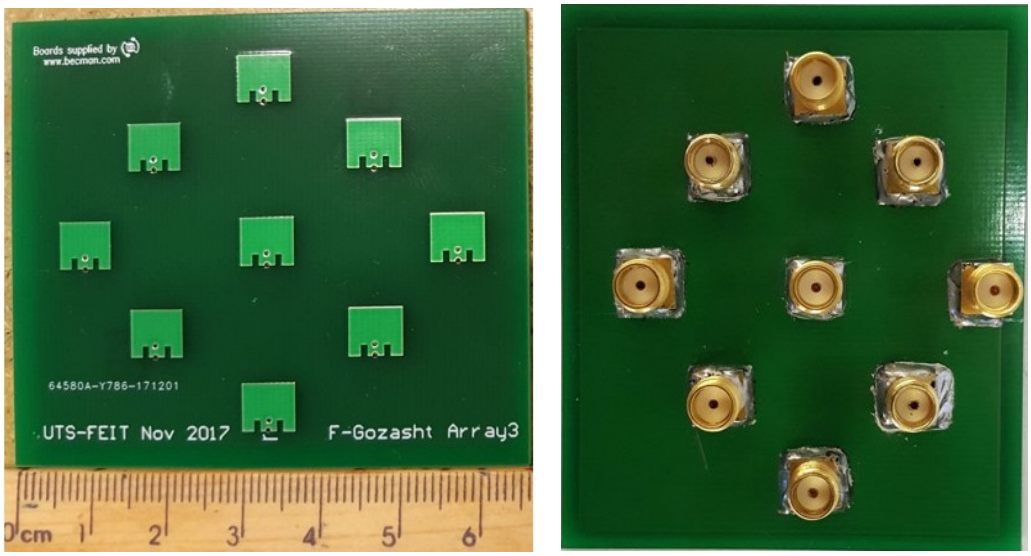

Figure 6-35. Printed NFF antenna array prototype: a) Top view and b) Bottom view.

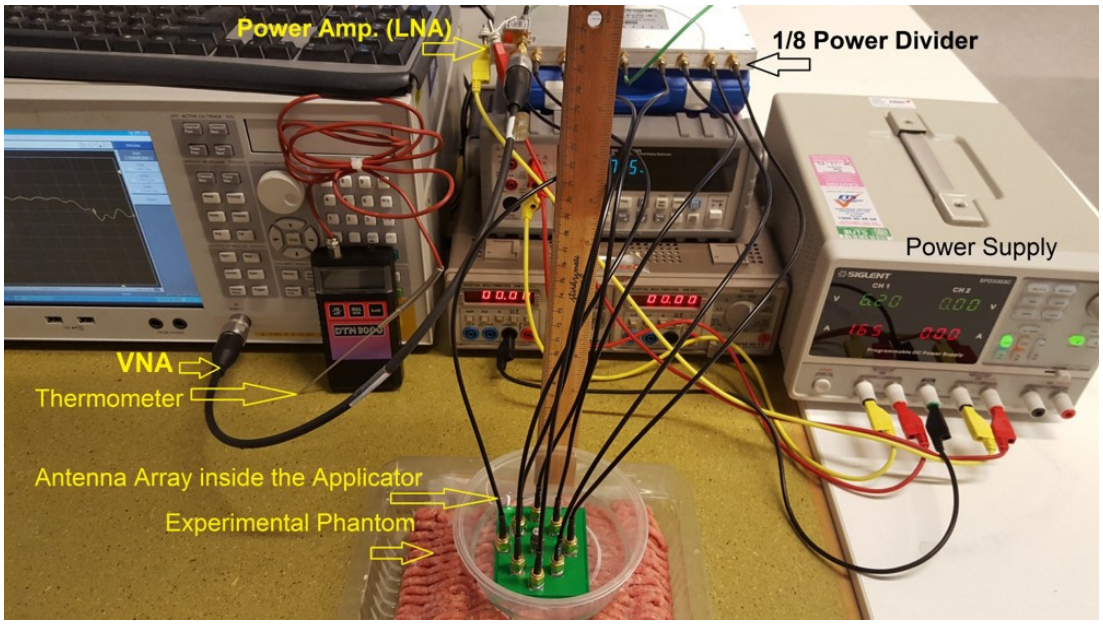

Figure 6-36. Temperature raise measurement setup.

In order to verify the impedance characteristic of the NFF antenna two ports of the eight active elements selected for verification (port 1 and 2). The measured result on reflection coefficient when the presented near field focused antenna array immersed inside the coupling bolus and placed close by inside the experimental phantom, shows a good agreement with calculated result using complex human body as shown in Figure 6-37. Furthermore, the measured and calculated results on scattering parameter,

S12, S13, S14, S15, S16, S17, S18 for the presented near field focused antenna array are also compared in Figure 6-38. This indicates the level of mutual coupling between the array's active elements which is acceptable for maintaining the near field focusing properties of the proposed NFF applicator.

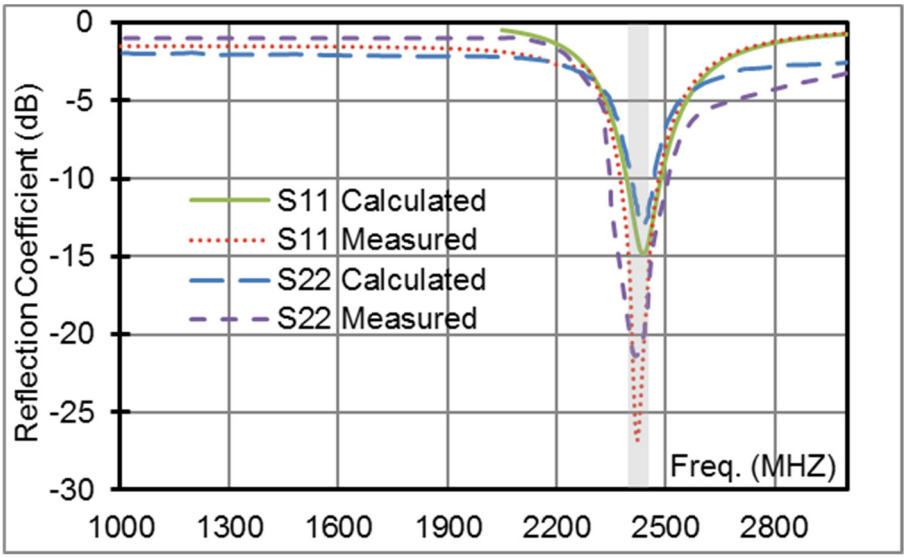

Figure 6-37. Reflection coefficient of the port 1 and 2 of the proposed NFF array: Calculated using Complex human body model vs Measured using experimental phantom.

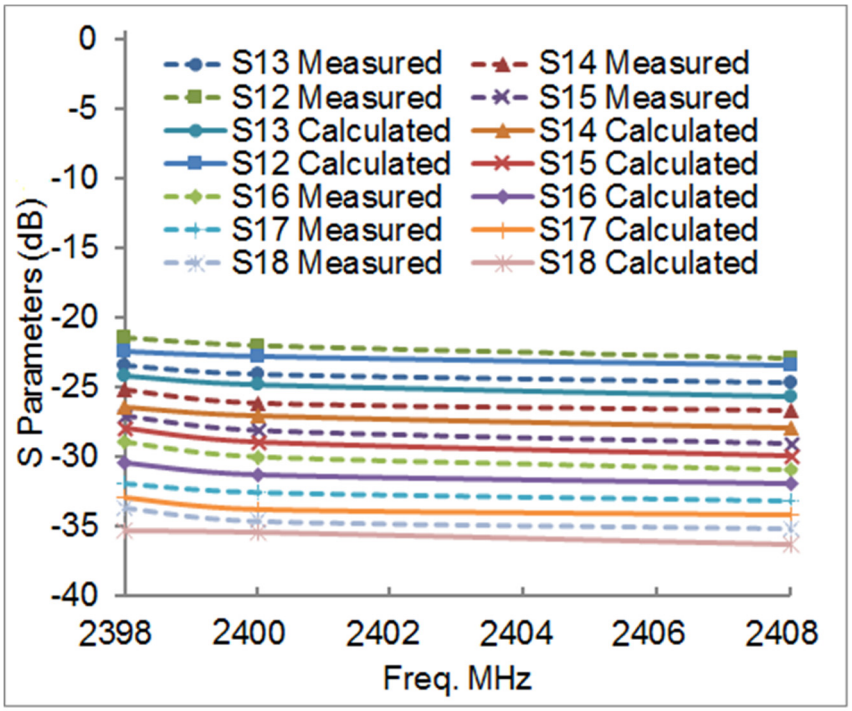

Figure 6-38. Power received at six receiver ports.

The average temperature distribution reaches to its maximum of 44.5 °C at depth of 30 mm when the duration of the heating time was set to 60 minutes. The room temperature set to 15 °C whereas the initial phantom temperature phantom increased to 37 °C using microwave oven a few seconds before conducting the experiment. The measured average temperature is 1 °C less than prediction (using calculations results). This is due to the feeding network loss and the difference between the dielectric properties of numerical and experimental phantoms. To make sure that the surrounding tissue is safe (the size of the hot spot is not greater than 15 × 15 mm), I have measured the temperature rise on the 15 mm boundaries and 5 mm away from the boundaries as shown in Figure 6-34 (in green color). My investigation shows that the surrounding temperature remains less than 42 °C after exposing the RF energy to the experimental phantom for 60 minutes. The exposing time and the total input power for the array must be controlled to prevent heating cells over 47 °C for safety of healthy tissue.

The proposed radiating NFF antenna array can deposit the electromagnetic energy deep inside the human tissue in a small desired area. The presented NI-LMH system is smaller and more efficient (consume less power) compare to systems presented in the literature [206, 207]. The blood flow may reduce the temperature raise inside the tumor, however, this would be easily compensated by increasing the applicator input power slightly.

Another benefit of the proposed NI-LMH system is that all the designed eight/nine element array can be connect easily to the system prototype only by connecting the desired array to the coaxial feeding cables. Here, I have also fabricated the “Outer Circular & Inner Square” without parasitic element as shown in Figure 6-29a. The temperature rise measurement is configured in four stages illustrated in

Figure 6-32. The signal generator delivers a low-power (10 dBm) continuous RF signal at 2450 MHz. The signal then transmitted into feeding network including power divider and amplifier. The signals are then used to excite the NFF antenna array immersed inside the coupling bolus. The applicator transmits the electromagnetic energy to the experimental mimicking phantom with an excitation power of 30 dBm.

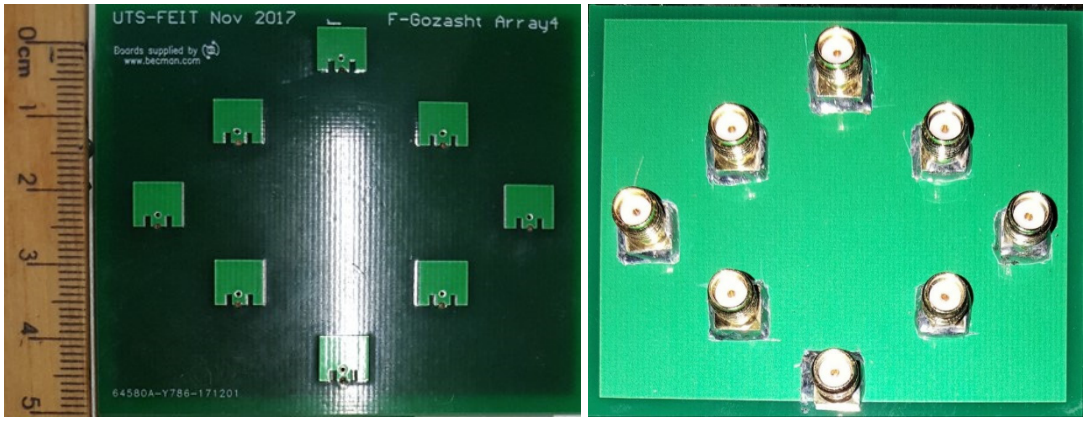

Figure 6-39. Printed NFF antenna array prototype: a) Top view and b) Bottom view.

The one layer equivalent experimental phantom is the same as the one that I used in pervious experiment. The coupling bolus is also the same with 15 mm thickness placed close by the experimental phantom. The configuration of the temperature measurement set up and the NFF antenna array prototype printed on FR4 substrate (top view and bottom view) are shown in Figure 6-36 and Figure 6-39 respectively. The thermal information at depth of 3 cm from the phantom surface has been observed at nine different points (in red color) on x-y plane as shown in Figure 6-34. The temperature rise has been measured using optical thermometer device.

The average temperature distribution reaches to its maximum of 44 °C at depth of 30 mm when the duration of the heating time was set to 60 minutes. The measured average temperature is 1 °C less than prediction (using calculations results). This is

mainly due to the feeding network loss and the difference between the dielectric properties of numerical and experimental phantoms. To verify the size of the hot spot, should be smaller than 15 × 15 mm, I have measured the temperature rise on the 15 mm boundaries and 5 mm away from the boundaries as shown in Figure 6-34 (in green color). My investigation shows that the surrounding temperature reaches to 42 °C after exposing the RF energy to the experimental phantom for 60 minutes. This shows that the focusing area is slightly bigger than 15 × 15 mm. I concluded that the performance of this array is similar to the proposed array with parasitic element. However, the parasitic element at the center of the array helps to focus on smaller targets more precisely.

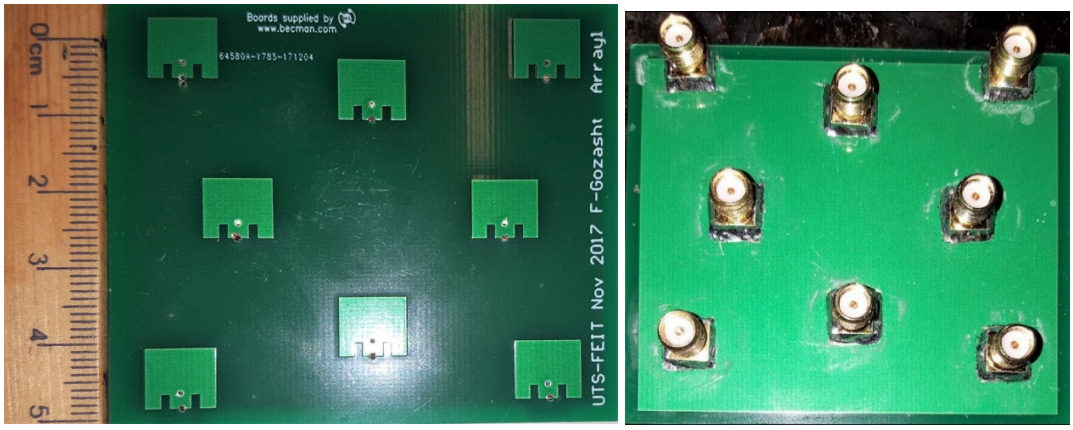

Figure 6-40. Printed NFF antenna array prototype: a) Top view and b) Bottom view.

I have also fabricated the “Outer Square & Inner Circular arrangement” without parasitic element as shown in Figure 6-27a. The proposed NI-LMH system prototype is the same as the one used for the above measurement. It consists of a signal generator, a low noise amplifier (LNA), an eight-channel power divider, coax phase shifters and eight elements NFF array. The temperature rise measurement is configured in four stages illustrated in Figure 6-32. The signal generator delivers a low-power (10 dBm)

continuous RF signal at 2450 MHz. The CW signal then amplified with a broadband LNA amplifier (Minicircuits Zx60-83LN+) generating +30 dBm power. The signal then transmitted into the array radiating-elements through power divider and coaxial feeding cables.

The coupling bolus, placed close by the experimental phantom, is the same as the one I used in my experiments with 15 mm thickness. The one layer equivalent experimental phantom is also the same as used in the pervious experiment. The configuration of the temperature measurement set up and the NFF antenna array prototype printed on FR4 substrate (top view and bottom view) are shown in Figure 6-36 and Figure 6-40 respectively. The temperature rise has been measured using optical thermometer device. The thermal information at depth of 3 cm from the phantom surface has been observed at nine different points (in red color) on x-y plane as shown in Figure 6-34.

The average temperature distribution reaches to its maximum of 43.5 °C at depth of 30 mm when the duration of the heating time was set to 60 minutes. The measured average temperature is 1.2 °C less than prediction (using calculations results). This is mainly due to the feeding network loss and the difference between the dielectric properties of numerical and experimental phantoms. To validate the calculation results, I have measured the temperature rise on the 15 mm boundaries and 5 mm away from the boundaries as shown in Figure 6-34 (in green color).

My investigation shows that after exposing the RF energy to the experimental phantom for 60 minutes, the reading on the left boundaries are higher than the reading on the right side, indicating possible extra hot spot on the left side the desired hot spot. This undesired hot spot was also found in calculations using numerical mimicking

phantom as shown in Figure 6-28. As predicted, the surrounding temperature remains less than 42 °C for the right side of the reading area. The exposing time and the total input power for the array must be controlled to prevent heating cells over 47 °C for safety of healthy tissue.

6.7 Discussion

The 5 × 5 NFF planar array for non-invasive hyperthermia is proposed to heat the target between 43 °C and 47 °C within a small spot area. The target depth is defined between 2 to 5 cm form the skin surface. The planar type array inside the coupling water based bolus can be attached on the surface of the human body and has a compact size of 8 × 8 cm (bolus size is 13 × 13 cm). The penetration depth and enhancement of non-invasive EM antenna hyperthermia is discussed. The temperature distribution is shown to verify the feasibility of the effective heating treatment. The challenges for advance antenna design in such application include effective coupling and penetration into heterogeneous lossy body tissues, operating in the antenna near field, and control of three dimensional power deposition patterns for heating target regions is considered during the design procedure.

To simplify the feeding network and reduce the system cost, I have also introduced different configuration for the NFF array that consists of eight active elements, I have verified their performance using numerical accurate human body model. The proposed ‘Outer Circle and Inner Square’ arrangement satisfies the entire requirements needed for the system and able to focus on small targets with a size of 15 × 15 mm, it has an effective penetration depth up to 50 mm. This configuration has

the advantage of excellent size reduction of 50% compared with the 25 elements array reported in this work and occupies a volume of 4.1 cm^3 (78.8 cm^3 including bolus).

CHAPTER – 07

7. CONCLUSION AND FUTURE WORK

7.1 Conclusion

The final chapter of this dissertation highlights the research findings of this study and summaries the discussions of each chapter. Initially, a recap of the ideas and their main advantage in each chapter is presented. This is followed by the demonstration of important findings and overview of the scientific contributions made in this work. Finally, a list of recommendations is provided for the potential future work to continue this study.

To extend the communication range, reduce the system size and use of prevalent components, this work tackled the far field data biotelemetry from inside the human body along with nearfield EM energy focusing within the body. The applications included but not limited to the wireless capsule endoscopy, cardiac care, vital signals monitoring from inside the human body (i.e. heart rate, glucose, temperature and pressure), thermal therapy etc. which are facilitated by different implantable and wearable devices. Taking into account an extensive range of medical and technical concerns, the focus has been concentrated on the implantable and body worn antennas, one of the most challenging components of an embedded systems targeting wireless data transmission.

The design of embedded microsystems is extremely challenging and comprises the integration of different compact components. While most of the components can be efficient for compact sizes, the antenna size miniaturization causes degradation of antenna radiation performance. Therefore, new geometries and techniques are proposed in this dissertation to tackle the contradictory conditions. In addition to the conventional antenna problems, such as physical size miniaturization and its consequent degrading the antenna radiation performance, I have also considered the coupling of the electromagnetic field with different human biological lossy tissues. Moreover, biocompatibility, physical and electrical requirements, and the confine co-existence in the presence of all other components in an entire microsystem have also been considered. The main contributions and major findings in this regard have been discussed in each chapter of this dissertation which are summarized as:

1. New class of miniaturized Dual Slot PIFAs of the following characteristics is developed in Chapter 3 for implantable biotelemetry devices:

- Simple geometry which is easy to tune for operating over a variety of biotelemetry bands.

- Wide impedance bandwidth.

- Higher radiation efficiency.

- Suitable to be integrated with small implants.

- Low profile and light weight.

In spite of the fact that some of these circumstances are contradictory, they all are satisfied due to the superior antenna structure design which enables easy tuning and excellent radiation performance. Using presented tuning techniques, my proposed

simple geometry can be simply modified to operate over different biotelemetry bands such as Medical Implant Communication Service (MICS) at 400 MHz, Zigbee at 868 MHz, Wireless Medical Telemetry Service (WMTS) band at 1430 MHz and Industrial, Scientific, and Medical (ISM) band at 2450 MHz. By embedding dual slots onto the antenna geometry, the current path on the top patch can be lengthened so that lowering the antenna resonant frequency, this feature is used to miniaturize antenna structure size. While miniaturized implantable antennas are presented in the literature [33, 49, 66, 120], the proposed DS-PIFAs in Chapter 3 of this thesis outperform them. This has been achieved since the proposed DS_PIFAs are optimized through a three-step design methodology for miniaturization leads to a wider impedance bandwidth, larger radiation efficiency and robustness in the anatomical body model. To enable low profile and reduce the overall weight of DS-PIFAs, light conducting and dielectric materials, such as FR4 or on Rogers 3210, has been employed.

I have also investigated the effect of the antenna geometry parameters on radiation performance using empirical parametric studies to miniaturize the DS-PIFA structure physical size. To validate the DS-PIFA radiation performance in more realistic tissue environment, I have considered the effects of interstitial fluid and air gap between the human body skin and the antenna when it is implanted. This has not been reported in pervious major studies in the literature [33-36, 55, 58]. Furthermore, the effects of the surrounding environment such as skin and fat thickness on the antenna performance are also investigated using numerical human tissue phantoms to verify antenna performance robustness when embedded in human body of different shape and size.

The average radiation efficiency reported in the literature [38, 45-48, 56, 57] for implantable antennas, operating in different biotelemetry bands and using different

miniaturization techniques, is less than 1%. For proposed DS-PIFAs, minimum radiation efficiency of 2.6% (1.8% when printed on Rogers 3210) achieved since I could successfully keep the radiation resistance dominant compare to the loss resistance over the antenna structure by adjusting the antenna size and the feeding position to keep the surface current flows uniformly over the radiator.

The impedance characteristics of the proposed antennas are measured using experimental tissue mimicking meat phantoms. Moreover, I have employed bio heat equations and optical fibre thermal sensors to establish an indirect thermal method to calculate the SAR inside the human body when the antenna is implanted, using this method and employing human body mimicking experimental meat phantom, I verified SAR simulations results. My statistical pass loss and link budget analysis also reveals the feasibility of reliable wireless communication link up to distance of 8 meters using the proposed 2450 MHz DS-PIFA. Proposed miniaturized DS-PIFAs, compare to pervious work reported in the literature [45-49, 56-59], exhibit smaller size, better radiation efficiency, lower standard SAR, and wider impedance bandwidth suitable for biomedical implant communications.

2. The study performed in the framework of this dissertation targets to facilitate the use of telemedicine employing wireless embedded microsystems. In Chapter 4, for the first time, a set of compatible transmitter and receiver antennas are proposed for the wireless capsule endoscopy systems, the proposed Tx novel antenna features:

- Printable simple structure which is easy to miniaturize and tune.
- Very wide impedance bandwidth.
- Higher radiation efficiency.

- Low profile and light weight.

- Suitable to be integrated with wireless capsule device.

the proposed Rx base station antenna features:

- Printable simple PIFA structure occupying small volume.

- Circular Polarization radiation over the operational band.

- Wide impedance bandwidth.

- Higher radiation efficiency.

- Low profile and lightweight.

The performed investigations in Chapter 4 provides a better understanding of the radiation characteristics of embedded antennas for wireless capsule endoscopy systems, and led to the realization of a CP body-worn array and compact a Tx antenna for far field data telemetry. Realizing such a transmitter and receiver antennas, providing a more reliable communication link, required the study of several aspects of an entire wireless implantable system for healthcare monitoring applications. The pair of proposed highly performance Tx-Rx antennas was used to study the influence of the human body tissues on electromagnetic wave propagation and in-body/on-body communication link performance when the Tx antenna placed in different locations inside the GI tract with different orientations. Such investigations are very important wireless capsule endoscopy system design and contribute to the following:

A printed loop antenna with bandwidth enhancement is presented for ingestible wireless capsule endoscopy systems operating over the MICS band. First, tuning elements added to the single turn loop antenna to minimize the loop length and bring in a second resonance. Then, matching elements introduced and connected to the feeding port to achieve better impedance matching. The radiator then folded and

printed on FR4 to further size reduction and fitting in the capsule compartment. The printed antenna occupies 40% lower space, a very small volume of 160mm^3, and has a bandwidth enhancement of 200%. To verify the antenna performance, measurements are carried out using experimental phantom, the result turns out that the impedance characteristics of the proposed antenna can be achieved. Furthermore, SAR measurements conducted successfully by employing optical fiber sensors and indirect thermal method. The proposed loop antenna exhibit smaller size, wider impedance bandwidth, and lower SAR compare to pervious work reported in literature [70-72].

Moreover, a compact CP-PIFA is also presented as receiving base station antenna for wireless capsule endoscopy systems. The antenna covers MICS band fully, has a compact size and circular polarization to enhance the low-level signal reception. The radiator structure has been miniaturized, has a low profile and occupies a very small volume. The proposed antenna has good impedance bandwidth, improved radiation efficiency and low SAR when performing close to the human body. The presented geometry, is capable to resonate at desired frequency bands when structure size is modified and shorting point location is adjusted. The antenna has also been employed in a conformal array close to human body to communicate with the wireless capsule inside the body, the received signals could also be used for estimation of the capsule position inside the human body using advance localization methods. The Tx antenna inside the capsule normally has liner polarization, the orientation of the wireless capsule also changes frequently while traveling inside the digestive system, so that, employing CP receiver elements improves the overall system performance by detecting linearly polarized transmitted signals with different orientations. To verify the single antenna and array performance, measurements are carried out using experimental phantom, the result turns out that the CP and impedance characteristics

of the proposed antenna and array configuration can be achieved. I have also evaluated the calculated Specific Absorption Rate (SAR) by using an indirect thermal method to measure the SAR inside the mimicking phantom.

Moreover, I presented an empirical PL model for homogeneous and heterogeneous human tissues using numerical phantom and equivalent experimental model. I employed proposed printed folded co-planar loop antenna as transmitter and compact CP-PIFA as receiving sensor in array of six Rx antennas. The relative permittivity ε_r has a variation of $5 \leq \varepsilon_r \leq 75$ for different tissues and the conductivity σ varies from $0.3\ \text{S/m} \leq \sigma \leq 3.5\ \text{S/m}$ when calculations are carried out for 400 MHz MICS band, the Tx and Rx have a separation distance up to 260 mm. To validate the calculations with measurement, array of six CP-PIFAs and a meat phantom with approximate size of 400 × 260 × 400 mm were employed. To examine the robustness of the designed Tx antenna and the accuracy of the developed path loss, the orientation of the capsule shifted by 90° while the orientation of the Rx antennas are fixed. I have observed the new results show a good agreement with previous ones. This shows that the functioning of the transmitter antenna is not affected by its orientation and receiving antennas are able to establish a communication link with the wireless capsule. This was also verified for a couple of different positions of the capsule within the numerical and experimental phantom.

3. The proposed head implantable antennas in chapter 5 of this dissertation could be employed for different biomedical applications such as integration in ICP monitors, trackers for patients with Alzheimer's disease, brain wave sensors for paralyzed patients.

The key contributions of this work, in Chapter 5, are:

1. Proposing new category of miniaturized Single Slot PIFAs of the following characteristics:

   - Simple geometry which is easy to tune to operate over a variety of biotelemetry bands.

   - Higher radiation efficiency.

   - Suitable to be integrated with small head implants.

   - Low profile and light weight.

2. Development of multiband miniaturized SS-PIFA, for the embedded biotelemetry devices, having:

   - Simple geometry which is easy to tune to operate over multiple biotelemetry bands.

   - Good radiation efficiency over multiple biotelemetry bands.

   - Wide impedance bandwidth over multiple biotelemetry bands.

   - Printable simple structure which is easy to miniaturize and tune.

3. Development of a very wideband compact loop antenna featuring:

   - Very wideband impedance bandwidth.

   - Round shape oval loop antenna structure.

   - Suitable to be implanted inside the human head.

   - Printable antenna geometry occupying small volume.

Chapter 5 of this dissertation describes the design and methods proposed in this study to monitor the critical vital signs inside the human head such as ICP for biotelemetry applications. During the neurosurgical procedure, a compact intracranial pressure monitoring device can be implanted inside the cranium to facilitate future ICP

measurement. A key component of this is the antenna which facilitate the wireless communication for the device. I have investigated and quantified new effective parameters such as operational frequency, complex surrounding environment and antenna geometry on overall antenna radiating performance along with numerical and experimental results. Such investigations are very important and contribute to the following:

- Confirm the excellence of the communication link with an external antenna.
- Identifying the effective radiated power (ERP) through a scalp-mimicking phantom using the transmission measurements.
- Provide valuable insight into the accurate evaluation and validation of the embedded antennas inside the anatomical human body head model.
- Variation of resonance frequency, transmission and reflection coefficients over the time, temperature and device orientation during the surgery process.

In Chapter 5, I have used a simple geometry to propose a class of miniaturized SS-PIFAs, suitable for scalp implantable devices, which can operate over a variety of standard biomedical frequency bands such as MICS band, Zigbee, WMTS band and ISM band. Compare to the PIFA type antenna presented in [35], useful for intracranial pressure monitoring systems resonating at 2450 MHz, my proposed SS-PIFA occupies 25% less volume when tuned to resonate at the same center frequency of 2450 MHz. To miniaturize the antenna size, I have conducted detailed parametric study and investigated the effects of each geometrical parameter of the SS-PIFA on the resonant frequency. Further size reduction of 92% for antenna covering ISM band, 89% for antenna covering WMTS band, 86% for antenna covering ZigBee and 60% for antenna covering MICS band achieved by reducing the lengths of the slots and placing the feed and the pin at proper locations.

Beside electrical size miniaturization, regardless of the operating frequency, head implantable antenna design has to deal with major challenges such as bandwidth enhancement and improved radiation performance. The communication link performance of a small loop antenna operating at MICS band is characterized when placed under the scalp for ICP monitoring [93], however, the calculated radiation efficiency is lower in comparison with my proposed miniaturized antenna. Furthermore, the previously reported [94] head implantable short dipole and loop antennas, operating at different frequency bands, shows smaller impedance bandwidth when compared to my proposed PIFA type head implantable antennas.

In general, due to the high dielectric loss, caused by the human body, the total radiation efficiency of the implanted antennas decrease. On the other hand, for the head implantable antennas, the overall structure size has to have a small size. The smaller size and lower efficiencies coupled with lower radiation power can lead to a shorter communication range. I could successfully overcome these issues using the slot and an additional shorting pin. The open slot on the proposed SS-PIFA geometry extends the current path to enhance the antenna size miniaturization and increasing the electric size of the antenna. The larger electric dimension leads to a wider bandwidth and higher gain. For the proposed SS-PIFAs, the lower resonant frequency is mainly due to the current distribution around the slot which is affected by the feed position. Compare to the previous studies reported in the literature [91-92], the proposed SS-PIFAs exhibit smaller size, good efficiency, standard SAR, and reasonable bandwidth suitable for biomedical head implant applications. For instance, the presented antenna resonating at 2450 MHz has 190 MHz measured bandwidth, good radiation efficiency of 1.8%, a compact size of 5×7 mm^2 and occupies a volume of 56 mm^3. I have also employed bio heat equations and optical fibre thermal sensors to establish an indirect

method to do SAR measurement for implantable antennas and verify related SAR calculation.

I have also presented a triple band Single Slot PIFA of size 19 × 30 mm for implantable biomedical applications in Chapter 5. The antenna can cover three bands viz., ISM band (2450 MHz), WMTS band (1427–1432 MHz) and MICS band (433–434 MHz). The antenna could be employed for multiple bandwidths applications which enable the functionalities of power saving and wireless power transfer. To verify the antenna performance in different part of the human body, I employed complex human body numerical tissue phantom and immersed the miniaturized triple-band SS-PIFA inside the mimicking phantom. The proposed DS-PIFA performed well in those locations and could cover the MICS, WMTS and ISM bands fully with a good impedance bandwidth margin. The design of highly compact antenna, operating over multiple biotelemetry bands, either printed on FR4 or on Rogers 3210 substrate is offered to enable low profile and reduce the overall antenna weight using light conducting and dielectric materials. The measured performance was obtained using a pork skin experimental phantom to validate the calculated results. The proposed implantable triple-band antenna exhibits good radiation efficiency, wide impedance matching, smaller size, low profile and lightweight.

Moreover, a very wideband compact head implantable antenna is also proposed in Chapter 5 to satisfy the wideband antenna requirement for scalp embedded healthcare monitoring systems. I have designed and fabricated a compact folded oval loop antenna covering MICS band up to 1 GHz. Two tunning strips connected to the oval loop are employed to excite a new resonance beside the antenna main resonance, leads to bandwidth enhancement of 200%. It is also possible to fabricate the antenna in 2D using air substrate or printed on dielectric materials. When the available room

in embedded device is limited the antenna could be folded to shape a 3D geometry for occupying minimum area. Moreover, the round shape of the proposed antenna helps to avoid vertexes that could cause tissue injuries.

4. In Chapter 6, I investigated design, modelling, fabrication and measurements of practical non-invasive hyperthermia applicator systems capable of effectively heating up the superficial as well as deep-seated cancerous cells without harming surrounding normal tissues. In this regard, the highlighting of this work is on:

- Design and evaluation of several antenna arrays with different configuration and number of elements performing near field focus radiation.
- Proposing NFF arrays able to focus on small spot inside the human body at different depth.
- Maximizing the power deposition at a prescribed spot to heat the unhealthy biological tissue by employing focusing optimization technique.
- Fabrication of system prototype to conduct the experimental work for selected NFF arrays.
- Conducting the four-stage temperature rise measurement in experimental phantom to investigate the applicator focusing properties.

In this work to conduct the electromagnetic energy deposition in prescribed region, I have employed nearfield focused antenna technology. NF focused antennas can be realized by pyramidal or conical horns with a focalizing lens in front of the antenna aperture, but usually they are heavy, bulky and expensive [187-190]. Alternative solutions are based on either reflector antennas or Fresnel Zone antennas [187, 188], however, they have non-planar structure not suitable for patient anatomy.

To overcome these issues, planar microstrip arrays featuring low cost, lightweight and low profile could be employed for NF focused applicators. My proposed system consists of simple and inexpensive components and employ introduced easy to fabricate array elements for an improved radiation efficiency and a practical approach. I presented a planar antenna array for non-invasive microwave hyperthermia applications. The proposed near field focused (NFF) array covers ISM 2.45 GHz and consists of 25 miniaturized DS-PIFAs. The array is immersed inside a coupling bolus occupying a volume of 8.3 cm^3 (152 cm^3 including bolus). The proposed NFF array, outperforming pervious work reported in the literature [117, 192-195], can focus on small target with a size of 10 × 10 mm and has an effective penetration depth up to 55 mm and generates minimum number of adverse hot regions to protect normal cells from generated artificial heat. The presented array has a compact size of 72 × 72 × 1.6 mm, so that the system size would be small and easy to fit to contoured patient anatomy.

To study how the array configuration and size, in term of number of elements, could enhance the focusing performance effect, first, I designed a four element linear array in the rectangular coordinate which could not focus on small area due to its lower directivity. Therefore, a circular array with a sixteen elements has been designed, however, my calculations indicate that circular array could not focus on the tumor precisely at lower depth inside the body. Consequently, I employed the square configuration to investigate its performance when using a similar and same number of radiating elements. The sixteen elements NFF square array is able to focus on single and smaller area compare to the sixteen elements NFF circular array. The array performance comparison between the proposed 4 × 4 and 5 × 5 rectangular arrays

revealed that for the same focal distance, the 5 × 5 array could enhanced the focusing properties significantly, however, its feeding network is more complicated.

To simplify the feeding network of the applicator and reduce the system cost, I designed twelve NFF planar arrays with different configuration consists of eight active elements and verified their performance using numerical accurate human body model. Here, the challenges, which I have overcome for the advance antenna array design, include but not limited to effective coupling and penetration into heterogeneous lossy body tissues, operating in the antenna near field, and control of three dimensional power deposition patterns for heating up target regions. The proposed "Outer Circle and Inner Square" arrangement satisfies the entire requirements needed for the system and able to focus on small targets with a size of 15 × 15 mm, it has an effective penetration depth up to 50 mm. Moreover, the introduced applicator also uses the limited number of miniaturized radiators with the compact size of 8 × 8 × 1.6 mm to reduce the applicator size. This configuration has the advantage of excellent size reduction of 50% compared with the 25 elements array reported in this work and occupies a volume of 4.1 cm^3 (78.8 cm^3 including bolus).

To maximize the energy deposition at a prescribed area precisely and heat up the unhealthy biological tissue, I have employed an appropriate optimization method to determine the excitation distribution for the array antenna elements. This is one of the most important procedure in the design of the NFF antenna array for medical applications such as non-invasive microwave hyperthermia. The focusing optimization technic used to enhance the amplitude and phase distribution of the array feeding network, could also successfully reduce the number of undesired hot spots by minimizing the side lobs level. By using this method, the focal distance could be adjusted in the Fresnel region of the proposed array and the optimal excitation

distribution for the array elements as well as the maximum power transmission efficiency for the system can be obtained.

To carry out the experimental work, a system prototype has been built using different electronics and microwave components. This setup could be used for all of the proposed arrays to measure the temperature raise inside the experimental meat phantom and investigate the applicator focusing performance. In order to verify the impedance characteristic of the proposed I arrays all of the twelve designed has been fabricated using FR4 substrate. I have reported the measured result on reflection coefficient and scattering parameters for the selected designs when the proposed near field focused antenna array immersed inside the coupling bolus and placed close by inside the experimental phantom. The comparison between measured and calculated results on scattering parameters show good agreement. Furthermore, I concluded that the level of mutual coupling between the array's active elements is small enough to maintain the near field focusing properties for the proposed NFF applicator.

The temperature rise measurement is configured in four stages as described in Chapter 6 to verify the feasibility of the effective heating treatment. The average temperature distribution reaches to its maximum of 44.5 °C at depth of 30 mm when the duration of the heating time was set to 60 minutes. The proposed radiating NFF antenna array can deposit the electromagnetic energy deep inside the human tissue in a small desired area. The presented NI-LMH system is smaller and more efficient (consume less power) compare to systems presented in the literature [200, 206, 207].

7.2 Future work

In this dissertation, several aspects relevant to the body-worn and implantable antennas have been addressed. Additionally, different ideas on how new research work could be carry out based on the findings of this study, these improvements and open issues may be considered for further investigations under the following categories:

New materials for antenna structure: Further studies on new materials such as biodegradable substance and organic based materials for biomedical implantable antennas should be conducted. The organic based materials show improved biocompatibility over long term of antenna implantation. On the other hand, the main advantage of biodegradable antennas and devices, for both patients and surgeons, is the safely degrading over the time. This will help to avoid additional removal surgery and can save the cost of the operation. Recently, biodegradable silk have been proposed for implantable antennas inside the human body, however, much more designs are still required.

Development of embedded flexible antennas: The introduction of flexible properties to the embedded antennas add enormous benefits to the implantable antennas in specific applications such as ocular implants. The bendable antenna could conform easily to the contour of the body organs, providing larger antenna aperture. For instance, design of intraocular and extraocular compact antennas is a solid topic for further studies. The research work may include investigation of antenna placement as well as different miniaturization techniques. The research work may also cover investigations on the most appropriate materials which can be employed as the antenna

substrate and/or superstrate. Furthermore, the effect of bending the antenna structure on the its radiation performance should be included.

In vivo characterization: The next step for this work is in vivo measurement, it was unfortunate that during the lifecycle of this project I could not obtain ethics approval to carry out such an experiment. Even though human body phantoms of brilliant precision are numerically available to mimic the antenna implantation in human tissue, the results must be validate before practical realization. In vivo experiment may include the adoption of rat, hare or pig in place of a human tissue due to the dielectric properties similarity between them. It is necessary to develop the entire implantable device since the antenna is fully functional, in a normal operation, when it is connected to the electronics. This is essential due to the fact that in vivo experiment is questionable (most improbable) without antenna integration with other components such as Tx circuit, power and control unit. The realization of fully implantable device requires a multidisciplinary approach which combine engineering and medicine. Here, collaboration with a medical team as well as prototyping team is needed prior the in vivo measurement could be materialized by embedding the entire device into a living human tissue.

PAPERS PUBLISHED SO FAR

Ananda S. Mohan, A. Boddupalli, F. Gozasht, S. H. Ling, “Techniques for RF Localization of Wireless Capsule Endoscopy”, In proceedings of the International Conference on Electromagnetics in Advanced Applications (ICEAA 2016), Sep. 2016, Cairns, Australia.

F. Gozasht, A. Boddupalli, S. H. Ling, Ananda S. Mohan, “Singly-fed Shaped Planar Inverted-F Antenna for Circular Polarization”, In proceedings of the 2nd Australian Microwave Symposium, Feb. 2016, Adelaide, Australia.

F. Gozasht, A. Sanagavarapu Mohan, “Miniature Implantable PIFA for Telemetry in the ISM Band: Design and Link Budget Analysis”, In proceedings of the International Symposium on Antennas and Propagation (ISAP2015), Nov, 2015. Hobart, Australia.

F. Gozasht, A. Sanagavarapu Mohan, “Miniaturized implantable DS-PIFA antenna for biomedical applications”, In proceedings of the 10th EAI International Conference on Body Area Networks (BodyNets 2015), pp. 67-70, Sep, 2015. Sydney, Australia. doi: 10.4108/eai.28-9-2015.2261517

F. Gozasht, A. Sanagavarapu Mohan, “IMPLANTABLE MINIATURAIZED DUAL SLOT-PIFA ANTENNA FOR BIOMEDICAL APPLICATIONS”, In proceedings of the Fourteenth Australian Symposium on Antennas, Feb. 2015. Sydney, Australia.

F. Gozasht, Kevin Po, A. Sanagavarapu Mohan, “Design of a UWB printed G-shaped monopole antenna using characteristic modes”, In proceedings of the International Workshop on Antenna Technology (iWAT 2014), pp. 332-335, March, 2014. Sydney, Australia. doi: 10.1109/IWAT.2014.6958679

F. Gozasht, A. Sanagavarapu Mohan, “Miniaturized Slot PIFA Antenna for Tripleband Implantable Biomedical Applications”, In proceedings of the 2013 IEEE MTT-S International Microwave Workshop Series on RF and Wireless Technologies for Biomedical and Healthcare Applications (IMWS-BIO), pp. 1-3 Dec. 2013, Singapore, Singapore. doi: 10.1109/IMWS-BIO.2013.6756180

F. Gozasht, Md. Delwar Hossain, Ananda Sanagavarapu Mohan, “Miniaturized E-Shaped PIFA Antenna for Wideband Implantable Biomedical Applications”, In proceedings of the International Conference on Electromagnetics in Advanced Applications (ICEAA 2013), pp. 832-835, Sep. 2013, Torino, Italy. doi:10.1109/ICEAA.2013.6632355

REFERENCES

[1] A. Rosen, M. A. Stuchly, and A. Vander Vorst, "Applications of RF/microwaves in medicine," *IEEE Transactions on Microwave Theory and Techniques,* vol. 50, no. 3, pp. 963-974, 2002.

[2] R. Bashirullah, "Wireless implants," *IEEE microwave magazine,* vol. 11, no. 7, pp. S14-S23, 2010.

[3] D. Panescu, "Emerging technologies [wireless communication systems for implantable medical devices]," *IEEE Engineering in Medicine and Biology Magazine,* vol. 27, no. 2, 2008.

[4] D. Halperin, T. S. Heydt-Benjamin, K. Fu, T. Kohno, and W. H. Maisel, "Security and privacy for implantable medical devices," *IEEE pervasive computing,* vol. 7, no. 1, p. 10, 2008.

[5] P. Valdastri, A. Menciassi, A. Arena, C. Caccamo, and P. Dario, "An implantable telemetry platform system for in vivo monitoring of physiological parameters," *IEEE Transactions on Information Technology in Biomedicine,* vol. 8, no. 3, pp. 271-278, 2004.

[6] K. Najafi, "Packaging of implantable microsystems," in *Sensors, 2007 IEEE*, 2007, pp. 58-63: IEEE.

[7] E. A. Johannessen, L. Wang, C. Wyse, D. R. Cumming, and J. M. Cooper, "Biocompatibility of a lab-on-a-pill sensor in artificial gastrointestinal environments," *IEEE Transactions on Biomedical Engineering,* vol. 53, no. 11, pp. 2333-2340, 2006.

[8] F. C. C. F. Std. (CFR, Part 95.601-673 Subpart E, Part 95.1201-1221 Subpart I, 2009, formerly Medical Implanted Communication System (MICS).). *Medical Device Radiocommunications Service (MedRadio)*. Available: http://wireless.fcc.gov/services/index.htm?job=servicehome&id=medicalimplant

[9] A. C. a. M. A. plan. (2018). *Australian Radiofrequency Spectrum, Plan 2017*. Available: www.acma.gov.au

[10] A. C. a. M. Authority. (2013). *Identifying spectrum opportunities for wireless biomedical telemetry devices in bands used by television and datacasting services, Spectrum Planning Team 2001, .* Available: www.acma.gov.au

[11] *ERC recommendation 70–3 relating to the use of short range devices (SRD)," in Eur. Postal Telecommun. Admin. Conf., Tromso, Norway, 1997, CEPT/ERC70-03, Annex 12.*

[12] *Standard for Safety Levels with Respect to Human Exposure to Radio Frequency Electromagnetic Fields, 3 kHz to 300 GHz*, Std C95.TM, 1999.

[13] C. Liu, Y.-X. Guo, and S. Xiao, "A review of implantable antennas for wireless biomedical devices," in *Forum for electromagnetic research methods and application technologies (FERMAT)*, 2016.

[14] W. Amer, G. Y. Tian, and C. Tsimenidis, "Sensing passive object existence within an antenna near field based on return loss," in *Antennas and Propagation Conference (LAPC), 2014 Loughborough*, 2014, pp. 400-404: IEEE.

[15] E. Hernández-Gómez, J. Olvera-Cervantes, A. Corona-Chávez, and M. Sosa-Morales, "Development of a low cost dielectric permittivity sensor for organic and inorganic materials in the microwave frequency range," in *Sensors (IBERSENSOR), 2014 IEEE 9th Ibero-American Congress on*, 2014, pp. 1-4: IEEE.

[16] N. Madan, "Embedded antennas for the measurement of electrical properties of materials," M.S. thesis, Dept. Elect. Comput. Eng.,, Utah State Univ., Logan, UT, 2002.

[17] C. Deffendol and C. Furse, "Microstrip antennas for dielectric property measurement," in *Antennas and Propagation Society International Symposium, 1999. IEEE*, 1999, vol. 3, pp. 1954-1956: IEEE.

[18] I. Bahl and S. S. Stuchly, "Analysis of a microstrip covered with a lossy dielectric," *IEEE Transactions on Microwave Theory and Techniques,* vol. 28, no. 2, pp. 104-109, 1980.

[19] D. Johnson, E. Cherkaev, C. Furse, and A. C. Tripp, "Cross-borehole delineation of a conductive ore deposit in a resistive host—experimental design," *Geophysics,* vol. 66, no. 3, pp. 824-835, 2001.

[20] D. Johnson, C. Furse, and A. C. Tripp, "FDTD modeling and validation of EM survey tools," *Microwave and Optical Technology Letters,* vol. 34, no. 6, pp. 427-429, 2002.

[21] P. Cherry and M. Iskander, "Calculations of heating patterns of an array of microwave interstitial antennas," *IEEE transactions on biomedical engineering,* vol. 40, no. 8, pp. 771-779, 1993.

[22] R. Nevels, D. Arndt, J. Carl, G. Raffoul, and A. Pacifico, "Microwave antenna design for myocardial tissue ablation applications," in *Antennas and Propagation Society International Symposium, 1995. AP-S. Digest*, 1995, vol. 3, p. 1572 vol. 3: IEEE.

[23] A. Rosen, "Microwave application in cancer therapy, cardiology and measurement techniques: A short overview," *IEEE MTT Newsletter,* pp. 17-20, 1990.

[24] B. Steinhaus, R. Smith, and P. Crosby, "The role of telecommunications in future implantable device systems," in *Engineering in Medicine and Biology Society, 1994. Engineering Advances: New Opportunities for Biomedical Engineers. Proceedings of the 16th Annual International Conference of the IEEE*, 1994, vol. 2, pp. 1013-1014: IEEE.

[25] R. Weir, P. Troyk, G. DeMichele, and T. Kuiken, "Implantable myoelectric sensors (IMES) for upper-extremity prosthesis control-preliminary work," in *Engineering in Medicine and Biology Society, 2003. Proceedings of the 25th Annual International Conference of the IEEE*, 2003, vol. 2, pp. 1562-1565: IEEE.

[26] G. Crumley, N. Evans, J. Burns, and T. Trouton, "On the design and assessment of a 2.45 GHz radio telecommand system for remote patient monitoring," *Medical Engineering and Physics,* vol. 20, no. 10, pp. 750-755, 1999.

[27] C. M. Zierhofer and E. S. Hochmair, "High-efficiency coupling-insensitive transcutaneous power and data transmission via an inductive link," *IEEE transactions on biomedical engineering,* vol. 37, no. 7, pp. 716-722, 1990.

[28] C. Furse, "Design an antenna for pacemaker communication," *Microwaves & Rf,* vol. 39, no. 3, pp. 73-+, 2000.

[29] W. Scanlon, N. Evans, and J. Burns, "FDTD analysis of close-coupled 418 MHz radiating devices for human biotelemetry," *Physics in Medicine & Biology,* vol. 44, no. 2, p. 335, 1999.

[30] H.-Y. Lin, M. Takahashi, K. Saito, and K. Ito, "Performance of implantable folded dipole antenna for in-body wireless communication," *IEEE Transactions on Antennas and Propagation,* vol. 61, no. 3, pp. 1363-1370, 2013.

[31] T. Karacolak, A. Z. Hood, and E. Topsakal, "Design of a Dual-Band Implantable Antenna and Development of Skin Mimicking Gels for Continuous Glucose Monitoring," *IEEE Transactions on Microwave Theory and Techniques,* vol. 56, no. 4, pp. 1001-1008, Apr. 2008.

[32] Y. Rahmat-Samii, J. Kim, and C. Balanis, *Implanted Antennas in Medical Wireless Communications (Synthesis Lectures on Antennas and Propagation)*. Morgan & Claypool Publishers, 2006, p. 82.

[33] X. Meng *et al.*, "Dynamic evaluation of a digital wireless intracranial pressure sensor for the assessment of traumatic brain injury in a swine model," *IEEE Transactions on Microwave Theory and Techniques,* vol. 61, no. 1, pp. 316-325, 2013.

[34] F.-J. Huang, C.-M. Lee, C.-L. Chang, L.-K. Chen, T.-C. Yo, and C.-H. Luo, "Rectenna application of miniaturized implantable antenna design for triple-band biotelemetry communication," *IEEE Transactions on Antennas and Propagation,* vol. 59, no. 7, pp. 2646-2653, 2011.

[35] R. Warty, M.-R. Tofighi, U. Kawoos, and A. Rosen, "Characterization of implantable antennas for intracranial pressure monitoring: Reflection by and transmission through a scalp phantom," *IEEE Transactions on Microwave Theory and Techniques,* vol. 56, no. 10, pp. 2366-2376, 2008.

[36] A. Kiourti, M. Christopoulou, and K. S. Nikita, "Performance of a novel miniature antenna implanted in the human head for wireless biotelemetry," in *Antennas and Propagation (APSURSI), 2011 IEEE International Symposium on*, 2011, pp. 392-395: IEEE.

[37] H. Usui, M. Takahashi, and K. Ito, "Radiation characteristics of an implanted cavity slot antenna into the human body," in *Antennas and Propagation Society International Symposium 2006, IEEE*, 2006, pp. 1095-1098: IEEE.

[38] W. Xia, K. Saito, M. Takahashi, and K. Ito, "Performances of an implanted cavity slot antenna embedded in the human arm," *IEEE Transactions on Antennas and Propagation,* vol. 57, no. 4, pp. 894-899, 2009.

[39] T. Karacolak and E. Topsakal, "Electrical properties of nude rat skin and design of implantable antennas for wireless data telemetry," in *Microwave Symposium Digest, 2008 IEEE MTT-S International*, 2008, pp. 907-910: IEEE.

[40] E. Y. Chow, Y. Ouyang, B. Beier, W. J. Chappell, and P. P. Irazoqui, "Evaluation of cardiovascular stents as antennas for implantable wireless applications," *IEEE Transactions on Microwave Theory and Techniques,* vol. 57, no. 10, pp. 2523-2532, 2009.

[41] Z. Duan, Y.-X. Guo, M. Je, and D.-L. Kwong, "Design and in vitro test of a differentially fed dual-band implantable antenna operating at MICS and ISM bands," *IEEE transactions on antennas and propagation,* vol. 62, no. 5, pp. 2430-2439, 2014.

[42] A. Kiourti, M. Tsakalakis, and K. S. Nikita, "Parametric study and design of implantable PIFAs for wireless biotelemetry," in *International Conference on Wireless Mobile Communication and Healthcare*, 2011, pp. 96-102: Springer.

[43] L.-J. Xu, Y.-X. Guo, and W. Wu, "Miniaturized dual-band antenna for implantable wireless communications," *IEEE Antennas and Wireless Propagation Letters,* vol. 13, pp. 1160-1163, 2014.

[44] A. Kiourti and K. S. Nikita, "Meandered versus spiral novel miniature PIFAs implanted in the human head: Tuning and performance," in *International Conference on Wireless Mobile Communication and Healthcare*, 2011, pp. 80-87: Springer.

[45] P. Soontornpipit, C. M. Furse, and Y. C. Chung, "Miniaturized biocompatible microstrip antenna using genetic algorithm," *IEEE Transactions on Antennas and Propagation,* vol. 53, no. 6, pp. 1939-1945, 2005.

[46] W.-C. Liu, S.-H. Chen, and C.-M. Wu, "Implantable broadband circular stacked PIFA antenna for biotelemetry communication," *Journal of Electromagnetic Waves and Applications,* vol. 22, no. 13, pp. 1791-1800, 2008.

[47] A. Kiourti and K. S. Nikita, "Miniature scalp-implantable antennas for telemetry in the MICS and ISM bands: design, safety considerations and link budget analysis," *IEEE Transactions on Antennas and Propagation,* vol. 60, no. 8, pp. 3568-3575, 2012.

[48] P. Soontornpipit, C. M. Furse, and Y. C. Chung, "Design of implantable microstrip antenna for communication with medical implants," *IEEE Transactions on Microwave theory and techniques,* vol. 52, no. 8, pp. 1944-1951, 2004.

[49] M. L. Scarpello *et al.*, "Design of an implantable slot dipole conformal flexible antenna for biomedical applications," *IEEE Transactions on Antennas and Propagation,* vol. 59, no. 10, pp. 3556-3564, 2011.

[50] K. Jaehoon and Y. Rahmat-Samii, "Implanted antennas inside a human body: simulations, designs, and characterizations," *IEEE Transactions on Microwave Theory and Techniques,* vol. 52, no. 8, pp. 1934-1943, 2004.

[51] T. Karacolak, R. Cooper, J. Butler, S. Fisher, and E. Topsakal, "In Vivo Verification of Implantable Antennas Using Rats as Model Animals," *IEEE Antennas and Wireless Propagation Letters,* vol. 9, pp. 334-337, 2010.

[52] H. Li, Y. X. Guo, C. Liu, S. Xiao, and L. Li, "A Miniature-Implantable Antenna for MedRadio-Band Biomedical Telemetry," *IEEE Antennas and Wireless Propagation Letters,* vol. 14, pp. 1176-1179, 2015.

[53] C. Liu, Y. X. Guo, and S. Xiao, "A Hybrid Patch/Slot Implantable Antenna for Biotelemetry Devices," *IEEE Antennas and Wireless Propagation Letters,* vol. 11, pp. 1646-1649, 2012.

[54] L. J. Xu, Y. X. Guo, and W. Wu, "Bandwidth Enhancement of an Implantable Antenna," *IEEE Antennas and Wireless Propagation Letters,* vol. 14, pp. 1510-1513, 2015.

[55] T. F. Chien, C. M. Cheng, H. C. Yang, J. W. Jiang, and C. H. Luo, "Development of Nonsuperstrate Implantable Low-Profile CPW-Fed Ceramic Antennas," *IEEE Antennas and Wireless Propagation Letters,* vol. 9, pp. 599-602, 2010.

[56] W. C. Liu, S. H. Chen, and C. M. Wu, "Bandwidth enhancement and size reduction of an implantable PIFA antenna for biotelemetry devices," *Microwave and Optical Technology Letters,* vol. 51, no. 3, pp. 755-757, 2009.

[57] W. C. Liu, F. M. Yeh, and M. Ghavami, "Miniaturized implantable broadband antenna for biotelemetry communication," *Microwave and Optical Technology Letters,* vol. 50, no. 9, pp. 2407-2409, 2008.

[58] J. Kim and Y. Rahmat-Samii, "Planar inverted-F antennas on implantable medical devices: Meandered type versus spiral type," *Microwave and Optical Technology Letters,* vol. 48, no. 3, pp. 567-572, 2006.

[59] C.-M. Lee, T.-C. Yo, C.-H. Luo, C.-H. Tu, and Y.-Z. Juang, "Compact broadband stacked implantable antenna for biotelemetry with medical devices," *Electronics Letters,* vol. 43, no. 12, pp. 660-662, 2007.

[60] C.-M. Lee, T.-C. Yo, and C.-H. Luo, "Compact broadband stacked implantable antenna for biotelemetry with medical devices," in *Wireless and Microwave Technology Conference, 2006. WAMICON'06. IEEE Annual*, 2006, pp. 1-4: IEEE.

[61] W. A. Qureshi, "Current and future applications of the capsule camera," *Nature reviews drug discovery,* vol. 3, no. 5, p. 447, 2004.

[62] S. H. Lee *et al.*, "A Wideband Spiral Antenna for Ingestible Capsule Endoscope Systems: Experimental Results in a Human Phantom and a Pig," *IEEE Transactions on Biomedical Engineering,* vol. 58, no. 6, pp. 1734-1741, June 2011.

[63] S. I. Kwak, K. Chang, and Y. J. Yoon, "The helical antenna for the capsule endoscope," in *Antennas and Propagation Society International Symposium, 2005 IEEE*, 2005, vol. 2, pp. 804-807: IEEE.

[64] P. M. Izdebski, H. Rajagopalan, and Y. Rahmat-Samii, "Conformal Ingestible Capsule Antenna: A Novel Chandelier Meandered Design," *IEEE Transactions on Antennas and Propagation,* vol. 57, no. 4, pp. 900-909, Apr. 2009.

[65] X. Cheng, D. E. Senior, C. Kim, and Y. K. Yoon, "A Compact Omnidirectional Self-Packaged Patch Antenna With Complementary Split-Ring Resonator Loading for Wireless Endoscope Applications," *IEEE Antennas and Wireless Propagation Letters,* vol. 10, pp. 1532-1535, 2011.

[66] H. Rajagopalan and Y. Rahmat-Samii, "Wireless medical telemetry characterization for ingestible capsule antenna designs," *IEEE Antennas and Wireless Propagation Letters,* vol. 11, pp. 1679-1682, 2012.

[67] C. Liu, Y. X. Guo, and S. Xiao, "Circularly Polarized Helical Antenna for ISM-Band Ingestible Capsule Endoscope Systems," *IEEE Transactions on Antennas and Propagation,* vol. 62, no. 12, pp. 6027-6039, Dec. 2014.

[68] C. Schmidt, F. Casado, A. Arriola, I. Ortego, P. D. Bradley, and D. Valderas, "Broadband UHF Implanted 3-D Conformal Antenna Design and Characterization for In-Off Body Wireless Links," *IEEE Transactions on Antennas and Propagation,* vol. 62, no. 3, pp. 1433-1444, Mar. 2014.

[69] F. Merli, L. Bolomey, J. F. Zurcher, G. Corradini, E. Meurville, and A. K. Skrivervik, "Design, Realization and Measurements of a Miniature Antenna for Implantable Wireless Communication Systems," *IEEE Transactions on Antennas and Propagation,* vol. 59, no. 10, pp. 3544-3555, Oct. 2011.

[70] S. Yun, K. Kim, and S. Nam, "Outer-Wall Loop Antenna for Ultrawideband Capsule Endoscope System," *IEEE Antennas and Wireless Propagation Letters,* vol. 9, pp. 1135-1138, 2010.

[71] S. i. Kwak, K. Chang, and Y. j. Yoon, "Small spiral antenna for wideband capsule endoscope system," *Electronics Letters,* vol. 42, no. 23, pp. 1328-1329, 2006.

[72] E. Y. Chow, M. M. Morris, and P. P. Irazoqui, "Implantable RF medical devices: The benefits of high-speed communication and much greater communication distances in biomedical applications," *IEEE Microwave Magazine,* vol. 14, no. 4, pp. 64-73, 2013.

[73] J. Abadia, F. Merli, J.-F. Zurcher, J. R. Mosig, and A. K. Skrivervik, "3D-spiral small antenna design and realization for biomedical telemetry in the MICS band," *Radioengineering,* vol. 18, no. 4, pp. 359-367, 2009.

[74] Y. Zhao, Y. Hao, A. Alomainy, and C. Parini, "UWB on-body radio channel modeling using ray theory and subband FDTD method," *IEEE Transactions on Microwave Theory and Techniques,* vol. 54, no. 4, pp. 1827-1835, 2006.

[75] A. Alomainy, Y. Hao, X. Hu, C. Parini, and P. Hall, "UWB on-body radio propagation and system modelling for wireless body-centric networks," *IEE Proceedings-Communications,* vol. 153, no. 1, pp. 107-114, 2006.

[76] K. L.-L. Roman, G. Vermeeren, A. Thielens, W. Joseph, and L. Martens, "Characterization of path loss and absorption for a wireless radio frequency link between an in-body endoscopy capsule and a receiver outside the body," *EURASIP Journal on Wireless Communications and Networking,* vol. 2014, no. 1, p. 21, 2014.

[77] W. Lei, H. Chu, and Y.-X. Guo, "Design of a circularly polarized ground radiation antenna for biomedical applications," *IEEE Transactions on Antennas and Propagation,* vol. 64, no. 6, pp. 2535-2540, 2016.

[78] T. W. Koo, Y. J. Hong, G. k. Park, K. Shin, and J. G. Yook, "Extremely Low-Profile Antenna for Attachable Bio-Sensors," *IEEE Transactions on Antennas and Propagation,* vol. 63, no. 4, pp. 1537-1545, Apr. 2015.

[79] P. J. Soh, G. A. E. Vandenbosch, S. L. Ooi, and N. H. M. Rais, "Design of a Broadband All-Textile Slotted PIFA," *IEEE Transactions on Antennas and Propagation,* vol. 60, no. 1, pp. 379-384, Jan. 2012.

[80] T. Alves, B. Poussot, and J. M. Laheurte, "PIFA–Top-Loaded-Monopole Antenna With Diversity Features for WBAN Applications," *IEEE Antennas and Wireless Propagation Letters,* vol. 10, pp. 693-696, 2011.

[81] W. E. Hajj, C. Person, and J. Wiart, "A Novel Investigation of a Broadband Integrated Inverted-F Antenna Design; Application for Wearable Antenna,"

IEEE Transactions on Antennas and Propagation, vol. 62, no. 7, pp. 3843-3846, July 2014.

[82] A. Fort, C. Desset, P. De Doncker, P. Wambacq, and L. Van Biesen, "An ultra-wideband body area propagation channel model-from statistics to implementation," *IEEE Transactions on Microwave Theory and Techniques,* vol. 54, no. 4, pp. 1820-1826, 2006.

[83] L. Roelens, S. Van den Bulcke, W. Joseph, G. Vermeeren, and L. Martens, "Path loss model for wireless narrowband communication above flat phantom," *Electronics Letters,* vol. 42, no. 1, pp. 10-11, 2006.

[84] A. Alomainy *et al.*, "Statistical analysis and performance evaluation for on-body radio propagation with microstrip patch antennas," *IEEE Transactions on Antennas and Propagation,* vol. 55, no. 1, pp. 245-248, 2007.

[85] P. S. Hall *et al.*, "Antennas and propagation for on-body communication systems," *IEEE Antennas and Propagation Magazine,* vol. 49, no. 3, pp. 41-58, 2007.

[86] L. Roelens, W. Joseph, E. Reusens, G. Vermeeren, and L. Martens, "Characterization of scattering parameters near a flat phantom for wireless body area networks," *IEEE Transactions on Electromagnetic Compatibility,* vol. 50, no. 1, pp. 185-193, 2008.

[87] E. Reusens *et al.*, "Characterization of on-body communication channel and energy efficient topology design for wireless body area networks," *IEEE Transactions on Information Technology in Biomedicine,* vol. 13, no. 6, pp. 933-945, 2009.

[88] A. Alomainy and Y. Hao, "Modeling and characterization of biotelemetric radio channel from ingested implants considering organ contents," *IEEE Transactions on Antennas and Propagation,* vol. 57, no. 4, pp. 999-1005, 2009.

[89] D. Kurup, W. Joseph, G. Vermeeren, and L. Martens, "Path loss model for in-body communication in homogeneous human muscle tissue," *Electronics letters,* vol. 45, no. 9, pp. 453-454, 2009.

[90] S. Agneessens, P. Van Torre, E. Tanghe, G. Vermeeren, W. Joseph, and H. Rogier, "On-body wearable repeater as a data link relay for in-body wireless implants," *IEEE Antennas and Wireless Propagation Letters,* vol. 11, pp. 1714-1717, 2012.

[91] A. Alomainy, Y. Hao, Y. Yuan, and Y. Liu, "Modelling and characterisation of radio propagation from wireless implants at different frequencies," in *Wireless Technology, 2006. The 9th European Conference on*, 2006, pp. 119-122: IEEE.

[92] A. Kiourti, K. A. Psathas, P. Lelovas, N. Kostomitsopoulos, and K. S. Nikita, "In vivo tests of implantable antennas in rats: antenna size and intersubject considerations," *IEEE Antennas and Wireless Propagation Letters,* vol. 12, pp. 1396-1399, 2013.

[93] Z. N. Chen, G. C. Liu, and T. S. See, "Transmission of RF signals between MICS loop antennas in free space and implanted in the human head," *IEEE Transactions on Antennas and Propagation,* vol. 57, no. 6, pp. 1850-1854, 2009.

[94] C. A. Roopnariane, M.-R. Tofighi, and C. M. Collins, "Radiation performance of small implanted antennas in head at MICS, ISM, and GPS bands," in *Bioengineering Conference, Proceedings of the 2010 IEEE 36th Annual Northeast*, 2010, pp. 1-2: IEEE.

[95] A. Yakovlev, S. Kim, and A. Poon, "Implantable biomedical devices: Wireless powering and communication," *IEEE Communications Magazine,* vol. 50, no. 4, 2012.

[96] M. R. Mahfouz, M. J. Kuhn, G. To, and A. E. Fathy, "Integration of UWB and wireless pressure mapping in surgical navigation," *IEEE Transactions on Microwave Theory and Techniques,* vol. 57, no. 10, pp. 2550-2564, 2009.

[97] K. Gosalia, G. Lazzi, and M. Humayun, "Investigation of a microwave data telemetry link for a retinal prosthesis," *IEEE Transactions on Microwave Theory and Techniques,* vol. 52, no. 8, pp. 1925-1933, 2004.

[98] M. H. Falk and R. D. Issels, "Hyperthermia in oncology," *Int J Hypertherm,* vol. 17, 2001.

[99] E. L. Jones *et al.*, "Randomized trial of hyperthermia and radiation for superficial tumors," *J Clin Oncol,* vol. 23, 2005.

[100] L. Dubois, J. Pribetich, J. J. Fabre, M. Chive, and Y. Moschetto, "Non-invasive microwave multifrequency radiometry used in microwave hyperthermia for bidimensional reconstruction of temperature patterns," (in eng), *Int J Hyperthermia,* vol. 9, no. 3, pp. 415-31, May-Jun 1993.

[101] K. R. Foster and J. L. Schepps, "Dielectric properties of tumor and normal tissue at radio through microwave frequency," *J Microwave Power,* vol. 16, 1981.

[102] A. P. O'Rourke *et al.*, "Dielectric properties of human normal, malignant and cirrhotic liver tissue: in vivo and ex vivo measurements from 0.5 to 20 GHz using a precision open-ended coaxial probe," *Phys Med Biol,* vol. 52, 2007.

[103] P. Wust *et al.*, "Hyperthermia in combined treatment of cancer," *Lancet Oncol,* vol. 3, 2002.

[104] V. E. Kouloulias *et al.*, "Intraoperative hyperthermia in conjunction with multi-schedule chemotherapy (pre-, intra- and post-operative), by-pass surgery, and post-operative radiotherapy for the management of unresectable pancreatic adenocarcinoma," *Int J Hypertherm,* vol. 18, 2002.

[105] K. D. Stephan, J. B. Mead, D. M. Pozar, L. Wang, and J. A. Pearce, "A Near Field Focused Microstrip Array for a Radiometric Temperature Sensor," *IEEE Transactions on Antennas and Propagation,* vol. 55, no. 4, pp. 1199-1203, 2007.

[106] E. Zastrow, S. C. Hagness, B. D. V. Veen, and J. E. Medow, "Time-Multiplexed Beamforming for Noninvasive Microwave Hyperthermia Treatment," *IEEE Transactions on Biomedical Engineering,* vol. 58, no. 6, pp. 1574-1584, 2011.

[107] J. T. Loane and S. W. Lee, "Gain optimization of a near-field focusing array for hyperthermia applications," *IEEE Transactions on Microwave Theory and Techniques,* vol. 37, no. 10, pp. 1629-1635, 1989.

[108] A. Buffi, P. Nepa, and G. Manara, "Design Criteria for Near-Field-Focused Planar Arrays," *IEEE Antennas and Propagation Magazine,* vol. 54, no. 1, pp. 40-50, 2012.

[109] J. Álvarez, R. G. Ayestarán, G. León, J. A. López-Fernández, L. F. Herrán, and F. Las-Heras, "Optimization framework on antenna arrays for near field multifocusing," in *Proceedings of the 2012 IEEE International Symposium on Antennas and Propagation*, 2012, pp. 1-2.

[110] E. Correia, H. P. Kok, M. de Greef, A. Bel, N. van Wieringen, and J. Crezee, "Body conformal antennas for superficial hyperthermia: the impact of bending contact flexible microstrip applicators on their electromagnetic behavior," *IEEE Trans Biomed Eng,* vol. 56, 2009.

[111] M. M. Paulides, J. F. Bakker, and G. C. van Rhoon, "A patch antenna design for application in a phased-array head and neck hyperthermia applicator," *IEEE Trans Biomed Eng,* vol. 54, 2007.

[112] M. Converse, E. J. Bond, S. C. Hagness, and B. D. Van Veen, "Ultrawide-band microwave space-time beamforming for hyperthermia treatment of breast cancer: A computational feasibility study," *IEEE Transactions on microwave theory and techniques,* vol. 52, no. 8, pp. 1876-1889, 2004.

[113] F. Jouvie, J. C. Bolomey, and G. Gaboriaud, "Discussion of the capabilities of microwave phased arrays for hyperthermia treatment of neck tumors," *IEEE Trans Micr Theor Tech,* vol. 34, 1986.

[114] R. L. Magin and A. F. Peterson, "Noninvasive microwave phased arrays for local hyperthermia: a review," *Int J Hyperthermia,* vol. 5, 1989.

[115] S. M. Yacoob and N. S. Hassan, "FDTD analysis of a noninvasive hyperthermia system for brain tumors," *BioMedical Engineering OnLine,* journal article vol. 11, no. 1, p. 47, August 14 2012.

[116] Y. Ishihara, Y. Gotanda, N. Wadamori, and J. Matsuda, "Hyperthermia applicator based on a reentrant cavity for localized head and neck tumors," *Rev Sci Instrum,* vol. 78, 2007.

[117] I. A. Gouzouasis and I. S. Karanasiou, "Uzunoglu NKP: FDTD Study of the focusing properties of a hybrid hyperthermia and radiometry imaging system using a realistic human head model," *Proceedings of the 29th IEEE Engineering in Med and Biology Soc,* vol. 3552, 2007.

[118] I. S. Karanasiou, K. T. Karathanasis, A. Garetsos, and N. K. Uzunoglu, "Development and Laboratory Testing of a Noninvasive Intracranial Focused Hyperthermia System," *IEEE Trans Micr Theor and Tech,* vol. 56, p. 12, 2008.

[119] I. A. Gouzouasis, K. T. Karathanasis, I. S. Karanasiou, and N. K. Uzunoglu, "Contactless passive diagnosis for brain intracranial applications: A study using dielectric matching materials," *Bioelectromagnetics,* vol. 31, 2010.

[120] R. S. Alrawashdeh, Y. Huang, M. Kod, and A. A. B. Sajak, "A broadband flexible implantable loop antenna with complementary split ring resonators," *IEEE antennas and wireless propagation letters,* vol. 14, pp. 1506-1509, 2015.

[121] C. Liu, Y.-X. Guo, and S. Xiao, "Capacitively loaded circularly polarized implantable patch antenna for ISM band biomedical applications," *IEEE transactions on antennas and propagation,* vol. 62, no. 5, pp. 2407-2417, 2014.

[122] R. Das and H. Yoo, "Biotelemetry and Wireless Powering for Leadless Pacemaker Systems," *IEEE Microwave and Wireless Components Letters,* vol. 25, no. 4, pp. 262-264, 2015.

[123] J. S. Ho *et al.*, "Wireless power transfer to deep-tissue microimplants," *Proceedings of the National Academy of Sciences,* vol. 111, no. 22, pp. 7974-7979, 2014.

[124] C. Liu, Y. X. Guo, and S. Xiao, "Compact Dual-Band Antenna for Implantable Devices," *IEEE Antennas and Wireless Propagation Letters,* vol. 11, pp. 1508-1511, 2012.

[125] A. Kiourti, K. A. Psathas, and K. S. Nikita, "Implantable and ingestible medical devices with wireless telemetry functionalities: A review of current status and challenges," *Bioelectromagnetics,* vol. 35, no. 1, pp. 1-15, 2014.

[126] L. J. Xu, Y. X. Guo, and W. Wu, "Miniaturised slot antenna for biomedical applications," *Electronics Letters,* vol. 49, no. 17, pp. 1060-1061, 2013.

[127] C. J. Sanchez-Fernandez, O. Quevedo-Teruel, J. Requena-Carrion, L. Inclan-Sanchez, and E. Rajo-Iglesias, "Dual-band microstrip patch antenna based on short-circuited ring and spiral resonators for implantable medical devices," *IET Microwaves, Antennas & Propagation,* vol. 4, no. 8, pp. 1048-1055, 2010.

[128] L. J. Xu, Y. X. Guo, and W. Wu, "Miniaturized Circularly Polarized Loop Antenna for Biomedical Applications," *IEEE Transactions on Antennas and Propagation,* vol. 63, no. 3, pp. 922-930, 2015.

[129] A. Kiourti, J. R. Costa, C. A. Fernandes, A. G. Santiago, and K. S. Nikita, "Miniature Implantable Antennas for Biomedical Telemetry: From Simulation to Realization," *IEEE Transactions on Biomedical Engineering,* vol. 59, no. 11, pp. 3140-3147, 2012.

[130] P. A. Floor *et al.*, "In-Body to On-Body Ultrawideband Propagation Model Derived From Measurements in Living Animals," *IEEE Journal of Biomedical and Health Informatics,* vol. 19, no. 3, pp. 938-948, 2015.

[131] F. Merli *et al.*, "Example of Data Telemetry for Biomedical Applications: An In Vivo Experiment," *IEEE Antennas and Wireless Propagation Letters,* vol. 11, pp. 1650-1654, 2012.

[132] A. Electromagnetics. *High Frequency Structure Simulator (HFSS) (Ver. 17.2 ed.)*. Available: http://www.ansys.com

[133] FEKO™. *EM Software & Systems (7.0.2 ed.)*. Available: http://www.feko.info

[134] E. Moradi *et al.*, "Miniature implantable and wearable on-body antennas: towards the new era of wireless body-centric systems [antenna applications corner]," *IEEE Antennas and Propagation Magazine,* vol. 56, no. 1, pp. 271-291, 2014.

[135] R. F. a. C. P. D.Andreuccetti. (2015). *An Internet resource for the calculation of the dielectric properties of body tissues in the frequency range 10 Hz - 100 GHz*. Available: http://niremf.ifac.cnr.it/tissprop/

[136] Y. Okano and H. Shimoji, "Comparison Measurement for Specific Absorption Rate With Physically Different Procedure," *IEEE Transactions on Instrumentation and Measurement,* vol. 61, no. 2, pp. 439-446, Feb. 2012.

[137] K. Saito, Y. Hayashi, H. Yoshimura, and K. Ito, "Heating characteristics of array applicator composed of two coaxial-slot antennas for microwave

coagulation therapy," *IEEE Transactions on Microwave Theory and Techniques,* vol. 48, no. 11, pp. 1800-1806, Nov. 2000.

[138] *IEEE standard for safety levels with respect to human exposure to radio frequency electromagnetic fields, 3KHz to 300 GHz*, 2006.

[139] Y. H. P. S. Hall, *Antennas and propagation for body centric wireless communications*. Artech House, Inc. , 2006.

[140] A. Kiourti, J. R. Costa, C. A. Fernandes, and K. S. Nikita, "A Broadband Implantable and a Dual-Band On-Body Repeater Antenna: Design and Transmission Performance," *IEEE Transactions on Antennas and Propagation,* vol. 62, no. 6, pp. 2899-2908, June 2014.

[141] C. M. Lee, T. C. Yo, F. J. Huang, and C. H. Luo, "Bandwidth enhancement of planar inverted-F antenna for implantable biotelemetry," *Microwave and Optical Technology Letters,* vol. 51, no. 3, pp. 749-752, Mar. 2009.

[142] R. Nilavalan, I. J. Craddock, A. Preece, J. Leendertz, and R. Benjamin, "Wideband microstrip patch antenna design for breast cancer tumour detection," *IET Microwaves, Antennas & Propagation,* vol. 1, no. 2, pp. 277-281, Apr. 2007.

[143] T. Dissanayake, K. P. Esselle, and M. R. Yuce, "Dielectric Loaded Impedance Matching for Wideband Implanted Antennas," *IEEE Transactions on Microwave Theory and Techniques,* vol. 57, no. 10, pp. 2480-2487, Oct. 2009.

[144] M. Grimm and D. Manteuffel, "On-Body Antenna Parameters," *IEEE Transactions on Antennas and Propagation,* vol. 63, no. 12, pp. 5812-5821, Dec. 2015.

[145] T. F. Kennedy, P. W. Fink, A. W. Chu, N. J. Champagne, G. Y. Lin, and M. A. Khayat, "Body-Worn E-Textile Antennas: The Good, the Low-Mass, and the Conformal," *IEEE Transactions on Antennas and Propagation,* vol. 57, no. 4, pp. 910-918, Apr. 2009.

[146] P. B. Samal, P. J. Soh, and G. A. E. Vandenbosch, "UWB All-Textile Antenna With Full Ground Plane for Off-Body WBAN Communications," *IEEE Transactions on Antennas and Propagation,* vol. 62, no. 1, pp. 102-108, Jan. 2014.

[147] T. Björninen and F. Yang, "Low-Profile Head-Worn Antenna With a Monopole-Like Radiation Pattern," *IEEE Antennas and Wireless Propagation Letters,* vol. 15, pp. 794-797, 2016.

[148] Z. Wang, L. Z. Lee, D. Psychoudakis, and J. L. Volakis, "Embroidered Multiband Body-Worn Antenna for GSM/PCS/WLAN Communications," *IEEE Transactions on Antennas and Propagation,* vol. 62, no. 6, pp. 3321-3329, June 2014.

[149] W. Thompson, R. Cepeda, G. Hilton, M. A. Beach, and S. Armour, "An Improved Antenna Mounting for Ultra-Wideband On-Body Communications and Channel Characterization," *IEEE Transactions on Microwave Theory and Techniques,* vol. 59, no. 4, pp. 1102-1108, Apr. 2011.

[150] M. Koohestani, J. F. Zürcher, A. A. Moreira, and A. K. Skrivervik, "A Novel, Low-Profile, Vertically-Polarized UWB Antenna for WBAN," *IEEE Transactions on Antennas and Propagation,* vol. 62, no. 4, pp. 1888-1894, Apr. 2014.

[151] A. International, *Handbook of Materials for Medical Device*. Materials Park: OH 44073-0002, 2003.

[152] F. Merli, B. Fuchs, J. R. Mosig, and A. K. Skrivervik, "The effect of insulating layers on the performance of implanted antennas," *IEEE Transactions on Antennas and Propagation,* vol. 59, no. 1, pp. 21-31, 2011.

[153] P. S. Hall and Y. Hao, *Antennas and Propagation for Body-Centric Wireless Communications*, 2 ed. Norwood, United States: Artech House, 2012, p. 410.

[154] C. A. Balanis, *Antenna theory: analysis and design,* , 3rd ed. Hoboken, NJ: : John Wiley & Sons, 2005.

[155] T. S. Rappaport, "Wireless Communications--Principles and Practice, (The Book End)," *Microwave Journal,* vol. 45, no. 12, pp. 128-129, 2002.

[156] P. A. Floor *et al.*, "In-body to on-body ultrawideband propagation model derived from measurements in living animals," *IEEE journal of biomedical and health informatics,* vol. 19, no. 3, pp. 938-948, 2015.

[157] U. Kawoos, X. Meng, S.-M. Huang, A. Rosen, R. M. McCarron, and M. Chavko, "Telemetric intracranial pressure monitoring in blast-induced traumatic brain injury," *IEEE Transactions on Biomedical Engineering,* vol. 61, no. 3, pp. 841-847, 2014.

[158] U. Kawoos, M.-R. Tofighi, R. Warty, F. A. Kralick, and A. Rosen, "In-vitro and in-vivo trans-scalp evaluation of an intracranial pressure implant at 2.4 GHz," *IEEE Transactions on Microwave Theory and Techniques,* vol. 56, no. 10, pp. 2356-2365, 2008.

[159] S.-M. Huang, M.-R. Tofighi, and A. Rosen, "Considerations for the design and placement of implantable annular slot antennas for intracranial pressure monitoring devices," *IEEE Antennas and Wireless Propagation Letters,* vol. 14, pp. 1514-1517, 2015.

[160] A. Kiourti and K. S. Nikita, "Recent advances in implantable antennas for medical telemetry [education column]," *IEEE Antennas and Propagation Magazine,* vol. 54, no. 6, pp. 190-199, 2012.

[161] C. Liu, Y.-X. Guo, and S. Xiao, "Compact dual-band antenna for implantable devices," *IEEE antennas and wireless propagation letters,* vol. 11, pp. 1508-1511, 2012.

[162] T. Saeed and Z. Iqbal, "A compact dual band implantable antenna design for biotelemetry applications using HFSS," in *Open Source Systems & Technologies (ICOSST), 2015 International Conference on*, 2015, pp. 165-169: IEEE.

[163] Y. Cho and H. Yoo, "Miniaturised dual-band implantable antenna for wireless biotelemetry," *Electronics Letters,* vol. 52, no. 12, pp. 1005-1007, 2016.

[164] L.-J. Xu, Y.-X. Guo, and W. Wu, "Dual-band implantable antenna with open-end slots on ground," *IEEE Antennas And Wireless Propagation Letters,* vol. 11, pp. 1564-1567, 2012.

[165] Y. Liu, Y. Chen, H. Lin, and F. H. Juwono, "A Novel Differentially Fed Compact Dual-Band Implantable Antenna for Biotelemetry Applications," *IEEE Antennas and Wireless Propagation Letters,* vol. 15, pp. 1791-1794, 2016.

[166] Z. Duan, Y.-X. Guo, R.-F. Xue, M. Je, and D.-L. Kwong, "Differentially fed dual-band implantable antenna for biomedical applications," *IEEE Transactions on Antennas and propagation,* vol. 60, no. 12, pp. 5587-5595, 2012.

[167] S. Xiao, C. Liu, Y. Li, X. M. Yang, and X. Liu, "Small-Size Dual-Antenna Implantable System for Biotelemetry Devices," *IEEE Antennas and Wireless Propagation Letters,* vol. 15, pp. 1723-1726, 2016.

[168] R. Das, Y. Cho, and H. Yoo, "High efficiency unidirectional wireless power transfer by a triple band deep-tissue implantable antenna," in *Microwave Symposium (IMS), 2016 IEEE MTT-S International*, 2016, pp. 1-4: IEEE.

[169] R. Das and H. Yoo, "A Multiband Antenna Associating Wireless Monitoring and Nonleaky Wireless Power Transfer System for Biomedical Implants," *IEEE Transactions on Microwave Theory and Techniques,* 2017.

[170] C.-K. Wu, T.-F. Chien, C.-L. Yang, and C.-H. Luo, "Design of novel S-shaped quad-band antenna for MedRadio/WMTS/ISM implantable biotelemetry applications," *International Journal of Antennas and Propagation,* vol. 2012, 2012.

[171] C.-L. Tsai, K.-W. Chen, and C.-L. Yang, "Implantable wideband low-SAR antenna with C-shaped coupled ground," *IEEE Antennas and Wireless Propagation Letters,* vol. 14, pp. 1594-1597, 2015.

[172] C.-L. Tsai, K.-W. Chen, and C.-L. Yang, "Implantable Wideband Low-Specific-Absorption-Rate Antenna on a Thin Flexible Substrate," *IEEE Antennas and Wireless Propagation Letters,* vol. 15, pp. 1048-1052, 2016.

[173] L. Huang *et al.*, "Ultra-Low Power Sensor Design for Wireless Body Area Networks-Challenges, Potential Solutions, and Applications," *JDCTA,* vol. 3, no. 3, pp. 136-148, 2009.

[174] B. Alarjani and J. Dahele, "Feed reactance of rectangular microstrip patch antenna with probe feed," *Electronics Letters,* vol. 36, no. 5, pp. 388-390, 2000.

[175] S. Gabriel, R. W. Lau, and C. Gabriel, "The dielectric properties of biological tissues: II. Measurements in the frequency range 10 Hz to 20 GHz," *Physics in Medicine and Biology,* vol. 41, no. 11, pp. 2251-2269, 1996.

[176] J. Nadobny *et al.*, "Experimental and numerical investigation of feed-point parameters in a 3-D hyperthermia applicator using different FDTD models of feed networks," *IEEE Transactions on Biomedical Engineering,* vol. 49, no. 11, pp. 1348-1359, 2002.

[177] C. H. Durney and M. F. Iskander, "Antennas for Medical Applications," in *Antenna Handbook: Theory, Applications, and Design*, Y. T. Lo and S. W. Lee, Eds. Boston, MA: Springer US, 1988, pp. 1729-1788.

[178] M. R. Horsman and J. Overgaard, "Hyperthermia: a potent enhancer of radiotherapy," *Clinical Oncology,* vol. 19, no. 6, pp. 418-426, 2007.

[179] M. Lazebnik *et al.*, "A large-scale study of the ultrawideband microwave dielectric properties of normal, benign and malignant breast tissues obtained from cancer surgeries," *Phys Med Biol,* vol. 52, 2007.

[180] M. Ettorre *et al.*, "On the near-field shaping and focusing capability of a radial line slot array," *IEEE Transactions on Antennas and Propagation,* vol. 62, no. 4, pp. 1991-1999, 2014.

[181] Y. J. Cheng and F. Xue, "Ka-band near-field-focused array antenna with variable focal point," *IEEE Transactions on Antennas and Propagation,* vol. 64, no. 5, pp. 1725-1732, 2016.

[182] J. L. Gómez-Tornero, D. Blanco, E. Rajo-Iglesias, and N. Llombart, "Holographic surface leaky-wave lenses with circularly-polarized focused near-fields—Part I: Concept, design and analysis theory," *IEEE Transactions on Antennas and Propagation,* vol. 61, no. 7, pp. 3475-3485, 2013.

[183] D. Blanco, J. L. Gómez-Tornero, E. Rajo-Iglesias, and N. Llombart, "Holographic surface leaky-wave lenses with circularly-polarized focused near-fields—Part II: Experiments and description of frequency steering of focal length," *IEEE Transactions on Antennas and Propagation,* vol. 61, no. 7, pp. 3486-3494, 2013.

[184] A. J. Martinez-Ros, J. L. Gómez-Tornero, and G. Goussetis, "Holographic pattern synthesis with modulated substrate integrated waveguide line-source leaky-wave antennas," *IEEE Transactions on Antennas and Propagation,* vol. 61, no. 7, pp. 3466-3474, 2013.

[185] F. Tofigh, J. Nourinia, M. Azarmanesh, and K. M. Khazaei, "Near-field focused array microstrip planar antenna for medical applications," *IEEE antennas and wireless propagation letters,* vol. 13, pp. 951-954, 2014.

[186] H.-T. Chou, N.-N. Wang, H.-H. Chou, and J.-H. Qiu, "An effective synthesis of planar array antennas for producing near-field contoured patterns," *IEEE Transactions on Antennas and Propagation,* vol. 59, no. 9, pp. 3224-3233, 2011.

[187] S. Karimkashi and A. A. Kishk, "Focusing properties of Fresnel zone plate lens antennas in the near-field region," *IEEE Transactions on Antennas and Propagation,* vol. 59, no. 5, pp. 1481-1487, 2011.

[188] S. H. Zainud-Deen, H. A. Malhat, and K. H. Awadalla, "8× 8 near-field focused circularly polarized cylindrical DRA array for RFID applications," *ACES Journal-Applied Computational Electromagnetics Society,* vol. 27, no. 1, p. 42, 2012.

[189] H.-T. Chou, T.-M. Hung, N.-N. Wang, H.-H. Chou, C. Tung, and P. Nepa, "Design of a near-field focused reflectarray antenna for 2.4 GHz RFID reader applications," *IEEE Transactions on Antennas and Propagation,* vol. 59, no. 3, pp. 1013-1018, 2011.

[190] J. Bor, S. Clauzier, O. Lafond, and M. Himdi, "60 GHz foam-based antenna for near-field focusing," *Electronics Letters,* vol. 50, no. 8, pp. 571-572, 2014.

[191] M. Bogosanovic and A. G. Williamson, "Microstrip Antenna Array With a Beam Focused in the Near-Field Zone for Application in Noncontact Microwave Industrial Inspection," *IEEE Transactions on Instrumentation and Measurement,* vol. 56, no. 6, pp. 2186-2195, 2007.

[192] H. D. Trefna, J. Vrba, and M. Persson, "Time-reversal focusing in microwave hyperthermia for deep-seated tumors," *Phys Med Biol,* vol. 55, 2010.

[193] S. Jacobsen and F. Melandso, "The concept of using multifrequency energy transmission to reduce hot-spots during deep-body hyperthermia," *Ann Biom Eng,* vol. 30, 2002.

[194] E. J. Gross, T. C. Ceetas, P. R. Stauffer, R. L. Liu, and M. L. Lumori, "Experimental assessment of phased-array heating of neck tumors," *Int J Hyperthermia,* vol. 6, 1990.

[195] E. Zastrow, S. C. Hagness, and B. D. Van Veen, "3D computational study of non-invasive patient-specific microwave hyperthermia treatment of breast cancer," *Physics in medicine and biology,* vol. 55, no. 13, p. 3611, 2010.

[196] F. Gozasht, M. D. Hossain, and A. S. Mohan, "Miniaturized E-shaped PIFA antenna for wideband implantable biomedical applications," in *2013 International Conference on Electromagnetics in Advanced Applications (ICEAA)*, 2013, pp. 832-835.

[197] K. J. Kim, W. C. Choi, and Y. J. Yoon, "Array structure for uniform heat distribution with modified dipole elements," in *2012 IEEE International Workshop on Antenna Technology (iWAT)*, 2012, pp. 358-361.

[198] D. Yang, M. C. Converse, D. M. Mahvi, and J. G. Webster, "Expanding the Bioheat Equation to Include Tissue Internal Water Evaporation During Heating," *IEEE Transactions on Biomedical Engineering,* vol. 54, no. 8, pp. 1382-1388, 2007.

[199] N. S. Karnik *et al.*, "Design, simulation and experimental study of near-field beam forming techniques using conformal waveguide arrays," *IET Microwaves, Antennas & Propagation,* vol. 4, no. 2, pp. 162-174, 2010.

[200] K. J. Kim, W. C. Choi, J. Kim, and Y. J. Yoon, "Penetration enhancement of non-invasive microwave hyperthermia applicator," in *The 8th European Conference on Antennas and Propagation (EuCAP 2014)*, 2014, pp. 1669-1670.

[201] C. Diederich and K. Hynynen, "The feasibility of using electrically focused ultrasound arrays to induce deep hyperthermia via body cavities," *IEEE transactions on ultrasonics, ferroelectrics, and frequency control,* vol. 38, no. 3, pp. 207-219, 1991.

[202] G. Oliveri, L. Poli, and A. Massa, "Maximum efficiency beam synthesis of radiating planar arrays for wireless power transmission," *IEEE Transactions on Antennas and Propagation,* vol. 61, no. 5, pp. 2490-2499, 2013.

[203] S. Karimkashi and A. A. Kishk, "Focused microstrip array antenna using a Dolph-Chebyshev near-field design," *IEEE Transactions on Antennas and Propagation,* vol. 57, no. 12, pp. 3813-3820, 2009.

[204] W. Geyi, "Foundations of applied electrodynamics," John Wiley & Sons, 2011, pp. 270-280.

[205] L. Shan and W. Geyi, "Optimal design of focused antenna arrays," *IEEE Transactions on Antennas and Propagation,* vol. 62, no. 11, pp. 5565-5571, 2014.

[206] J. Stang, M. Haynes, P. Carson, and M. Moghaddam, "A preclinical system prototype for focused microwave thermal therapy of the breast," *IEEE Transactions on Biomedical Engineering,* vol. 59, no. 9, pp. 2431-2438, 2012.

[207] W. C. Choi, K. J. Kim, J. Kim, and Y. J. Yoon, "Compact microwave radiator for improving heating uniformity in hyperthermia system," *IEEE Antennas and Wireless Propagation Letters,* vol. 13, pp. 1345-1348, 2014.